

The Pennsylvania State University
The Graduate School

CHARACTERIZATION AND APPLICATIONS OF HYBRID CMOS
DETECTORS IN X-RAY ASTRONOMY

A Dissertation in
Astronomy and Astrophysics
by
Stephen Bongiorno

© 2013 Stephen Bongiorno

Submitted in Partial Fulfillment
of the Requirements
for the Degree of

Doctor of Philosophy

August 2013

The dissertation of Stephen Bongiorno was reviewed and approved* by the following:

Abraham Falcone
Senior Research Associate and Associate Professor of Astronomy
Dissertation Advisor, Chair of Committee

David Burrows
Professor of Astronomy

Larry Ramsey
Professor of Astronomy

Mike Eracleous
Professor of Astronomy

Stephane Coutu
Professor of Physics

Donald Schneider
Professor of Astronomy
Department Head

*Signatures are on file in the Graduate School.

Abstract

The hybrid CMOS detector (HCD) is a powerful focal plane array (FPA) architecture that has begun to benefit the visible-infrared astronomical community and is poised to do the same for X-ray astronomy. Since Servicing Mission 4 in 2009, an HCD has given the Hubble Space Telescope's Wide-field Camera 3 improved imaging capability in the near-infrared. HCDs have been specified to operate at the focal plane of every science instrument on board the James Webb Space Telescope. A major goal of the Penn State X-ray Detector Group has been to modify the flexible HCD architecture to create high performance X-ray detectors that will achieve the currently unmet FPA requirements set by next-generation telescopes. These devices already exceed the radiation hardness, micrometeoroid tolerance, and high speed noise characteristics of current-generation X-ray charge coupled devices (CCDs), and they are on track to make a breakthrough in high count rate performance.

This dissertation will begin with a presentation of background material on the detection of X-rays with semiconductor devices. The physics relevant to photon detection will be discussed and a review of the detector development history that led to the current state of the art will be presented. Next, details of the HCDs that our group has developed will be presented, followed by noise, energy resolution, and interpixel capacitance measurements of these detectors. A large part of my work over the past several years has consisted of designing, building, and carrying out tests with a laboratory apparatus that measures the quantum efficiency of HCDs. Details of this design process as well as the successful measurements that resulted will be presented. The topic of discussion will then broaden to the HCD's current and future roles in X-ray astronomy. The dissertation will close with the presentation of a successful project that used *Swift* XRT data to confirm the binary nature of the TeV emitting object HESS J0632+057, making it one of five confirmed TeV high mass X-ray binaries.

Table of Contents

List of Figures	viii
List of Tables	xii
Acknowledgments	xiii
Chapter 1	
The Detection of X-rays with Silicon Devices	1
1.1 The Interaction of Radiation With Silicon	3
1.1.1 Photon Absorption and Charge Generation	4
1.1.1.1 Photon-matter Interaction Mechanisms	5
1.1.1.2 Consequences of the Solid State	6
1.1.2 Charge Collection	7
1.1.3 Charge Transfer and Readout	11
1.2 CCDs	13
1.2.1 Basic Operation	13
1.2.2 Advantages	14
1.2.3 Disadvantages	15
1.2.3.1 Destructive Readout	15
1.2.3.2 Power Consumption	16
1.2.3.3 Radiation Hardness	16
1.2.3.4 Pile-up	18
1.3 CMOS: A New Competitor in the X-ray	19
1.3.1 Monolithic CMOS	22
1.3.1.1 CTE and Radiation Hardness	22
1.3.2 Sensitivity	23
1.3.3 Hybrid CMOS Devices	23

1.3.3.1	The PIN diode	26
1.3.3.2	HCDs: The Good and the Bad	27
Chapter 2		
	PSU Detector Hardware	30
2.1	TIS HAWAII Arrays	30
2.1.1	Reference Pixels	33
2.1.2	Bare MUX	34
2.1.3	Anti-Reflection Coating	35
2.1.4	Filter Deposition	35
2.2	TIS SIDECAR TM	37
Chapter 3		
	Data Reduction and Measurements of HCD Characteristics	41
3.1	Test Stand	41
3.1.1	Temperature Control	41
3.1.2	Vacuum Chamber	42
3.1.3	X-ray Sources	42
3.2	Data Acquisition	43
3.2.1	Readout Schemes	43
3.2.2	FET Leakage Current	44
3.2.3	Row Noise Correction	45
3.2.4	Substrate Bias Optimization	47
3.3	Grading	49
3.4	System Gain	51
3.4.0.1	Preamplifier Gain Optimization	52
3.4.0.2	Gain Measurement	53
3.5	Interpixel Capacitance	54
3.5.1	Deconvolution	61
3.5.2	IPC Discussion	62
3.6	Read Noise	64
3.7	Energy Resolution	65
3.8	Permanent Threshold Shift	69
Chapter 4		
	Measurements of HCD quantum efficiency	73
4.1	Motivation	73
4.2	Various Methodologies	78
4.2.1	NIR and Optical QE	79
4.2.2	UV and X-ray QE	80

4.3	Experimental Design	84
4.3.1	Vacuum System	85
4.3.2	Cryogenics and Temperature Control	93
4.3.3	Laboratory X-ray Sources	101
4.3.4	Gas Flow Proportional Counter	115
4.3.5	Detector Alignment	135
4.4	Experimental Result	137
4.4.1	Window Calibration Result	137
4.4.2	QE Data Acquisition	138
4.4.3	H1RG QE Data Reduction	142
4.4.4	Proportional Counter Data Reduction	145
4.4.5	QE Result	147
4.4.6	QE Error Analysis	150
4.5	Modeling HCD Quantum Efficiency	153
4.6	Future QE Measurements	155
Chapter 5		
	The future use of HCDs in X-ray astronomy	156
5.1	Small Missions	156
5.2	Large Missions	157
Chapter 6		
	The X-ray Confirmation of HESS J0632+057 as a γ-ray Binary	158
6.1	Introduction	158
6.2	The Observations	160
6.3	Analysis	161
6.4	Results	162
6.4.1	Peak Fitting	163
6.4.2	Lomb-Scargle	164
6.4.3	Autocorrelation	165
6.4.4	Significance of the Period	166
6.5	Discussion & Conclusions	168
Appendix A		
	Mechanical Drawings	172
A.1	Introduction	172
Appendix B		
	Electronics Schematics	189
B.1	Introduction	189

B.2	QE Test Stand	189
B.2.1	Heater Power Supply	189
B.2.2	RTD Current Source	195
Appendix C		
	Code	201
C.1	Introduction	201
C.2	Data Reduction	201
C.3	QE Teststand	234
C.4	Thesis	274
	Bibliography	276

List of Figures

1.1	Energy level splitting	7
1.2	Energy levels of a solid	8
1.3	Semiconductors used in photon detectors	9
1.4	CCD operation	14
1.5	Passive and active pixel sensors	21
1.6	APS amplifiers	21
1.7	HyViSI TM cutaway schematic	24
1.8	PN junction band structure	27
2.1	H1RG-125 picture	32
2.2	Simplified HxRG electronics schematic	35
2.3	<i>Suzaku</i> OBF transmission	37
2.4	<i>Chandra</i> OBF transmission	38
2.5	JWST SIDECAR TM	39
3.1	Cube chamber picture	43
3.2	SIDECAR TM signal chain	46
3.3	Row noise subtraction	47
3.4	Simulation of charge cloud spreading as a function of bias voltage	48
3.5	Measurement of charge cloud spreading as a function of bias voltage	49
3.6	Percent split histogram	51
3.7	Low secondary threshold spectrum	54
3.8	Event pixel number distribution	55
3.9	Line emission peak position as a function of energy	56
3.10	Schematic of the 5 pixel IPC model	57
3.11	Copper L and Manganese K X-ray images showing charge spreading and IPC	58
3.12	IPC deconvolution	63
3.13	Aluminum, chlorine, and manganese combined spectrum	67
3.14	Energy resolution as a function of energy	68
3.15	Optimized secondary event thresholds as a function of energy	69

3.16	Manganese spectrum optimized for energy resolution	70
3.17	Permanent threshold shift	71
4.1	Example optical QE(E) for an H2RG	75
4.2	Density of states in silicon	76
4.3	Reflectance and absorption coefficient for silicon as a function of energy	78
4.4	Silicon photodiodes from IRD	81
4.5	Synchrotron X-ray light source facility layout	83
4.6	QE measurement apparatus used by Kenter <i>et al.</i>	84
4.7	Drawing of the QE test-stand in the PSU vacuum chamber	85
4.8	X-ray transmission through air, vacuum, and helium	87
4.9	Sublimation curve on the phase diagram of water	88
4.10	Routing layout of the QE test-stand	94
4.11	Mechanical drawing of the QE test-stand	98
4.12	Picture of the disassembled cryostat cold strap	102
4.13	Temperature data of the test-stand dewar and H1RG during QE data acquisition	103
4.14	Electronic transitions that produce X-ray emission	104
4.15	X-ray generation, active layer self-attenuation, and sealant layer attenuation in the VZ-2937 ^{55}Fe source	108
4.16	^{55}Mn $K\beta/K\alpha$ line ratio plotted as a function of angle with respect to the source normal	109
4.17	Exploded diagram of the ^{55}Fe source holder	110
4.18	Schematic of a simple α particle fluorescent X-ray source	111
4.19	Technical drawing of a Henke tube X-ray source	112
4.20	Diagram of a typical Manson X-ray tube	113
4.21	Cross-section view of a coil of filament wire	115
4.22	Cross-section schematic detailing the gas flow proportional counter theory of operation	117
4.23	Typical gas gain and count rate behavior as a function of propor- tional counter anode voltage	120
4.24	Oscilloscope measurements of proportional counter output	124
4.25	Results of the proportional counter dead time experiment	125
4.26	Mechanical failure of a proportional counter window	130
4.27	Comparison of PSU X-ray transmission and cross section code out- put to NIST and LBNL code outputs	133
4.28	Vector diagram of the detector alignment parameters	137
4.29	Pixel value distribution of the center (brightest) pixel of events detected with a primary threshold of 40 DN	143

4.30	Energy spectrum of the total charge in events, summed using a 39 DN secondary threshold	144
4.31	Combined HIRG data set	145
4.32	Background subtracted proportional counter spectra acquired dur- ing QE data acquisition	147
4.33	QE error analysis Monte-Carlo result	152
4.34	Slab model of QE as a function of X-ray energy	154
6.1	Background-subtracted X-ray light curve of XMMU J063259.3+054801 from <i>Swift</i> -XRT observations	167
6.2	Lomb-Scargle periodogram of <i>Swift</i> -XRT data	168
6.3	z -transformed discrete correlation function as a function of time lag	169
6.4	X-ray light curve of XMMU J063259.3+054801 folded over the pro- posed period of 321 days	170
A.1	Carriage frame from Ralph A. Hiller Company	173
A.2	Detector module frame from Ralph A. Hiller Company.	174
A.3	Detector module breadboard.	175
A.4	Detector pedestal bottom plate.	176
A.5	Detector pedestal side strut.	177
A.6	Detector pedestal top plate.	178
A.7	Liquid nitrogen vessel	179
A.8	Henke tube source port plate	180
A.9	Port plate containing all of the QE test stand feedthroughs	181
A.10	Spacers that allow attaching the fluorescent target wheel to the Henke tube source port plate	183
A.11	<i>Top</i> , the source port plate. <i>Bottom</i> , the source shutter.	184
A.12	The source holder rod and shutter rotational feedthrough shaft.	185
A.13	The source shield.	186
A.14	An exploded view of the source plate.	187
A.15	Proportional counter window plate.	188
B.1	Schematic of the 4-channel heater power supply.	192
B.2	Heater power amplifier top surface silk screen.	193
B.3	Heater power amplifier top copper trace deposition.	193
B.4	Heater power amplifier upper inner power plane.	194
B.5	Heater power amplifier lower inner ground plane.	194
B.6	Heater power amplifier bottom copper trace deposition.	195
B.7	Difference amplifier configuration	196
B.8	Schematic of the 6-channel RTD current source.	197

B.9	Current source top surface silk screen.	198
B.10	Current source top layer copper deposition.	198
B.11	Current source top inner copper layer.	199
B.12	Current source bottom inner copper layer.	199
B.13	Current source bottom layer copper deposition.	200

List of Tables

1.1	Definition of the electromagnetic spectrum	2
2.1	Penn State HCDs	31
3.1	Fluorescent X-ray line sources	53
3.2	Second brightest pixel and standard deviation measured IPC results	59
3.3	Paired pixel IPC results	60
4.1	A definition of vacuum regimes	86
4.2	Outgassing rates of common vacuum materials	91
4.3	X-ray emission line energies of materials commonly used as X-ray sources.	105
4.4	Alignment rangefinder data for both the H1RG and proportional counter	136
4.5	Summary of data taken to calibrate the proportional counter window	139
4.6	Summary of H1RG quantum efficiency data	141
4.7	Summary of proportional counter quantum efficiency data	141
4.8	Summarized metrology of the measured parameters that enter into the H1RG QE calculation and their associated 1σ uncertainties . .	151

Acknowledgments

Thank you, Abe Falcone, for allowing me the freedom to solve problems my own way and for being generous with your time when my direction wandered astray of a productive path and required adjustment. I promise to always do a back of the envelope calculation before I spend 2 weeks writing a numerical simulation.

Thank you, Dave Burrows, for happily sharing your encyclopedic knowledge of detector hardware with me.

Thank you, Mom and Dad, for supporting my interest in science from an early age and for your unwavering support as I pursued a career path with questionable employment prospects.

Thank you, Jing Liang, for your love, support, and technical advice while I completed this work. While we both completed our dissertations, our relationship deepened and somehow we both managed to get more yoked at the same time. I aspire to live in the present as you do.

Chapter 1

The Detection of X-rays with Silicon Devices

For as long as humans have possessed an observant eye and inquisitive mind, we have been gazing upwards at the sky, wondering what governed the behavior of the sun and moon, what were the seemingly unchanging points and swaths of light visible at night, and how far the darkness reached. Considering the millennia over which these questions have been posed, the human eye was the only detector at our disposal for the vast majority of this study. While the eye is a fantastic, highly functional piece of biological machinery, it makes for a fickle scientific photodetector. The brain does a marvelous job of concealing the fact that our eyes have varying spatial response (blind spots, off-axis intensity/color sensitivity variation), non-uniform energy response, and saturation limits with significant persistence effects. This, coupled with the subjectivity of our ability to accurately quantify phenomena observed by eye, limited progress in the study of astrophysics for many centuries. Over the past 150 years, there has been an explosively productive symbiotic relationship between technological innovation and scientific progress. Astronomers now have at their disposal a vast array of highly optimized and ever-improving detectors with their combined sensitivities covering much of the electromagnetic spectrum, from radio waves to γ -rays. See Table 1.1 for a definition of electromagnetic radiation energy regimes. The performance of some of these detectors is approaching limits that are set not by manufacturing precision or design ingenuity, but by physics. Amazingly, it can almost be taken

for granted that for every advancement in instrument capability, some existing questions will be answered and new ones will be inspired.

Regime	Frequency	Wavelength	Energy
	<100 kHz	> 3 km	< $4 \cdot 10^{-10}$ eV
Radio	1 GHz	30 cm	$4 \cdot 10^{-6}$ eV
Microwave	0.3 THz	1 mm	$1.2 \cdot 10^{-3}$ eV
Sub-mm	3 THz	100 μm	$1.2 \cdot 10^{-2}$ eV
Infrared	$4 \cdot 10^{14}$ Hz	750 nm	1.65 eV
Optical	$0.75 \cdot 10^{15}$ Hz	400 nm	3.1 eV
Ultra-violet	$2.4 \cdot 10^{16}$ Hz	12.4 Å	0.1 keV
Soft X-ray	$2.4 \cdot 10^{18}$ Hz	1.2 Å	10 keV
Hard X-ray	$2.4 \cdot 10^{19}$ Hz	$1.2 \cdot 10^{-11}$ m	100 keV
γ -ray	$2.4 \cdot 10^{25}$ Hz	$1.2 \cdot 10^{-17}$ m	100 GeV
VHE γ -ray	> $3 \cdot 10^{26}$ Hz	< $1 \cdot 10^{-18}$ m	>1 TeV

Table 1.1: Despite the electromagnetic energy spectrum being continuous, it has been divided into regimes to aid in communicating about different energies of radiation. Shown here is a definition of the electromagnetic radiation energy regimes that concentrates on high energy and ignores the many sub-divisions of the radio, microwave, sub-mm, and infrared bands. Since this dissertation will deal solely with soft X-ray detectors, the regime has been highlighted. The left-most column's vertical offset indicates that each number is the dividing point between the regimes above and below it. Some of the boundary definitions are arbitrary while some are due to particular generation/detection mechanisms/technologies that apply only to certain energy ranges. While the frequency, wavelength, and energy of a photon are all interchangeable terms, the quantities shown in bold are those most commonly used in the literature. VHE abbreviates Very High Energy.

A detector can be broadly defined as any device that produces an observable response when it is exposed to radiation. Most generally, detectors can be categorized as either photon, thermal, or coherent, based on how that response is produced. In photon detectors, bound states absorb and are altered by the energy of incident photons. In the eye or a photographic emulsion these are chemical states, while in electronic detectors, they are charge carrier states. In thermal detectors, incident photon energy is absorbed into the detector material, raising

its temperature. In coherent receivers, the oscillating electric field of an incoming electromagnetic wave produces a voltage signal that, when combined with the signal of a local oscillator, can be directly detected. This dissertation will cover the performance characterization and relevant astrophysics applications of novel variants on a specific type of photon detector, an X-ray sensitive device made from an array of silicon PIN diodes hybridized to a CMOS readout circuit. The device is called the Hybrid CMOS detector (HCD). The goal of this body of work has been to test a batch of these detectors and further the technology's long-term development toward astrophysics applications. It will be shown that HCDs are already an efficient choice for small X-ray missions, due to their low power consumption, and that they may become the optimal detector for future large-aperture telescopes, due to their novel readout capabilities.

This dissertation will be arranged as follows. The remainder of this introductory chapter contains a general discussion of the history and physics associated with detecting X-rays with silicon array devices. Chapter 2 presents details of the readout device and prototype HCDs tested in the project. A description of the data reduction pipeline developed specifically for these detectors will be included. Chapter 3 contains the results of the detector characterization, specifically read noise, energy resolution, and inter-pixel capacitance. Chapter 4 details the design and fabrication of, and results obtained from, an apparatus built for measuring the quantum efficiency of HCDs. Chapter 5 outlines the existing and potential science applications of these devices. Chapter 6 concludes the dissertation with a presentation of the X-ray data and analysis that led to the discovery of a new TeV γ -ray binary, HESS J0632+057. The work was accomplished with data acquired with the *Swift* observatory. A brief discussion of how similar work may be carried out in the future using HCDs will conclude Chapter 6.

1.1 The Interaction of Radiation With Silicon

Modern, silicon-based semiconductor device fabrication is arguably the most advanced technology ever developed by humans. Ultra-high resistivity silicon in the ingots used for electronics manufacturing is the purest commercially produced material, with impurity concentrations approaching 0.1 parts per trillion. The in-

dustry achieved its current state because the broad prospective appeal of silicon devices fueled the justification of further developmental research, which yielded new scientific discovery and even broader prospective appeal. The story of silicon photodetectors, like many advanced technologies, draws from the success of a mountain of prior research. From Becquerel's 1885 observation of the photovoltaic effect, to Einstein's 1910 theoretical explanation of the photoelectric effect, to Czochralski's 1916 invention of a single crystal silicon growth method, to Nishizawa's 1955 invention of the PIN diode, to Wanlass's 1967 invention of CMOS circuitry, the development of the HCD has certainly been a long time in the making. Before narrowing the focus of this chapter to the HCDs themselves, it might be instructive to first explore the details of how radiation detection occurs in depleted semiconductor devices.

Any biased-semiconductor photon detector has to perform four main functions in order to detect light: photon absorption and charge generation, charge collection, charge transfer, and charge readout.

1.1.1 Photon Absorption and Charge Generation

The detection process begins when a photon enters a detector's active volume. In order for charge to be generated, the photon must interact with the material in some way and transfer at least a fraction of its energy to the material in the process. The probability that an interaction will occur depends on the energy of the photon, the composition of the material, and the physical mechanism through which the interaction occurs. The three mechanisms available in the photon-matter interaction are bound state absorption, Compton scattering, and pair production. The chance that an incident photon will interact with an atom via a particular mechanism is characterized by the cross section, $\sigma(E, Z)$, of that mechanism. Cross section is defined as an area, although it is commonly written as cross section per quantity of matter, usually $\text{cm}^2 \text{ gram}^{-1}$ or barns atom^{-1} and is dependent on both photon energy, E , and the atomic number, Z , of the absorbing atomic species.

1.1.1.1 Photon-matter Interaction Mechanisms

In the pair production mechanism, a photon interacts with the strong field of an atomic nucleus, transforming into a positron and an electron with total kinetic energy $h\nu - (m_{e^-} + m_{e^+})c^2$, where m_{e^-} and m_{e^+} are the rest masses of an electron and a positron, respectively. This mechanism is only available if the photon's energy is greater than the electron-positron pair's rest mass (1.022 MeV) and therefore only has an effect in γ -ray detection.

Compton scattering occurs when a photon scatters off of either a bound or free electron, imparting a fraction of its energy to the electron in the process. After the interaction, both propagate in directions that conserve momentum. This mechanism only begins to dominate the total cross section for incident photon energies greater than 100 keV and for absorption in very light atomic species where the photoelectric cross section is small.

Photoelectric absorption occurs when an incident photon's energy is completely absorbed by a bound electron. It is the dominant cross section for photon energies in the soft X-ray and below. When photon energy equals the energy of a transition, be that transition between two bound electron states, molecular energy state, or the binding energy of an electronic state, the cross section of this level is at its maximum. As photon energy increases past the transition energy, the cross section of this particular transition drops. A relevant consequence of this concept is that low-energy electronic transitions dominate the photoelectric cross section for low-energy photon illumination, and inner-shell ionizations dominate the cross section for photons in the keV range. For the remainder of the text, when I speak of cross sections, unless otherwise noted, it is the photoelectric cross section that is being implied due to its dominance in the soft X-ray and optical bands.

Since the contribution of scattering and stimulated emission are negligible and absorption will dominate the interaction of soft X-rays with the detector, the radiative transfer equation simplifies to $I/I_0 = \exp(-\sigma(E, Z) dn)$, where I/I_0 is the ratio of the intensity at penetration depth, d , to the initial intensity, the cross section, σ , per unit atom has units $\text{cm}^2 \text{atom}^{-1}$, and n is the number density of absorbers. I/I_0 is also known as the transmission fraction. This leads to the greatest number of absorptions per unit depth occurring at the surface. Mathematically, this can be shown by differentiating the transmission equation with

respect to depth, which results in another exponential. Qualitatively, it can be justified by noting that if the absorbing material is divided into differential slabs normal to the surface and the incident beam is only attenuated, the flux entering subsequent slabs, and therefore the amount of absorption that occurs in the slab, will progressively decrease. For high cross section interactions, this leads to most of the absorptions occurring near the front surface of the volume. For low cross section interactions, the number density of absorptions will approach a uniform distribution as a function of depth through the volume.

1.1.1.2 Consequences of the Solid State

When photons illuminate a solid instead of isolated atoms, the picture changes slightly. As two atoms are brought closer together, their respective electric fields begin to perturb the other atom's energy levels and cause them to split, as shown in Figure 1.1. When many atoms are arranged closely together as in a solid, the discrete energy levels become pseudo-continuous bands due to the splitting action of the many atoms in the solid, which lie at a range of distances. Figure 1.2 shows the band structure of a solid. Generally speaking, electrical insulators are solids where the valence band is nearly filled and the energy gap between the valence and conduction bands, called the band gap, is large. Since the valence electrons in such a solid cannot gain any energy in their crowded band and rarely have enough energy to jump the large band gap, they cannot gain the kinetic energy required to move and form a current, which results in the solid being a poor electrical conductor. If the valence band is unfilled or the conduction band overlaps with the valence band, there will be many allowed energies that an electron can take, and the material is a good electrical conductor. Semiconductors are special materials where the valence band and conduction band are separated in energy by a small band gap. These materials can be made into excellent detectors because photons with energies greater than the band gap excite electrons into an empty conduction band where they are mobile and can physically move through the solid to a collection point and be read as a voltage. While there are a number of compounds that can be coaxed into behaving like semiconductors, a more difficult problem is finding semiconductor materials with amenable physical properties. For example, exotic semiconductors can be extremely brittle, difficult to grow with high purity, or

difficult to bond with metal contacts and integrate with electronics. A variety of semiconductors that have been successfully fabricated into detector devices are shown in Figure 1.3.

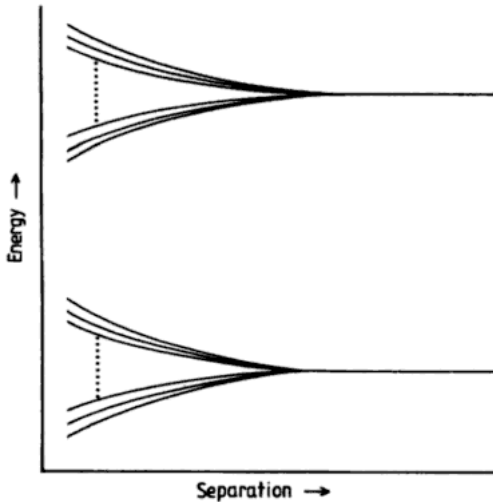


Figure 1.1: Shown is the effect where as the separation between two atoms decreases, the splitting of their energy levels increases. When many atoms are brought close together, the split levels form semicontinuous bands. Figure borrowed from *Astrophysical Techniques* [1].

1.1.2 Charge Collection

With design features that vary between styles of detectors, semiconductor detectors are able to collect the charge generated by photoelectric absorption by creating an active region. The active region is depleted of free charge carriers by an electric field that fills the region, permeating the semiconductor's bulk. Accordingly, this region is called the depletion region and it is where the detector is most readily able to detect photons. The charge carrier concentrations of a particular material are determined by its intrinsic properties or doping level. An intrinsic semiconductor is a pure semiconductor where the number and polarity of charge carriers in the bands is a property of the material. n-doped semiconductors are intrinsic materials that have been doped, or mixed in very small amounts, with an element that has one or more valence electrons than the element(s) in the intrinsic material. p-doped semiconductors are intrinsic materials doped with an element that has one or

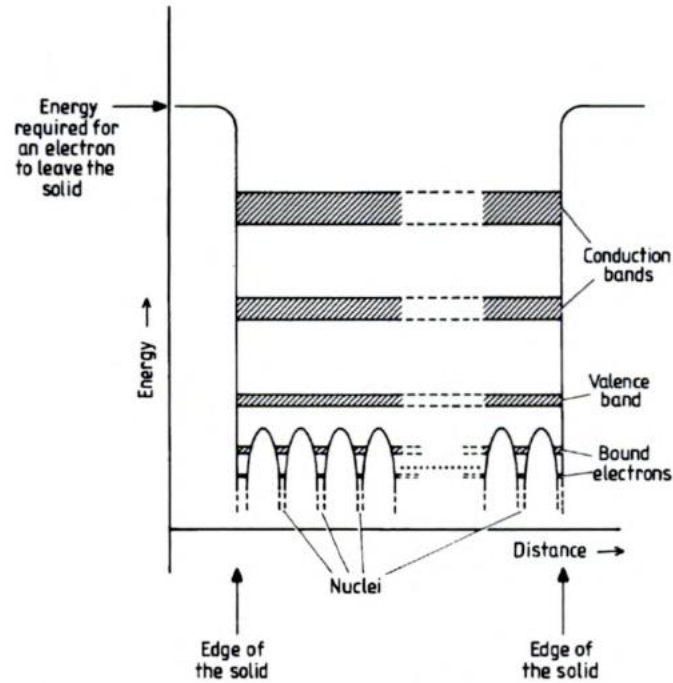


Figure 1.2: The energy level diagram for a solid. Figure borrowed from *Astrophysical Techniques* [1].

fewer electrons than the intrinsic material. n-doped and p-doped semiconductors are so-named because their majority charge carriers are negative and positive, respectively. Positive charge carriers in a semiconductor are called holes. Most literally, they are an unoccupied space in a sea of electrons that fills the valence band, but they can be treated like a positively charged particle with an effective mass and effective mobility in the solid.

The electric field in the depletion region applies a force to free charge carriers generated in the bulk and confines them in a potential well where there are no opposite polarity carriers to recombine with them. When a Near-IR or optical photon is absorbed by a valence electron in the depletion region, it promotes the electron into the conduction band where it is now a free charge carrier, capable of drifting into the potential well. For an ideal detector with linear response, the number of electrons in the well is proportional to the flux incident on the pixel. When an X-ray is absorbed by an inner-shell electron in the depletion region, the electron has enough kinetic energy to excite other electrons into the

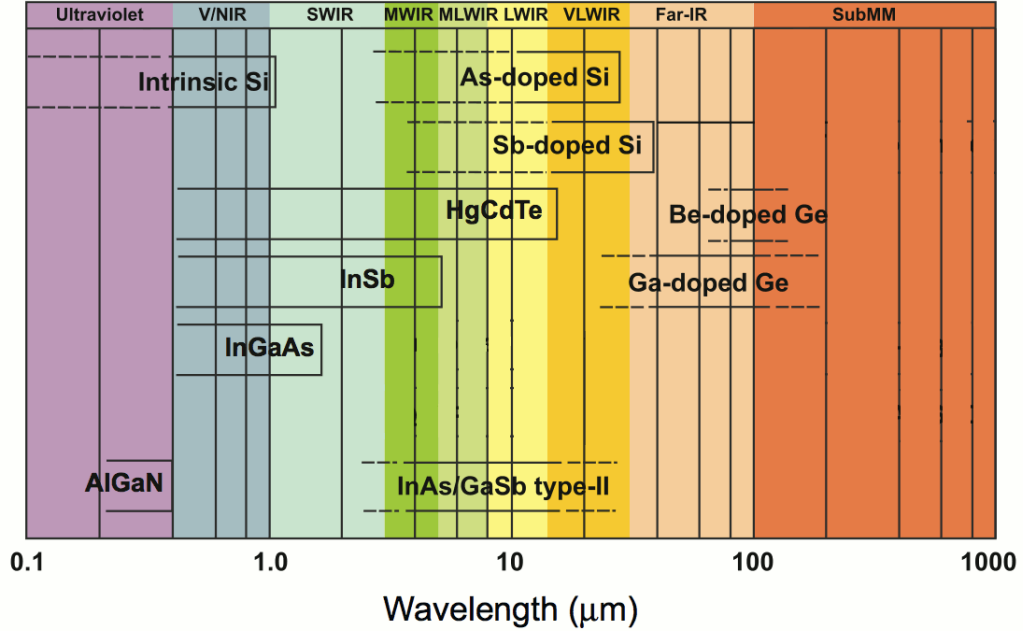


Figure 1.3: The wavelength sensitivity of various semiconductors when used in photon counting detectors. Note, this dissertation will focus on detectors with absorbers made from intrinsic silicon. Figure borrowed from Rogalski [2].

conduction band as it zips through the lattice, losing most of its energy to collisions with bound electrons along its path. In silicon, the transition from producing one electron-hole pair per absorbed photon to distributing an absorbed photon's energy across multiple electron-hole pairs happens in the ultra-violet when incident photon energies are greater than 3.3 eV [3]. Since an electron's mean free path in silicon is very small, the resulting cloud of charge, which starts as a $\sim 1 \mu\text{m}$ wide cloud for a 10 keV X-ray [4], is likely to be initially contained by a single pixel. The number of electrons created in the cloud, which is also called the quantum yield, is

$$\langle N_{e^-} \rangle = \frac{E}{\omega} \quad (1.1)$$

where E is the energy of the incident X-ray and $\omega = 3.68 \text{ eV}$ [5] is the average electron-hole pair creation energy in silicon. The fact that, in silicon devices, X-rays produce a signal proportional to an absorbed photon's energy is the basis of very useful feature; the detectors are simultaneously efficient imagers and low resolution spectrographs. The number of electrons produced in the cloud is shown

as an average number in Equation 1.1 because there is an inherent uncertainty in the number of electron-hole pairs created by a photon. In an over-simplified picture of X-ray absorption, all of the photon's energy would be transformed into the generation of electron-hole pairs and there would be no uncertainty. However, complexities of solid state physics, such as electron-phonon interaction, lead to the spurious addition or subtraction of energy from the process of converting a high-energy electron's kinetic energy into electron-hole pair creation. The discrete pair generation process is not entirely random, in which case the variance would be proportional to the number of pairs as with a Poisson distribution, nor is it deterministic, where the variance would be zero. The Fano factor, F , is a number between 0 and 1 that characterizes the fractional randomness of a particular pair generation process in a particular medium [6]. Although it was initially developed to characterize the uncertainty in electron-ion pair generation in particle counters, the theory applies just as well to the case of X-ray absorption in silicon. In this case, the factor characterizes electrons generating electron-hole pairs in a silicon lattice and has been experimentally measured to be 0.158 [6, 7]. The variance in the number of electron-hole pairs in the cloud due to this effect, the so-called Fano noise, is

$$\sigma_F^2 = \frac{FE}{\omega}. \quad (1.2)$$

This quantity is the lower limit on the precision with which an absorbed X-ray's energy can be measured in silicon. In general, a detector's ability to measure the energy of an absorbed X-ray, which includes many factors such as Fano noise, read noise, charge spreading, and post processing, is called the detector's *energy resolution* and it is one of the important metrics that will later be used to judge the performance of HCDs. Energy resolution is usually quoted as the full width at half maximum (FWHM) of an emission line in an energy spectrum.

As the cloud of electrons generated by an absorbed X-ray drifts towards the potential wells of the detector pixels, the electrons continue to scatter off fixed charges in the lattice. Instead of resulting in more electron-hole pair generation, these scattering events only cause the cloud to diffuse outwards and increase in size. Depending on where the X-ray was absorbed in the silicon, the cloud could

be split between two or more pixels, creating what is called a split event. Split events require that the signal, and its associated noise, from more than one pixel be summed to reconstruct the total energy deposited in the detector.

Irrespective of the details of a detector's construction, electric field strength, or bias voltage levels, there are electron-hole pairs being spontaneously created and recombining continually in any given volume of semiconductor. The energy to create these pairs comes from phonons, the quanta of lattice vibration energy that are buzzing around in any solid with a temperature above absolute zero. Pairs thermally created in the depletion region will drift into the potential well, just as if they were created by photon absorption. This contaminant signal is called *dark current* and not only does it produce a signal that can cause detectors to saturate, but the charge carriers it adds into the potential well also give it an associated Poisson distributed noise term that cannot be subtracted out. As with any noise source, it is usually best to minimize dark current. A higher temperature in the material is equivalent to a higher energy phonon energy distribution, which leads to an increased rate of electron-hole pair creation in the bulk, making dark current correlated to detector temperature. In addition to the bulk dark current, which can be generated both in and outside of the depletion region since some charge carriers will diffuse into the depletion region by chance, dark current is also generated at band gap deformation sites called surface states. At the boundary between the depleted bulk and the material that borders it (usually an oxide), irregularities in the lattice cause irregularities in the band structure, which can severely leak dark current if they are not addressed with special design techniques.

1.1.3 Charge Transfer and Readout

After being collected in the potential well, photo-charge is then transferred to the readout node, a component that functions like a capacitor, allowing the charge to be converted into a voltage signal. The uncertainty in this pixel voltage measurement is referred to as *read noise*, and is another important detector performance characteristic. When the readout electronics are reset between pixel reads, the value at which they settle has some uncertainty to it that is known as *reset noise*. This uncertainty can be reduced by a technique known as correlated double sam-

pling (CDS). In this technique, the output signal is sampled during reset, sampled a second time after the read pixel's value is transferred to the output node, and the two values are subtracted to yield the final output. This can be implemented through various circuit designs, including analog sample and hold and dual slope digitization, and also accomplished digitally in post-processing.

After the pixel charge is converted to a voltage, the signal is amplified and then digitized by an analog to digital converter (ADC). The integer output of the ADC, a unit referred to as a digital number (DN), is then recorded by a computer. The conversion gain, G [e^-/DN], is a number that accounts for the total gain of the detection process, from charge, to voltage, to amplified signal, to digital number. Note that this gain convention is the inverse of the typical sense, where increased gain usually results in greater output for a given input.

Combining detector performance characteristics and including instrument and light source properties, one can estimate an upper limit for the signal to noise ratio (S/N) of the data. In the near-IR and optical bands, where the quantum yield of silicon is unity, the signal to noise ratio in a given pixel will be

$$\frac{S}{N} = \frac{F_{\text{obj}} \text{QE} t}{\sqrt{[(F_{\text{obj}} + F_{\text{sky}} + F_{\text{bg}}) \text{QE} + D] t + \sigma_R^2 + (\frac{G}{2})^2}} \sqrt{n_{\text{pix}}}, \quad (1.3)$$

where F_{obj} is the photon flux of the object, F_{sky} is the photon flux of the sky, F_{bg} is the photon flux of the background, QE is the quantum efficiency of the detector, t is the integration time, D is the dark current count rate in $e^- \text{ s}^{-1}$, σ_R read noise of the detector in electrons, n_{pix} is the number of pixels used to record the object's flux, and the $(G/2)^2$ factor is quantization noise. While it may not seem necessary to distinguish between sky and background flux, in the case of mid-IR observations the difference is important because thermal emission from instrument optics contributes significantly to the background. In the X-ray band, where the quantum yield is much greater than 1, it is more useful to calculate S/N for individual X-ray events. In this case, the S/N expression must be multiplied by a factor of $\sqrt{E/\omega}$ to correctly account for the number of electrons that are generated by the absorbed X-ray. Also in this case, n_{pix} refers to the number of pixels covered by each event, leading to the dependence of S/N on event geometry. This effect will be further discussed in Chapter 3.

1.2 CCDs

1.2.1 Basic Operation

The charge-coupled device (CCD) was the first widely-successful pixellated solid state detector. Very generally, the device is built by patterning an array of metal-oxide-semiconductor (MOS) capacitors onto a p- or n-type silicon substrate with photolithographic techniques. A schematic of the CCD's structure is shown in Figure 1.4. When a voltage is applied to the surface electrode (also called the gate), the mobile charge carriers in the doped substrate are driven away from the surface, creating a depletion region below the electrode.

The process of photon absorption described in the previous section adequately describes how light is absorbed in a CCD, but this process is not unique to the CCD since it describes the light absorption process in all biased semiconductor devices. However, the process that is unique to the CCD, and the feature from which its name is derived, is the method by which the charge is read out. The CCD measures the charge in each pixel by transferring the packets of charge in each pixel through the bulk of the detector to one or more readout amplifiers positioned near the edge of the array. As seen in Figure 1.4, electrodes deposited on the surface of the substrate, usually three per pixel, form a potential well in each pixel when they are positively biased. The electrode-induced well confines charge along the direction of the column. The columns are separated by p+ doped (heavily doped) borders, called channel stops, which confine the charge in the direction perpendicular to the column direction. Slow, synchronous clocking of the three electrodes transfers the charge in each pixel vertically down each column, in parallel, to a horizontal serial register row at the bottom of the chip. The serial row is then quickly clocked so that once per fast clock cycle, a pixel's charge is transferred to the output node, where it is converted into a voltage. A cartoon that visualizes this so-called bucket-brigade charge transfer and readout is shown in Figure 1.4. The output signal is then amplified and digitized off-chip. Once per column clock cycle (slow), a new row of pixel charge is transferred to the serial register.

Following the invention of the CCD in 1970 [10, 11] and the first report of the CCD's sensitivity to X-rays in 1977 [12], Burrows *et al.* were the first to use a CCD for X-ray astronomy in 1989 [13]. The device has undergone extensive development

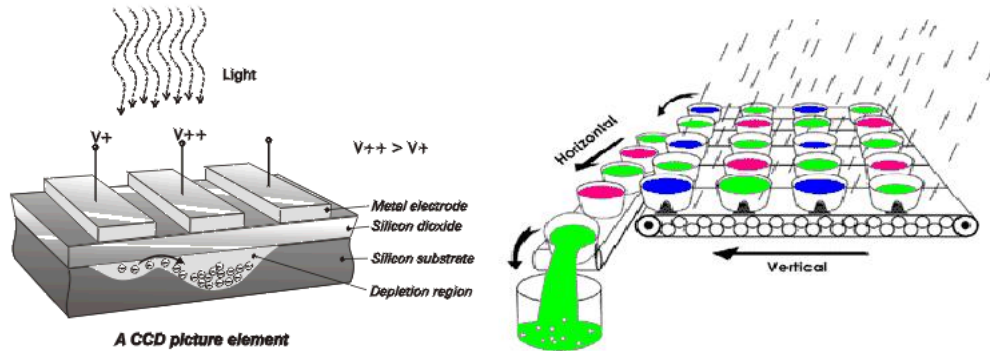


Figure 1.4: *Left* A diagram of a single CCD pixel showing the three electrodes that enable charge transfer to occur. *Right*, a diagram that literally uses buckets to illustrate the bucket-brigade readout scheme that CCDs use to transfer charge down the vertical columns and across the horizontal serial register to the readout node. Figures adapted from content on the web [8, 9].

since its invention and a vast array of designs that are significantly more complex and capable than the simplified picture described above are readily available on the market. Due to sub-electron read noise, extremely low dark current in pinned phase devices, the availability of enormous format sizes up to $10k \times 10k$, and Fano-limited energy resolution in the X-ray band, the CCD has been the optimal choice in many commercial and scientific applications for many years.

1.2.2 Advantages

While the CCD's operational method of transferring charge across the entire bulk of a detector may seem like an unusually difficult way to measure the signal in each pixel, not only does it get the job done, but it gives the device two subtle advantages. In ground-based optical surveys, where it is desirable to image large areas of sky, the technique of drift scanning is sometimes used. In this technique, the telescope is kept stationary, the CCD's columns aligned with the diurnal movement of the sky, and the CCD's columns are clocked so that as the image of a star moves down the chip, the cloud of photo-charge that it generates is transferred down the chip at the same rate. With this technique it is possible to image large swaths of sky at a constant airmass without the complication of telescope guiding. Another advantage of the CCD's charge transfer process is that of on-chip binning. If less

spatial resolution is required of a detector in a particular application, perhaps due to the optical point spread function (PSF) being oversampled or the desire for faster frame rates, the array clocking patterns can be altered so that charge from multiple pixels is combined (binned) on-chip before it is read out. Binning charge on-chip is essentially noiseless, so it eliminates the addition of extra read noise due to extra pixel reads required to bin digitally. Also, it eliminates the extra read time required to measure the voltage in those pixels that would have eventually been added together in a computer. In the Hobby Eberly Telescope's High Resolution Spectrograph, variable on-chip binning is used to efficiently match the detectors' spatial resolutions to the variety of dispersions produced by different operational modes of the spectrograph. Additionally, since the spectrograph is fiber fed, spatial resolution perpendicular to the dispersion direction is marginally useful. There exists the option to bin in this direction to decrease readout time and the size of data products. On the *Swift* XRT, pixel binning is used to achieve higher frame rates in the instrument's windowed timing mode.

1.2.3 Disadvantages

Despite the many strengths of CCD technology, its inherent weaknesses, such as high power consumption, destructive charge readout, limited radiation hardness, and pile-up in X-ray applications, have left room for new technologies to replace it.

1.2.3.1 Destructive Readout

The readout of a CCD is a destructive process, where once the charge in a pixel has been transferred to the readout node, sampled, and the next pixel clocked into the readout node, the original pixel's charge is gone and cannot be sampled again. A consequence of this is that during an exposure, which in optical astronomy can be up to an hour or two in length, the observer is unable to know anything about what is happening on the chip. In addition to missing out on practical, mid-exposure information like the saturation of a target, the CCD's destructive readout prevents knowing any temporal information about the science target. Time-series data could be acquired with a CCD by taking N short exposures, but then the

advantage of performing a long integration would be lost. When the many short, destructively read exposures are co-added, the resulting data will contain a factor of \sqrt{N} more read noise than a single integration of the same duration.

1.2.3.2 Power Consumption

A CCD camera, which consists of the CCD and the electronics required to bias, clock, and read out the array, is a relatively power-hungry system, with a typical device requiring 25 W during readout [14]. Since some of that power is deposited directly into the chip, additional power will be required to remove it in order to maintain a constant detector temperature. On ground-based telescopes, such power requirements are inconsequential, but in space they can drastically increase the power requirements and mass of a satellite, which eventually translate into increased mission cost.

1.2.3.3 Radiation Hardness

In reality, the operation of transferring charge between pixels of a CCD during readout is imperfect. As photo-charge is pushed through the crystal lattice, small amounts of charge get caught in undesirable potential wells called traps. In a perfect lattice, the band structure is uniform and traps do not exist. However, real materials have defects in the periodic lattice that create local minima in the energy band structure. Once caught in a trap, a charge carrier is held fixed for some amount of time, before being released and becoming mobile again. The trouble with this effect is that the charge carrier is sometimes freed after the charge packet from which it originated has been transferred to the next pixel. The so-called charge transfer efficiency (CTE), the average fraction of a charge packet that will remain after one transfer, is usually on the order of 0.99999-0.999995 for a science grade CCD. While a CTE of “five nines” might seem so close to unity that the difference can be considered negligible, the 2048 transfers that a maximally distant charge packet must make on its way to the readout node of a modest size 2048×2048 CCD amounts to a degradation factor of CTE^{2048} , which equals $\sim 2\%$.

For detectors operating in the harsh environment of space, despite radiation shields, the steady accumulation of damage due to ionizing radiation is unavoid-

able. This ionizing radiation is collectively known as space weather and consists of the high-energy protons and electrons that make up the solar wind and very-high-energy heavy-ion radiation originating from cosmic sources. Detectors operating in laboratories or at ground-based observatories are largely protected from radiation damage because of attenuation by the Earth's atmosphere and deflection by its magnetic field. Satellites in low-Earth orbit experience between 0.2 and 10 krad (Si) year⁻¹ total ionizing dose (TID), depending on orbital inclination [15]. JWST's focal plane arrays are expected to experience up to a 50 krad (Si) lifetime TID [16]. On orbit, these particles bombard a detector and cause displacement defects (a non-ionizing damage effect typically caused by protons) or massive charge carrier deposition (an ionizing damage effect typically caused by electrons and gamma-rays) where they are absorbed by the semiconductor lattice. Although any given chunk of silicon will accrue the same number of radiation induced defects regardless of the type of detector it is in, detectors do not respond identically to radiation damage. Due to the way that CCDs transfer charge across the width of the detector, they are inherently disadvantaged when it comes to resisting radiation damage. Radiation hardness is the detector performance metric that indicates the radiation dose that a detector can receive before it is damaged to the point that it can no longer function within nominal specifications. A CCD's CTE is sensitive to radiation dose because lattice defects not only affect photo-charge deposited in the damaged pixel, but the charge deposited in all pixels upstream of it in the read direction. Reduced CTE leads to degraded energy resolution and position-dependent gain. Also, the occurrence of a radiation induced lattice defect in an optimally bad location can cause a large increase in dark current such that a pixel or even an entire column may become non-functional.

To cite an example, it was estimated that the *Swift* XRT would be exposed to a total 10 MeV equivalent proton dose of 10^9 protons cm⁻² during the first 6 years of its mission [17]. On orbit, the exposure led to a 50% increase in emission line widths. Bi-annual efforts to map charge traps in the XRT detectors and incorporate correction factors into the detector gain file have recovered a significant fraction of the initial energy resolution, but the stochastic nature of the trap release process adds an intrinsic noise into the system that cannot be corrected with calibration [18]. In the end, the use of radiation hard devices will ensure the best long-term

mission performance.

1.2.3.4 Pile-up

In X-ray applications, the issue of pile-up [19, 20] puts further limitations on the CCD's utility. The nominal operation mode of an X-ray CCD is known as *photon counting*, where the entire array is continually clocked out at some chosen frame rate as X-rays pepper the surface of the array, depositing clouds of charge into the silicon. If two X-rays land in the same or adjacent pixels during one read frame they are said to be piled-up because they can no longer be distinguished from one another. Increasing the frame rate will reduce pile-up, but doing so requires that the pixels be read faster, which increases read noise and reduces CTE. Commercially available, deep depletion CCDs from an industry front-runner like E2V are limited to read rates of about 5 Mpixels s⁻¹. Pile-up is a problem for photon counting because when two or more X-rays fall in the same pixel, it is not possible to distinguish whether the resulting signal in the detector was generated by two or more low-energy photons or one high-energy photon. If left untreated, pile-up will artificially harden an observed X-ray spectrum, decreasing the apparent low-energy flux and increasing the apparent high-energy contribution, and decrease the observed count rate relative to its true value. While it is possible to reduce pile-up by increasing the effective frame rate of a CCD with creative clocking or windowed readout modes, all of these methods involve making concessions in spatial resolution, imaging area, or read noise. Defocusing has been used to reduce focused X-ray pile-up in laboratory testing [21], but this is not a practical solution for most orbiting observatories where angular resolution is important and the use of large-travel mechanical stages is a high-risk design choice.

Taking a few operating X-ray satellites as an example, the *Swift* XRT CCD's two typical modes of operation are Windowed Timing and Photon-Counting (600 × 600 pixels). The maximum unpiled-up source fluxes for these modes are 600 and 1 mCrab, respectively [22] given the instrument's 110 cm² effective area at 1.5 keV. The *XMM* EPIC-pn CCD's Timing, Small window, Large window, and Full frame (376 × 384 pixels) modes can acquire unpiled-up data on 160, 14, 1.3, and 0.9 mCrab point sources, respectively, given the instrument's 1300 cm² effective area [23]. Current designs of the *XEUS* mission concept predict that the telescope will

have 3 m² of effective area at this energy. These large optics will impose a much higher performance requirement on the observatory's detectors, a factor of > 20 increase in effective frame rate, so that they can process all of the photons.

1.3 CMOS: A New Competitor in the X-ray

As was already mentioned, CMOS technology has been around since 1967, but the CMOS imager's rise to prominence is only just beginning. The mechanism through which photo-charge is generated in CMOS detectors and CCDs is identical. The most significant difference between the two architectures is in their operation, where in CMOS chips, photo-charge is not transferred from pixel to pixel on its way to the readout node as with CCDs, but instead each pixel is individually addressed with digital logic circuitry and its charge directly transferred to an output amplifier. The CMOS detector design is very similar to that of solid state memory devices, but instead of reading digital information from an array of memory locations, the analog signal from an array of photodiodes is read out.

One might wonder why CCDs have shown performance characteristics superior to CMOS for so many years. In truth, the fantastic performance of CCDs is not entirely attributable to inherent advantages of the technology, but rather the enormous development effort that has been invested in the CCD since its invention. Early CCD sensors had performance advantages like reduced fixed pattern noise, large open area due to simple pixel design, and easy scalability to small pixels (and therefore lighter optics) that gave developers good reason to channel their effort and funding towards the improvement of CCDs. However since that era, the steady, computer industry-led march towards smaller CMOS feature sizes has enabled solutions to many of the problems encountered with early CMOS devices. A good historical review of the development differences between CCDs and CMOS devices was given by Fossum [24].

Early CMOS imaging devices were passive pixel sensors (PPS), meaning that there was no active signal buffering or amplification happening in the pixel. In fact, early incarnations of the design were not integrating detectors; the first CMOS-like photo-detector was demonstrated in 1965 and used high gain electronics to amplify instantaneous measurements of the photocurrents being generated in a monolithic

array of photodiodes [25, 26]. It was not until the following year that an integrating detector was demonstrated [27]. As shown in Figure 1.5, the readout of a PPS is accomplished by a single switch in each pixel and a multiplexer switching the passive pixels into connection with on-chip amplifiers. The future advantages of the CMOS architecture, like the extraordinarily low power consumption (tens of mW) of camera-on-a-chip systems, were visible in these early incarnations of the device, but several problems inhibited its further development. As the size of a PPS imaging array is increased, the capacitance of the line that connects the pixel to the amplifier, the read bus, increases. This increased capacitance led to a larger conversion gain, which severely decreased S/N, and limited read speed.

As CMOS process size decreased, it became possible to place an amplifier within each pixel for buffering the photodiode readout. In this active pixel sensor (APS) architecture, the output node is located in the pixel, so its capacitance can be made small, resulting in an increase in S/N and readout speed. A simplified schematic of the difference between PPS and APS is shown in Figure 1.5. In general, the more circuitry that can be placed in a pixel, the greater the detector's functionality. Imagine an optical detector that never saturates because the pixel is able to anticipate the saturation condition and signal that it needs to be read out or an X-ray detector that only reads out pixels containing X-ray photo-charge. Some specific designs that exist outside the realm of astronomical detectors have demonstrated in-pixel CDS [28], per-column analog to digital conversion [29], and even in-pixel analog to digital conversions [30]. These are the types of things that are possible with CMOS APS. There are three amplifier designs commonly used in a CMOS APS: Source follower (SF), Capacitive Trans Impedance Amplifier (CTIA), and Direct Injection (DI). The general trade-offs that exist between these circuit designs are summarized in Figure 1.6. Since our devices all contain the SF circuit in each pixel, that circuit will be the assumed in-pixel amplifier, unless otherwise noted.

An important consequence of the CMOS APS design concept is that an integrating pixel's value can be read non-destructively. This means that sampling does not alter the charge distribution in the pixel and a separate digital command must be issued to flush all of the accumulated charge from a pixel, resetting it. The primary advantage of this scheme is that integration and readout can occur at the

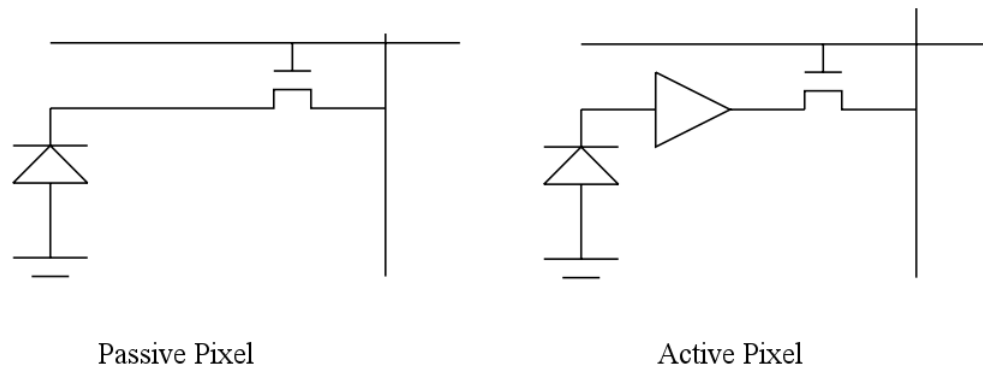


Figure 1.5: A simple schematic depicting the difference between passive and active pixel sensors. In the APS, the photodiode's charge is buffered by the in-pixel amplifier.

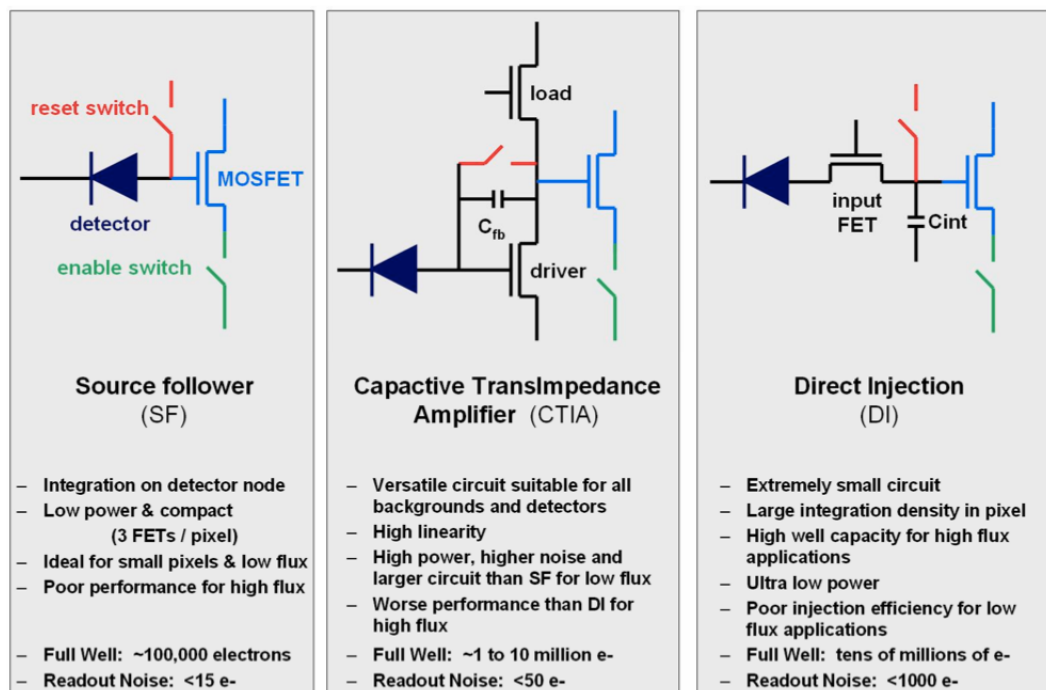


Figure 1.6: The three amplifier designs typically used in CMOS APS. Figure borrowed from Beletic *et al.* [31].

same time, enabling advanced readout schemes like Fowler and up-the-ramp sampling. Also, the lack of charge transfer means that a mechanical shutter is no longer needed to expose all pixels identically. Among the myriad of CMOS APS design variants, two major subgroups are monolithic and hybridized sensors. Monolithic sensors are built from a single silicon substrate that contains both the photodiode for converting light into charge and the electronics necessary for reading out the charge. Hybridized sensors are designed such that the readout integrated circuit (ROIC) is built on one substrate and the photodiode array is built from a second substrate that is later bonded to the ROIC.

1.3.1 Monolithic CMOS

Monolithic devices are built on the same process lines that fabricate integrated circuits for the computer industry, making them very cost-efficient to produce. At the time of this writing, this cost efficiency has led monolithic CMOS sensors to dominate the commercial market, from mobile phones, to point-and-shoots, and, more recently, even high-end DSLR cameras. While monolithic devices have the readout speed and flexibility inherent to all CMOS detectors, their use in science applications has been limited because they cannot yet produce low dark current and high QE.

1.3.1.1 CTE and Radiation Hardness

The effect of CTE, which was shown to be important in CCDs, especially those accumulating particle radiation dose, is negligible in CMOS detectors. This is because the charge in a given pixel only experiences one transfer, making the effect orders of magnitude less than any other source of uncertainty involved in measuring the pixel voltage. Accordingly, the CMOS sensor design is inherently more resistant, relative to CCDs, to proton radiation damage than CCDs because lattice displacement sites affect one charge transfer in the pixel where they occur as opposed to many charge transfers that have to pass through the damage site. An additional factor may also be that in a CCD, traps are given one fast clock cycle to release trapped charge, while in a CMOS detector, they have an integration time to release it.

1.3.2 Sensitivity

Utilizing the cost-effectiveness of existing CMOS fabrication facilities means that most monolithic devices are fabricated on low-resistivity silicon. As will be shown in the next section, this gives them poor red-optical and X-ray sensitivity. Recent efforts to use high-resistivity, epitaxial silicon in monolithic sensors have seen laboratory success with soft X-ray detection [32]. However these detectors are currently limited to a depletion depth of 15 μm , giving them poor hard X-ray sensitivity. Front-illuminated (FI) devices will always have lower QE compared to back-illuminated (BI) devices, but the QE of both devices is limited due to relatively short depletion depths.

While increasing the complexity of pixel circuit design clearly enables increased functionality and performance, for front-side illuminated monolithic sensors, the added circuitry blocks incident light, decreasing the area of the pixel capable of detecting incident photons. Commercial optical sensors use lenslet arrays, with one lens for each pixel, to focus light between the surface circuitry and improve QE. However, this technique is not generally used in scientific detectors because it induces non-uniform spatial response, blurring, and decreased angular response [33]. The use of lenslets yields no benefit to the QE of an X-ray detector because conventional refractive optics only absorb and do not refract X-rays. Backside thinning, that is, removing material from the silicon substrate's back surface by mechanical polishing and chemical etching, is currently being pursued to produce BI monolithic sensors [32]. In such sensors, the readout circuitry does not block incident light because they're illuminated from the bare back-side, enhancing QE. At the time of this writing, these detectors are still in active development and while they have shown good soft X-ray QE and read noise characteristics, they still exhibit poor high-energy X-ray response. Some of these issues are currently addressed by an alternative CMOS design, the hybrid CMOS detector (HCD).

1.3.3 Hybrid CMOS Devices

As the name implies, HCDs are constructed by connecting, or hybridizing, a dedicated semiconductor absorber array substrate to a ROIC. A schematic depicting HCD construction is shown in Figure 1.7. The absorber layer is patterned with

one photodiode per pixel and nothing else, giving the detector 100% open area. The ROIC, positioned below the absorber, is not illuminated and has the sole duty of reading out the photo-charge integrated on the photodiode. As will be shown, the key advantage of this design is that the performance of both the absorber and ROIC can be individually optimized with regard to their respective functions.

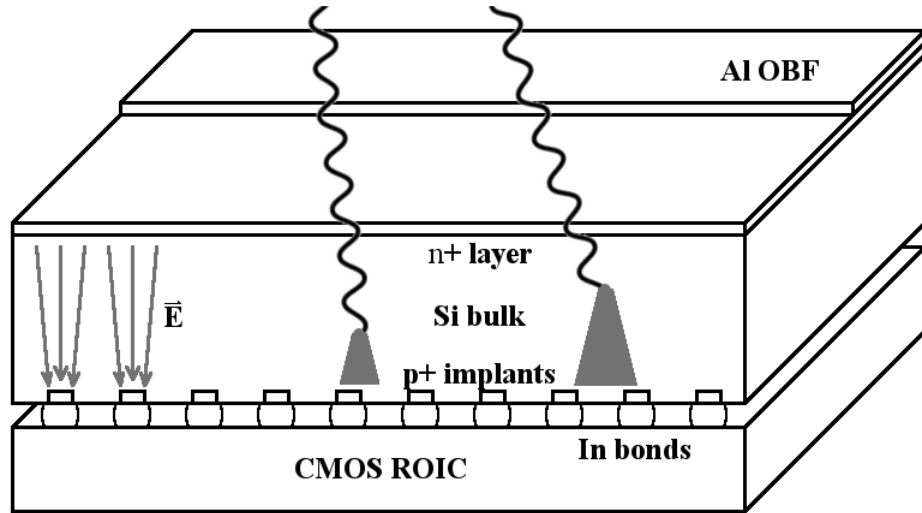


Figure 1.7: A cutaway schematic showing the basic design of the HyViSI™ HCD. The silicon absorber on top is patterned with an array of p-doped intrinsic n-doped (PIN) diodes formed between the top-side, heavily n-doped layer, the heavily p-doped implants below, and the intervening lightly n-doped (nearly intrinsic) silicon. The indium bump bonds connect each absorber pixel to its corresponding readout pixel in the ROIC below. Shown are X-rays being absorbed at two different depths in the detector. The charge carrier cloud formed by absorbed X-rays will diffuse laterally as it moves toward the potential wells on top of each implant. X-rays absorbed higher up will tend to diffuse more and produce signal in more than one pixel. On top of the absorber, and shown partially covering it, is the deposited aluminum optical blocking filter (Al OBF).

An introduction of the HCD would not be complete without noting that the development of this architecture was primarily motivated and, more importantly, funded not by the curiosity-driven research of astronomy, but instead by its utility in advancing room-temperature thermal emission and night vision imagers with military applications. Interestingly, researching the origins of adaptive optics tells

a similar story [34]. While the concept of adaptive optics originated in astronomy, the majority of the technology’s development was accomplished by the military industrial complex. This delicate interplay between the advancement of pure science and military technology is not a new phenomenon and will likely continue to play an important role in the advancement of astronomy as a whole.

The HCD design was developed in the late 1970s [35] in response to the need for better forward looking infrared (FLIR) camera detectors. In the original design, the ROIC was positioned in front of the absorber and window cutouts in the ROIC allowed radiation to penetrate through it, to the low band gap, semiconductor absorber array bonded below it. During the 1980s, the design evolved into the current configuration where the absorber array is positioned in front, and flip-chip bonded to the silicon ROIC. A number of manufacturers currently produce large-format hybridized arrays, including Goodrich Corporation, Raytheon Vision Systems, Teledyne Imaging Sensors (TIS), Sofradir, Selex, IAM, SCD, and DRS Technologies [2].

The astronomical X-ray detector development projects at Penn State have focused on developing hardware through an ongoing collaboration with TIS. Using very similar architectures, TIS produces HCDs with two different absorber substrates so that the sensors can be used in different wavelength regimes. For mid and short-wavelength infrared sensing, HgCdTe substrates are grown via molecular beam epitaxy on CdZnTe substrates. In recent designs the CdZnTe substrate has been removed to improve response. As with CCDs and monolithic CMOS sensors, TIS uses silicon to absorb radiation in the near-IR, optical, and X-ray. The absorber is made from thick ($50 - 350\mu\text{m}$ [36]), high-resistivity silicon and is called HyViSITM for “Hybrid Visible Silicon Imager” [37]. From this point forward, references to the HCD will be referring to variants of the TIS HyViSITM silicon p-doped intrinsic n-doped (PIN) diode hybrid imager that have been optimized for X-ray detection. A detailed description of these detectors will follow in Chapter 2, but it will be useful to first understand how the PIN diode works since HCDs are based on this device and draw their performance advantages from it.

1.3.3.1 The PIN diode

The PIN diode's design is an extension of one of the most basic semiconductor devices, the PN diode. The PN diode is a two terminal device that consists of a single semiconductor in which a p-doped region is created directly next to an n-doped region. The electronic transport properties of the junction between these alternatively doped regions are different than either the p or n components alone. The hallmark characteristic of the PN junction is its asymmetric transport, meaning it will allow current to flow across the boundary in one direction, but not the other. By itself, this device is a diode and can be used as an AC rectifier, for over-voltage protection, or, as in our case, a photodiode. Creating an intrinsic region between the p- and n-type regions turns the device into a PIN diode, the properties of which are similar to the PN junction. The diode's behavior depends on the voltage placed across its two terminals, the bias voltage, leading to three general performance regimes (See Figure 1.8):

1. Terminals disconnected (floating) - holes from the p-type region and electrons from the n-type region diffuse across the junction boundary, into the intrinsic semiconductor, creating a depletion region. When electrons recombine with holes this leaves behind an immobile *space charge* in the doped regions, positive ions in the n-region and negative ions in the p-region. The coulomb force from this space charge prevents more free charge carriers on both sides from diffusing across the boundary, resulting in the development of an equilibrium condition. With no external voltage or photon excitation, there will be a non-zero voltage across the diode, the *built-in* voltage.
2. Forward Bias - When an external positive voltage, V_{sub} , is applied to the p-type substrate, the diode is said to be forward biased. The electric field created in the solid imparts energy to the charge carriers, making it possible for them to overcome the space charge coulomb barrier and flow across the junction. In this regime, the diode is highly conductive.
3. Reverse Bias - When an external positive voltage is applied to the n-type side of the diode, the depletion region increases in size with increased voltage. This increase in the depletion depth makes reverse bias the operation regime

where the diode is most sensitive to incident radiation.

TIS has reported that the PIN diodes in the HyViSITM arrays are fully depleted (the depletion region completely fills the intrinsic region of the diode) at $V_{sub} = 15V$ [38] and simulations have shown that a $100\ \mu m$ detector, akin to the PSU H1RGs, is fully depleted at 10V [39]. In the aforementioned TIS report, the absorber thickness was not listed. This ability to produce very thick depletion regions enables the HCD's performance advantages.

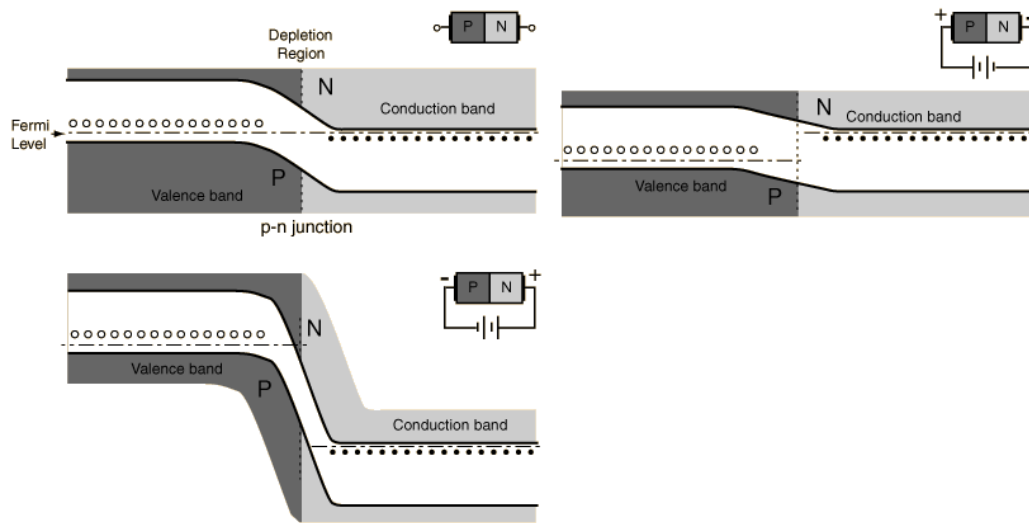


Figure 1.8: A cartoon schematic of the different band structures of a PN junction at different bias voltages. Figure adapted from content on the Hyperphysics website [40].

1.3.3.2 HCDs: The Good and the Bad

To summarize, CMOS detectors, in general, exhibit the following performance advantages,

- **Non-destructive readout** - multi-sample readout schemes such as up-the-ramp and Fowler sampling reduce read noise,
- **Random-access readout** - Non-trivial readout schemes dramatically increase detector frame rate (potential for multiple target windows and event driven readout), without increasing read noise.

- **Read speed** - Free from the limitations of transferring charge through semiconductor, CMOS architecture is less fundamentally limited in its pixel rate than CCDs.
- **Low power** - CMOS electronics are inherently low power due to low switching and standby power consumption. Additionally, CMOS detectors compare favorably to CCDs in this regard because they do not use high clock voltages to transfer charge across the chip.
- **Radiation hardness** - The hybrid design is inherently radiation hard. HyViSITM H2RGs have been shown to withstand 90 krad (Si) total ionizing dose [41], which greatly exceeds the lifetime JWST dosage requirement and corresponds to a ~ 9 year mission lifetime in a low-inclination, low-earth orbit.

and CMOS detectors exhibit the following disadvantages,

- **Read noise** - The slow pixel rate (100 kHz) read noise of the 3T source follower pixel design used in TIS HxRG detectors is currently limited at $\approx 7 e^-$, making it higher than that found in the best CCDs. However, at MHz readout rates, HCDs have lower read noise than CCDs operated at similarly high rates [37]. Detectors employing a 4T design, known as a pinned photodiodes, have achieved read noise levels below $1 e^-$, which is comparable to the performance of CCDs.
- **Dark Current** - Multi-pinned phase (MPP) CCDs exhibit extremely low dark current, making it difficult for CMOS to compete in this metric. Dark currents of 5-10 nA/cm² have been achieved in 3T HyViSITM HCDs at 298 K [36], 3T monolithic sensors from TIS have produced 200-500 pA cm⁻² [42], and pinned photodiode 4T monolithic sensors from TIS have produced 1-10 pA cm⁻² at unspecified temperatures [42]. Modern production MPP CCDs from E2V show $\sim 200 e^-s^{-1}pixel^{-1}$ in 20 micron devices (8 pA cm⁻²) at 298 K.

The separate absorbing and readout layers in the HCD design enable several performance advantages over monolithic CMOS detectors. Specifically, HCDs have the following advantages,

- **Deep Depletion** - depletion depths up to 350 μm have been achieved in HCDs compared to a few tens of microns in monolithic CMOS and 50 μm in CCDs [43]. This leads to improved red optical and hard X-ray QE.
- **Fill factor** - HyViSITM HCDs are back illuminated giving them 100% fill factor.
- **Micrometeoroid resistant** - HCDs are expected to be more robust than FI CMOS and CCD imagers because the gate structures are protected behind the absorber array. Should pixel-level damage occur, its effect would be localized, and not result in blooming across the detector. *Suzaku*, *XMM*, and *Swift* have all experienced damage on orbit that has been likely due to micrometeoroid damage.

A notable disadvantage of current HyViSITM HCD designs is that they are susceptible to inter-pixel capacitance, where nearby pixels are coupled to one another by an unintended, parasitic capacitance. The end-result of this capacitive coupling is that signal is spread into adjacent pixels, i.e., the detector's modulation transfer function is degraded. Details of this effect and our characterization of it will be presented in Chapter 3.

PSU Detector Hardware

The Penn State X-ray Astronomy Detector Lab is actively engaged in a collaboration with TIS (originally Rockwell Scientific) to produce next generation HCD X-ray detectors. A distinct advantage of collaborating with TIS stems from the large amount of development that their product line has undergone in order to produce focal plane arrays for the James Webb Space Telescope's fine guidance sensor, NIRC*am*, and NIRS*pec* [44] instruments. The Penn State X-ray group has taken the results of this effort as a starting point and begun our own development of the TIS HCD optimized for X-ray astronomy. In this chapter I will discuss the design specifications of the particular devices that PSU received from TIS in addition to the hardware and software required for their operation.

2.1 TIS HAWAII Arrays

To date, five X-ray TIS HyViSITM HCDs have been tested at PSU. All devices are HxRGs (HAWAII $x \times x$ pixels with Reference pixels and Guide mode). The device serial numbers, as well as a summary of the TIS test reports for the devices, are summarized in Table 2.1. Fabrication of the four listed H1RG (1024 \times 1024 pixel) devices was commissioned in 2006 and funded by the PSU X-ray group. The H2RG (2048 \times 2048 pixel) was designed and built for a different TIS client and was loaned to PSU for testing.

The H1RGs are devices with an 18 μm pitch absorber array bump bonded to an 18 μm pitch ROIC with indium interconnects. A picture of the full device is shown

Detectors in the joint TIS PSU development program						
Serial Num.	Sub. pitch	ROIC pitch	Noise	Dark current	Gain	Filter
H1RG-118	36	18	15.8	0.107	208	500 Å half
H1RG-125	18	18	12.2	0.284	90	500 Å half
H1RG-161	18	18	10.3	0.007	110	1000 Å full
H1RG-167	18	18	9.4	0.069	129	180 Å half
MUX	18	-	-	-	-	-
H2RG-122	36	18	-	-	-	None

Table 2.1: A list of all HCDs that Penn State has received from TIS. Noise characteristics shown in this table are values reported by TIS. Penn State measured superior noise performance in these same detectors [45]. *Sub. pitch* is the pixel pitch of the top absorber substrate layer of the HCD, in microns. *Mux pitch* is the pixel pitch of the bottom ROIC layer, in microns. *Noise* is given in RMS e^- , *Dark current* in $e^- \text{ sec}^{-1} \text{ pix}^{-1}$, and *Gain* in $e^- \text{ mV}^{-1}$.

in Figure 2.1. The ROIC is designed to be very flexible and adaptable to many different modes of operation. Mode selection is controlled by the programming of 13 internal registers of width between 4 and 11 bits. There are two readout rates: the 100 kHz slow data rate, which provides the lowest read noise, and a high speed mode that can achieve data rates up to 5 MHz at the expense of increased read noise. In our tests, we have used the slow 100 kHz pixel rate mode exclusively. The H1RG can output pixel data through up to 16 parallel channels (32 channels for H2RG), with heavily parallelized output providing high frame rates at the expense of greater power consumption. Specifically, total power consumption is $\lesssim 300$ mW per channel in unbuffered and 800 mW per channel in buffered 100 kHz readout mode. We have exercised the parallel output capability of the device by acquiring all test data using two output readout. One of these outputs can be assigned to read out a window, a detector sub-array region of programmable size and location. Windowed readout is typically used to read out a small region of the array that covers a bright source. The region is read at a higher frame rate while the rest of the array integrates, which is useful for fast telescope guiding or preventing X-ray pileup on a bright source.

The device itself was bonded to a gold plated package machined from Invar, nickel/iron alloy. Invar was chosen due to its uniquely low coefficient of thermal

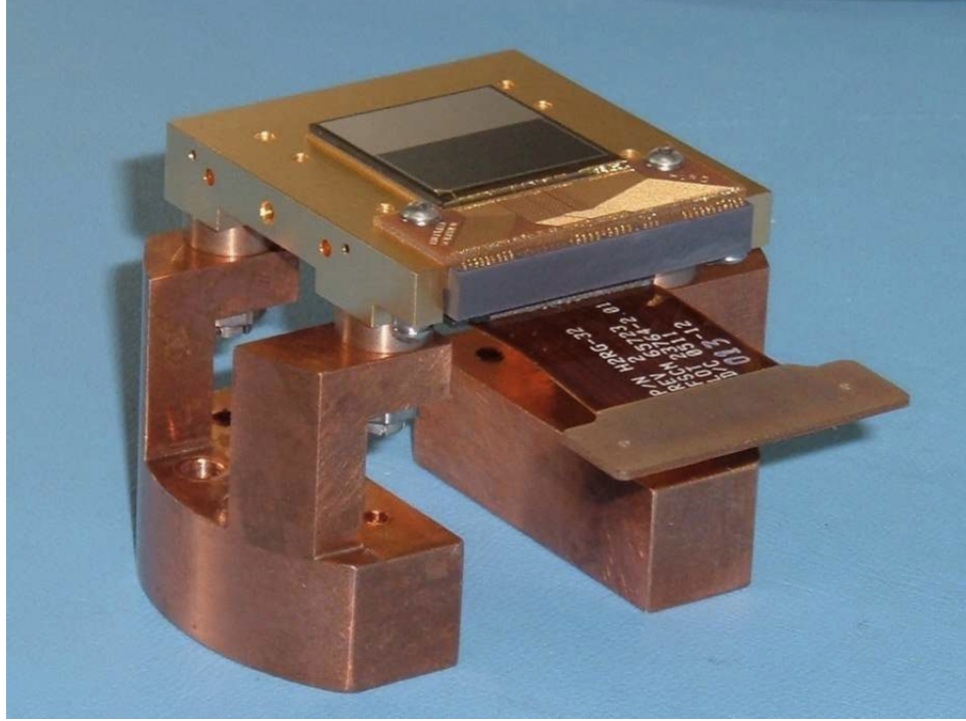


Figure 2.1: H1RG-125 attached to the cold finger mount. The flex cable can be seen protruding from the bottom of the detector package.

expansion ($\alpha = 1.3 \cdot 10^{-6} \text{ K}^{-1}$), which is relatively well matched to the thermal expansion of the silicon ($\alpha = 2.7 \cdot 10^{-6} \text{ K}^{-1}$) in the HCD. Closely matching the thermal expansion coefficients of materials that are bonded to one another is critically important in both device package design as well as the design of the device itself. Significant mismatch in thermal expansion can lead to strain induced failures that occur when the device is cooled to cryogenic temperatures. For laboratory tests and ground-based operation, Invar represents a good compromise between cost and performance. For flight applications, where a material with high rigidity per mass is needed, in addition to good thermal conduction and low thermal expansion, the packages are typically cast from sintered silicon carbide. In our devices, the gold coating is applied to the package to decrease the thermal IR emissivity, making it possible to maintain the device at cryogenic operating temperatures with less cooling power. Fully packaged H2RG devices are 3-side abutable, with clearance necessary on the fourth side for signal lines to be routed to the underside of the package via wirebonds. Our H1RG devices are not abutable because they were

designed for detector development.

All bias voltage, clock, and signal lines enter and exit the HCD through a series of 92 pads located in a straight line along the top edge of the ROIC substrate. These pads are wire bonded to a breakout PCB mounted on the package. The signal lines are routed, via a second set of wire bonds, from the breakout PCB to a ceramic connector that wraps around the top and underside of the package. This connector terminates at an array of 92 pins underneath the package. Lines are then routed off chip by a flexible circuit cable (flex cable) that terminates at a 92 contact Hirose connector. The Invar package, the breakout PCB, ceramic connector, and the flex cable are designed and fabricated by Gerry Lupino at GL Scientific.

2.1.1 Reference Pixels

The arrays themselves consist of a 1016×1016 pixel active area surrounded by four columns of reference pixels on the left and right and four rows of reference pixels on the top and bottom, to form a 1024×1024 array. The reference pixels are standard ROIC pixels that are not connected to photodiodes in the absorber array, but instead connected to capacitors with value $C_{pix} = 40$ fF, a value chosen to be similar to the detector capacitance. However, in reality the effective capacitance of the reference pixels will be ~ 60 fF due to the parasitic capacitances of other components in the signal chain such as amplifiers and switches. These pixels were designed for tracking sensitivity variations in the signal chain due to temperature variations or bias voltage drift. They are sampled with each image and can therefore be used during data post processing to remove row offsets. However, they can be used most effectively by sampling their values mid-data stream, a scheme that can be implemented natively using the ROIC's programable readout capability.

Also, at the top of the array, there is an additional row of reference pixels that are connected to capacitors with a range of values. The capacitors have values of $C_{pix} = 10, 20, 40, 80$ fF. This row is intended to be used for testing and diagnostics, and is automatically deactivated during normal readout.

An additional reference and calibration feature of the H1RG is the inclusion of temperature sensors directly on the ROIC substrate. Two long, thin, line-

structures of aluminum metal deposited around the ROIC perimeter form two individual resistive thermal device (RTD) temperature sensors. In our devices, the temperature sensors have not been wire bonded to the output and therefore cannot be used. If they were bonded, the sensors would be used in the usual way, where a small constant current is passed through the sensor, the voltage drop across the sensor is measured, and its resistance calculated. Using such a method, there is always a tradeoff between temperature resolution and self heating. For large currents, the voltage drop across the sensor will be large and easily measurable, but self-heating due to Joule heating will be non-negligible. For small currents, the voltage drop will be small and difficult to measure. A current of 1 mA is suggested.

The ROIC pixel is a seven-transistor design patterned using a 250 nm CMOS process. A simplified schematic of the pixel, with the various reset and read controls, is shown in Figure 2.2. The schematic shows individual horizontal and vertical pixel reset logic lines, indicating that single pixels can be individually reset, in addition to the more standard row and global chip resets. This is useful because, unlike with global or row reset, where pixels at the end of a row or end of the frame integrate for longer times, it allows for a constant integration time between the reset and readout of each pixel. Also, with row and global resets, the smallest achievable integration time is limited to the row and full frame read time, respectively. With single pixel reset, the minimum pixel integration time is limited by the readout clock speed. In all of our tests we use the default row reset clocking mode. The small, $512/100 \text{ kHz} = 5.12 \text{ msec}$, increase in integration time of the pixels at the end of a row is minor in comparison to the $1024^2/(1/100 \text{ kHz}) = 5.24 \text{ sec}$ integration time of the pixels. Additional transistors, not shown in the diagram, enable the detector's guide mode feature.

2.1.2 Bare MUX

With the original shipment of detectors, we also received a fully packaged, bare ROIC device known as the Mux. Such devices have packages and ROICs identical to the real HCDs, which gives them digital, thermal, and mechanical properties very similar to the fully-functioning devices. Since the ROIC has not been flip-chip bonded to an absorber, they are significantly cheaper than full devices. Obviously,

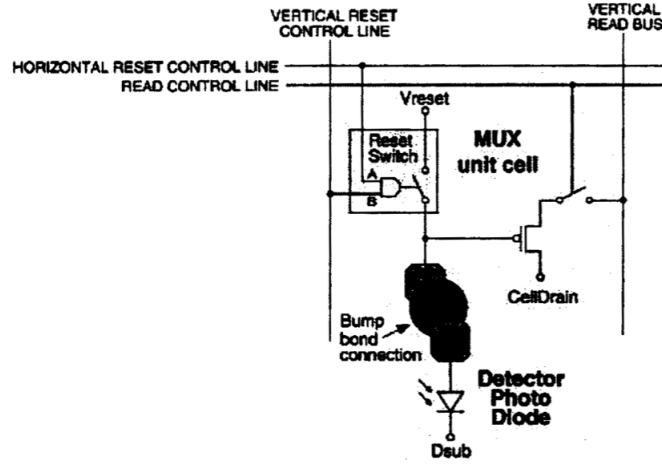


Figure 2.2: A simplified electronic schematic of an HxRG pixel.

they will not respond to radiation like an HCD, but their similarities and low cost made the Mux excellent for electronic and thermal system validation testing.

2.1.3 Anti-Reflection Coating

Traditionally, HyViSITM detectors have an Anti-Reflection (AR) coating applied to the front surface of the absorber substrate. The coating is intended for optical spectrum applications, where it reduces the fraction of photons that are reflected from the absorber's surface. This improves transmittance through the boundary between the vacuum and the silicon bulk and, therefore, improves the detector's quantum efficiency. However, in the X-ray regime, where the reflectance of surfaces is negligible at all but extremely small angles of incidence, the AR coating provides no benefit and only attenuates the incident flux. Consequently, we specified that all of the PSU devices be fabricated without an AR coating.

2.1.4 Filter Deposition

Regardless of whether the focal plane array of an X-ray telescope is a CCD or CMOS device, in both cases the active region of the detector consists of biased silicon. Due to silicon's 1.17 eV band gap at detector operating temperatures, biased silicon is sensitive to near infrared, optical, soft X-ray, higher energy electromag-

netic radiation, and cosmic rays. In order to isolate the signal of interest, which in this case is soft X-rays, all sources of background must somehow be prevented from reaching the detector or removed after detection. On board the *Chandra* satellite, low energy (< 100 keV) electrons focused by the X-ray mirror are prevented from reaching the focal plane by a magnetic baffle and unfocused X-rays are blocked by tantalum baffles. Shielding cosmic rays is very difficult, requiring either a powerful magnetic field to redirect or a heavy shield to absorb the particle radiation. Since cosmic rays generate a detector response that is both unique in its size and geometry, the background signal is instead removed from X-ray satellite data during post processing. Near-infrared and optical photons, which are both efficiently focused by X-ray optics, cannot be effectively removed with post processing, necessitating an optical blocking filter (OBF) in the telescope design.

On *Suzaku*, *XMM*, *Chandra*, and *ASCA* the OBFs consist of aluminum deposited onto a thin polymer film. In this design, the aluminum heavily attenuates optical light and the polymer film acts as a deposition substrate and mechanical support. While these filters have been shown to work very well in space, a drawback of the design is that the filter's mechanical support does not contribute to blocking optical light, but it increases X-ray attenuation, especially near the support material's absorption edges. On *Suzaku*, photoelectric absorption due to carbon (284.2 eV), nitrogen (409.9 eV), and oxygen (543.1 eV) in the polyimide ($C_{22}H_{10}N_2O_5$) OBF substrate produces clearly visible edges in the measured soft X-ray transmission of the filters [46] (Figure 2.3). On *Chandra*, the filter's spectral response is well fit by a model that includes significant absorption edges from carbon and oxygen in the Lexan ($C_{16}H_{14}O_3$) OBF [47] (Figure 2.4). The ultimate observatory sensitivity loss due to these edges is localized to energies in the vicinity above the absorption edges and can be significant, with up to 20% transmission loss in the carbon edge. The PSU X-ray group has developed a new technique for filtering background optical light that avoids absorption from the polymer filter component; the aluminum filter is instead applied directly to the surface of the detector. This technique was not practical in the past because X-ray CCDs were primarily front-illuminated detectors. Such detectors have exposed gate structures on their front surfaces, which would have to be electrically insulated from a directly applied metallic optical blocking filter and would complicate the process of

depositing a uniform OBF film. Our HCDs on the other hand, have a uniform SiO_2 front-side surface, which readily accepts the deposition of an aluminum OBF. We successfully experimented with front-side deposited OBF thicknesses of 180, 500, and 1000 Å.

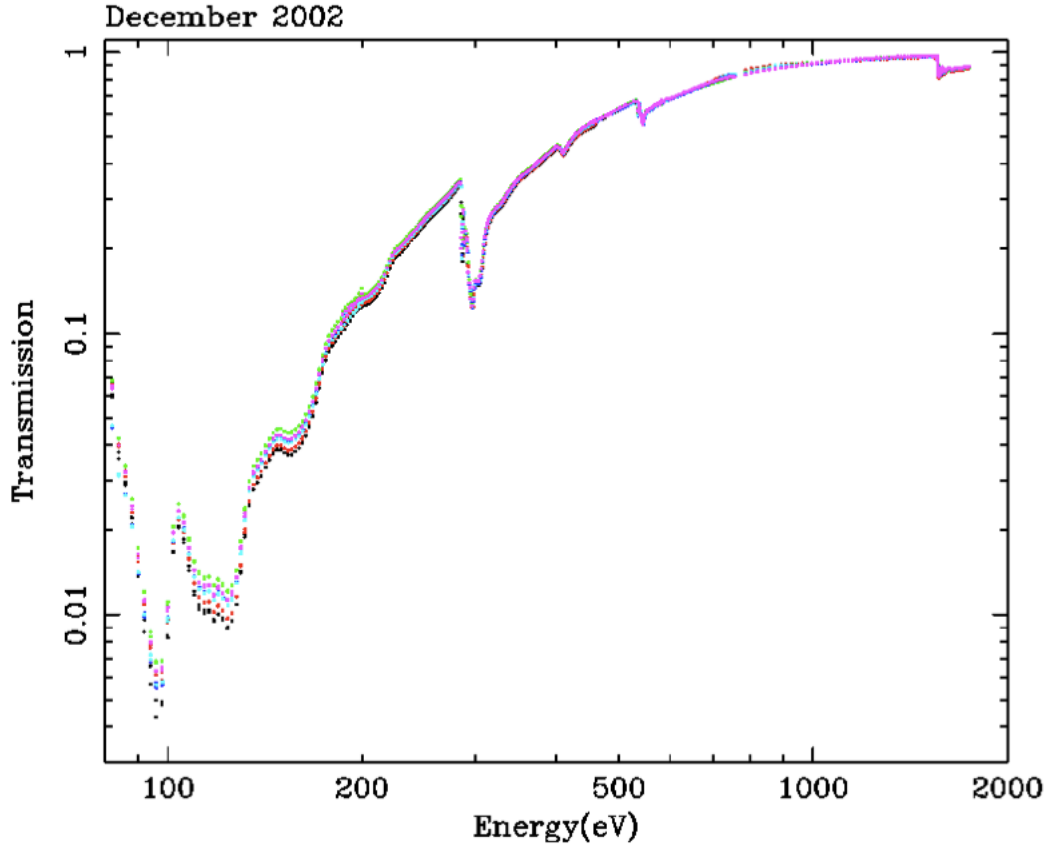


Figure 2.3: Measured soft X-ray transmission of six OBFs built for *Suzaku*. Note the carbon, nitrogen, and oxygen absorption edges from the OBF substrate at 284.2, 409.9, and 543.1 eV, respectively. [46]

2.2 TIS SIDECARTM

The SIDECARTM (System for Image Digitization, Enhancement, Control and Retrieval) is an application specific integrated circuit (ASIC) designed and sold by TIS for the express purpose of controlling HxRG detector hardware. The operation

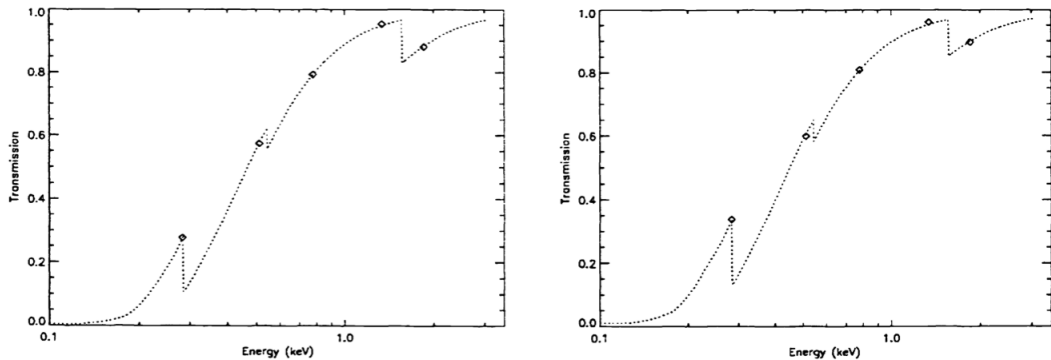
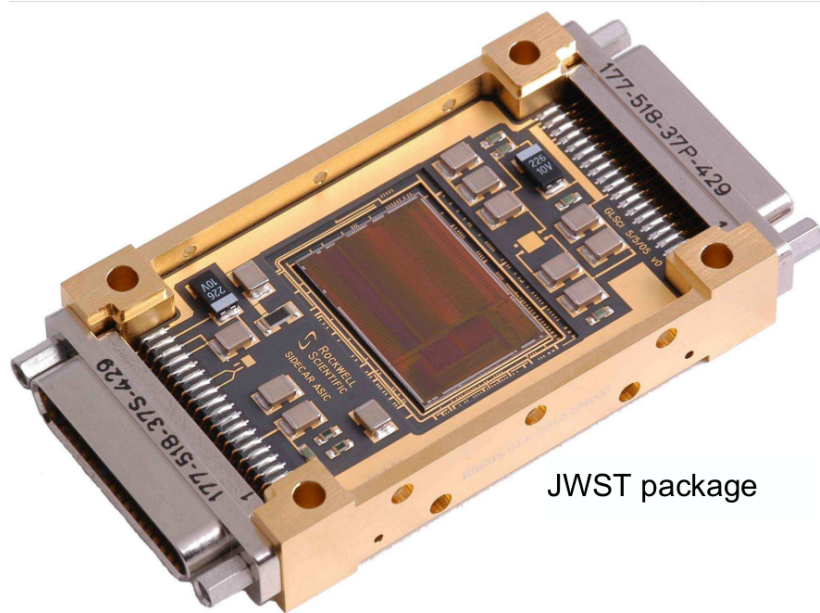


Figure 2.4: A model fit to the soft X-ray transmission profile of two *Chandra* OBFs. The left plot shows data and model fit for an imaging filter and the right plot for a spectroscopic filter. Note the strong attenuation above the carbon edge. [47]

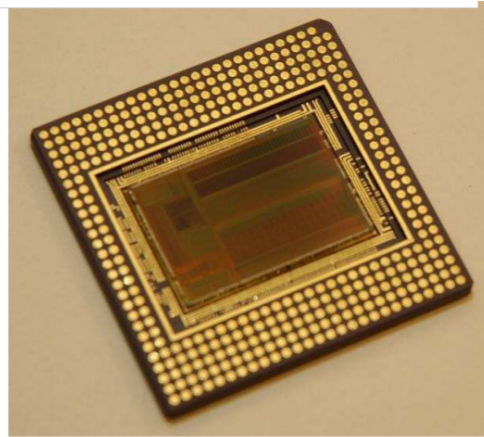
of any imaging detector is no simple task. Many digital clock signals and analog bias voltages are required as inputs and the data-containing analog video signal that the detector outputs needs to be amplified, digitized, and buffered before it can be permanently stored by the data acquisition (DAQ) system on a computer. In the past, discrete-component circuit boards powered by bench top power supplies were used for clock driving and video signal processing. It is not uncommon for science cameras to be powered by custom designed electronics. Astronomical Research Cameras (ARC) is a private company that develops high quality camera controllers that have been variously known as “Leach controllers”, “ARC controllers”, as well as “SDSU controllers” due to their origins at the San Diego State University. While these controllers perform very well, they are relatively large, heavy, and power-hungry devices. Altering the way that they function sometimes requires physically swapping circuit boards or soldering new components into the controller. To address the need for a small, low-power, flexible detector control solution, TIS developed the SIDECARTM.

The SIDECARTM combines all of the various driver and signal chain electronics required to operate an HxRG detector onto a single 22×14 mm die. Shown in Figure 2.5, the SIDECARTM is available in multiple packaging variants. For laboratory use, the land grid array (LGA) package is available in both cryogenic and room-temperature development kits. All of the X-ray data shown in this dissertation was acquired with a room-temperature SIDECARTM development kit. With

creative mount design, we were able to run the room-temperature SIDECARTM with the cryogenic detector and connect the two with a short flex cable to reduce noise pickup. Besides the USB connection, the only other electronic lines required to run the camera are an external V_{sub} (substrate bias) and a 5 V bias power line that bypasses the USB power. Both of these voltages are supplied externally to reduce noise.



JWST package



LGA package

Figure 2.5: The flight-ready JWST SIDECARTM package and the laboratory LGA packaging options.

Regarding operation, our room-temperature development kit SIDECARTM was mounted to a circuit board that interfaces the device with a computer through

a USB connection. With the SIDECARTM Interactive Development Environment (IDE) software running on the computer, assembly code is compiled and uploaded to the SIDECARTM to begin every power-up procedure. Both the IDE and the assembly code give the user full access to the plethora of tuning knobs and reconfiguration options designed into the SIDECARTM. Upon power-up, the SIDECARTM will program the H1RG registers (memory locations). The TIS JAC is an IDL GUI that automates many operations in the SIDECARTM and gives the user simplified, high-level control of the data acquisition process.

Data Reduction and Measurements of HCD Characteristics

The measurement of a detector's performance characteristics is a critical step in evaluating its suitability for science applications. As discussed earlier in Chapter 1, the noise characteristics of a focal plane array play an important role in determining the final sensitivity of, and therefore the science accessible to, a given instrument. In this chapter, I will discuss the progress that we have made in measuring and understanding the noise, energy resolution, and interpixel capacitance in TIS HCDs. I will discuss the mechanisms that have been found to dominate noise in these devices as well as the digital post-processing that we have developed to reduce the noise contributed by some of these mechanisms. Methods for optimizing energy resolution with post-processing event selection will be shown. Many of the results shown in this chapter have been published in Bongiorno *et al.* [48] and Bongiorno *et al.* [49] and have been reproduced with permission of the SPIE.

3.1 Test Stand

3.1.1 Temperature Control

In principle, HyViSITM detectors can be run at room temperature. However, in practice, room temperature operation is limited to electronics connectivity testing and not acquiring data from the imaging array. At room temperature, the detec-

tor’s output signal is dominated by dark current, making it difficult to measure the detector characteristics that dominate in the high-performance regime where it is capable of making scientific measurements. To prevent dark current from saturating the detector, all HIRG data presented in this chapter were acquired with the detector held at 150 K. The temperature was measured with a Lakeshore Cryotronics platinum RTD sensor mounted with a screw fastener to the detector package. Temperature control was achieved with a proportional integral derivative (PID) control loop modulating the duty cycle of a liquid nitrogen (LN2) pulsing system. The LN2 was pulsed into a cavity built into the detector’s mount. At 100% duty cycle, the detector reached ~ 90 K. A LabVIEW virtual instrument (VI) controlled a National Instruments DAQ to perform temperature measurement with the RTD and operate the LN2 pulsing relay. The LabVIEW VI also ran the PID loop.

3.1.2 Vacuum Chamber

Operating at low temperature required that the detector be maintained in an environment free of condensable gasses. At 150 K, water vapor is the most readily condensable gas and the best way to avoid it is to operate inside a vacuum chamber. All tests were made with the detector mounted to a LN2 cooled cold finger inside a light-tight, stainless steel vacuum chamber. The chamber was evacuated to $\sim 10^{-6}$ mbar by a turbomolecular pump backed by a diaphragm pump.

3.1.3 X-ray Sources

X-rays were produced by a source mounted to a flange on the chamber wall opposite to the detector, at a distance of ~ 10 cm. The primary X-ray source was the radioactive isotope ^{55}Fe , which emits ^{55}Mn $K\alpha$ (5.89 keV) and $K\beta$ (6.49 keV) X-rays. Additionally, a source that excited fluorescent emission in target samples with ^{210}Po α -particle emission was also used for testing. Neither source was focused or collimated in any way. This so-called “cube” chamber is shown in Figure 3.1. For a much more thorough description of vacuum chamber, cryogenic dewar, and X-ray source design, see Chapter 4, where I describe a different test stand that I designed and built.



Figure 3.1: Pictured is the cube chamber. *Left*, the pulsed liquid nitrogen fill (stainless steel hose) and vent (dark-colored, insulated hose) are shown entering and exiting the cold finger vacuum flange. *Right*, a view of the chamber’s interior through the source flange porthole. An H1RG can be seen mounted to the cold finger with the room temperature SIDECAR[™] mounted to the upper right of the detector. The copper braid insulated line seen connected to the detector’s left edge is the RTD temperature sensor. Figure borrowed with permission from Prieskorn *et al.* [45]

3.2 Data Acquisition

3.2.1 Readout Schemes

The simplest method for acquiring data with the H1RG is with the CDS subtraction scheme. To begin the acquisition, the array is reset and read out, row-by-row, to acquire a bias or “reset frame”, a data frame with effectively zero integration time. After the reset frame has been read out, the detector again reads out the pixel values, addressing them in a consecutive, rasterized order. While this reset frame readout is taking place, the pixels that have already been read are integrating. When the reset frame is finished, the mux immediately begins reading the array a second time. At this point in the process, the pixels have had a read frame worth of time to integrate. For the 100 kHz pixel rate that we elected to use and the 1024×1024 size of the array, this corresponds to a 10.486 sec frame time. To exercise the capabilities of the hardware and speed up the frame rate, we quickly switched to 2 channel readout. In this mode, the array is addressed simultaneously in terms of both readout and reset functionality, in two 512×1024 pixel columns. Since in two channel mode, two pixels are being addressed at any given time, the

frame time is cut in half. Therefore our working frame time for all data acquisition was 5.243 s. Regardless of the number of readout channels, the reset frame was digitally subtracted from the read frame during post-processing to produce a CDS subtracted frame. This process removes fixed pattern noise (FPN), a manageable defect that is common to all CMOS detectors. FPN is not noise in the typical sense because as the name indicates, it is a fixed pattern across the detector that is highly correlated from one frame to the next. In our HyViSITM HCDs, the FPN is approximately 1,400 RMS e⁻ and the digital CDS subtraction removes it.

The more capable readout scheme that we quickly adopted for all standard data acquisition is known as up-the-ramp sampling. In this mode, the detector first resets the array a programmable number of times to flush charge that may have accumulated in traps from the pixels. After the final reset, the array non-destructively reads out a programmed number of data frames without any resets. In optical and infrared data acquisition, the pixel values will steadily increase due to the gradual accumulation of photons. This pattern in the pixel intensity as a function of frame number looks like a ramp with constant slope, giving the readout scheme its name, since sampling happens up the ramp at evenly spaced intervals. Compared to an equivalent number of CDS reads, up-the-ramp sampling saves a factor of $\sim 2N_{frames}/(N_{frames} + 1)$ on read time, where N_{frames} is the number of data frames. While the efficiency improves with increasing N_{frames} , the technique cannot be used with reckless abandon because the pixels will eventually saturate and, thereafter, become unresponsive. This readout scheme was baselined for the H2RGs in the *JANUS* mission concept XCAT instrument [50].

For our data analysis pipeline, I wrote the IDL procedure `ramp_cds.pro` to perform the filename parsing and image subtraction necessary for simple CDS and up-the-ramp CDS data reduction.

3.2.2 FET Leakage Current

When the H1RG was first plugged into the SIDECARTM and run with the default machine code, we observed an extreme gradient pattern in the image data instead of the expected image of a noisy background speckled with X-rays. After consulting the literature and finding no indication of the source of the problem, we spoke

with TIS engineers and discovered that the pattern was due to current leakage onto the input of a FET in the SIDE CAR™ preamplifiers. The FET leakage current is pertinent to a discussion of detector noise characteristics because it results in an offset of the pixel signals, which decreases dynamic range. See Figure 3.2 for an electronics schematic that shows the relevant circuitry. In the preamplifiers, a reference voltage is compared to the input signal. When the SIDE CAR™ is run at room temperature, thermally excited charge carriers accumulate on C_{fb} , the feedback capacitor, altering the preamplifier’s reference voltage level. This current’s temperature dependence follows the Shockley diode equation, where $I_L \propto e^{(1/T)}$, which indicates that the effect should be negligible when the SIDE CAR™ is run at cryogenic temperatures. TIS confirmed through private communication that FET leakage current is negligible at cryogenic temperatures, however, we were not able to take advantage of this because this PSU SIDE CAR™ can only be run at room temperature (note, there is a cryogenic version of the SIDE CAR™). With the SIDE CAR™ at room temperature, we observed that enough charge was accumulating on C_{fb} to shift the ADC output by thousands of DN. The solution, which was implemented on existing hardware, was to alter the SIDE CAR™ assembly code such that the preamplifier FET’s input capacitor was reset before each row of the detector was read out.

3.2.3 Row Noise Correction

Despite the marked improvement in the data after the row-by-row FET reset scheme was implemented, we were still left with horizontal artifacts, or “row noise”, in the images after the CDS subtraction. This horizontal banding is uncorrelated between different rows and different frames. TIS has stated that it is due to uncertainty in the amount of charge left on the preamplifier feedback capacitor after reset. Attempts were made to subtract off the row noise by using the H1RG’s reference pixels. The reference pixels are a four pixel wide border of Mux pixels that surround the imaging array and are connected to passive capacitors rather than a PIN photo-diode. Such methods did not provide optimal solutions because, as seen in Figure 3.17 at the end of this chapter, the row noise is not constant across a row. To solve the problem, a specialized boxcar filter function, `pixcal.pro`, was

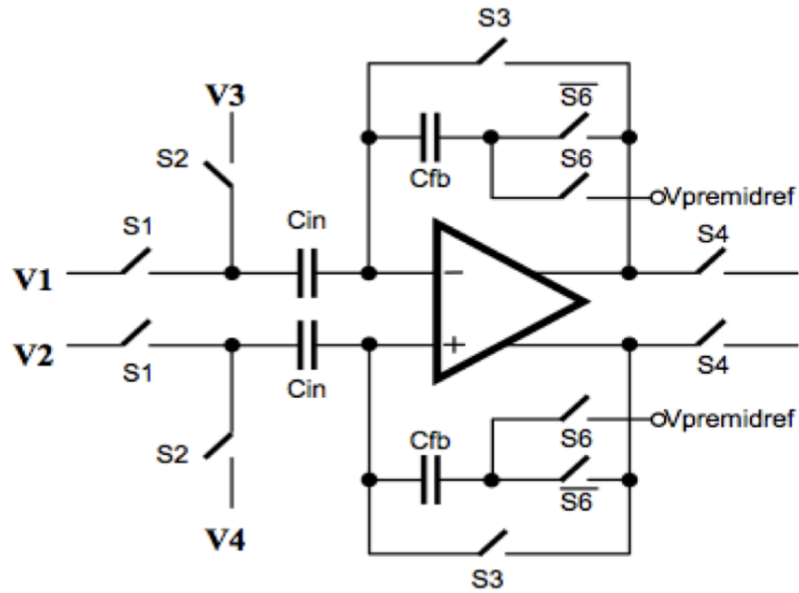


Figure 3.2: Electronics schematic of a preamplifier in the SIDECAR[™]. Each of the SIDECAR[™]'s 32 channels contains an entire signal chain, including the shown preamplifier circuitry.

developed. A 1 row \times 15 column boxcar moves across each row, subtracting a value calculated with the boxcar function from the center pixel. We experimented with multiple boxcar functions, including the 15 pixel mean, median, and the robust mean. The robust mean, an algorithm that rejects outliers before averaging a set of numbers, was chosen because its value was not skewed by pixels containing X-ray signal (unlike the mean) and did not significantly alter the noise distribution (unlike the median). The boxcar function treats each detector output channel individually because there is a discontinuity in the row noise at the channel border. This technique was successful, producing images free of horizontal artifacts. Figure 3.3 shows an early demonstration of the median filter subtraction, which was eventually replaced with robust mean filtering. Note, the only reason that this technique works is because all X-ray data consists of very small (3×3 pixel) regions of high signal overlaid on top of a flat, low-signal background.

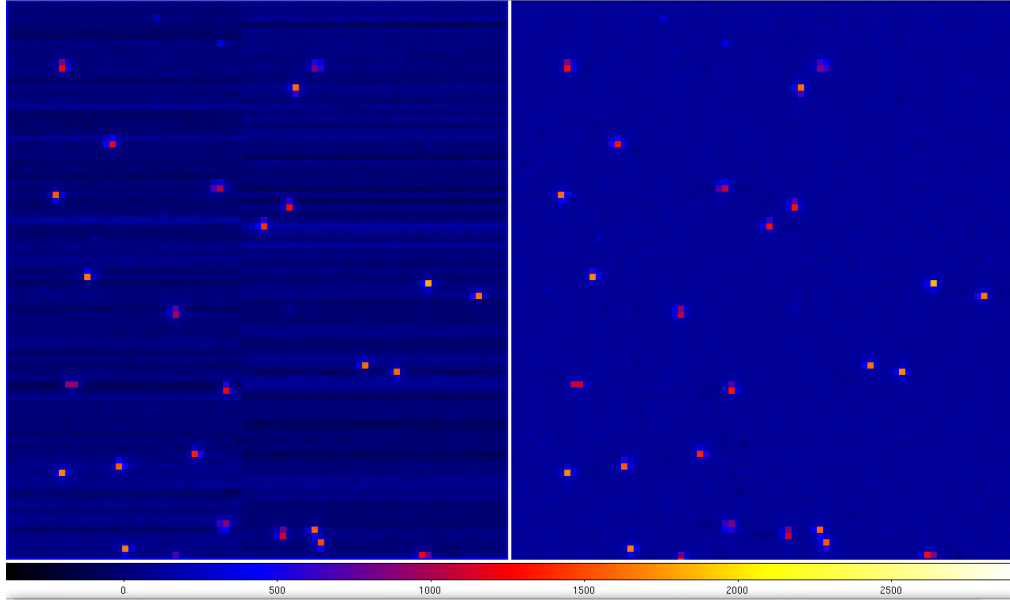


Figure 3.3: A CDS subtracted ^{55}Fe data image before (left) and after (right) median filter subtraction to reduce row noise. Note the flat background in the median filter processed image. Bright pixels are X-ray events.

3.2.4 Substrate Bias Optimization

An experiment was carried out to optimize substrate bias voltage, V_{sub} , with respect to charge spreading of X-ray events. V_{sub} is the voltage across the PIN diodes in the detector's absorber substrate and it performs the critical functions of reverse biasing the diode array, maintaining depletion in the bulk intrinsic silicon, and forcing photocharge clouds into the pixel potential wells. Setting V_{sub} higher creates a stronger electric field inside the depletion region, which more efficiently accelerates charge clouds into the pixel potential wells. This stronger electric field reduces the amount of charge spreading due to charge cloud diffusion. TIS [42] reported simulation results that show this relationship in HIRGs (Figure 3.4).

To test the relationship, V_{sub} was varied from 3.2 - 30 V in 5 V increments, and 20,000 events (5 discrete CDS subtracted frames) were acquired at each voltage. We used 4×4 pixel event regions to ensure that charge spreading farther than 1 pixel distance from the local maximum (primary event pixel) would not be lost. In order to measure the charge spreading of a given event, we calculated the average percent charge in the primary (brightest) event pixel and compared it to the total

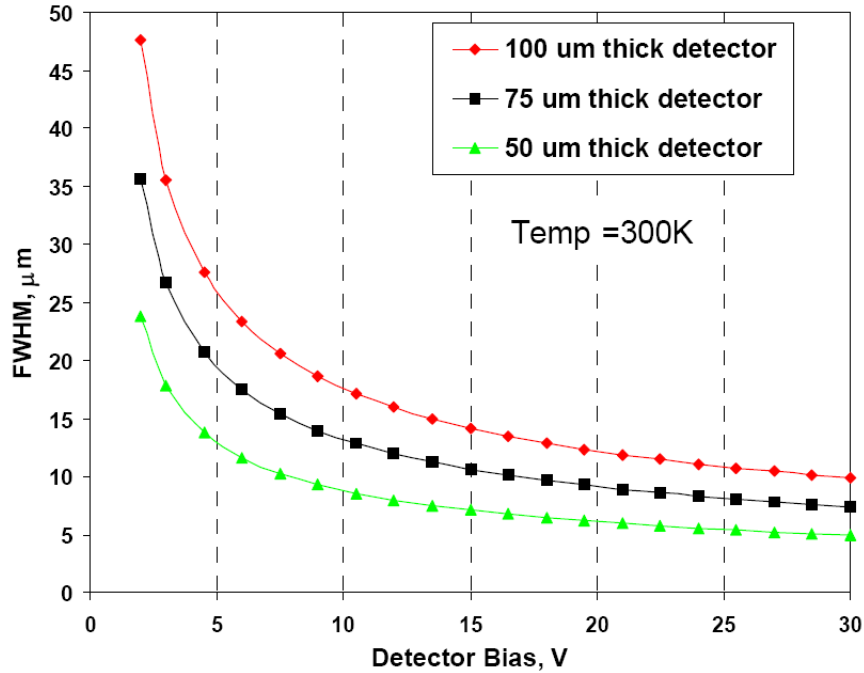


Figure 3.4: A simulation of charge cloud spreading as a function of bias voltage in various thickness detectors [42].

charge in the event, for all events at a given voltage. The results are shown in Figure 3.5. In agreement with TIS’s report, which shows that the charge cloud’s ultimate width at the bottom of the pixel becomes smaller as V_{sub} is increased and approaches an asymptotic value, we observed that the percentage of charge outside of the primary event pixel decreases with increasing V_{sub} . The trend of the shown data appears to abruptly turn over at $\sim 55\%$, an effect that we believe is due to the transition from a regime where signal spreading is dominated by charge carrier diffusion to one where spreading is dominated by interpixel capacitance (IPC), which is relatively independent of V_{sub} . In a separate series of experiments, spatially symmetric events were chosen and their signal spreading percentage was measured in order to characterize the inherent PSF of the IPC effect. It is assumed that charge spreading due to charge carrier cloud diffusion is minimal in the most symmetric events and that these events correspond to what would be a single pixel event on a CCD. The results of the experiment were that IPC causes $\sim 59\%$ of an event’s signal to remain in the primary event pixel, which is very close to

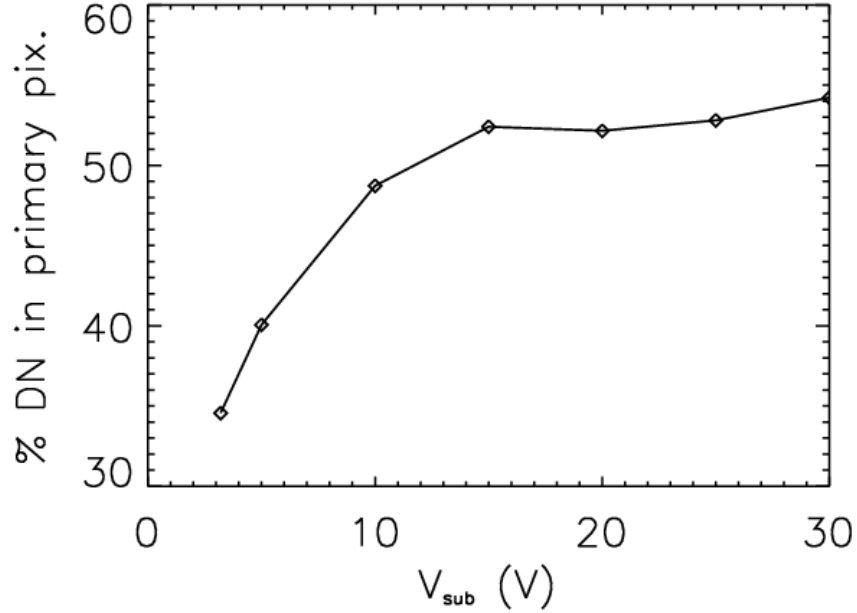


Figure 3.5: A measurement of percent charge left inside of a local maximum as a function of bias voltage for a $100\ \mu\text{m}$ thick absorber array and $18\ \mu\text{m}$ pixels. Charge spreading is due to both IPC and charge cloud diffusion. In this figure, DN is digital number.

our observed roll off at $\sim 55\%$. In light of these results, all subsequently reported data were acquired with the detector substrate biased at 15 V. Also, while we do not explicitly verify the TIS charge spreading result, our experiment shows that a similar relationship exists between V_{sub} and charge spreading.

3.3 Grading

As we have shown, when an X-ray interacts with a HyViSITM HCD, the signal is spread over multiple pixels. Grading is the process of identifying regions of the array where single X-rays have generated photocharge in the substrate and recording properties of the event. We are particularly interested in which pixels surrounding the interaction site contain signal, and also the morphology of that pixel arrangement.

Our first step in event grading is to identify events. In order to be considered an event, we require that a pixel satisfy a primary threshold value that is set $\approx 4\sigma$ above the noise floor. Additionally, the pixel must also be a local maximum, greater in value than its 8 surrounding pixels. Next, we identify which of the 8 pixels in the surrounding 3×3 region contain significant signal by requiring that they satisfy a 3σ secondary event threshold in order to be counted in the event sum. Setting the secondary threshold as high as possible allows fewer surrounding pixels to be counted towards the sum and minimizes the read noise affecting the event sum. However, setting the secondary threshold too high causes signal to be excluded from the event sum. These parameters must be tuned. The IDL procedures `event_detect.pro` and `make_evtlist.pro` were written to accomplish these tasks.

In X-ray CCDs, events are also assigned a number according to their morphology. The IDL procedure `grade_evts.pro` was written to perform this task. This grade number indicates which pixels in the event satisfy the secondary threshold and are used to separate good events from bad detections. However, due to the $\approx 30\%$ charge spreading effect of IPC in our HCD, the direct application of morphology grades has not proven to be as useful for HCD analysis as it has been for X-ray CCDs. Instead, to quantify event morphology, we calculate the fraction of the primary event pixel contained in the second brightest pixel; simply the value of the second brightest pixel in an event divided by the value of the brightest pixel. We have named this quantity the “percent split”. Note that despite being named percent split, the quantity is always shown as a fraction.

During the hardware and software development process it was very useful to be able to visualize the large numbers ($\sim 10^6$) of events in the event list data products. The IDL procedure `disp_evts.pro` takes event list data as input and outputs a FITS image where the events have been arranged in a regular grid pattern for easy visual inspection. The intentional inclusion or exclusion of X-ray events from post-processing analysis based on various criteria, something we call “filtering”, has proven to be very useful for improving energy resolution. The highly vectorized IDL function `evt_filter.pro` was written to accomplish this task.

To visualize what the percent split of all events looks like, we plot a histogram

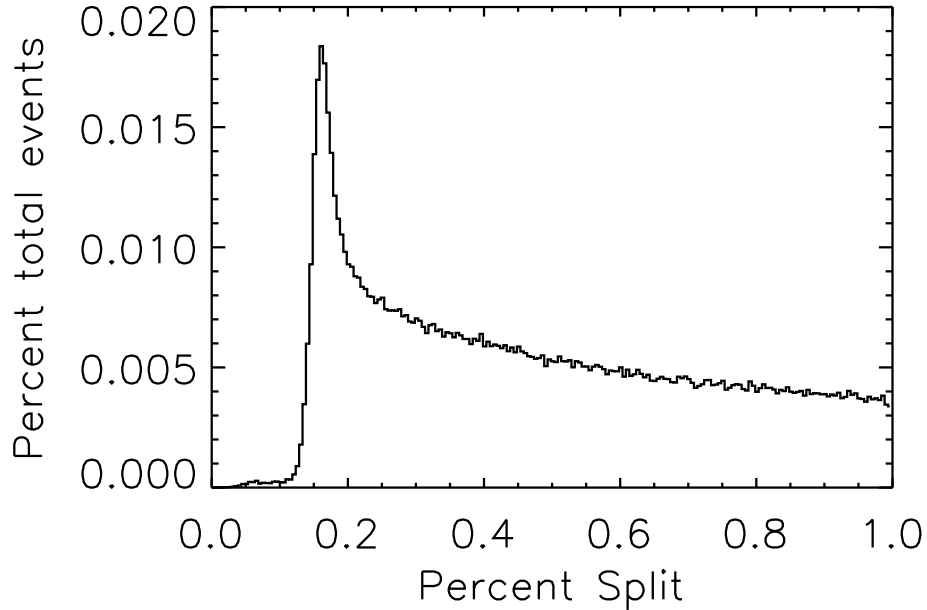


Figure 3.6: The percent split is calculated by dividing the value of the second brightest pixel in an event by the value of the brightest. Note that this is a misleading naming scheme; while the name indicates a percent, the quantity is always shown as a fraction. This quantity provides a simple measure of how much spreading the event exhibits. Plotting a histogram of the percent split values for every event in the dataset shows that a greater relative fraction of events have a percent split of ≈ 0.2 . We believe that these were single pixel events prior to IPC.

of the parameter for ^{55}Fe events in Figure 3.6. The strong low percent split peak visible in the histogram indicates that a larger than average fraction of events exhibit a percent split between 0.1 and 0.2. Compared to other events in the dataset, these low percent split events have a larger fraction of their signal contained within the center pixel. This leads us to believe that these were single pixel events prior to IPC, and will therefore be the best events to use in energy resolution characterization.

3.4 System Gain

The gain of the entire X-ray detector system is the number, in units of electrons per digital number (DN), that represents the complete conversion of charge into a digital number. The total system gain, G_S , can be broken down into several

factors,

$$\frac{1}{G_S} \left[\frac{\text{DN}}{e^-} \right] = \frac{1}{C} \left[\frac{\text{V}}{e^-} \right] G_E G_{\text{ADC}} \left[\frac{\text{DN}}{\text{V}} \right]. \quad (3.1)$$

When the charge in a pixel is read, the capacitance, C , of the output node determines the voltage signal produced by a given amount of charge in the pixel. Finally, this voltage is amplified by an electronics gain, G_E and digitized by an ADC that outputs a digital number DN_{SAR} . The ADC has its own gain, G_{ADC} . We measure the total system gain by producing graded event spectra and observing the DN value of the ^{55}Mn K_α 5.9 keV X-ray line.

All measurements in this dissertation were taken with the 16-bit successive approximation (SAR) ADCs. The approximate digital number output of the electronics, DN_{SAR} , as a function of input voltage V_{in} , is

$$DN_{\text{SAR}} = 32768 G \frac{V_{in} - V_{ref}}{V_{RP} - V_{RN}} + 32768 \quad (3.2)$$

[39], where $V_{ref} = 1.29228$, $V_{RP} = 1.81417$, and $V_{RN} = 0.123167$ are bias voltages that were used to acquire all data and $G = 8$ is the SIDE CARTM preamp gain. These quoted bias voltages are nominal DAC output values reported by the SIDE CARTM control software. Their precision is not known. Later it will be useful to know the shift, in DN of the ADC output for a given change, in mV, at the analog input, something I will refer to as the ADC gain. This number is calculated by differentiating the expression for DN_{SAR} with respect to V_{in} , which results in $32768 G / (V_{RP} - V_{RN}) = 443.286 \text{ DN mV}^{-1}$. Removing the preamplifier gain gives an ADC gain of $55.411 \text{ DN mV}^{-1}$.

3.4.0.1 Preamplifier Gain Optimization

With register programming, the preamplifier gain can be set to one of 16 different settings separated by 3 dB, ranging from -3 dB to 27 dB . To optimize the gain, dark images were taken with a 150 K detector at successive gain values and examined for saturation. In order to leave additional dynamic range headroom for dark current and X-ray signal, gain setting 11, which corresponds to $G = 8$, was chosen and used in all successive data acquisition.

X-Ray Line Sources	
Target	Energy [keV]
Copper	0.92
Zinc	1.01
Aluminum	1.486
Silicon	1.739
Chlorine	2.62
Mn $K\alpha$	5.898
Mn $K\beta$	6.490

Table 3.1: A list of fluorescent X-ray sources used in the cube test stand. The copper and zinc lines are L-shell transitions and are therefore a superposition of multiple, unresolved, closely spaced lines. Note that silicon was not a pure material target, but instead an alloying element in our 4000 series aluminum target. The line was only marginally resolved.

3.4.0.2 Gain Measurement

Grading is a non-trivial process with significant freedom for parameter adjustment. To achieve an accurate value for the system gain, we strive to account for all charge in the pixel region surrounding each event and include it in the final spectra. If some amount of charge were to be lost, then the calculation that every $K\alpha$ photon contains $E_{K\alpha}/\omega_{Si} = 1601 e^-$ would no longer be valid. We accomplish this by using a low, 3σ secondary event threshold, and producing an energy spectrum (Figure 3.7) consisting almost exclusively of events where all 9 pixels in the 3×3 island are included in the event sum. This is confirmed by the histogram in Figure 3.8, which shows that the largest fraction of all events in the dataset contain 8 pixels that satisfy the given secondary threshold. The 5.9 keV peak of the 3σ secondary threshold energy spectra is located at 2576 DN in H1RG-125, making the system gain $0.626 e^-/\text{DN}$, assuming negligible offset. We have gone a step further with H1RG-161 and applied the same 3σ secondary threshold to the copper, aluminum, chlorine, and manganese lines listed in Table 3.1. The line positions are plotted as a function of their known energies and the correlation is fit with a line, as shown in Figure 3.9. The resulting slope yields a system gain of $0.652 e^-/\text{DN}$.

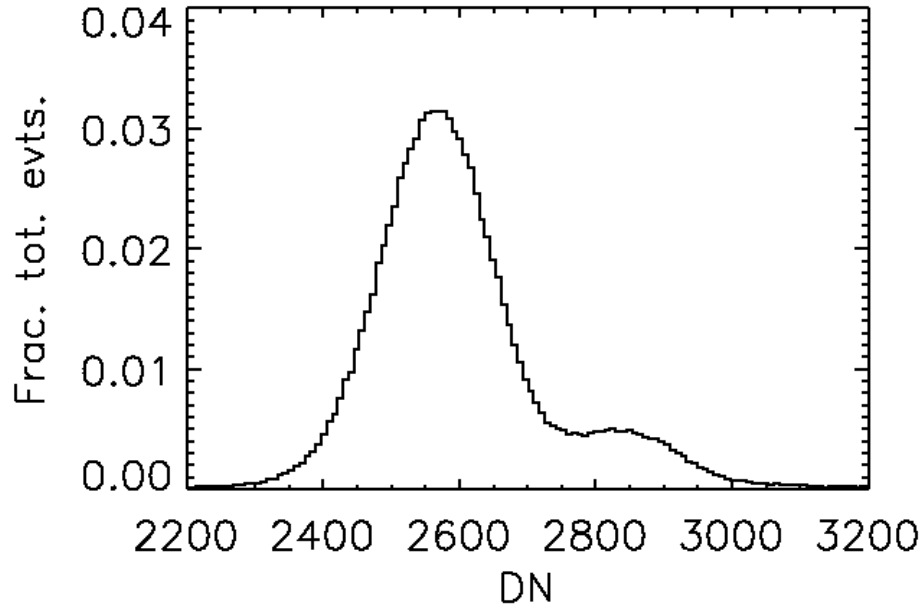


Figure 3.7: Varying the secondary event threshold during event grading will impact the energy spectra. Here, a low 3σ event threshold was used during event grading, resulting in the inclusion of nearly all event island pixels into the event sum. This increases the line width due to the addition of more read noise into the sum, an effect that will be discussed in §3.7.

3.5 Interpixel Capacitance

Interpixel Capacitance (IPC) is the unintended capacitance that exists between pixels in HyViSITM HxRG detectors that are close to one another. This capacitance affects the detector PSF by spreading the signal from one pixel into multiple surrounding pixels. Figure 3.10 illustrates the circuit diagram of a simplified 5 pixel model that accounts for both the capacitance between each pixel and its readout node, C_0 , and the IPC, C_c . The resulting cross shaped spreading of the detector PSF can be seen in the small sub-arrays taken from a copper and an ^{55}Fe image shown in Figure 3.11. It has been reported that IPC should conserve photometry [51], meaning that the decrease in signal of one pixel will equal the summed increase in signal of the surrounding pixels.

X-rays are convenient for characterizing the IPC because very often they will deposit charge in one or two pixels, behaving effectively like an impulse function.

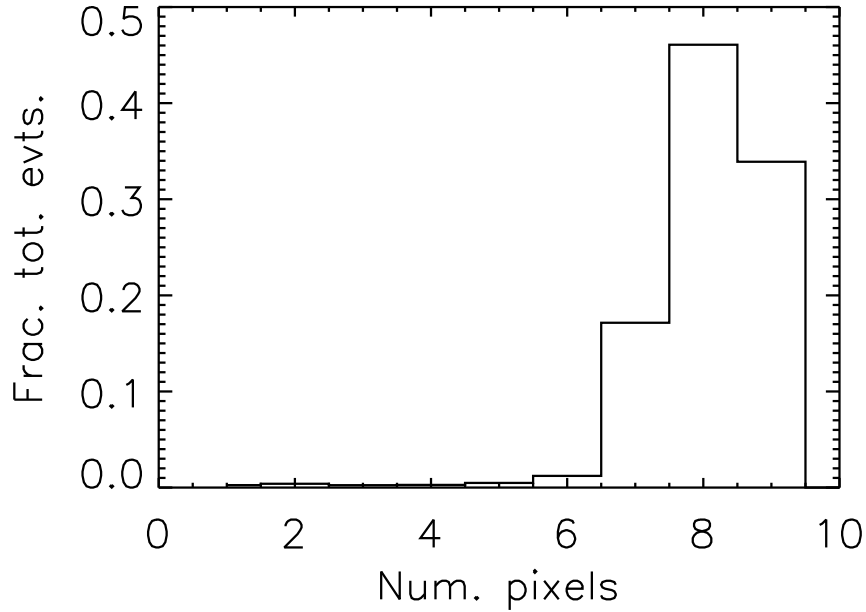


Figure 3.8: Every X-ray that interacts with our detector spreads charge over multiple pixels. When we want to calculate the system gain, we set the secondary event threshold low (3σ) to ensure that we catch most of the charge in each event. This histogram shows the fraction of events in the dataset where some number of pixels satisfied the secondary event threshold. With a conservatively set secondary threshold, most of the pixels in each event island are included in the sum.

However, in reality this characterization process is not trivial. The effects of charge spreading and IPC combine to create events that are both split and blurred across multiple pixels. The HCD charge carrier diffusion simulations by Bai *et al.*, cited earlier in the bias voltage optimization analysis, predict that a charge carrier cloud will diffuse to a FWHM of $\sim 15 \mu\text{m}$ in a $100 \mu\text{m}$ detector biased at 15 V. Even though these results were calculated for a 300 K detector and the charge cloud size will decrease for a colder detector, this suggests that most X-ray events will exhibit some degree of charge splitting in a detector with $18 \mu\text{m}$ pixels. X-rays that interact deep in the absorber or along the pixel's center axis will exhibit the least charge spreading. A more thorough analysis, which is beyond the scope of this chapter, could better predict the split fraction by accounting for the energy dependent exponential X-ray absorption depth distribution and the complex 3D geometry of the electric field near the base of the absorber layer. It is likely that the field geometry at the base of the pixel will strongly influence how charge clouds

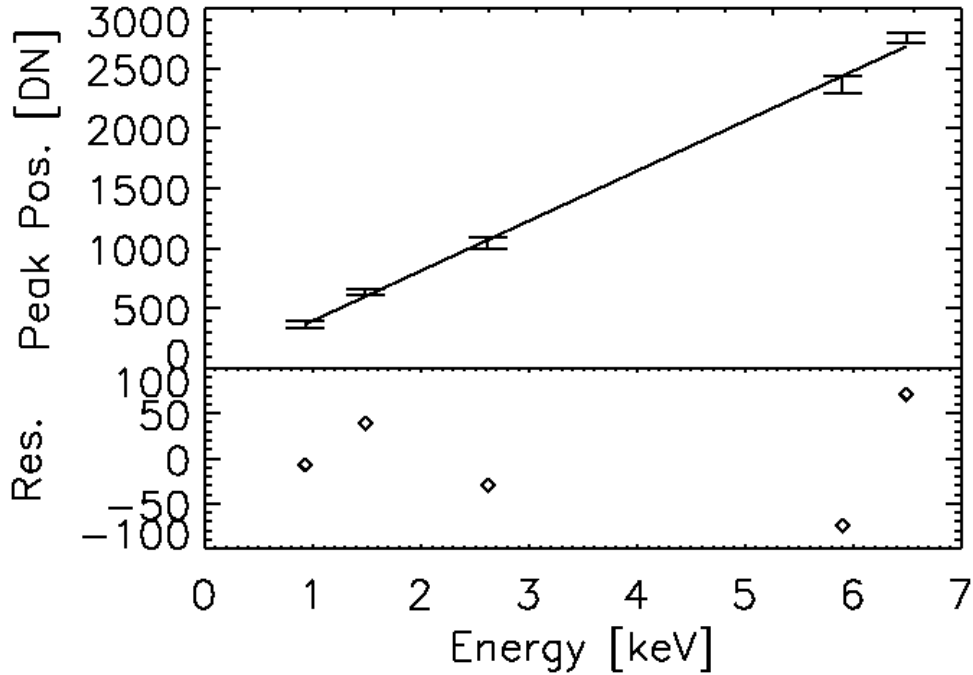


Figure 3.9: The fit peak positions of copper, aluminum, and chlorine, Mn $K\alpha$ and Mn $K\beta$ lines are plotted as a function of their known energies. Error bars are 1σ uncertainty estimates in the fit peak positions. After converting from keV to e^- ($3.68 \text{ eV}/e^-$), the inverse of the slope yields H1RG-161’s system gain of $0.652 \text{ } e^-/\text{DN}$. Residuals (data - fit) are plotted below, also in units of DN.

are physically divided into the potential wells of multiple pixels. Additionally, a thorough understanding of charge splitting can lead to achieving sub-pixel spatial resolution as was demonstrated by Mori *et al.* on *Chandra’s* ACIS [52]. On a separate note and further indicating that most of the events observed by our detectors are split, the tail of the percent split histogram, shown in Figure 3.6, is very heavy on the high-split side of the distribution.

In light of the complication posed by charge splitting, two filtering methods were developed to exclude split events from the IPC analysis, leaving behind events where photocharge was initially deposited in one pixel. These so-called “single pixel events” will characterize the IPC. In the first method, events where the second brightest pixel in the event is between 0 and $\sim 15\%$ of the value of the brightest pixel are selected. The latter percentage was adjusted until $\approx 5\%$ of the total

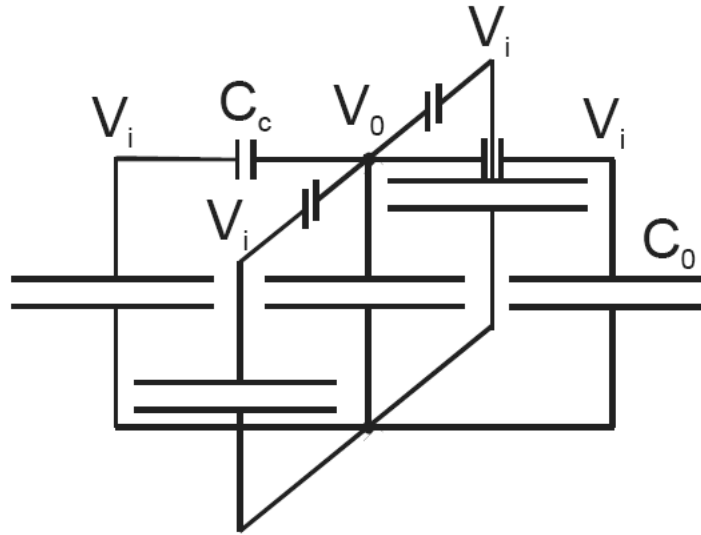


Figure 3.10: An electronics schematic of the 5 pixel IPC model where the center pixel is coupled to its top, bottom, left, and right neighbors. C_0 is the expected capacitance between the pixel and readout node and C_c is the parasitic capacitance between adjacent pixels. In the text these values are individually referred to as C_i , which correspond to the top, bottom, left, and right coupling capacitances. This IPC causes integrated signal to spread between neighboring pixels.

number of events in the dataset made it into the filtered sample. In the second method, the standard deviation of the 8 pixels surrounding the primary (brightest) pixel of each event is calculated. A threshold value is set to exclude events with a large 8 pixel standard deviation. An IDL procedure called `calc_ipc.pro` was written to implement both of these methods on the X-ray event list output of my standard X-ray data reduction pipeline.

The effect of both filtering methods is that only the most symmetric events are selected for analysis, events that originally contained all of their charge in one pixel before IPC took effect. An ^{55}Fe source was used to generate the X-rays for all IPC analyses because it was the highest energy source in the lab, and therefore produced events with the best S/N. Additionally, being relatively hard X-rays, the ^{55}Fe photons are more likely to interact deep in the pixel where they are more likely to produce the single pixel events that best approximate the IPC. The resulting PSFs are shown in Table 3.2. Since these values may be skewed high by charge

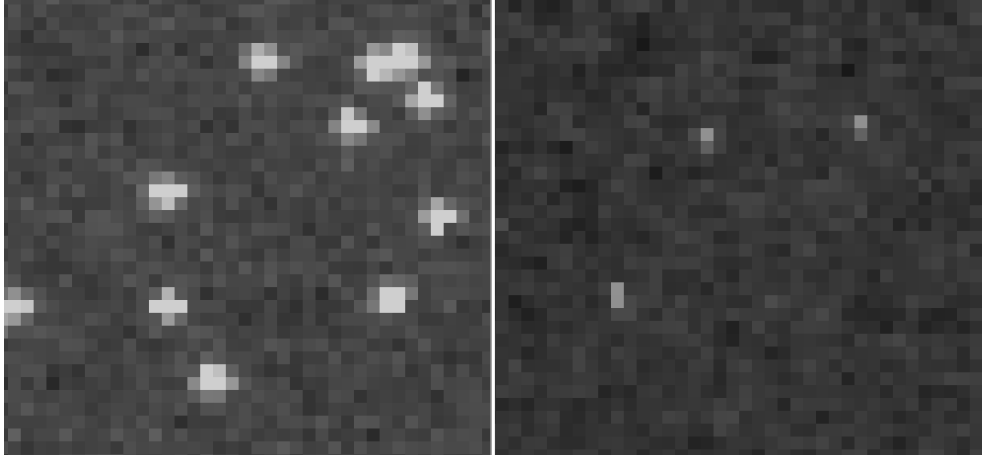


Figure 3.11: Two image sub-arrays showing charge spreading effects in 5.98/6.49 keV ^{55}Fe (*left*) and ~ 0.9 keV fluoresced copper L (*right*) X-ray events. In a CCD, X-ray events are typically confined to one or two pixels. However, in HyViSITM H1RG arrays, events typically spread to 8 or 9 pixels. IPC spreading is less visible in copper X-Rays because they are ≈ 6 times less energetic than ^{55}Fe X-rays and signal from charge spread into adjacent pixels falls below the detector noise floor.

splitting, they should be considered as upper limits.

Prieskorn *et al.* [45] used a third approach, termed the “Paired Pixel” method to vet X-ray events that included charge spreading. Instead of calculating the standard deviation of all eight pixels surrounding the central pixel, this technique calculates the standard deviation of the two pixels above/below and to the left/right of the central pixel individually. If either of these two values is larger than 1σ of the noise floor, the event is considered asymmetric and rejected. Compared to the eight pixel standard deviation method, this technique is more sensitive to asymmetry, and consequently, more sensitive to charge spreading. The IPC in four HCDs was measured with this method using ^{55}Fe data. The results are shown in Table 3.3

The IPC of HyViSITM H1RG detectors has been characterized by Finger *et al.* [51], though their method is different and involves producing an inverse IPC pattern by continually resetting a 1 pixel window region in an array under uniform illumination. Their result, shown in Table 3.2, has been truncated to a normalized 3×3 region so that it can be directly compared to our work.

With the measured IPC and the assumption that IPC conserves photometry,

Second Brightest H1RG-125			Second Brightest H1RG-161			Window Reset		
0.013	0.047	0.012	0.012	0.046	0.012	0.022	0.060	0.021
0.076	0.701	0.068	0.072	0.712	0.071	0.069	0.668	0.058
0.014	0.049	0.013	0.012	0.047	0.012	0.021	0.056	0.021

Standard Deviation
H1RG-125

0.013±0.009	0.070±0.027	0.020±0.011
0.070±0.024	0.630±0.140	0.024±0.024
0.024±0.019	0.070±0.019	0.013±0.013

Standard Deviation
H1RG-161

0.008±0.010	0.063±0.020	0.009±0.009
0.067±0.022	0.71±0.14	0.061±0.020
0.011±0.013	0.064±0.022	0.008±0.009

Standard Deviation
H1RG-167

0.017±0.037	0.077±0.010	0.018±0.004
0.082±0.009	0.610±0.049	0.081±0.002
0.017±0.004	0.080±0.014	0.018±0.004

Standard Deviation
H2RG-122

0.007±0.010	0.016±0.009	0.007±0.011
0.017±0.009	0.905±0.110	0.017±0.010
0.007±0.010	0.017±0.009	0.007±0.011

Table 3.2: *Top*: the 3×3 IPC PSF obtained by averaging symmetrical events selected with the second brightest pixel method in our detectors H1RG-125 and H1RG-161 and the IPC PSF of a different HyViSITM H1RG using a 1×1 pixel window reset method [51]. The remainder of the table presents results for different detectors with the standard deviation method from Griffith *et al.* [53]. Quoted uncertainties were calculated individually for each pixel position in the 3×3 grid. The standard deviation of each set of values was calculated and scaled by the normalization to yield the uncertainty. Both read noise and the unintended inclusion of charge spreading are represented in the uncertainties.

Paired Pixel
H1RG-125

0.017±0.007	0.054±0.010	0.018±0.008
0.097±0.013	0.626±0.068	0.097±0.013
0.018±0.007	0.054±0.010	0.018±0.007

Paired Pixel
H1RG-161

0.011±0.008	0.044±0.014	0.012±0.008
0.087±0.015	0.690±0.098	0.087±0.015
0.011±0.009	0.045±0.013	0.011±0.007

Paired Pixel
H1RG-167

0.012±0.006	0.040±0.007	0.013±0.005
0.093±0.010	0.685±0.062	0.093±0.010
0.012±0.004	0.039±0.006	0.013±0.005

Paired Pixel
H2RG-122

0.007±0.012	0.017±0.010	0.007±0.011
0.018±0.010	0.901±0.11	0.018±0.011
0.007±0.012	0.017±0.010	0.007±0.012

Table 3.3: Paired Pixel IPC analysis results, as reported by Prieskorn *et al.* [45].

the 5 pixel model can be used to calculate the nodal capacitance, C_0 , and the top, bottom, left, and right coupling capacitances, C_i , where $i = 1, 2, 3, 4$. The total capacitance, C , between the center pixel and read node is

$$C = \sum_{i=1}^4 \left(\frac{C_0 C_i}{C_0 + C_i} + C_0 \right). \quad (3.3)$$

Given a charge, Q , deposited in the pixel, a voltage signal of

$$V_0 = \frac{Q}{C} = \frac{Q}{\sum_{i=1}^4 \left(\frac{C_0 C_i}{C_0 + C_i} + C_0 \right)} \quad (3.4)$$

will be produced in the center pixel and

$$V_i = V_0 - \frac{Q_i}{C_i} = \frac{Q \frac{C_i}{C_0 + C_i}}{\sum_{i=1}^4 \left(\frac{C_0 C_i}{C_0 + C_i} + C_0 \right)} \quad (3.5)$$

will be produced in each of the four adjacent pixels. An average ^{55}Fe X-ray will produce $Q = \left(\frac{5.89r}{1+r} + \frac{6.49}{1+r} \right) \frac{1}{\omega_{Si}} = 1621 \text{ e}^-$ in the detector, where $r = 6.79$ is the $K\alpha/K\beta$ line intensity ratio that will be derived in Chapter 4 §4.3.3. This signal level, in number of electrons, can be converted to DN with the measured gain of $0.652 \text{ e}^- \text{ DN}^{-1}$. To find the single pixel voltage, V , of an average ^{55}Fe X-ray, the DN value is divided by the ADC gain from §3.4 and the preamp gain. This number, multiplied by the normalized IPC values, yields V_0 and V_i . Solving for C_0 and the four C_i values with IDL's Newton algorithm yields values of $C_0 = 8.1 \cdot 10^{-15} \text{ F}$ and $C_i = 9.4 \cdot 10^{-16}, 6.5 \cdot 10^{-16}, 1.1 \cdot 10^{-15},$ and $6.9 \cdot 10^{-16} \text{ F}$, which correspond to the right, top, left, and bottom components of the IPC, respectively. Alternatively, the DN values of a set of averaged X-ray events that have been filtered to include only those with minimal asymmetry (charge spreading) could be divided by the ADC gain and preamp gain to calculate V_i and V_0 .

3.5.1 Deconvolution

We performed a pathfinder study to evaluate the potential benefits of deconvolution techniques for mitigating the negative effect that IPC has on HCD X-ray performance. In our tests, we used the IDL Astronomy User's Library's maximum likelihood estimator, `max_likelihood.pro`. The algorithm performs Lucy-Richardson (LR) deconvolution to iteratively solve for the maximum probability latent image, given an observed image and a convolution kernel. In any detector system, the latent, or ideal, unblurred image is convolved with the detector system's response, or PSF, to form the observed image. The PSF characterizes the output image's departure from the ideal at each point in the detector plane. In optics, it includes factors such as blurring caused by diffraction, distortion inherent to the optical prescription, and additional distortion due to misshapen optics. In the case of an HIRG detecting unfocused X-rays, the PSF is dominated by IPC and charge spreading.

In our experiment, the measured IPC and CDS-subtracted, row noise-corrected ^{55}Fe images were input into the algorithm as the deconvolution kernel and observed image, respectively. Since the noise was dominated by pixel read noise, the gaussian noise variant of the algorithm was used. The results are shown in Figure 3.12. It was found that the algorithm helps to restore the expected 2-pixel split event geometry, which shows potential for improving event detection in high-flux data, where events may overlap. When the events were combined to form an energy spectrum, it was found that the deconvolution did not improve energy resolution.

In addition to being a tool for separating X-ray events that are blurred together, deconvolution also has the potential to become a tool for measuring IPC. In the LR algorithm, the deconvolution kernel is a required input. In the myopic deconvolution family of algorithms, the PSF is iteratively refined during deconvolution [54]. These algorithms were developed for adaptive optics applications and represent an interesting option for improving the characterization of IPC.

3.5.2 IPC Discussion

Griffith *et al.* used the aforementioned IPC calculation methods and code to show that the H2RG-122 exhibits a factor of > 3 less total IPC than the H1RGs, a difference explained by the larger pitch of its absorber array ($36 \mu\text{m}$ compared to $18 \mu\text{m}$) [53]. If the coupling between two pixels is modeled as simple parallel-plate capacitor, doubling the distance between the plates will reduce the capacitance by a factor of two.

It is not immediately clear where the capacitance that causes IPC is physically located in the HCD pixel. Bai *et al.* have run models which indicate that it exists between the Si PIN diode of the absorber array [38]. Internal TIS experimentation with two pixel redesign schemes, one that “employs geometric optimization” and a second that “provides control over the fringing field in the detector material”, have shown decreased IPC.

An interesting control study that has not been performed, as far as I know, is to expose a bare HxRG Mux to X-rays and observe the IPC. While the active region in each pixel will be limited to a very small volume surrounding the output source follower, the bare Mux should exhibit some non-zero sensitivity to X-rays. If X-ray

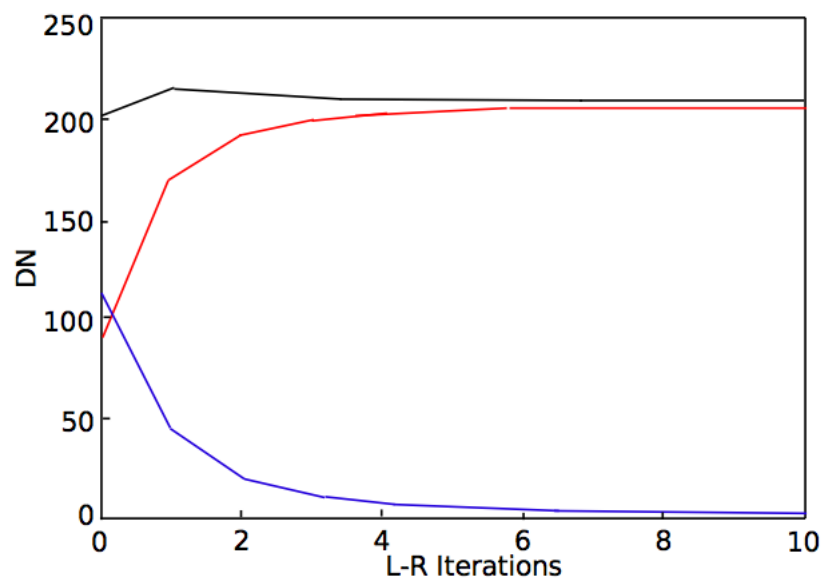
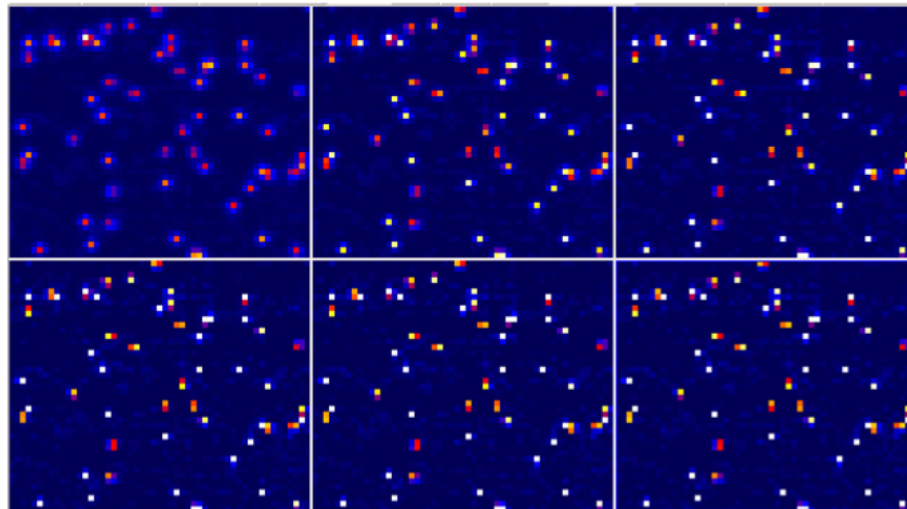


Figure 3.12: *Top*, A progression from left to right of 0, 1, 3, 5, 10, and 15 iterations of the LR algorithm. It is necessary to view this figure in color in order to best see the how the deconvolution effectively reverses IPC signal spreading. *Bottom*, testing LR signal conservation. One single-pixel event was monitored as deconvolution progressed. The central pixel (red, middle), surrounding 8 pixels (blue, bottom), and 9 pixel total (black, top) values are plotted as a function of LR iteration number. In this application the algorithm stabilizes very quickly at ~ 9 iterations.

events detected in a bare Mux exhibited undetectable spreading, the ROIC could be definitively ruled out as a source of IPC.

Future detectors, notably those with the TIS Speedster architecture, are being built with capacitive trans-impedance amplifiers (CTIAs) in place of the source followers. Since these amplifiers maintain a constant potential at the sense node, it is expected that they will eliminate IPC. It should be noted that the CTIA architecture is not a blanket solution to the IPC problem because they have the design tradeoff of requiring more pixel real estate than the source follower design. However, since eliminating IPC means that fewer pixels will need to be summed to reconstruct the energy of an X-ray, devices with CTIAs will likely exhibit better energy resolution because they minimize the read noise contribution to event energy.

3.6 Read Noise

We have measured the CDS noise in each frame of our dataset of X-ray images by measuring the FWHM of the noise peak in a histogram computed from image pixel values. This quantity is not skewed high by bright pixels containing X-ray charge and provides a measurement of the noise as data are being taken. Assuming that the noise is normally distributed allows us to calculate the noise RMS from the pixel histogram FWHM. Using the previously calculated system gains we calculate the CDS noise for H1RG-125 and H1RG-161 to be 7.48 and 8.87 e⁻ RMS respectively. In detector test reports, Teledyne calculates H1RG-125 and H1RG-161's mean CDS noise at 150K to be 12.2 and 10.3 e⁻ RMS. Differing array readout, offset correction (such as the row noise correction), noise calculation, or conversion gain may account for the difference.

An interesting idea that takes advantage of the CMOS sensor's ability to non-destructively read pixels, is to perform what amounts to Fowler sampling of the X-rays during post-processing. Low-energy event detection and overall energy resolution can be improved by processing the pixel values as a function of frame number with a time series pattern matching algorithm as opposed to the simple pixel value differencing and threshold detection approach taken in our CDS subtraction scheme. Once an event is detected, pixels in the surrounding region could

be fit with step functions, effectively decreasing the read noise with multiple reads. Since such a scheme derives its advantage from the X-ray arrival times being separated by multiple pixel sample periods, it would not do well for flux rates that are approaching the pileup limit. Similarly, in a detector such as the Speedster, which contains an in-pixel comparator, perhaps the absorption of an X-ray could trigger a series of fast reads that would eventually be averaged.

3.7 Energy Resolution

Among the most useful features of X-ray HCDs is that they are imaging spectrographs; they have the ability to do simultaneous imaging and non-dispersive spectroscopy since the energy and location of every X-ray event is recorded by the detector. The ability of a detector to measure the energy of an incident photon is described by its energy resolution: $R = \Delta E/E$. The fundamental limit of energy resolution is set by Fano [6, 7] noise and a detector that performs at this level is said to be Fano limited. The noise originates in the uncertainty in the number of electrons generated when an X-ray interacts with a silicon detector. The variance is

$$\sigma_F^2 = \frac{FE}{\omega}, \quad (3.6)$$

where F is the Fano factor (0.113 for Si), E is the X-ray energy, and ω is the average electron-hole pair generation energy (3.68 eV for Si). Inserting numbers, Fano limited performance at 5.898 keV is 0.116 keV, corresponding to an energy resolution of 2%. Due to the complicated details of solid state physics that they contain, both F and ω are always measured empirically.

In H1RG HCDs, energy resolution is strongly influenced by the combined effects of read noise, IPC, and charge spreading. As we have shown, IPC spreads signal in an event into N pixels, where N depends on the level of IPC in the particular device. Therefore, in order to fully reconstruct the signal from an event, N pixels must be summed, and their associated read noise must be summed in quadrature. If all events were spatially symmetric, we could avoid this significant addition of noise by reading only each event's central pixel value and accounting for the missed

adjacent pixel charge with a constant factor that would be absorbed into our measurement of the system gain. Unfortunately this method, and similar variants, fail because many events are asymmetric because of electron cloud diffusion charge spreading. To improve energy resolution, we first specify a low percent split range, essentially picking out only the most symmetric events, events that will require the fewest read pixels to accurately measure charge content. Second, we tune the secondary threshold to find a balance between excluding low signal pixels that contribute more noise than signal to the total energy and including pixels that contribute asymmetrically distributed charge that cannot be accounted for by constant factors in the system gain.

The spectrum that results from this method is shown in Figure 3.13 and the measured energy resolutions are plotted as a function of energy in Figure 3.14. We have found that the optimal secondary threshold increases with energy and we have shown this measured relationship in Figure 3.15. This relationship is expected since the height of each event's spatial profile will scale with total energy. If we expect to use the secondary threshold to cutoff a constant fraction of dim pixels to maintain ≈ 5 pixels in each event, the secondary threshold will have to scale with energy.

In our system energy resolution is dependent on particular parameters used in data reduction. The choice of primary and secondary event thresholds and event morphology strongly affect the energy resolution. Using events with a split percent between 0 and 0.2, and specifying a very large 9σ secondary event threshold, we obtain the spectrum in Figure 3.16, which has $\Delta E/E = 4.2\%$. Specifying such a high event threshold is simply a roundabout method for choosing a particular shape for summing pixels in the events. 95% of the events were cross shaped after specifying such a high threshold, implying a centralized X-ray hit with IPC inducing signal in pixels above, below, and to the sides of the center pixel. Such filtering produces a well resolved spectrum because we require that the events be single or nearly single pixel events before IPC and then effectively choose to sum only the top, bottom, left, right and center pixels. The method is minimizing the number of pixel reads required to get an accurate measurement of event energy.

In general, the nondispersive X-ray energy resolution of a photon detector (in-

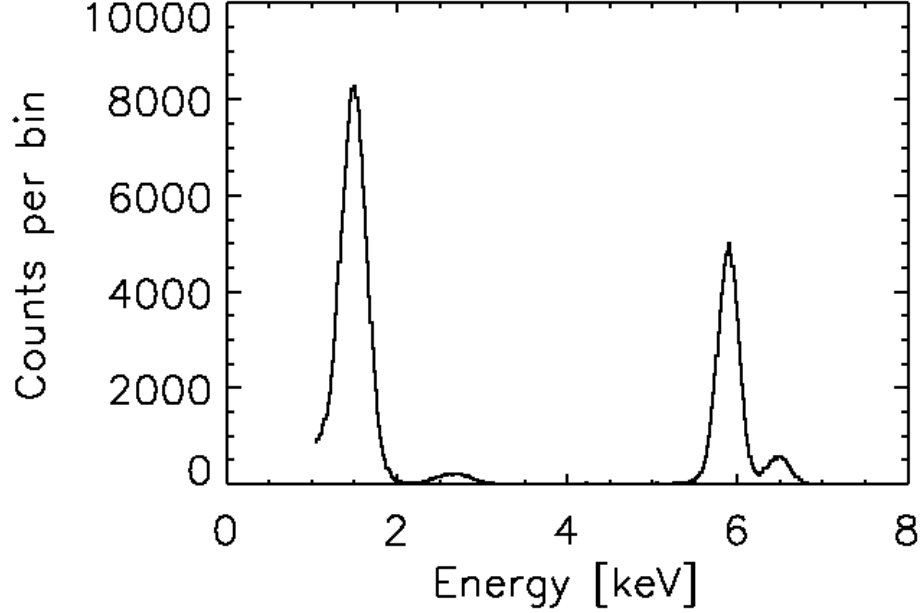


Figure 3.13: A combined aluminum, chlorine, and manganese $K\alpha/K\beta$ energy spectrum generated by selecting events with low percent split and tuning secondary event threshold for each energy. This spectrum has $\Delta E/E=4.2\%$ at 5.9 keV.

cluding proportional counters, CCDs, and HCDs) can be expressed as

$$\frac{\Delta E}{E}(FWHM) = \frac{2.354\omega}{E} \sqrt{\frac{FE}{\omega} + \sigma^2}, \quad (3.7)$$

where σ is the total noise associated with the detection and 2.354 is the conversion factor between 1σ and FWHM. In the case of first-generation HyViSITM X-ray HCDs, the IPC necessitates summing charge from more than one pixel to reconstruct the X-ray energy. This leads to $\sigma = \sqrt{N_{pix}\sigma_{RN}}$, where N_{pix} is the number of pixels that are summed per event in an event list and σ_{RN} is the single-pixel read noise. Noting the peak at ~ 8 pixels in the N_{pix} distribution for H1RG-125 with a 3σ secondary threshold on a ^{55}Fe source, which was shown in Figure 3.8, and the 7.48 e⁻ single-pixel read noise quoted for that detector in §3.6, we can predict that the energy resolution should be 3.9%. However, looking back at the unfiltered 3σ secondary threshold ^{55}Fe data shown in Figure 3.7, the spectrum

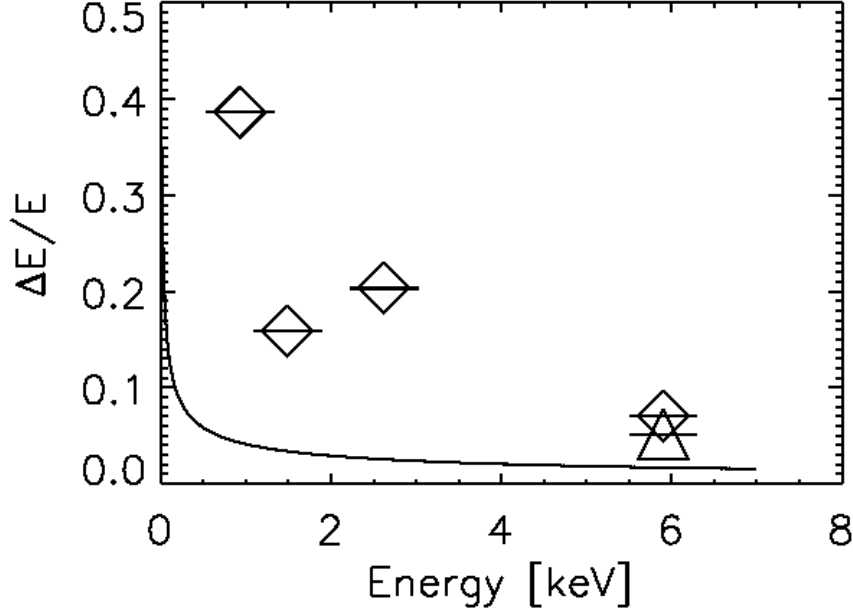


Figure 3.14: The measured $\Delta E/E$ of copper, aluminum, chlorine, and manganese $K\alpha$ lines as a function of line energy. The diamond data points were calculated using H1RG-161 data (7.0%) and the triangle data point was calculated using H1RG-125 data (4.2%). The very small vertical error bars represent the 1σ uncertainty in $\Delta E/E$ calculated from uncertainty in the emission line peak width. Scatter in the trend is therefore not due to fitting error and is likely caused by thresholding. The solid line is the Fano limit.

shows $\frac{\Delta E}{E}(FWHM) = 7.2\%$. If the increase in measured energy resolution was due to missing charge during event recognition as a result of using too small of a region, the added distribution width would manifest as a low energy tail on the emission line. While some line asymmetry exists (See §4.4.3), it does not dominate the width. Two untested effects that may account for the diminished energy resolution are that IPC may not conserve signal and the pixel-to-pixel gain may vary. If the 1% RMS pixel-to-pixel gain variation typically quoted by TIS is informally included in the energy resolution estimate by adding a factor of $(0.01E/\omega)^2$ under the square root in Equation 3.7, the resulting predicted energy resolution is 4.5%.

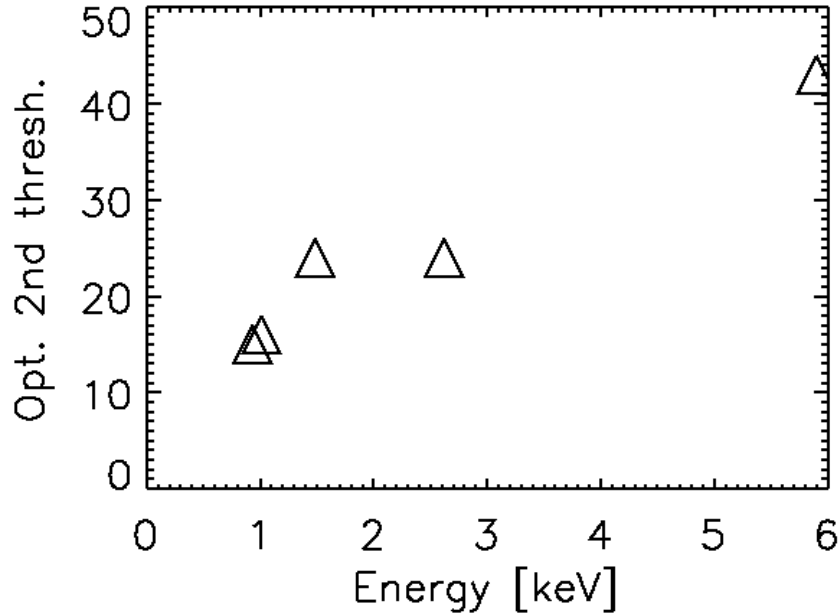


Figure 3.15: The optimized secondary thresholds for copper, zinc, aluminum, chlorine, and manganese $K\alpha$ are shown here to increase as a function of energy. The unit for the secondary threshold is DN.

3.8 Permanent Threshold Shift

It is critical to note that while a reduction in charge spreading from the use of a large V_{sub} may seem like a good idea, operating the HIRG at high substrate bias voltage is potentially dangerous to the HIRG under certain conditions. Teledyne reported [42] that it is possible to damage the CMOS ROIC if the array is exposed to room light while the substrate is biased at greater than 5.2 V. The damage occurs because as a pixel becomes saturated, voltage at the pixel's sense node (a source follower gate) will approach V_{sub} . CMOS process electronics are designed to withstand ~ 5.2 V. Therefore, if V_{sub} is set greater than 5.2 V and the array is allowed to saturate, the gate oxide will be stressed and the source follower's response will be permanently altered.

After acquiring the large amount of ^{55}Fe data presented in this work and while

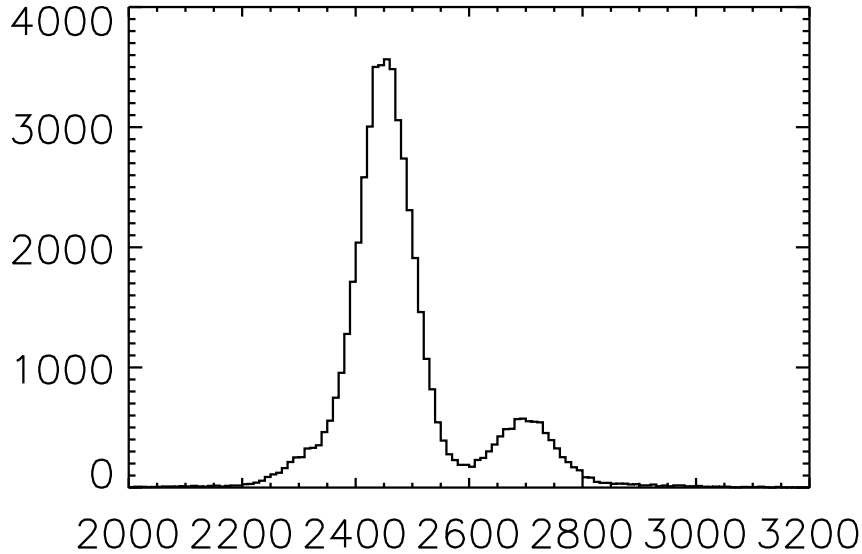


Figure 3.16: An ^{55}Fe energy spectrum generated by selecting events with percent split less than 0.2, approximately equivalent to selecting single pixel events prior to IPC spreading, and setting the secondary event threshold to 99 DN. This spectrum has $\Delta E/E = 4.2\%$.

attempting to acquire additional X-ray line data, we unknowingly exposed the powered H1RG-125 to room light, causing a permanent threshold shift in the unfiltered half of the array. The aluminum-coated half of the array was relatively protected from damage. The effect can be seen in the raw (pre-CDS subtraction) column data plotted in Figure 3.17. These plots correspond to before and after the threshold shift damage occurred. Note that most of the noise and structure seen in the background of these plots is fixed pattern noise. These artifacts appear in all raw images and cleanly subtract out with the CDS subtraction. In fact, the threshold shift is constant enough that it also subtracts out with the CDS subtraction, however the effect still decreases dynamic range and produces excess noise in the entire chip. Prior to the threshold shift H1RG-125 exhibited a total noise of 12 DN RMS. After the threshold shift, the affected region showed noise of 20 DN RMS.

It has been suggested by TIS that room temperature annealing may slowly fix the permanent threshold shift over time. The array will be tested in the future to evaluate whether or not any change is taking place. Finally, we note that this

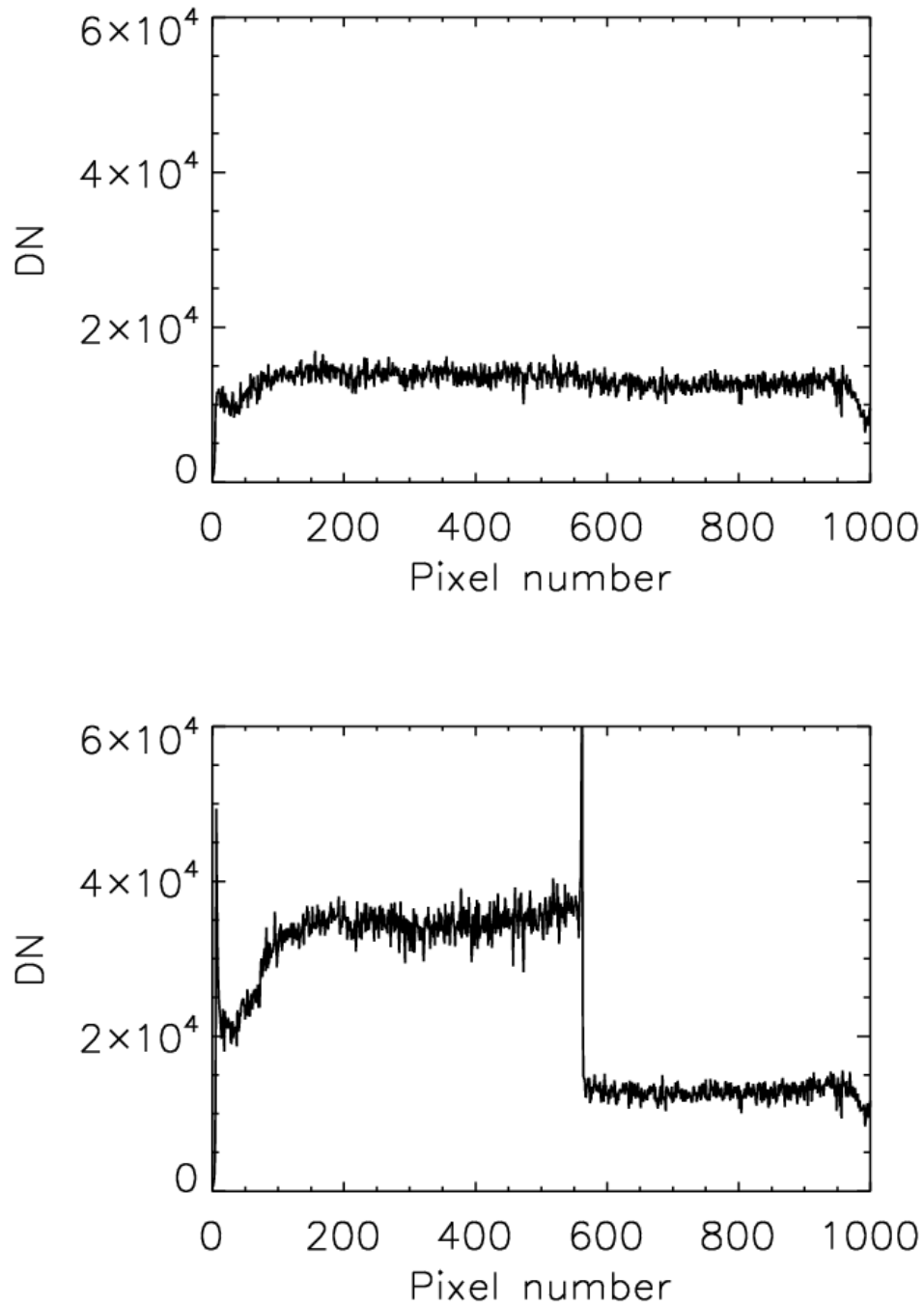


Figure 3.17: A vertical cut through a raw (pre-CDS subtraction) image before (*top*) and after (*bottom*) the permanent threshold shift damage occurred. In this device, the aluminum OBF covers the array for pixel numbers $\gtrsim 560$, which explains the sharp drop in threshold shift seen in the bottom plot.

sensitivity to array saturation at high bias voltage is only present in ROICs that use source follower sense nodes. Future detectors will be built with CTIAs, a technology that will eliminate both permanent threshold shift and IPC by holding the sense node at a constant potential.

Measurements of HCD quantum efficiency

Using a multi-purpose test-stand that I designed and built for this project, I have measured the X-ray quantum efficiency (QE) of a Teledyne HCD at X-ray energies of 5.89 and 6.49 keV. This chapter will begin with a definition of QE and an explanation of why it is a useful quantity to measure, followed by a description of physical mechanisms that influence the QE of an HCD. Next, there will be a description of various methods that can be used to measure this quantity. I will then describe the method that we chose for this particular QE measurement experiment, give a detailed description of the test-stand that was used to make the measurement, and explain the many design decisions that influenced how the test-stand was built. The design and operation principles of the laboratory X-ray sources that are useful for QE measurements will be described. Finally, our QE test results will be presented at the end of the chapter, accompanied by a Monte Carlo error simulation. The results will be compared to a physical model that predicts the QE of an HCD device.

4.1 Motivation

The QE of a detector is the fraction of incident radiation, at a particular energy, that registers a response in a detector. As I described earlier in Chapter 1, Equation 1.3, it is one of the parameters that contributes significantly to the overall

performance of an instrument. In conjunction with the energy dependent response of the other parts of an instrument, such as optics and filters, the noise and dark current properties of the detector, and the source/background flux, the QE determines the instrument’s final sensitivity limit. Regardless of whether the goal is to allow a camera phone’s 1.5 μm CMOS pixels to take crisp photos in a dimly lit bar or enable new science by improving the flux limit of a survey telescope, detector designers strive to build detectors with high QE. Doing so enables the design of instruments with improved sensitivity without incurring the usual tradeoff penalties, such as the increased cost of a larger aperture instrument. Detector QE is, therefore, a quantity that must be measured and maximized during detector design and seriously considered during the instrument design process.

During the process of developing a detector itself, measuring the QE enables one to infer and verify the sometimes uncertain parameters of a detector’s physical structure. In the case of our HCD, deposited filter thickness, top-surface dead layer thickness, and depletion depth can be constrained by fitting the measured QE with models where layer thicknesses are the only free parameters. Finally, measuring the QE of science instruments during commissioning calibrations enables future investigators to make absolute flux measurements of on-sky science sources. Our QE test-stand was designed to accommodate a variety of future detector calibration measurements. In order to guide the design process and ensure that our engineering effort produced a test-stand large enough for generalized use, we designed it to be capable of calibrating the flight detector modules from the X-ray Coded Aperture Telescope instrument proposed in the *JANUS* mission concept. This means that a mosaic of four HIRGs can be tested simultaneously with the detectors held at a temperature setpoint between 150 and 200 K, with better than ± 0.05 K temperature stability.

The QE is often highly dependent on incident photon energy due to the combined effect of the various physical energy dependent mechanisms that impact the detector’s response to light. In the specific case of a photo detector that is built from biased silicon, low-energy response begins at $E_\gamma \approx 1.1$ eV ($hc/E_\gamma = \lambda \approx 1.1\mu\text{m}$), shown in Figure 4.1. At this energy the silicon changes from being largely transparent to partially absorptive because a mechanism for absorption has become available; the incident photons have enough energy to promote an electron

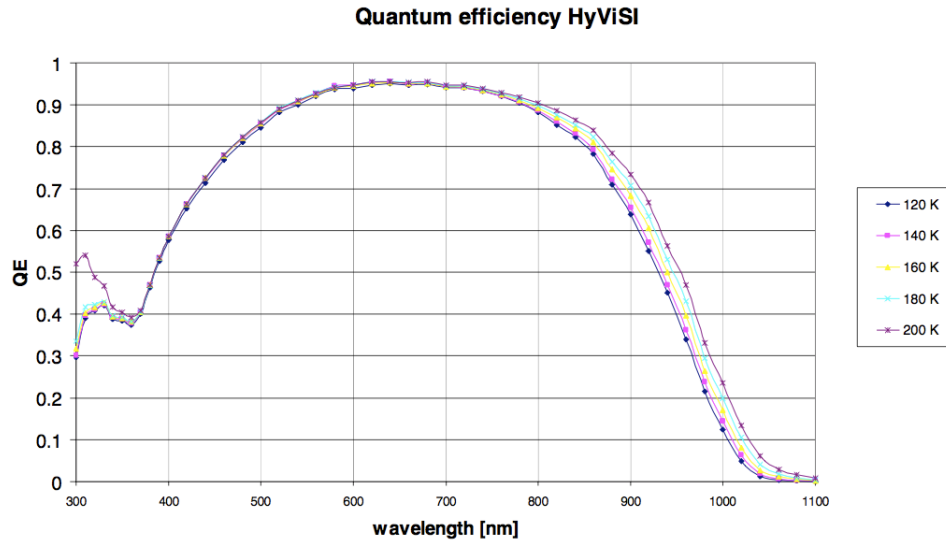


Figure 4.1: Example of an optical QE curve for an optically optimized (anti-reflection coated) H2RG borrowed from Dorn *et al.* [55]. These data are shown only to illustrate the general behavior of a silicon detector in the optical regime and not to make comparisons with our X-ray QE measurements.

from the silicon’s valence band to the conduction band, i.e., to jump the band gap. Interestingly, this transition of the silicon from transparent to absorptive is smooth, not a discontinuous step function like in an absorption edge, where an electron’s binding energy is suddenly exceeded. This is a consequence of the energy dependence of the semiconductor’s density of states. The density of states, D , is the number of available states per unit volume that an electron can occupy. The energy bands of a semiconductor are usually shown as two solid, rectangular bands, but the true picture is much more complicated. Figure 4.2 depicts a model of the density of states in the valence and conduction bands of silicon. In the case where an incident photon has energy $h\nu \approx E_{gap}$, the photon has a chance of being absorbed, but the absorption will not be efficient because the density of states at the top of the valence band and the bottom of the conduction band is low and, consequently, there are few allowable transitions per volume of silicon. As the incident photon energy increases, many more potential transitions per unit volume become available, the photon is more likely to be absorbed, and the QE goes up.

Although they all constitute minor effects, a number of mechanisms cause sil-

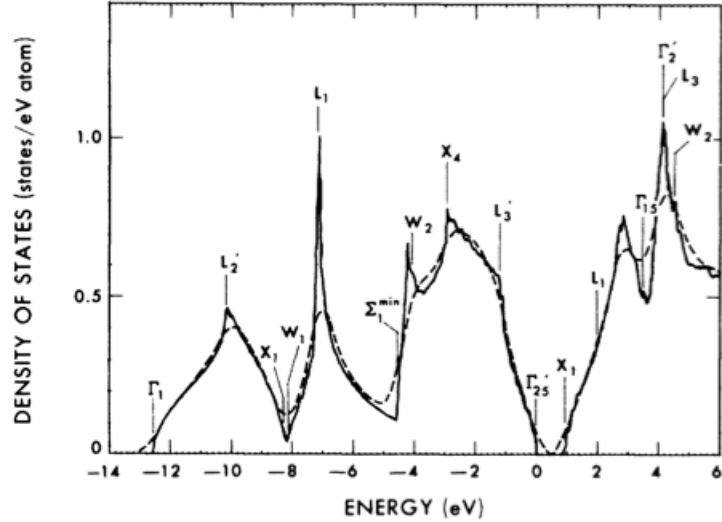


Figure 4.2: A theoretical representation of silicon's density of states. While this function is very complicated, the feature to note is the behavior of the function near 0 eV. The function drops smoothly down to zero at 0 eV, where the valence band ends, and becomes non-zero again at ≈ 1.1 eV, the band gap energy. Here, instead of being plotted as number volume⁻¹, the density of states is shown as number atom⁻¹ eV⁻¹. Figure was borrowed from Chelikowsky [56].

icon to exhibit very limited, but non-zero, response to photon energies below the quoted band gap. Exciton states are energy levels that exist slightly below the valence band and give the detector a small response below the band gap energy. Phonon + photon interaction with electrons can cause response below the band gap. Also, warmer silicon has better response near the band gap energy because the more energetic phonon distribution gives valence electrons the momentum they need to jump the material's indirect band gap. This effect is visible in the H2RG QE data shown in Figure 4.1.

As shown in Figure 4.1, the QE continues to rise when incident photon wavelength decreases from $1.1 \mu\text{m}$ to ~ 600 nm, since photons no longer have trouble creating electron-hole pairs in silicon. However, two major problems begin to arise that will limit the detector's response to blue and UV light: surface reflectance and shallow absorption. Figure 4.3 shows the opposing nature of these two effects. Surface reflectance increases towards the blue and ultraviolet end of the spectrum, which leads to a decrease in QE. To mitigate the problem, detector designers will often apply anti-reflection coatings to the detector's surface. When a blue (~ 500

nm) or UV ($< 400\text{nm}$) photon does penetrate into the silicon bulk, its penetration depth will be very small because of silicon's increasing absorption coefficient with shorter wavelength. This does not directly cause a drop in QE, but practical issues with detector construction cause the reduced absorption depth of blue and UV light to correlate with lowered response. In front-illuminated CCDs, the gate structures that partially cover the illuminated surface heavily absorb blue and UV photons. In back-illuminated CCDs, electron-hole pairs produced very close to the illuminated surface have a low probability of making it into the pixel's potential well because of recombination and surface traps, decreasing QE. In HCDs, charge carriers must diffuse through the top-side n-doped layer, where they are more likely to recombine, before reaching the depletion region. For this reason, the layer is made as thin as possible. In both cases, detector coatings like our aluminum optical blocking filter and the native oxide that forms on the front surface will significantly attenuate radiation with short penetration depth.

As the incident photon energy increases from the UV into the soft X-ray (100 eV), surface reflection drops to zero and penetration depth again increases, reducing response problems associated with the front surface. When incident photons have sufficient energy to induce ionizations in silicon, the absorption coefficient increases abruptly and detector response improves. Silicon has L-shell binding energies of 100 and 150 eV and a K-shell binding energy of 1,839 eV. In the X-ray, these silicon inner-shell ionizations are the dominant absorption mechanism. For hard X-rays ($\gg 2\text{ keV}$), the photoelectric cross section continues to decrease, causing photons to over-penetration through the detector's depleted bulk and leading to a drop in the detector's response. Increasing the detector's depletion depth is the only way to improve the hard X-ray response, but this improvement comes at the expense of elongating the pixel aspect ratio, increasing the bias voltage required for full depletion, increased dark current due the increased volume of biased silicon per pixel, and increased cosmic ray background on orbit. The thickest PIN diode arrays are currently $\sim 350\ \mu\text{m}$.

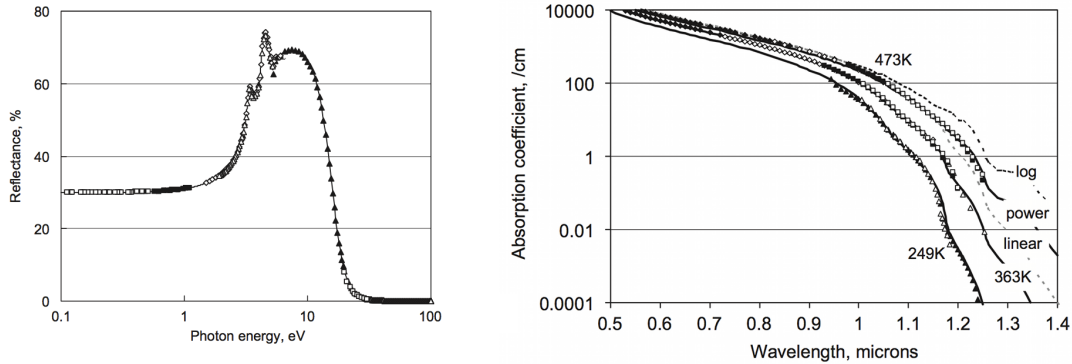


Figure 4.3: The left plot shows the energy dependence of surface reflectance in pure polished silicon at 300 K. High reflection in the UV makes efficient photon detection difficult. The right plot shows the wavelength dependence of the absorption coefficient in silicon at a variety of temperatures. The rise in the coefficient toward smaller wavelengths causes the absorption depth to decrease, leading to difficulties in detecting blue/UV photons. Figures were borrowed from Green [57].

4.2 Various Methodologies

Quantum efficiency is an inherently difficult parameter to measure because, unlike the characterization of read noise, dark current, and energy resolution, which are all calibrated by the known energy of X-ray emission lines, the measurement of QE requires the absolute measurement of the X-ray flux. This can be accomplished using one of two general strategies; either by observing the test detector's response to illumination by a calibrated source of radiation or by using a second detector with a known or calculable response to calibrate the radiation source and compare it to the test detector's response. The first strategy relies upon the precision of the source's luminosity calibration as well as understanding uncertainties in geometry, the contribution of radiation scattered into the detector from off-axis angles, and attenuation of the source beam due to intervening material. In the second strategy, the systematic effects of source calibration uncertainty, scattering, beam attenuation, and illumination can be made negligible, so long as the detectors are located close to one another, relative to the source. Due to these advantages, we have chosen the latter method. In order to provide context and motivate our decision to measure the QE of HCDs in this way, I will first review some of the most popular methods for making the measurement.

4.2.1 NIR and Optical QE

In the near-infrared (5 μm - 700 nm) and optical (700 - 400 nm) wavelength regimes, it is possible to create a calibrated source of radiation using a blackbody oven, narrowband filters with known transmission, and a pinhole. McCulloch *et al.* [58] have used this experiment configuration to measure the QE of a Teledyne HgCdTe HCD. In this experiment, the blackbody source produces a predictable specific intensity spectrum that follows the Planck function

$$B_\nu(T) = \frac{2h\nu^3/c^2}{e^{h\nu/kT} - 1}, \quad (4.1)$$

where B has units of energy time⁻¹ area⁻¹ solid angle⁻¹ frequency⁻¹, where h is Planck's constant, ν is frequency, c is the speed of light, k is Boltzmann's constant, and T is the blackbody temperature. Since the source spectrum varies strongly as a function of the blackbody temperature, it is necessary to measure it with a calibrated sensor and control its value. With the source temperature known and constant, the source will produce a known number of photons per area per solid angle per time. The narrowband filter, which must be cooled to reduce background in the case of infrared measurements, is placed in front of the source to limit transmission to a narrow range of frequencies. This is done so that the QE's wavelength dependence can be measured. Integrating B_ν over the narrowband frequency range yields the number of photons per solid angle per area per time. Finally, a calibrated pinhole is placed in front of the filter for two reasons. First and foremost, it significantly reduces the large photon flux that reaches the highly sensitive astronomical detector. Without the pinhole, most detectors would saturate. Second, it limits detector illumination to a small, on-axis solid angle and a known area of emitting source material. Knowing the distance from the source to detector and the Airy pattern produced by a pinhole camera allows one to calculate the photon flux in the plane of the detector. Also, while an ideal blackbody is a Lambertian emitter [59], no real-world material behaves ideally. Restricting the detector's illumination to a small solid angle of source with the pinhole reduces non-Lambertian off-axis illumination by the source.

The blackbody narrowband filter method is limited to wavelengths at which a calibrated filter is available. To address the problem and extend the measure-

ments to a continuous wavelength range, McCulloch *et al.* use a PbSe diode with NIST-traceable calibration and an incandescent lamp behind a monochromator to calibrate their HCD. Additionally, the PbSe diode was used to verify that the specific intensity of the blackbody oven was within experimental error of the calculated Planck function prediction. The choice of the PbSe diode over a silicon diode was motivated by the need to perform measurements out to the HgCdTe HCD's long wavelength response limit of approximately $5 \mu\text{m}$, a region of the spectrum where no silicon detector has any response. Note that the quoted long wavelength response limit of the HgCdTe array in McCulloch's experiment is not true for all HgCdTe arrays. The band gap can be tuned by changing the material's composition ratios during growth, thus changing the long wavelength response [60].

4.2.2 UV and X-ray QE

In the UV (400 - 25 nm) and X-ray (25nm or 50 eV - 10 keV) regimes, blackbody ovens are no longer practical, laboratory sources. The general strategy for measuring the QE of a test detector remains the same as with the PbSe diode: a calibrating detector of known response is moved in and out of a radiation beam and its response is compared to that of the test detector. It is important to note that in the UV and X-ray, air has a high photoelectric cross section and consequently absorbs a significant fraction of the radiation. The entire experimental apparatus must, therefore, be contained within a chamber evacuated to high vacuum. For UV detector efficiency experiments [61], silicon photodiodes with UV optimized anti-reflection coatings and a NIST-traceable calibration serve as the detector of known response. A differentially-pumped hollow-cathode UV light source, which produces both line and continuum emission, optically coupled to a monochromator is often used to produce the necessary radiation. [62]

In the soft X-ray, the problem becomes somewhat more tractable due to the availability of sources and detectors. Calibrated silicon photodiodes make excellent X-ray calibration detectors because they are compact, low cost, low noise, have adequate response through the soft X-ray regime, and do not require high voltage. See Figure 4.4 for examples. When exposed to optical or UV photons, a reverse biased photodiode produces a voltage across its output that is proportional

to the flux incident on its active region. This mode of operation is typically called photodiode mode. For photon energies in the soft X-ray and greater, if the diode's output node capacitance is made small enough, which in turn makes the conversion gain large enough, the charge generated by each absorbed X-ray produces a voltage large enough to be detected by external electronics as a distinct pulse. The counting and subsequent pulse height analysis of these voltage peaks is called photon counting. The advantages of working in photon counting mode, assuming negligible pileup, are that flux measurement uncertainties are limited purely by photon statistics and the uncertainty in the detector's previously calibrated QE. There is no electronic contribution to the uncertainty in the rate and no hidden systematic offset of the rate via mechanisms such as capacitive cross-talk or resistive wire losses. A downside of Si photodiodes is that their absolute response is not readily calculable, and in order to serve as calibrating detectors themselves, they must first be calibrated.

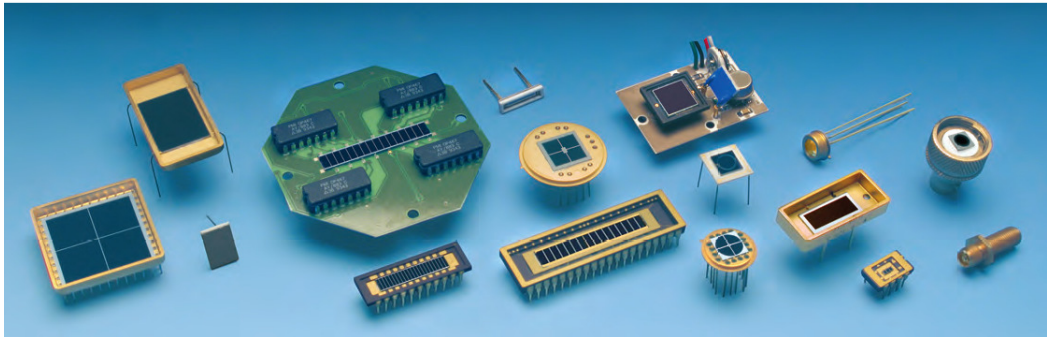


Figure 4.4: A variety of silicon photodiodes currently available from International Radiation Detectors. These detectors have been successfully used in absolute calibration experiments [63, 64].

Gas proportional counters are a second type of detector suitable for X-ray QE measurement. They have been in use as X-ray detectors since their invention in the mid-20th century [65]. While the proportional counter's sensitivity does not extend into the optical as with the Si photodiode, it is, regardless, a workhorse detector with many advantages. Proportional counters have linear response in their proportional regime, are robust to extremely high count rates, and do not exhibit or accumulate radiation damage like solid state detectors. Most importantly for a quantum efficiency investigation, proportional counters have an efficiency that can

be reliably calculated. The efficiency depends only on the number of gas particle absorbers in the counter's active volume and the window transmission, which are both measurable quantities. For these reasons and also because of the heritage of hardware already existing in our lab, we chose to perform QE measurements with a proportional counter.

There is a large variety of soft X-ray sources suitable for measuring the QE of a detector, ranging from simple pieces of radioactive material to highly complex \$100 million facilities. Monochromatic soft X-rays are, in general, produced in the laboratory by creating atomic K, L, or M-shell vacancies in a source material so that higher level electrons will fill the vacancies and emit X-ray photons. Ionizing these inner shell electrons is one way to create a vacancy and initiate a transition. The ionization can be produced in a target material by bombarding it with electrons or alpha particles or by irradiating it with higher energy X-rays. The vacancy can also be spontaneously produced in certain materials by the radioactive decay of the atom's nucleus. Continuum emission is commonly produced via bremsstrahlung radiation by colliding electrically accelerated electrons with some target anode in an X-ray tube. There are a number of tube sources commercially available that can generate both line and continuum emission. Those and the line emission sources directly relevant to our work will be discussed in greater detail in §4.3.3.

Outside of academic laboratories, special X-ray light source facilities exist at nationally funded labs to provide controlled X-ray radiation to a large variety of research fields including materials research, biological protein analysis, and, occasionally, astrophysics. An illustrative cutaway diagram of such a facility is shown in Figure 4.5. The synchrotron beams at the Advanced Light Source (ALS) at the Lawrence Berkeley National Lab (LBNL) [66], the Synchrotron Radiation Source (SRS) in Daresbury, UK [67], BESSY I at PTB Helmholtz-Zentrum Berlin [68], and Soleil at Orsay [69], enable astronomical X-ray instruments to undergo end to end absolute calibration. These facilities typically have test chambers large enough to fit an entire instrument, collimated beams, and tunable beam intensities that can be varied over many orders of magnitude. They employ double Bragg crystal monochromators to produce very pure photon energy distributions when narrowband flux is required. While not a synchrotron, the PANTER X-ray tube beamline at Max Planck München has played a role in calibrating nearly every

X-ray astronomical satellite from ROSAT [70] to Astro E2 [71] and *Swift* [72].

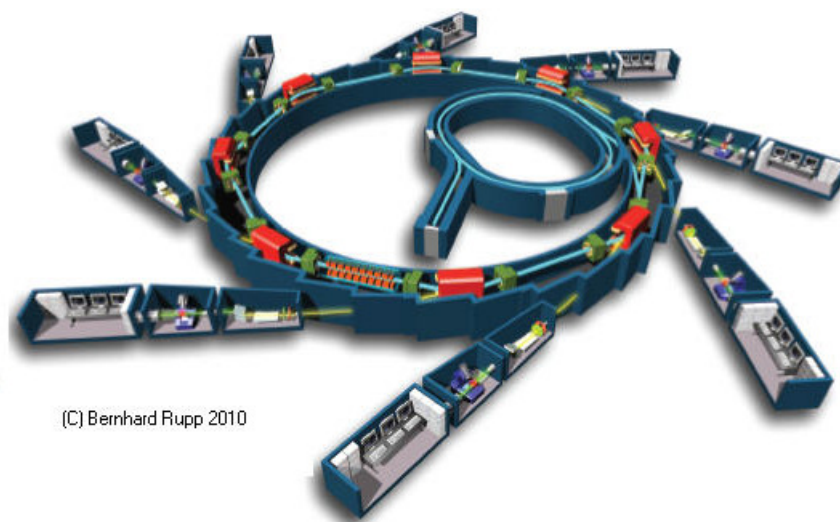


Figure 4.5: A diagram showing the basic layout of a synchrotron X-ray light source facility. The central circular structure is the electron storage ring, a continuous vacuum space where electrons moving at relativistic speeds are kept in pseudo-circular orbit via the bending action of magnets placed around the ring. Tangent to each magnet, evacuated tubes allow beamed synchrotron radiation to propagate into one of multiple laboratories situated along the ring's periphery. Figure is from *Biomolecular Crystallography: Principles, Practice, and Application to Structural Biology* [73].

Concerning laboratory QE measurement methods, Kenter *et al.* [74] have used a proportional counter and an X-ray tube mounted in a split chamber, shown in Figure 4.6, to measure the QE of early-stage HCD prototypes. Their measurement technique relies upon the assumption that both detectors, which are illuminated by the X-ray tube's anode from different viewing angles, through different chamber pipes, and through different continuum filters, receive identical illumination. In our QE analysis we do not need to make these assumptions, thanks to the availability of a vacuum chamber large enough to mount both the test and calibration detectors side by side at the end of a long path length. In the following section I will describe the design and construction of the PSU system in detail.

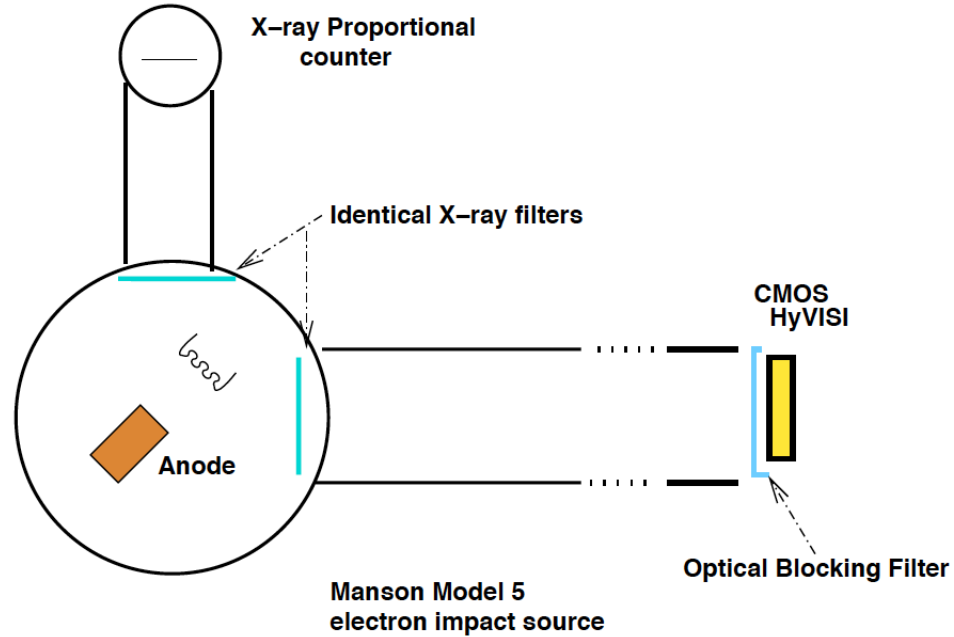


Figure 4.6: The experimental apparatus used by Kenter *et al.* to measure the QE of an early HyVISITM HCD. The X-rays are created by a Manson Model 5 source at the lower left of the diagram, after which they propagate down both tubes of the chamber and illuminate the test and calibration detectors simultaneously. Figure is from the original paper [74].

4.3 Experimental Design

As indicated previously, there is more than one way to measure the X-ray QE of a detector. We chose to make the measurement by placing the test detector, a Teledyne H1RG HCD, and the calibration detector, a heritage, custom-built, gas flow proportional counter, side by side so that they could both measure the flux of the same source, simultaneously. The illuminated-side surface normals of both detectors were aligned with the X-ray source and the source was placed as far away from the detectors as the chamber allowed. In this arrangement, shown in Figure 4.7, small errors in detector alignment translate into negligibly small differences between the illumination of each detector. With a distance, d , between the detectors and the source, the approximate fractional contribution of the distance error, δd , to the flux normalization is $\delta d/d$. Assuming a positioning

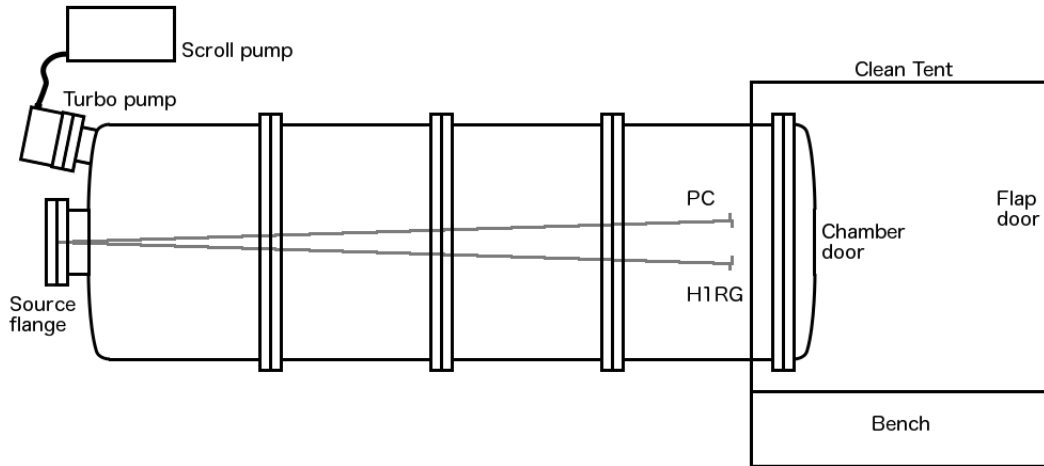


Figure 4.7: Overhead drawing of the QE test-stand in the PSU vacuum chamber. The proportional counter (PC) and HIRG are aligned so that their center normals are pointed at the source, which is mounted in the source flange. The clean tent keeps the bench and area around the door free of airborne particle contamination. For reference, the source-detector distance is 256 cm in the final experimental apparatus.

error of $\delta d = 0.1$ cm (See §4.4.6 for more details on error analysis) and a tolerable fractional error of 10^{-3} , this requires that $d > 100$ cm. Beginning with these basic design premises in the following sections, I will motivate and explain the choices that led to the final, working design.

4.3.1 Vacuum System

The entire experimental apparatus needed to be contained inside of a vacuum chamber. A vacuum chamber is any sealed, enclosed space built with rigidity sufficient to resist the 14.69 psi compressive force of the Earth’s atmosphere and equipped with the necessary hardware to evacuate gas from inside the chamber. It is not possible to create a perfect vacuum. Fortunately, even the most sensitive laboratory experiments do not require a perfect vacuum and some require only a very small degree of vacuum. Table 4.1 lists standard terms that have been coined to identify ranges in pressure below one atmosphere.

Our entire experiment apparatus needed to be contained within a vacuum chamber for two reasons. First, as seen in Figure 4.8 an air path length of $d > 100$

Vacuum regime	Pressure [mbar]	Experimental examples
Coarse Vacuum	1000 - 1	Exploding marshmallows, radiometers
Rough Vacuum	1 - 10^{-3}	First cathode ray experiments
High Vacuum	10^{-4} - 10^{-8}	Sputtering, CVD, cryogenics
Ultra High Vacuum	10^{-9} - 10^{-12}	MBE, semiconductor, accelerators

Table 4.1: A definition of vacuum regimes. An important note; as pressure decreases, flow switches from the continuum to the molecular regime. In continuum (or viscous) flow, the mean free path of gas particles is small compared to the size of the chamber, and these interactions dominate the behavior of the flow. In the molecular regime, the mean free path of gas particles is large compared to the size of the chamber. A significant consequence of this transition is that a given chamber geometry’s resistance to flow *increases* with decreasing pressure.

cm, the required source-detector separation, heavily absorbs soft X-rays. Evacuating the chamber to 10^{-5} mbar results in $< 0.01\%$ absorption in all regions of the bandpass, which is small enough to be ignored. A quick aside: An alternative solution to the problem of X-ray absorption by the air is to fill a simpler chamber with helium instead of spending money on building a rigid, sealed chamber and evacuating it. As Figure 4.8 shows, such a setup would have good transmission above 1 keV. However, this strategy would fail in our experiment, primarily because of our second reason for using a vacuum chamber; the H1RG detector needs to be cold. Helium would not condense or freeze on a detector at our 150 K test temperature, but convective heat transfer from 1000 mbar of helium would make keeping the detector at 150 K a problem. Also, a significant amount of helium would need to flow through the chamber in order to prevent the buildup of contamination and the temperature gradient would make calculation of the intervening helium column density prone to systematic errors.

Concentrating again on vacuum design, water vapor is the enemy of good performance at high and ultra high vacuum. When a chamber is at atmosphere, it readily sticks to all surfaces inside the chamber and diffuses into the metal walls through grain boundary pores and into the bulk of any hygroscopic material in the chamber. At vacuum, water’s high surface area coverage and low vapor pressure mean that it presents a long lasting gas load that begins to dominate pumping in the high vacuum regime. In our apparatus, the formation of water ice on the cold detector drives the vacuum requirement more than the X-ray transmission.

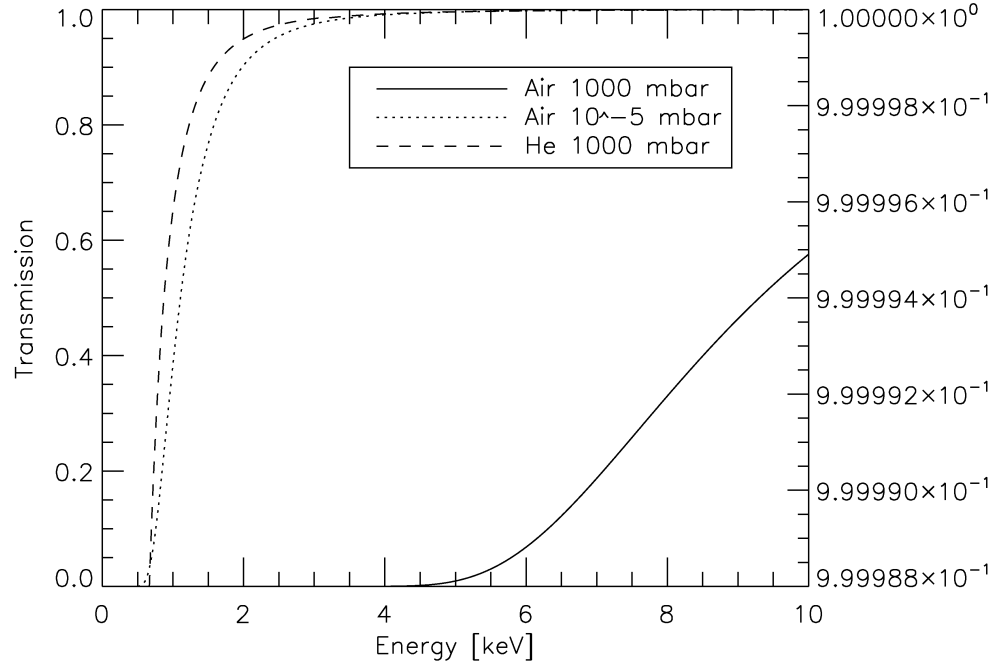


Figure 4.8: Assuming a path length of 100 cm, shown are the 0.5 - 10 keV transmission curves for 300 K air at atmospheric pressure (solid line, left vertical axis), 300 K air at high vacuum (dotted line, plotted with right vertical axis), and 300 K helium at atmospheric pressure (dashed line, left vertical axis). Air at atmospheric pressure has poor soft X-ray transmission, while air at vacuum transmits very well. Helium has $> 50\%$ transmission above 1 keV, making it a reasonable choice for some work. The composition of air is 78.08% N_2 , 20.94% O_2 , and 0.93% Ar. These values were calculated from partial pressures given in *The Art of Cryogenics* [75]. This is a conservative estimate since high vacuum pumps preferentially remove heavy elements and would therefore alter the gas composition in favor of greater soft X-ray transmission. The IDL procedure `gas_trans.pro` (see Appendix C) and Henke's cross sections [76] were used to generate the transmission curves.

Figure 4.9 shows the sublimation curve for water extrapolated to 100 K. For a given detector temperature, this line represents the water vapor partial pressure at which ice will begin to form on the cold surface. Extrapolating the sublimation curve p_{subl} down to 150 K, the partial pressure of water in the chamber needs to be below 10^{-7} mbar in order to prevent icing. Given the high partial pressure of water at high vacuum, in an ideal case, the total pressure should be nearly the same.

In the field of vacuum research, attempts to reduce water adsorption with surface passivation (Au or TiN coating) or cleaning procedures have not been successful [77]. The only reliable method for improving chamber wall water vapor desorption is by heating (baking) the entire chamber; the warmer the better. Unfortunately, we are not prepared to bake a vacuum chamber at this time. Next, I will discuss guidelines for designing a chamber that can produce the required pressure.

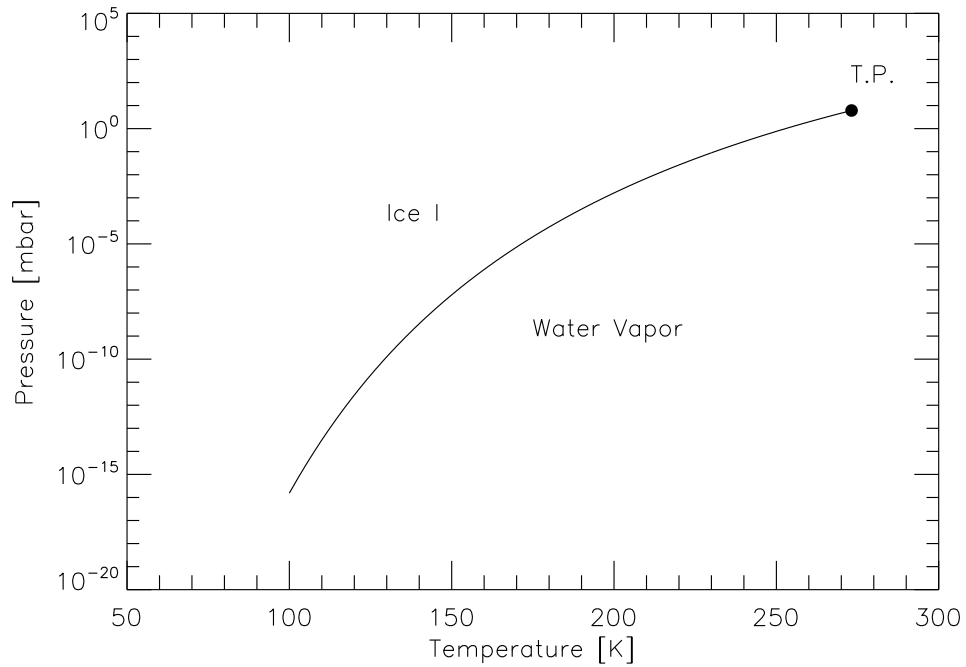


Figure 4.9: Sublimation curve on the phase diagram of water. The locus of points was plotted using the phenomenological fit $\ln[p_{subl}/p_t] = a_1(1-\theta^{-1.5}) + a_2(1-\theta^{-1.25})$ where $\theta = T/T_t$, $T_t = 273.16$ K, $p_t = 611.657$, $a_1 = -13.9281690$, $a_2 = 34.7078238$ and has been shown to match experimental data to within 0.001 mbar over the temperature range $190 \text{ K} \leq T \leq 273.16 \text{ K}$ [78]. TP is the triple point.

The PSU X-ray group owns a cylindrical chamber that is 76.2 cm inner diameter and 282.2 cm long that will hereafter be referred to as the caterpillar (see Figure 4.7 for a sketch and Appendix A.1 for mechanical drawings). The caterpillar's length satisfied the source-detector distance requirement and its inner diameter allowed for enough space to mount both detectors, making it an excellent choice for the QE measurement apparatus. In reality, the caterpillar's vacuum system was refurbished, but not designed from the ground up for this project. The assembly

was completed by working with pump components that were available in the lab at the time. For the sake of completeness, I will show a more formal justification of the pump system's specifications.

The first step of the vacuum design process is to estimate the size of the pump system that will be able to evacuate the chamber to the required pressure in a specified amount of time. Following the notation of O'Hanlon [79], the basic equation of vacuum system design is

$$P_{ult} = \frac{Q}{S_c}, \quad (4.2)$$

where S_c [liters second⁻¹] is the effective pumping rate at the mouth of the chamber's pump flange, Q [millibar liter second⁻¹] is the total gas load entering the chamber space, either from leaks or outgassing, and P_{ult} [millibar] is the ultimate pressure achieved in the chamber. All materials release gasses from their surface and/or interiors, into the surrounding environment. If you have ever smelled rubber from a new tire or detected any smell for that matter, then you are already familiar with the fact that materials expel volatile compounds. This is called outgassing and some materials do it significantly more than others. The above equation describes the vacuum equilibrium where the rate of gas entering the chamber due to outgassing (gas load) divided by the volumetric rate of gas removal results in the ultimate chamber pressure. Since this pumping speed is characterized by volume of gas removed per time and the speed does not vary with pressure over the pump's usable range, the rate of removing gas particles from the chamber is proportional to the number density of particles and therefore proportional to the pressure. This leads to the pressure as a function of time taking the exponential form,

$$P(t) = (P_{init} - P_{ult})e^{-\frac{S_c t}{V}} + P_{ult} \quad (4.3)$$

where P_{init} is the initial chamber pressure, typically atmosphere, P_{ult} is the ultimate chamber pressure, where pumping and outgassing are in equilibrium, S_c is the pumping speed at the chamber's pump flange (*not* the same as the pump's rated speed), t is time, and V is the volume of the chamber. To aid in system design, commercial vacuum pumps are rated by their volumetric pumping rate, in L sec⁻¹.

However, the pump's rated speed, S_p is calculated by running the pump with inlet capped, severely over-estimating the pumping speed in a real chamber. The pump speed and the chamber speed are related by

$$\frac{1}{S_p} = \frac{1}{C} + \frac{1}{S_c} \quad (4.4)$$

where C [liters second⁻¹] is the conductance of the connection between the chamber and the pump. Long thin tubes present resistance to the flow of gas and have a low conductance. However, even if the pump is connected directly to the chamber, there will still be some resistance to the flow due to the inlet's finite area. In reality, the conductance of a conduit drops with pressure, leveling off as the system enters into the molecular flow regime. To simplify vacuum calculations and make a more conservative estimate, the molecular flow conductance will always be assumed. Combining Equations 4.3 and 4.4 and solving for S_p ,

$$S_p = \left[\left[-\frac{V}{t} \ln \left(\frac{P_c - P_{ult}}{P_{init} - P_{ult}} \right) \right]^{-1} + \frac{1}{C} \right]^{-1} \quad (4.5)$$

To calculate pump size, the quantities in the above equation were estimated: chamber volume, $V = 1.2 \cdot 10^6$ cm³, pump down time $t \equiv 86.4$ ks (1 day), initial pressure $P_{init} = 1000$ mbar, and final chamber pressure, $P_c = 10^{-6}$ mbar. The ultimate pressure, Equation 4.2, is a function of outgassing and the chamber pumping speed, so the solution must be solved iteratively. The surface outgassing rates, in mbar liter sec⁻¹ cm⁻², of common materials are known and tabulated in vacuum handbooks. However, in the high vacuum regime, pumping is dominated by water desorption from the chamber's surface and not the actual outgassing of the chamber. Given the chamber surface area of $\sim 7.6 \cdot 10^4$ cm² and taking the water desorption outgassing rate from Table 4.2, the chamber surface will produce $3 \cdot 10^{-2}$ mbar L sec⁻¹ of gas load.

Using the quasi-Newton iterative non-linear solver built into IDL, the required pump speed estimate is 790 L sec⁻¹. The code can be found in `pumpspeed.pro` in Appendix C. Since a 500 L sec⁻¹ pump was available, we worked with what we had and the system's performance was satisfactory. Given that at 50% relative humidity the partial pressure fraction of water in air is $\approx 5\%$, and that the fraction

of water in the vacuum environment will increase due to differential pumping speed, and finally that our measured ultimate pressure is $9 \cdot 10^{-6}$ mbar, we are probably causing some minor icing on the detector. In an apparatus similar to ours, Jacquot *et al.* attributed an unexpected drop in UV QE as a function of time to icing of the detector's front surface [80]. Since soft X-rays are far more penetrating than UV photons, our application was not sensitive to this minor icing and we deemed the effect negligible.

Material	Outgassing 10^{-10} [mbar centimeter ⁻² liters sec ⁻¹]
Aluminum (fresh)	84.0
Aluminum (anodized)	3,679.0
Brass	5,332.0
Copper (fresh)	533.0
Copper OHFC (fresh)	251.0
Steel (nickel-plated)	368.0
Stainless steel	192.0
Zinc	2,946.0
PTFE	4,000
Silicone	93,000
Viton A (unbaked)	15,200
Viton A (12 h 200°C)	2.7
Water desorption	4,000

Table 4.2: Outgassing rates for common vacuum materials. Metals are listed above the partition and elastomers/polymers are listed below it. Values have been converted using the factor $\text{mbar centimeter}^{-2} \text{ liters sec}^{-1} = 10^{-3} \cdot \text{Pascals meters sec}^{-1}$. In-situ baking can reduce these values by up to 4 orders of magnitude. All values except water were taken from O'Hanlon's text [79]. The value for water was taken from Li & Dylla [81] and is an estimate of the desorption of water from an unbaked stainless steel surface at the beginning of a pump cycle after the chamber was exposed to ambient air.

With the pump size established, the next order of business is to pick a type of pump. Throughout the history of vacuum technology, many different types of pumps have been invented to solve the problem of removing gas particles from a sealed chamber volume. In the most general sense, vacuum pumps fall into two categories: gas transfer and gas capture. Gas capture pumps use special surfaces to immobilize gas particles. Examples include cryogenic sorption, cryogenic, and ion

pumps. Advantages of gas capture pumps are that they are dry, meaning that they use no oil, and retain their pumping speed at ultra high vacuum. Disadvantages are that they need to be periodically regenerated and they require moderate to high backing vacuum. Gas transfer pumps force gas particles in a preferred direction via a mechanical action, either positive displacement or momentum transfer. Positive displacement pumps seal a volume of gas from the chamber, reduce its size, and vent the compressed volume to atmosphere. Examples include diaphragm, rotary vane, piston, scroll, and roots pumps. The pumping speeds of these pumps all drop off severely in the rough vacuum regime, so their use is limited to rough vacuum applications and being placed in series with high vacuum pumps that require low backing pressure. Momentum transfer pumps impart a preferential momentum on gas particles to redirect them out of the chamber. Examples include diffusion and turbomolecular pumps (TMPs).

In the range of 500 L sec^{-1} pumps, TMPs can maintain pumping speed into the high vacuum and are dry and safe. The risk of damaging the contents of a vacuum chamber is an issue with diffusion pumps, because they will spray oil into the chamber in the event of power loss, the development of a vacuum leak, or a mechanical pump failure causing the backing pressure to rise. A 500 L sec^{-1} TMP was our high vacuum pump of choice. TMPs require a backing pressure of $< 10^{-1}$ mbar, so we place a dry and reliable scroll pump in series, behind the TMP. The caterpillar system routinely achieves vacuum in the low 10^{-6} mbar range when empty and in the high 10^{-6} mbar range when filled with equipment, after ~ 72 hours of pumping.

Cleanliness and electrostatic discharge (ESD) safety are two important factors that must be considered when working with delicate detectors and test hardware. Environmental contamination in the form of airborne dust, machining oils, or pieces of human (skin dander, hair, skin oils, and even bits of saliva) can degrade the vacuum with their outgassing, cause sensitive components to malfunction, and/or give rise to systematic error via unintended X-ray absorption. A clean tent that surrounds the caterpillar's main access door, shown in Figure 4.7, was built so that components could be cleaned and assembled and detectors could be removed from their protective packaging in a clean environment before installation. The air is filtered with a HEPA filter. Tests with a laser air particle counter showed no

detectable $> 5 \mu\text{m}$ particle contamination on the workbench and < 500 particles foot^{-3} in the main area. All of the silicon based detectors that we test contain very thin gate structures with breakdown voltages in the realm of tens of volts. The simple action of shuffling one's feet on the floor can generate tens of thousands of volts potential difference between the body and a work surface, creating the potential for catastrophic ESD detector damage. To combat the problem, the tent is constructed with ESD PVC plastic, the tent's work surface is covered with an ESD dissipative mat, and the tent's workstation is outfitted with ESD ground monitors and straps that are worn on the user's wrist.

4.3.2 Cryogenics and Temperature Control

All of the H1RG measurements that our lab is likely to make in the near future will be made with the detector in the 150-220 K temperature range. The lower end of the range is defined approximately as a temperature at which detector performance does not continue to improve with further cooling. The upper end of the range is determined by the noise characteristics of these devices, which make meaningful soft X-ray measurements difficult above 220 K. A search for a commercially manufactured solution for cooling and controlling the detector in this temperature range was carried out, but due to the significant cost of adapting those systems to our chamber, we chose to custom design and build a temperature controlled cryostat to accomplish the design requirement. The general strategy of our cryostat design is to cool the detector by physically affixing it to a cold object (cold sink) with a flexible device of known conductance (cold strap), and then use a closed loop controller consisting of a temperature sensor, a variable power heater, and a digital control algorithm to maintain the detector's temperature at a desired setpoint. In traditional cryostat design, a dewar filled with cryogenic liquid, either nitrogen (77 K) or helium (4.2 K) depending on the required temperature, is the cold sink. Using a dewar has low up-front cost, no maintenance cost, and moderate consumable cost (cryogen). Cold head refrigerators (CryoTiger[®] is a commonly used model), and more recently Stirling coolers, are a popular cooling option because their closed-cycle designs do not require dewar filling to run continuously and they recoup their high initial cost after a few years of operation [82]. Multi-stage Peltier

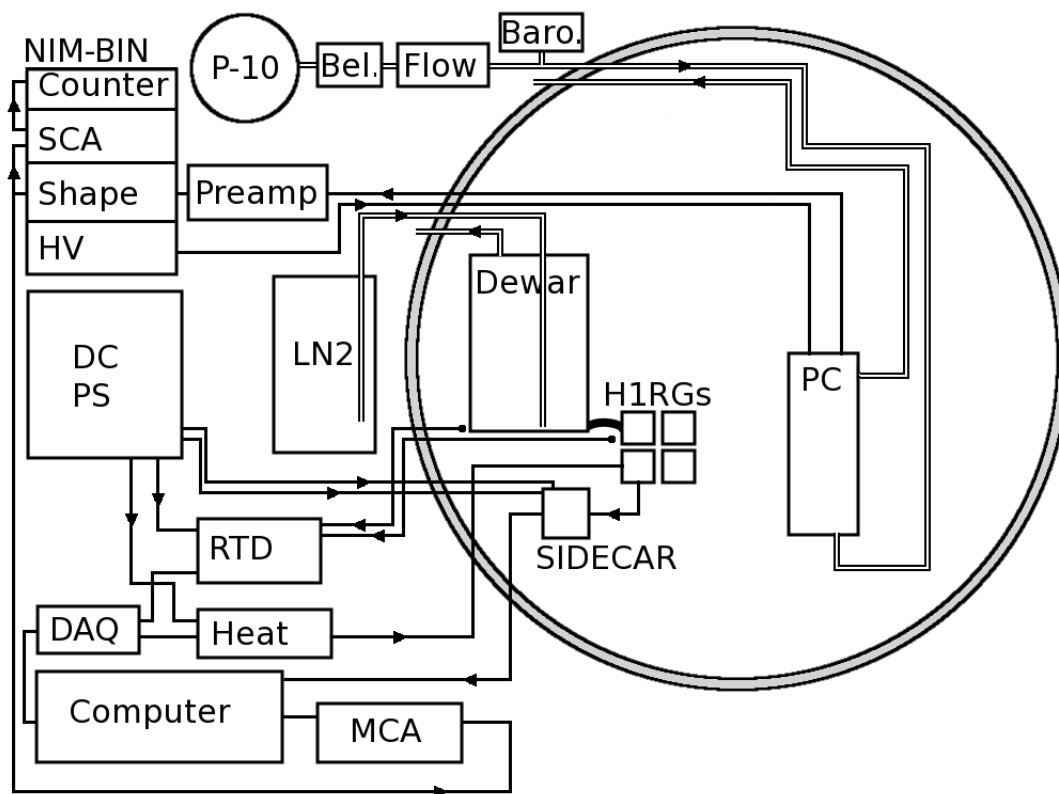


Figure 4.10: (Continued on the following page.)

coolers are a very low-cost, low-maintenance cooling option if a process requires moderately low temperatures (~ 220 K) with low heat load (< 5 watts)[83]. For our QE measurement, I chose to build a liquid nitrogen (LN_2) dewar due to the low up-front cost, high heat load handling capability, and the cryogen's ability to cool significantly below our desired setpoint. The basic system design is shown in Figure 4.10.

The most common options for fabricating an LN_2 dewar are welded stainless steel, welded aluminum, and silver soldered copper. Tungsten inert gas (TIG) welded stainless steel has excellent tensile and joint strength, and is easy to weld. However steel is heavy and has low thermal conductivity. When fastening stainless steel bolts to threaded stainless steel, either different alloys must be chosen or vacuum grade anti-seize compound must be applied to the fasteners to prevent thread galling/seizing. TIG welded aluminum is a lightweight dewar design option that also has good thermal conductivity, but the welds are prone to warping and

Figure 4.10: Routing layout of the QE test-stand. The large gray circle at right represents the caterpillar vacuum chamber. Inside the chamber the QE test apparatus components are shown in their approximate orientations. Note that the proportional counter (PC) and H1RGs are positioned below the chamber centerline because the X-ray source pipe is offset below the centerline. The hollow lines represent tubes: 1/8 inch copper tube with Ultra-torr fittings for the PC fill/vent and 1/4 inch hydroformed corrugated stainless steel tube with VCR fittings for the liquid nitrogen (LN2) dewar. The barometer (Baro.) is shown in the position where it was used to measure the proportional counter gas (P-10) line pressure. The pressure of gas was regulated first by a standard Harris cylinder regulator, then by a 0-5 psi Belofram regulator (Bel.). The flow was measured and regulated with a flowmeter (Flow). The proportional counter's two electrical connections are an HV and BNC signal cable. The signal line passes out of the chamber, through a preamplifier (Preamp) and into a shaping amplifier (Shape) before being split between a single channel analyzer (SCA) and counter combination and a multi-channel analyzer (MCA) that outputs to a computer. The computer runs a Labview data acquisition (DAQ) device that controls both the heater and RTD temperature sensor power supplies. The heater and RTD power supplies are powered by external DC power supplies (DC PS). The H1RGs are programmed, clocked, and read out by the SIDECARTM, which has two DC power inputs coming from the DC PS and one USB output that connects directly to the computer. The cold strap can be seen connecting the dewar to the H1RGs. In the lab, the various electrical and fluid lines are fed into the caterpillar through a single large feedthrough plate, but are shown scattered in this diagram, for the sake of clarity. Arrows indicate the direction of gas, fluid, data, or power flow.

also tend to develop porosity. Warpage is more common in aluminum because its high conductivity requires the use of more heat to maintain adequate weld pool temperature. Also, unless the joint is carefully preheated, small bubbles can develop in the weld and eventually lead to vacuum leaks. Silver soldered copper has high conductivity, but is an expensive material that is difficult to solder well. Additionally, the material and its joints have the lowest strength among the available choices. Both aluminum and copper require thread inserts to avoid tearing out threads in the high torque fastener connections that are necessary to make good thermal contact between components. We concluded that welded stainless steel was the best choice for the dewar because of its previously listed advantages and also because it was straightforward to attach cryogenic vacuum tube fittings. The material's weight issue was addressed by avoiding the use of thick

stock material and the poor thermal conductivity was improved by minimizing the distance between the cryogen and the cold strap attachment point.

As seen in Figure 4.10 the dewar was placed inside the chamber and required a detachable tube fitting to run the LN₂ fill and vent lines from the cryogenic-liquid vacuum-feedthrough into the dewar. SwagelokTM brand compression fittings are ubiquitous in the laboratory because the connections are cheap and easy to make. After trial and error in the lab, I found that it is possible to make a vacuum tight connection with these fittings, but it is difficult to get a consistent seal when reattaching the same fitting more than once. This alone makes the fittings unsuitable for the QE apparatus, but in addition they are also not rated to work below 230 K. Industry research led me to SwagelokTM VCR fittings and Conflat (CF) vacuum flanges. Both fittings are rated for cryogenic temperatures and ultra high vacuum, but the VCR metal gasket fittings were eventually chosen due to their compact form factor. Stainless steel gaskets were chosen over copper and nickel because the stainless gasket's coefficient of thermal expansion match with the fitting body insured that the fitting's vacuum seal would maintain integrity over the course of many thermal cycles.

A good cryostat design should be efficient, meaning that heat input from any source other than the test detector should be minimized. In that vein, the dewar design seeks to maximize the thermal resistance between the dewar's cryoliquid contents and the warm 300 K environment. The primary design goal for our dewar was for it to have a hold time of 12 hours, which is long enough to enable continuous, 24 hour operation of the QE apparatus. Since there is no significant convective heat transfer inside the vacuum chamber, radiation and conductive heat transfer dominate the thermal dynamics. The only source of conductive transfer will be through the dewar's mechanical supports. Materials with high tensile strength per thermal conductivity are the most appropriate choice. Making the support longer, with a smaller cross section, and from a lower thermal conductance material will all improve overall performance. G10 is a composite material created by laminating layers of woven glass with epoxy. The material has high tensile strength, low thermal conductivity, and is low outgassing and non-hygroscopic. Complex, cut-away strut designs can dramatically reduce the conductivity of an element while retaining stiffness. Strut design can be further improved with pre-

tensioning. Pre-tensioned struts can be designed to have the same stiffness as a non-tensioned strut, except with the use of less material. In the end, I opted for simple, solid rectangle struts made from 3/32 inch sheets of G10 because they can be fabricated very easily (and cheaply) with a shear and a drill. Complicated machining of G10 is unusually costly for two reasons: its glass filler quickly dulls cutters and machining of the glass filler produces a dust with health hazards similar to asbestos. In the laboratory setting, the mass-performance ratio is not as critical as it would be in an aerospace application. Therefore, complex strut design was not worth the added cost. Properly designed mechanical supports contribute a negligible efficiency loss to the cryostat.

On the other hand, radiative heat transfer from the warm vacuum chamber walls to the cold dewar is a significant problem that is worth spending effort to mitigate. The percent of radiation absorbed by a material is proportional to its surface emissivity, ϵ . Emissivity is the fraction of energy that an object radiates compared to an ideal blackbody at the same temperature. High emissivity surfaces are flat black and both very good absorbers and good radiators. Low emissivity surfaces tend to be mirror-like and are both good reflectors and good radiative insulators. Flat black coffee cups may be stylish, but they are a bad idea if you want to minimize the radiative cooling of your delicious hot beverage. If the surface of a dewar is polished, it will reflect a larger percent of incident radiation and heat up slower. If we were to put a second reflective surface between the warm chamber and the cold dewar, radiative conductivity into the dewar would be further reduced by a factor of $\sim \epsilon$ so long as the surfaces do not touch and thermally short to one another. The continuation of this concept leads to the idea of a thermal blanket or multi-layer insulation (MLI). Multiple layers of thin (~ 0.001 inch) plastics that have been vacuum deposited with metal (aluminum or gold) are interleaved with thermally insulating mesh, also made from either woven glass fiber or plastic. For our MLI, I made a 6 layer stack of alternating metallized Mylar[®] and 1.5 mm pitch PTFE (Polytetrafluoroethylene) mesh that was sourced from a medical supply company. Note that PTFE is often casually referred to as Teflon[®], but this is not entirely accurate since Teflon[®] is a registered trademark of the DuPont[™] company. Officially, only DuPont[™] fluoropolymers can be referred to as Teflon[®]. The stack was sewn together by hand along the perimeter with

PTFE thread. Gold coated Mylar[®] is preferred over aluminum coated Mylar[®] because its emissivity is lower in the infrared, where most of the radiation from our 300 K chamber is being emitted. The 4 piece MLI is visible in Figure 4.11. In the end, the dewar was capable of a 15 hour hold time while subject to a standard operational thermal load.

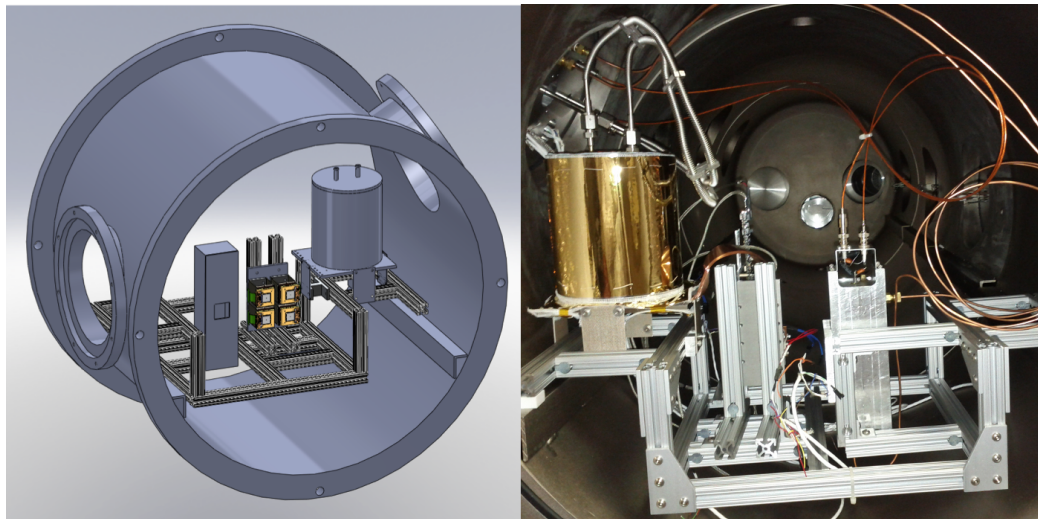


Figure 4.11: A mechanical drawing of the test-stand and a photo of the final assembly. Note that in the photo, the camera is behind the test-stand and in the render, the camera is viewing it from the front. The gold cylinder at left in the photo is the cryostat, the armature to its right is the HIRG mounting platform, and the gray box to its right is the back of the proportional counter.

Moving on to the cold strap design, in general, it is best to choose the thermal conductance of the cold strap such that the detector will be in equilibrium slightly below the desired setpoint. If the heater is only required to provide a few watts of heat, the control algorithm will perform better and less power will be wasted. It is also important to note that attaching the detector to the cold sink with a cold strap instead of direct attachment introduces an important failsafe into the system. HCDs and silicon detectors in general are complicated devices composed of many layers of different materials. Teledyne has gone through great expense to match the coefficient of thermal expansion between adjacent layers such that differential contraction during cooling does not exceed layer bond shear strength and result in delamination. Even with the careful choice of material thermal expansion coefficients in the detector, we have been advised to cool the detectors at

$< 2 \text{ K min}^{-1}$. If the detectors are directly attached to the cold sink, the heater is the only mechanism that regulates their cooling rate. If the heater were to fail, as things in a laboratory often do, the cooling rate would exceed its maximum and the detector could be damaged.

Estimating the detector's equilibrium temperature for a particular strap configuration was best accomplished with experimentation. To reach a desired equilibrium temperature, we started with a thin strap and added more straps as needed. Theoretical estimation of the equilibrium temperature is a complicated calculation which relies heavily on two parameters that are difficult to estimate: contact resistances and surface emissivities. While the conductive heat transfer through a solid is easily calculable, the thermal contact resistances between the many components in the apparatus vary strongly with surface roughness as well as the compressive force fastening the surfaces together. Radiative heat transfer is also calculable in principle, but the precision of that calculation depends strongly on good estimates of the emissivity of both the absorbing and emitting surfaces. Surface oxidation and RMS roughness both have a drastic effect on emissivity, making the calculation of radiative heat transfer worthwhile in only the most demanding applications.

The cold strap itself is constructed from 12 inch lengths of 0.005 inch thick, 1 inch wide oxygen free copper foil. I chose to make the strap instead of buying a prefabricated foil stack or braid because we wanted the flexibility to optimize the strap's conductivity for different temperature regimes. Oxygen free copper was chosen due to its superior vacuum outgassing rate. Aluminum and graphite are also popular cold strap materials. While it was cheaper, aluminum's lower conductivity and higher tensile strength would make the strap thicker and less flexible. The graphite was prohibitively expensive. Graphite straps are used primarily in aerospace applications where it is important to maximize a strap's conductivity mass⁻¹ ratio. Choosing the 0.005 inch copper foil thickness involved balancing strap flexibility with build practicality. Given two straps with the same total thickness, the one made from thinner foil will be more flexible. However, the foils cannot be made too thin because of the difficulty of sourcing exceedingly thin material and the added complexity of aligning and assembling a strap made from many thin foils.

Various methods for assembling the ends of the strap were tested, including sol-

dering, diffusion welding, and clamping with cap screws. In the solder method test, we fluxed and soldered a stack of 10 foils using 90% Pb 10% Sn cryogenic solder. The solder method was abandoned because the solder wicked too far up the stack, the resulting soldered ends were not flat enough to make good thermal contact, the foils partially delaminated when I drilled mounting holes, and destructive testing showed voids in the solder's penetration through the stack, despite adequate fluxing. In brazen defiance of my advisor's better judgement, I experimented with diffusion welding the cold strap foils. In this test, I polished a stack of 10 foils with rock wool and removed dirt and oil from the surfaces with an acetone bath. The stack was assembled immediately after cleaning, with smaller stainless steel foils interleaved between copper, leaving the ends of the copper foils in contact. The ends of the stack were clamped between two mild steel torque plates which were then bolted together and placed with powdered charcoal into a foil bag made from soft temper 309, 0.001 inch thick stainless steel. The bag was crimp-sealed and placed in a 1900°F furnace (approximately the recommended 50°F below copper's melting point of 1980°F) for 3 hours and allowed to cool inside the furnace. The diffusion weld was successful, however the copper's surface had become rough with oxidation and the strap was significantly more flexible than its already soft-annealed original condition. The diffusion weld method was abandoned because the difficult process was not worth the time spent and both the annealing and oxidation made me question whether the material was still high vacuum compatible. In the clamp method test, a paper template, an arch hole punch, and an aluminum backing block were used to punch consistently spaced, clean holes through the copper foil. The punch was required because drilling the holes with a standard Jobbers bit tore the foil. This method was the most successful.

See Figure 4.12 for a photo that shows the components of the cold strap assembly's detector end. The translucent orange Kapton[®] washers visible in the picture were used to electrically insulate the H1RG from the cold strap. PTFE washers were tried first, but these failed. During test cooling runs with the PTFE washers, the temperature was maintainable at 150 K, as expected, but after remaining constant for longer than approximately one hour, the cryostat was unable to resume cooling the detector to a temperature below 150 K. I attributed this to PTFE creep. Materials that exhibit creep or "cold flow" will undergo plastic deformation

when subjected to even a small force if the force is applied for a long amount of time. The initial cold strap bolt torque caused the PTFE to creep and thermal contraction exacerbated the effect. As the washers deformed, thermal conductance between the strap and the HIRG reduced and detector could no longer be cooled. The Kapton[®] washers that replaced the PTFE did not exhibit creep and, with these washers, the cryostat worked as designed. Figure 4.13 shows an example of the cryostat cooling down, maintaining temperature for an extended time, and resuming cooling.

In order to achieve this control, custom temperature control and heater power electronics were designed and built. Heater power for up to four detectors is provided by a 4-channel low-gain power amplifier circuit. Up to six temperature sensors are powered by a 6-channel, 0.988 mA differential-amplifier current-source circuit. Both circuits were designed and the boards laid out and printed using ExpressPCB[®] software. Detailed schematics and layout diagrams are shown in Appendix B.2. Using prewritten LabVIEW proportional integral derivative (PID) control application control interfaces (APIs), a larger virtual instrument (VI) was written to handle the temperature measurement, heater power, and temperature control of the detector(s). The VI also records dewar and detector temperature data in a file. Through experimentation, it was found that the best method for achieving good temperature control is to allow the detector to cool at the maximum rate, which is set by the choice of cold strap thickness, and with control loop parameters $P = 3.0$, $I = 1.0$, and $D = 0.0$, initiate the PID as the temperature nears the setpoint. In order to control the detector at 150 K, the heater needed to produce 1.2 watts.

4.3.3 Laboratory X-ray Sources

The ideal X-ray source for the QE experiment would be collimated, of known intensity, monochromatic, and tunable in photon energy. Since we do not have access to such a source, we have to make accommodations to get the desired result. Placing a source far away from the detector and making simultaneous measurements with a gas flow proportional counter provides both a sufficient substitute for collimation and a reference that enables source calibration. As discussed in §4.2.2 there are

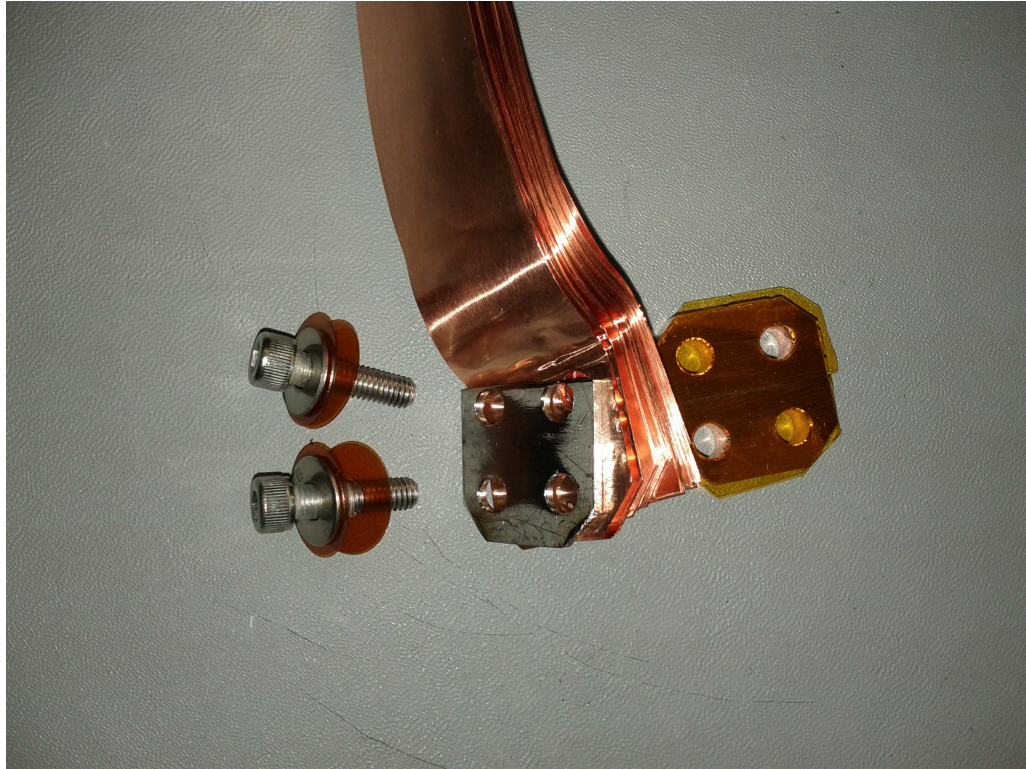


Figure 4.12: The cold strap's detector end, disassembled to illustrate the assembly's components. As described in the text, the design goal of the strap end was to provide an easily detachable high thermal conductivity, electrically insulating mechanical connection between the strap and the detector mounting plate (not shown). The top half inch of two 0.75 inch 10-32 18-8 stainless steel cap screws was wrapped with PTFE shrink tube to prevent it from contacting the strap. Two Kapton[®] washers were used to electrically insulate the screws from the strap. Stainless washers were included in the stack so that the cap screw heads did not tear the Kapton[®] washers. The stainless steel plate was included so that the heavily torqued bolts applied even pressure to the entire end of the strap. Shown is the 20 foil stack used in our experiments. The solid copper standoff to the right was covered with acrylic adhesive Kapton[®] tape to prevent it from electrically contacting the strap. Since the tape is so thin, it imposes minimal thermal resistance. In fact, the film may have improved heat transfer. In the heat sink industry, thin polymer films are often used to improve thermal conduction between metal surfaces because their softness allows them to conform to irregularities in the mating metal surfaces, increasing contact area.

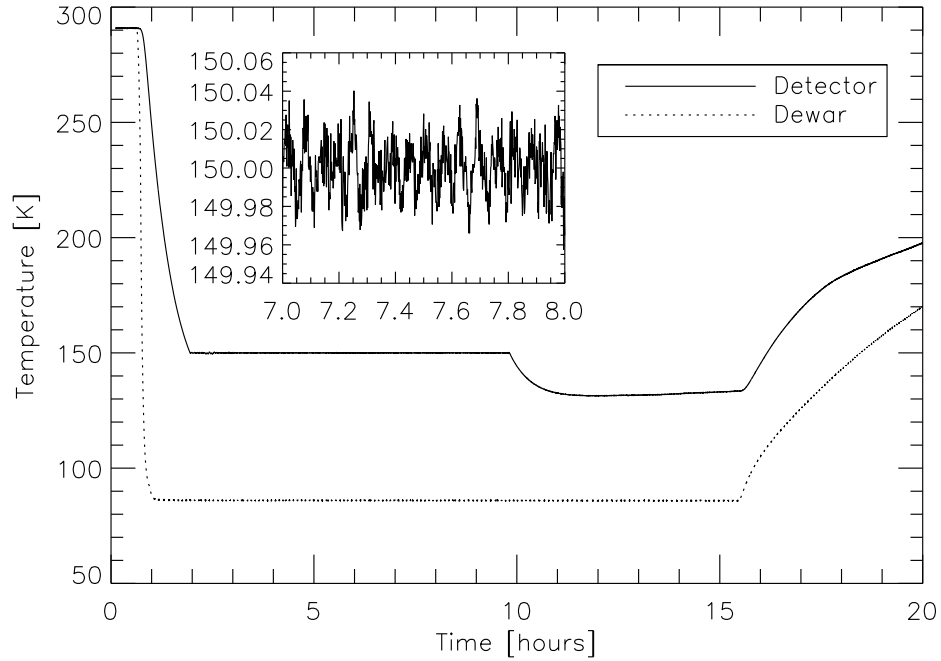


Figure 4.13: Temperature data from the dewar and detector during the December 17, 2012 QE data run. Time data are shown as the number of hours elapsed after the 14:06:57 start of the run. The inset plot shows small variations in the detector temperature data and has the same units as the larger plot. The thermal control is shown to be stable to within a few tenths of a degree around the 150 K setpoint over both long and short time intervals. In this run, the dewar was filled at 14:37 and began to warm at 05:29 the next morning, making for a 14 hour 52 minute hold time. The ~ 20 K drop in detector temperature that occurred 10 hours after the dewar fill (23:30 local time) was due to the detector heater being turned off as a safety precaution. Note that, with the same thermal strap, controlling the detector at a higher temperature or for a longer time period will decrease the hold time.

sources that can produce nearly monochromatic tunable emission, but we do not have access to such sources in the lab. We concentrate on producing monochromatic emission by producing K-shell electron vacancies in various materials, which causes the production of X-rays when the vacancy is filled by an electron falling from a higher energy level. To a lesser extent, L and M-shell transitions can also be used, but they are less spectrally pure since they are composed of multiple tightly grouped lines. See Figure 4.14 for an illustration of the allowed transitions that

produce X-rays and their nomenclature. These transitions are not tunable, but if one carefully selects source materials, a range of X-ray emission line energies can be produced that gives adequate coverage of the 0.5-10 keV spectral region for many test applications. Table 4.3 shows a list of elements that produce lines in this energy range and common materials that contain them.

Generic Energy Level Diagram

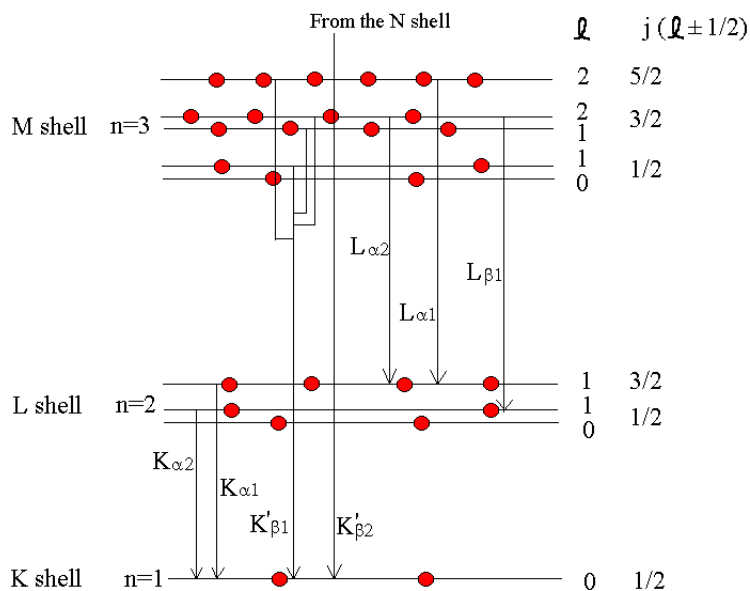


Figure 4.14: Allowed electronic transitions that produce X-ray photons. Quantum selection rules make transitions between s-s, p-p, d-d, etc. orbitals extremely unlikely, so they are not shown with a downward arrow in this illustration. The $K\alpha$, $K\beta$, etc. notation is known as Siegbahn notation.[84]

Before I delve into sources that produce X-rays via ionization, I will explain our use of ^{55}Fe , the simplest and most common laboratory soft X-ray source. ^{55}Fe is a radioactive isotope of iron that is produced by neutron bombardment of its high natural abundance isotopes ^{54}Fe , through the (n,γ) reaction, and ^{56}Fe , through the $(n,2n)$ reaction [86]. The isotope has a half-life of 2.73 years and decays through orbital electron capture [87]. After decay, the newly formed ^{55}Mn atom now has a K-shell vacancy that can be filled by an L-shell electron, producing a $K\alpha_1$ or $K\alpha_2$ photon, an M-shell electron, producing a $K\beta_{1,3}$ photon or by an electron cascade that results in the ejection of an Auger electron.

Element	Transition	Energy [keV]	Material
Carbon	$K\alpha_{1,2}$	0.277	Graphite
Oxygen	$K\alpha_{1,2}$	0.5249	
Flourine	$K\alpha_{1,2}$	0.6768	PTFE, LiF
Copper	$L\alpha_{1,2}$	0.9297	Pure metal
Copper	$L\beta_1$	0.9498	Pure metal
Zinc	$L\alpha_{1,2}$	1.0117	Pure metal
Zinc	$L\beta_1$	1.0347	Pure metal
Sodium	$K\alpha_{1,2}$	1.041	NaCl
Magnesium	$K\alpha_{1,2}$	1.2536	Pure metal
Aluminum	$K\alpha_2$	1.4863	Pure metal
Aluminum	$K\alpha_1$	1.4867	Pure metal
Silicon	$K\alpha_2$	1.7394	Detector material
Silicon	$K\alpha_1$	1.7400	Detector material
Sulfur	$K\alpha_1$	2.3066	Pure S crystal
Sulfur	$K\alpha_2$	2.3078	Pure S crystal
Chlorine	$K\alpha_2$	2.6208	PVC plastic, NaCl
Chlorine	$K\alpha_1$	2.6224	PVC plastic, NaCl
Argon	$K\alpha_2$	2.9556	P-10
Argon	$K\alpha_1$	2.9577	P-10
Potassium	$K\alpha_1$	3.3111	KCl
Potassium	$K\alpha_2$	3.3138	KCl
Calcium	$K\alpha_1$	3.6881	Calcite
Calcium	$K\alpha_2$	3.6917	Calcite
Titanium	$K\alpha_1$	4.5108	Pure metal
Chromium	$K\alpha_2$	5.4055	Pure metal foil/plating
Chromium	$K\alpha_1$	5.4147	Pure metal foil/plating
Manganese	$K\alpha_2$	5.8876	^{55}Fe emission
Manganese	$K\alpha_1$	5.8988	^{55}Fe emission
Manganese	$K\beta_{1,3}$	6.4904	^{55}Fe emission
Iron	$K\alpha_2$	6.3908	Pure metal
Iron	$K\alpha_1$	6.4038	Pure metal
Iron	$K\beta_{1,3}$	7.0580	Pure metal
Nickel	$K\alpha_2$	7.4609	Pure metal
Nickel	$K\alpha_1$	7.4782	Pure metal
Copper	$K\alpha_2$	8.0278	Pure metal
Copper	$K\alpha_1$	8.0478	Pure metal

Table 4.3: The X-ray emission line energies of materials commonly used as X-ray sources. [85]

Commercial ^{55}Fe sources are available in different activity levels, so the first step in procuring one is to calculate the optimal activity level. If the source were too warm (high activity), there would be a greater fraction of piled up X-ray events and the source would be needlessly hazardous and expensive. If the source were not warm enough, excessively long integration times would be required to achieve adequate statistical significance in the analysis. Long data runs are undesirable because they increase the likelihood of accumulating systematic errors, such as temperature drift effects, in the data. In earlier experiments, we used a ^{55}Fe source that, from logbook records, had a 0.767 mCi activity level in 1999. With this source the data showed ~ 3500 events per 5.242 second integration frame at a source-detector distance of 6 inches, which ended up producing a very desirable X-ray filling fraction that I wanted to replicate in the caterpillar. Using the relation for a source's activity

$$A_t = A_0 \left(\frac{1}{2} \right)^{t/t_{1/2}} \quad (4.6)$$

where A_t is the activity at time t , $t_{1/2}$ is the half-life, and A_0 is the activity at time $t = 0$, and projecting 12 years forward from 1999, the source had an activity level of 0.036 mCi when the data were taken in 2011. Given the caterpillar's approximate source-detector distance of 100 inches, we needed a factor of $(100/6)^2$ increase in source activity to maintain the same desirable X-ray occupancy fraction in the H1RG data. This results in a necessary activity of 10 mCi. We purchased a VZ-2937 source (10 mCi nickel-sealed ^{55}Fe) from Eckert & Ziegler Isotope Products in Valencia, CA.

The intrinsic $K\beta/K\alpha$ line intensity ratio for ^{55}Mn is 0.1195 [88]. This is a theoretical estimate based on relativistic Hartree-Slater theory. To calculate the ratio, the probabilities of transitions from the M_{1-5} subshells (dominated by M_2 and M_3 which correspond to the degenerate $K\beta_1$ and $K\beta_3$, respectively) are summed and divided by the summed probability of transitions from the L_{1-3} subshells (dominated by the L_2 and L_3 which correspond to $K\alpha_2$ and $K\alpha_3$ respectively). This ratio holds true for an isolated manganese atom, not a close arrangement of many atoms with non-negligible thickness. To calculate the line ratio for our particular source, I began with the transmission fraction of radiation through a material, considering

only absorption,

$$\frac{I}{I_0} = e^{-\sigma n s}, \quad (4.7)$$

where I is the intensity, in units of photons per second, σ is the atomic cross section, in units of cm^2 , n is the number density of the absorbers (atoms) in the material, in units of cm^{-3} , and s is the path length through the material, in cm. In our source, photons are produced through the decay process at random locations throughout the $s_{\text{Fe}} = 17.5 \pm 2.5 \mu\text{m}$ thick active iron layer. See Figure 4.15 for an illustration of the source in cross-section. The active layer will self-attenuate and, in doing so, change the emitted line ratio because low-energy photons will be preferentially absorbed. I solved for the average transmission fraction of a photon produced at a random depth in the iron,

$$\left\langle \frac{I}{I_0} \right\rangle_{\text{Fe}} = \frac{\cos \theta}{s_{\text{Fe}}} \int_0^{s_{\text{Fe}}/\cos \theta} e^{-\sigma_{\text{Fe}}(E) n_{\text{Fe}} s} ds \quad (4.8)$$

$$= \frac{\cos \theta}{s_{\text{Fe}}} \left(\frac{e^{-\sigma_{\text{Fe}}(E) n_{\text{Fe}} s_{\text{Fe}}}}{-\sigma_{\text{Fe}}(E) n_{\text{Fe}}} + \frac{1}{\sigma_{\text{Fe}}(E) n_{\text{Fe}}} \right) \quad (4.9)$$

$$= \frac{\cos \theta}{\sigma_{\text{Fe}}(E) n_{\text{Fe}} s_{\text{Fe}}} [1 - e^{-\sigma_{\text{Fe}}(E) n_{\text{Fe}} s_{\text{Fe}}/\cos \theta}] \quad (4.10)$$

where the $\cos \theta$ factor accounts for the increased projected thickness of the layer when the source is viewed at an angle, θ . This is done individually for the $\text{K}\alpha$ and $\text{K}\beta$ photon energies. On their way out to the surface of the source, the photons are then further attenuated by the $s_{\text{Ni}} = 4 \pm 1 \mu\text{m}$ sealant layer that covers the iron. Again for both energies,

$$\left\langle \frac{I}{I_0} \right\rangle_{\text{Fe+Ni}} = \left\langle \frac{I}{I_0} \right\rangle_{\text{Fe}} e^{-\sigma_{\text{Ni}}(E) n_{\text{Ni}} s_{\text{Ni}}/\cos \theta} \quad (4.11)$$

Taking the ratio of the transmission at the $\text{K}\alpha$ energy and the $\text{K}\beta$ energy and dividing by the initial $\text{K}\beta/\text{K}\alpha$ ratio, I arrived at the final $\text{K}\alpha/\text{K}\beta$ ratios plotted in Figure 4.16. At zero angle with respect to the source's surface normal, $\text{K}\alpha/\text{K}\beta = 8.36, 7.46,$ and 6.79 for the intrinsic, $17.6 \mu\text{m}$ Fe, and the $17.6 \mu\text{m}$ Fe + $4 \mu\text{m}$ Ni cases, respectively.

A dedicated housing was designed and used to mount and shutter the ^{55}Fe source in the caterpillar. Although handling this sealed, moderate-activity source

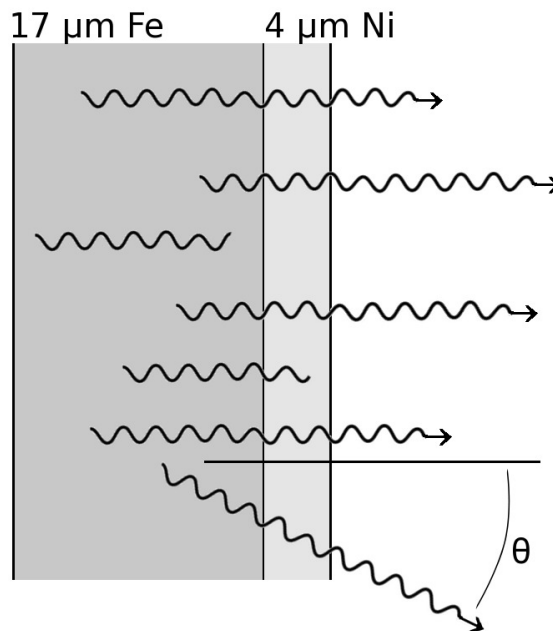


Figure 4.15: Cartoon depicting X-ray generation, active layer self-attenuation, and sealant layer attenuation in the VZ-2937 ^{55}Fe source. As the viewing angle, θ , becomes larger, the projected thickness of the layers becomes larger. As shown in the figure, for a bare ^{55}Fe film, when the radioactive layer's projected thickness increases past the $1/(\sigma\rho) \sim 40 - 50\mu\text{m}$ average absorption length of both energies, the line ratio asymptotes. This is because X-rays produced deep within the material rarely escape the material's surface. For the actual nickel plated source, the line ratio continues to harden with increased projected thickness. In reality, using the source at high viewing angle would be impractical because the intensity drops off severely.

for short periods of time is not considered hazardous since the X-rays are heavily absorbed by clothing and a person's outer layer of dead skin, the housing was nonetheless designed to minimize a person's exposure during servicing. Shown in Figure 4.17, the source mounts to a handling rod with a set screw and slides under the shielding block. Mounted in this way, the operator does not need to place any part of their body in front of the source and the operator's fingers will always be > 3 inches from the source. The circular source locates to a consistent position every time the plate is assembled by contacting two pins that are press fit into the flange plate, underneath the shield. A 0.25 inch aluminum plate attached to a steel rod that is fed outside of the vacuum through an O-ring rotary feedthrough

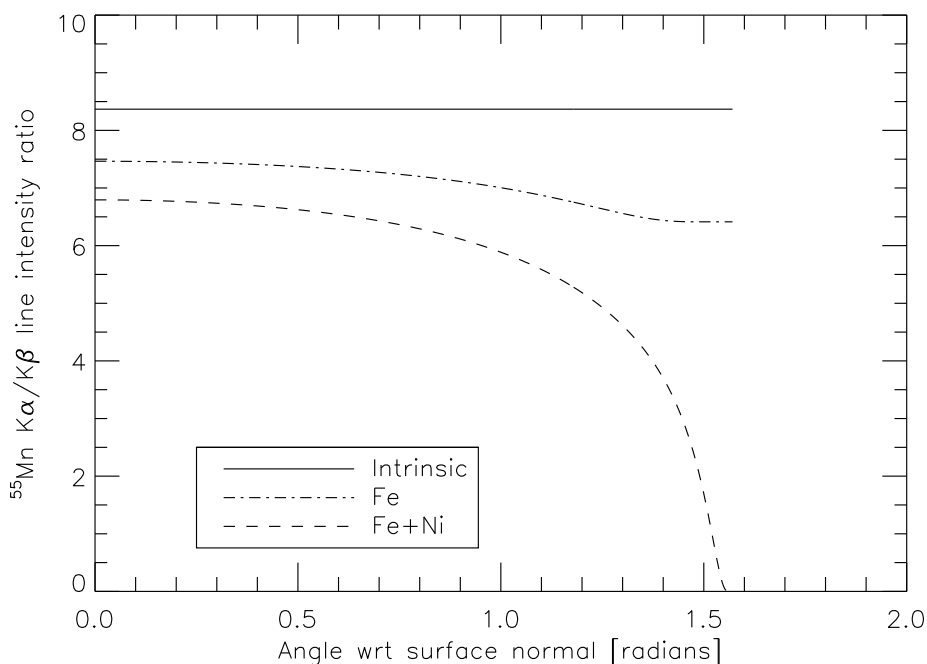


Figure 4.16: The ^{55}Mn $K\beta/K\alpha$ line ratio plotted as a function of angle with respect to the source normal. The intrinsic ratio is valid for isolated atoms, the Fe ratio curve for a $17\ \mu\text{m}$ thick source, and the Fe+Ni for a $17\ \mu\text{m}$ thick source covered by $4\ \mu\text{m}$ Ni.

is used to shutter the source. The transmission of 0.1-10 keV X-rays through 0.25 inches of aluminum is $< 10^{-18}$.

I will now move on to the discussion of laboratory sources that produce X-rays with ionization. Ionizing low-level, bound electrons can be accomplished with either particle or photon radiation. In either case, the ionizing radiation must have an energy greater than the electron binding energy. The simplest design of this type is that of the α -particle fluorescent source, shown in Figure 4.18. In such a source, a radioactive α emitter is positioned over a specially chosen sample of target material. The alpha particles ionize atoms in the target, causing them to emit fluorescent X-rays characteristic of the elements that are present in the chosen material. Since most elements have only one or two useful fluorescent lines in the soft X-ray range, multiple targets are typically mounted on a wheel inside the source so that a variety of lines can be produced without breaking the vacuum.

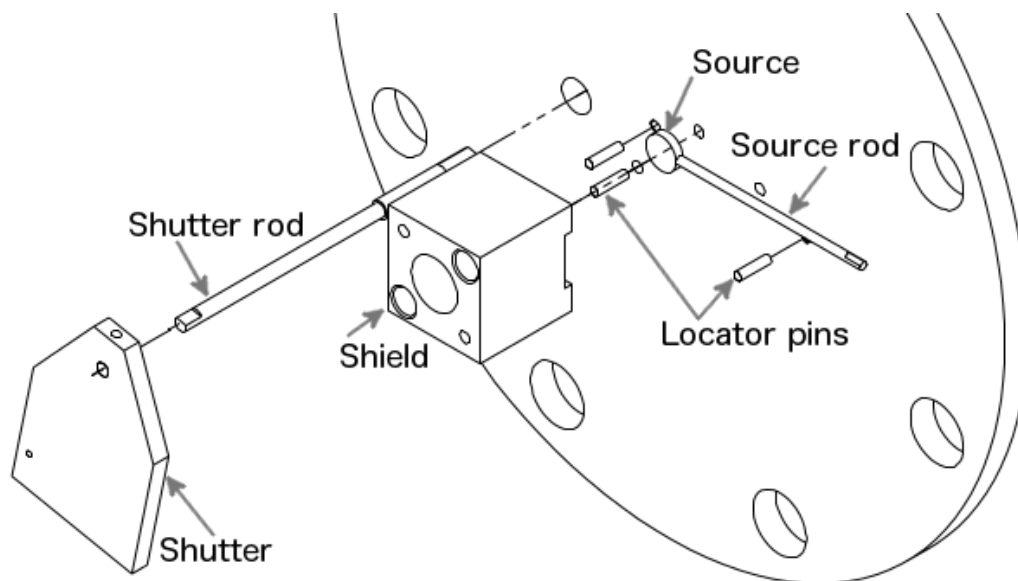


Figure 4.17: Exploded diagram of the ^{55}Fe source holder. The pictured flange plate bolts directly to the caterpillar and seals with an elastomer gasket.

The wheel is rotated to expose one target at a time, to the α radiation. Curium-244 and polonium-210 are common α sources, emitting 5.902 and 5.304 MeV alphas, respectively. In our lab polonium was chosen because it is sold in relatively easy to obtain anti-static units. Its major drawback is that the 138.4 day half life means that it must be replaced periodically. A disadvantage of the α fluorescent source compared to other fluorescent sources, is that it cannot be made very bright due to the difficulty of obtaining high activity ^{210}Po . Additionally, any material that is in the line of sight of the source and the detector will fluoresce, contaminating the spectrum with unwanted X-ray line emission. Common metals such as aluminum and iron, used to build the source need to be shielded with a material that has low-energy fluorescent emission such as graphite paint (C), Kapton[®] (H, C, N, & O), or Mylar[®] ($\text{C}_{10}\text{H}_8\text{O}_4$). Due to the constraint on brightness, the α fluorescent source could not be used in the caterpillar.

Yet another group of X-ray sources generate the ionizing radiation necessary to produce fluorescent X-rays under their own power, as opposed to using a radioactive source. These sources are generally categorized as X-ray tubes, two examples of which are shown in Figures 4.19 and 4.20. These devices use resistive heating to induce the thermionic emission of electrons from a thoriated tungsten filament.

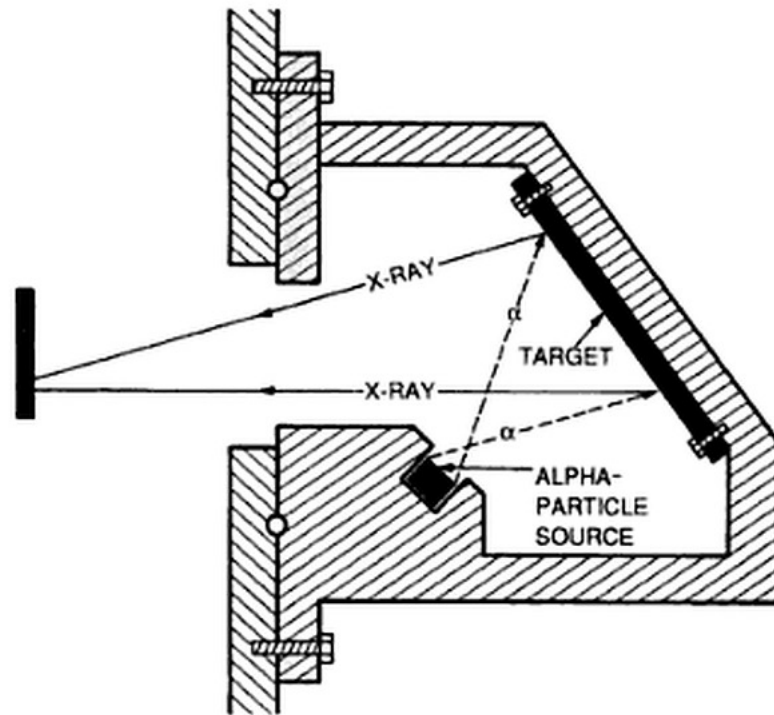


Figure 4.18: Schematic of a simple α particle fluorescent X-ray source. The particle emitter is positioned such that it irradiates the target material, but not the detector (left). The target is positioned so that X-rays generated within its surface illuminate the detector. Figure adapted from *Scientific Charge-Coupled Devices* [14].

An interesting aside; the wire is “thoriated” (the tungsten is alloyed with $\sim 1-2\%$ thorium) to reduce the filament material’s work function (the energy required for an electron to exit the surface of the solid). When the tungsten is heated, the thorium migrates outward through the wire, along the metal’s grain boundaries, and settles on the wire surface [89]. A decreased work function allows the filament to emit more thermionic electrons for a given wire temperature, yielding better performance. Returning to the operation of the X-ray tube, in the tube’s vacuum environment, the electrons produced by the filament are accelerated by the electric field produced by holding the target anode at a positive high-voltage (~ 10 kV at ~ 3 mA). The electrons collide with the anode and these collisions produce X-rays through two mechanisms: first, the electrons themselves emit bremsstrahlung radiation as their trajectories are altered by the influence of atomic nuclei in the target

and second, the electrons ionize target atoms inducing them to emit fluorescent X-rays. Popular variants of this design are the Manson tube and the Henke tube. As seen in the figures, the two differ only in the geometric arrangement of the anode and filament cathode. In the Henke tube, the cathode is positioned behind the anode and electrons are accelerated toward and collide with the opposite side of the anode because of its sharp, triangular shape. In the Manson tube, the electrons are accelerated along a straight path before striking the anode, which can viewed at a 45° angle from either side.

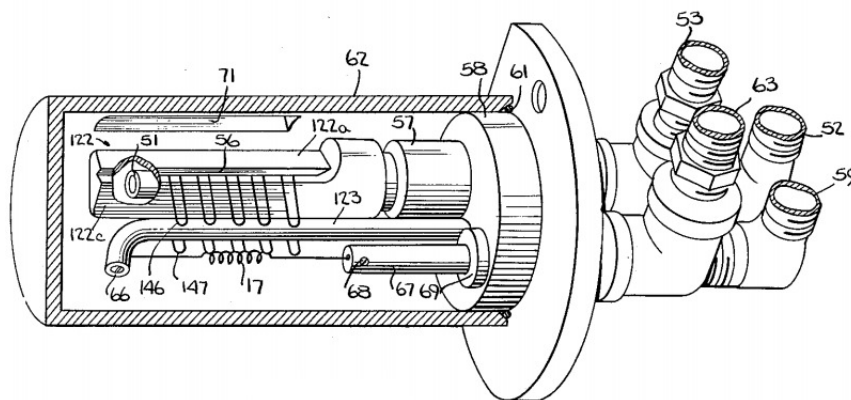


Figure 4.19: A technical drawing of a Henke tube X-ray source. The important parts are labeled in the diagram: the filament (17), anode (122), window (71), vacuum seal (61), and cooling water plumbing (52, 53, 59, and 63). The U-shaped wires (146) help to shape the electric field and guide more electrons around and to the other side of the anode. Figure is taken from the original 1961 US patent application, by Burton Henke for an “Ultra-soft X-ray Source” [90].

In some applications the continuum bremsstrahlung emission that both of these tubes produce is considered desirable, but for calibration purposes, it is a contaminant. This broadband emission can be attenuated by using a foil filter made from the same material as the anode. This technique works because a filter made from anode material will always have an absorption edge just above the line emission energy. This causes it to transmit well at the emission line energy, while heavily attenuating above the edge and, most importantly, at low energy, where the bremsstrahlung continuum is the most intense. A method that eliminates all of the bremsstrahlung continuum from an X-ray tube source involves using the tube’s X-ray emission to stimulate fluorescent emission from a target material.

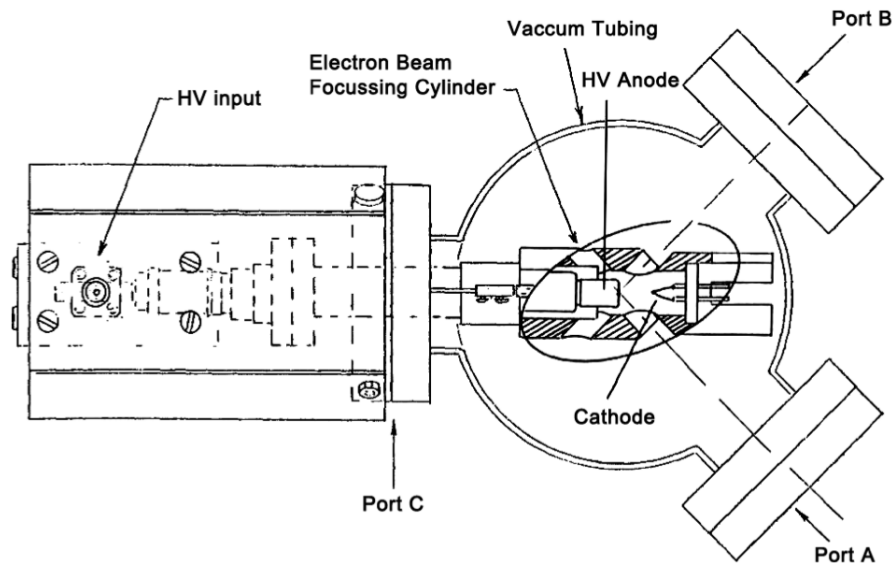


Figure 4.20: A diagram of a typical Manson X-ray tube. Figure borrowed from Yang [91].

In this cascade of emission processes, from accelerated thermionic electrons, to bremsstrahlung/fluorescent X-rays, to fluorescent X-rays, an important practical consideration to note is that the energy of the source radiation needs to be significantly higher than the transition being excited, usually by a factor of 1.5, in order to be efficient.

Our lab owns a Henke source that had not operated for many years. At the beginning of my project I set out to refurbish the source so that it could be used for the QE measurement. One of the problems encountered with this undocumented device was the matter of deciding how much current should be used to heat the coil. Heating the coil in air to test the required current is not a good idea because in atmosphere, the hot filament will oxidize, causing it to prematurely burn out. A back-of-the-envelope calculation for estimating the current required to heat the filament to a given temperature was carried out. The power, P , dissipated by a wire with resistance, R , due to current, I is

$$P = I^2 R. \quad (4.12)$$

The wire resistance can be expressed as the product of the wire material resistivity,

ρ , multiplied by the ratio of wire length, l , to the wire's cross-sectional area, $\pi(t/2)^2$, resulting in

$$P = I^2 \rho \frac{l}{\pi(t/2)^2}, \quad (4.13)$$

where t is the wire thickness. According to the Stefan-Boltzmann law, the power emitted by a body at temperature, T , with emissivity, ϵ , and surface area, A , in an environment of temperature, T_e , is

$$P = \epsilon \sigma A (T^4 - T_e^4), \quad (4.14)$$

where σ is the Stefan-Boltzmann constant. Equating the two expressions for power and solving for I ,

$$I = \sqrt{\frac{\sigma \epsilon \pi^2 t^3 (T^4 - T_e^4)}{4\rho}} \quad (4.15)$$

This works for a straight wire, but like many filaments, ours is coiled and will partially illuminate itself, leading to an effective emitting surface area that is smaller than the true wire surface area. The wire's surface area can be roughly corrected with a self-illumination factor,

$$F = 1 - \frac{t}{2s} \epsilon, \quad (4.16)$$

where Figure 4.21 shows the definition of the coil separation distance, s . The ratio of t/s characterizes the open fraction of the coil winding. For high emissivity, the factor ranges from 0.5 to 1 because s can never be less than t . The emissivity is factored into the self-illumination because, for a highly reflective surface (low emissivity), the material would not efficiently self-illuminate. For this calculation a wire temperature of 2400 K, comfortably below the 3687 K melting temperature of tungsten will be assumed. At this temperature the most intense emitted wavelength is $\lambda = 0.2898/T = 1.2 \mu\text{m}$ and, at this wavelength, the emissivity can be roughly estimated to be $\epsilon = 0.4$ [92]. With a wire thickness of $t = 0.02$ inches, $s = 0.5$ cm, tungsten resistivity at 2400 K being $\rho = 70.39 \cdot 10^{-6} \Omega\text{-cm}$, the current

required to produce the given temperature wire is $I = 29$ amps.

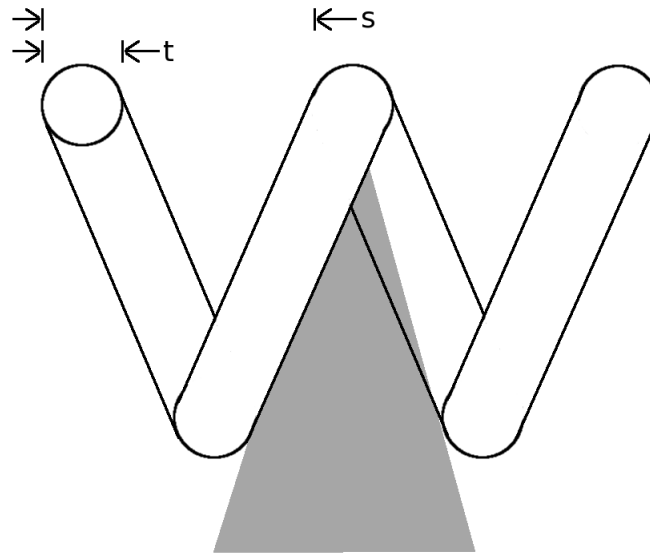


Figure 4.21: Cross-section view of a coil of filament wire. The wire thickness, t , and the coil separation distance, s , both contribute to the filament's self-illumination.

Due to time constraints, the QE measurement project had to be descoped by putting the Henke tube refurbishing project on hold. While the test-stand was built to accommodate either the ^{55}Fe source or the Henke tube, the HIRG QE was measured using the two X-ray lines emitted by the ^{55}Fe source.

4.3.4 Gas Flow Proportional Counter

We chose to use a gas flow proportional counter to make our absolute source calibration measurement. The counter's theory of operation is illustrated in Figure 4.22. The device is basically a hollow, gas-filled, electrically conductive cavity with a conductive wire strung down the middle. The wire and cavity wall are insulated from one another so that when a positive voltage is placed on the wire, an electric field fills the counter's cavity. Any radiation, charged particle or electromagnetic, that makes it into the cavity and has enough energy to ionize an atom in the gas, will have a finite probability of being detected. Focusing the discussion on X-rays, if a photon with energy greater than the binding energy of a gas atom electron, E_b , enters the counter and ionizes a gas atom, an electron with kinetic energy

$E_{e^-} = (h\nu)_{X\text{-ray}} - E_b$ and an unstable gas atom ion will be produced. The two do not recombine because the counter's electric field drives the charged particles in opposite directions and the electron is moving fast enough that it quickly becomes very far from the ion. After the initial ionization, the unstable gas ion will de-excite through a radiative (fluorescent X-ray emission) or non-radiative process. While the relatively heavy ion slowly moves towards the outer wall of the proportional counter, where it will eventually recombine with an electron, the original ionized electron, with its initial kick and additional energy imparted by the electric field, moves quickly through the gas. As it moves, it ionizes other gas atoms along the way, losing speed with each interaction, until its kinetic energy is fully absorbed through ionizations of the counter gas. As shown in the figure, each of these electrons will move toward the wire and produce a charge pulse in the conductor.

To help explain the remarkable performance characteristics of the proportional counter, allow me to first indulge in a back-of-the-envelope calculation. In our counter we used a common proportional counter gas called P-10, a mixture of 90% argon and 10% methane. This choice of the gas will be motivated later in this section. Let us assume for a moment that the previously mentioned charge pulse in the wire consists only of electrons that were ionized by the initial high-energy electron that was liberated by the incident X-ray. If all of the energy of an incident Mn $K\alpha$ photon were to go towards generating electron-ion pairs, there will be $E_{Mn\ K\alpha}/\omega_{P10} = 225\ e^-$ produced. In this equation $E_{Mn\ K\alpha} = 5.98\ \text{keV}$ is the energy of the Mn $K\alpha$ photon and $\omega_{P10} = 26.6\ \text{eV}$ is the average electron-ion creation energy for P-10. Assuming a cylindrical proportional counter with a round wire, the detector will have a capacitance $C = \epsilon 2\pi l / \ln(b/a) = 17.03\ \text{cm} = 1.89 \cdot 10^{-11}\ \text{F}$, where the dielectric permittivity of P-10 is $\epsilon_{P10} \approx \epsilon_0 \approx 1$ [93], $l \approx 10\ \text{cm}$ is the length of the wire, $b \approx 2\ \text{cm}$ is the radius of the cavity, and $a \approx 12.5\ \mu\text{m}$ is the radius of the wire. Given this capacitance, the voltage pulse produced will be $225[e^-](1/6.24 \cdot 10^{18})/C = V = 1.9 \cdot 10^{-6}\ \text{V}$. A signal of this amplitude would be lost in the noise of the readout electronics. Something more is going on in the proportional counter and to explain why, I will derive the equation for the electric field as a function of position within the cavity.

As before, assuming a cylindrical chamber of radius, $r = b$, a proportional counter wire of radius, $r = a$, a permittivity of the intervening gas ϵ , and a voltage,

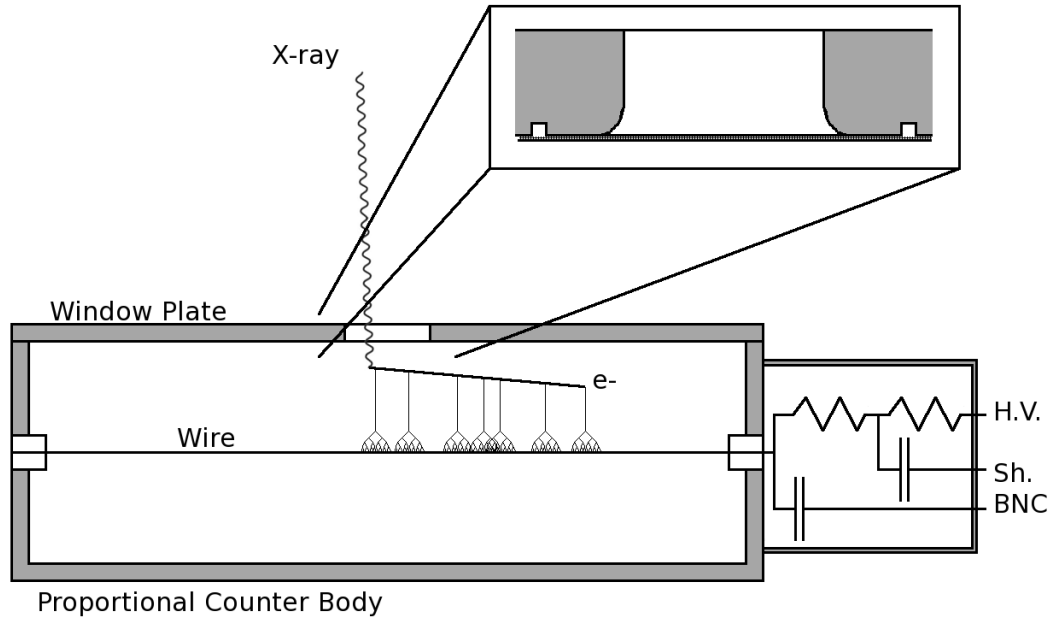


Figure 4.22: Shown is a cartoon cross-section schematic detailing our gas flow proportional counter's theory of operation. The electronic inputs are a MHV high voltage connect (H.V.), a BNC signal connector (BNC), and the BNC signal's shield (Sh.). An X-ray is shown entering the counter through the window, and ionizing an argon atom in the P-10 fill gas. This energetic electron subsequently ionizes other argon atoms in the counter, which move towards the wire under the influence of the counter's electric field. Near the wire, the electrons are accelerated faster causing a Townsend avalanche. The inset (upper right) shows the Mylar[®] window supported by a stainless steel mesh, secured using an epoxy filled glue-groove. Not shown are two Ultra-Torr[™] fittings used for gas input/vent. The drawing is not to scale.

V_0 , between the two, calculation of the electric potential begins with Poisson's equation,

$$\nabla^2 V(\vec{r}) = \frac{\rho(\vec{r})}{\epsilon}, \quad (4.17)$$

with boundary conditions,

$$V(a) = V_0 \qquad V(b) = 0. \quad (4.18)$$

In the gas, where $a < r < b$, there is no free charge, so Poisson's equation reduces to Laplace's equation,

$$\nabla^2 V(\vec{r}) = 0. \quad (4.19)$$

Since this special case has cylindrical symmetry, we know that the potential will not be a function of azimuthal angle or distance along the wire, so the potential can be reduced to a function of r . Using the cylindrical coordinate system Laplacian operator identity, the equation becomes

$$\frac{1}{r} \frac{\partial}{\partial r} \left(r \frac{\partial V(r)}{\partial r} \right) = 0 \quad (4.20)$$

$$\int \frac{\partial}{\partial r} \left(r \frac{\partial V(r)}{\partial r} \right) dr = \int dr \quad (4.21)$$

$$r \frac{\partial V(r)}{\partial r} = C_1 \quad (4.22)$$

$$\int \frac{\partial V(r)}{\partial r} = \int \frac{C_1}{r} \quad (4.23)$$

$$V(r) = C_1 \ln(r) + C_2 \quad (4.24)$$

Since $V(a) = V_0$ and $V(b) = 0$,

$$C_1 = -\frac{V_0}{\ln(b/a)} \quad C_2 = \frac{V_0 \ln(b)}{\ln(b/a)} \quad (4.25)$$

Solving for the electric field between the wire's surface and the counter walls,

$$E(\vec{r}) = -\nabla V(\vec{r}) = \frac{V_0}{\ln(b/a)} \frac{1}{r} \hat{r} \quad (4.26)$$

The most important point is that the electric field becomes very large close to the wire. For a small wire diameter, usually a few tens of microns, and sufficient V_0 , usually ~ 1500 V, close to the wire, the electric field is strong enough that the electrons it is accelerating can now ionize other gas atoms. Those liberated electrons go on to be accelerated and ionize more gas atoms. The number of ionizations continues to grow exponentially until the so called Townsend avalanche of electrons reaches the wire where it becomes a voltage pulse. The gas ion created

in that first interaction with the incident X-ray has some chance of emitting a fluorescent X-ray when it de-excites. If that photon is absorbed in the counter, the avalanches that it produces will sum together with the avalanches produced by the initial ionized electron into one large pulse. If the fluorescent X-ray is not absorbed in the gas because it penetrated through the counter gas and was absorbed by one of the counter's walls, it is said to have escaped. The avalanches created by the initial ionized electron will result in a smaller pulse and form a separate peak in the spectrum at energy $E = h\nu - E_b$, which is called the escape peak. This energy is the same as the kinetic energy of the initial ionized electron.

If V_0 is large enough to prevent recombination and create a detectable avalanche, but not so large that electrons ionize more than one gas atom per collision, the counter's voltage output will be proportional to the energy of the incident X-ray, hence the name proportional counter. This amplification effect, where a small number of electrons are converted into tens of thousands of electrons is called gas gain and is usually on the order of $10^5 - 10^6$. Figure 4.23 shows the different response regimes that become apparent when gas gain is plotted as a function of wire voltage. In the context of the QE test-stand, it was desirable to operate the counter in the proportional regime, but not stray into the Geiger regime where the response becomes non-linear. We know that our counter is operating in the proportional regime because the energy spectrum data presented in §4.4 show that the position of the escape peak and the fully absorbed ^{55}Mn $K\alpha$ emission line have the correct ratio.

Like the detection of photons in semiconductor detectors, the process of converting the energy of an incident X-ray to a proportional counter wire voltage contains inherent sources of uncertainty. Electron-ion pair creation in proportional counters is subject to the same Fano noise that affects electron-hole pair creation in silicon detectors, though the problem is much worse in proportional counters. Since Fano noise variance is inversely proportional to the detector's average electron-ion pair generation energy ($\omega_{\text{Si}} = 3.7$ eV [95] and $\omega_{\text{Ar}} = 26.3$ eV [96]) and proportional to the detector material's Fano factor ($F_{\text{Si}} = 0.158$, $F_{\text{Ar}} = 0.16$ [96]), optimal proportional counter line widths are a factor of ~ 10 greater than in silicon detectors. Care should be taken when using these numbers in calculations. In argon, electron-hole/ion pair creation energies vary with temperature. Also, the

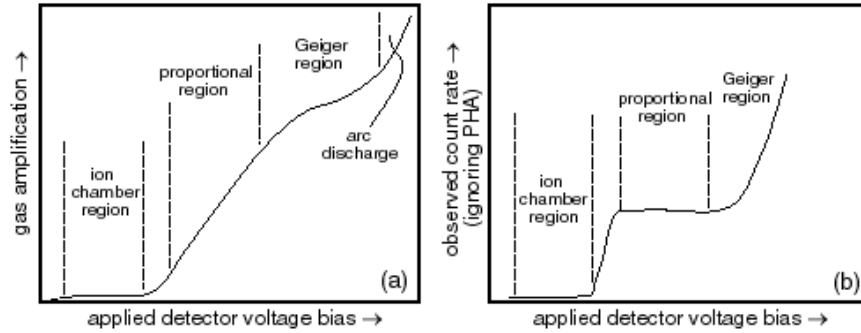


Figure 4.23: Plots show the behavior of the gas gain, *left*, and count rate, *right*, as a proportional counter’s anode voltage is varied. The important feature of proportional counters is the large “proportional” region of linear gain and constant count rate seen here. Plots were borrowed from a Northern Arizona University webpage on proportional counter detector theory [94].

Fano factor differs significantly for electrons and α -particles [96] and the factors are found to exhibit minor energy dependence [97]. The increase in α -particle Fano factors when compared to those for electrons was attributed to the nuclear elastic collision pathway that is available to alpha particles and not to electrons. No appreciable difference was found between measured Fano factors for pure argon and a P-10 gas mixture [98].

The gas in a proportional counter is specially chosen to allow the described cascade of ionizations to happen unabated. The most important consideration when choosing the gas is that it needs to have low electronegativity. Electronegative gasses, despite the atoms being neutral, have the tendency to capture free electrons. This is bad for a proportional counter’s performance because electrons that are captured before making it to the wire translate into degraded energy resolution. Oxygen is an electronegative gas that happens to make up a large fraction of our atmosphere, so it must be flushed out of the counter to ensure optimal detector response. P-10 (nominally 90% argon, 10% methane) is a standard choice for proportional counter gas. Argon has an undefined electronegativity, a reasonable X-ray cross section, and is a readily available gas. Methane is included in the mixture as a “quench gas”. If argon were the only gas present in the counter, positive argon ions left over from an avalanche would eventually make their way to

the counter wall, long after the avalanche pulse was detected and recombine with electrons donated by the wall material. This recombination would emit a photon that has a good chance of ionizing a counter gas atom. The electrons produced from these ionizations would cause distinct avalanches that would contaminate the energy spectrum. The quench gas stops this from happening by donating an electron to the positive argon ion before it can reach the counter's wall. Instead of releasing a photon itself, the quench gas molecule dissociates. This consumption of the quench gas is not a problem in our counter because we operate in flow mode, where the quench gas is continually replenished.

Our particular counter was originally built from a solid rectangular bar of aluminum that was end milled to create a 6 inch long \times 2 inch wide \times 2.125 inch deep rectangular cavity. The wire had already been strung through the counter, tensioned and soldered between two glass HV feedthroughs, co-linear with counter's long center axis. In our counter, on the left end the wire is left electrically floating in the HV feedthrough and on the other end, it is connected to a simple electronic circuit shown in Figure 4.22. The counter wire is connected to a NIM-BIN Tennelec 0-5 kV power supply outside of the vacuum chamber with an MHV connector on the counter body through very large current-limiting resistors. The HV is routed into the chamber with a floating-shield feedthrough. The BNC signal output is AC coupled to the counter wire via a HV capacitor. Only the time-transient signal pulse will transmit through the capacitor, not the HV DC offset. The BNC shield is capacitively coupled to the HV. The rectangular shape of our counter's interior actually distorts the electric field, departing from the cylindrical ideal, but for our application, this is not a problem. Our small window restricts illumination to the central region of the counter, where the electric field is most uniform and the energy resolution and QE will be the most predictable. Also, as indicated by the functional form of the electric field inside the counter, the geometry of the wire is far more important than the geometry of the cavity. Bends, kinks, or surface irregularities in the wire cause electric field variance in the high-field region, close to the wire, where it matters. For example, a longitudinal surface crack, a common defect in die-drawn tungsten wires, would create a significantly higher field near the rim of the crack compared to the smooth surface next to it. Signal electrons that travel through the high field region would experience higher gain than those

that did not, degrading the energy resolution.

The counter was found in its native laboratory environment mounted with a non-vacuum compatible window and the electronics potted in a solid wax block, most likely to prevent high voltage corona/shorts. In order to prepare the instrument for vacuum use, the window had to be replaced and the vacuum suitability of the wax had to be investigated. Given the uncertain composition of the wax, and that paraffin, a common wax, is a material with outgassing characteristics unacceptable for high vacuum applications, the block was removed. First, the majority of the wax was melted away with a heat gun. Next, the remaining wax was dissolved with a 3 day xylene bath, followed by an acetone rinse, and finished with an ethanol rinse. All of the electronics shown in Figure 4.22, were replaced with new parts to avoid the risk of future malfunctions resulting from the harsh solvent baths. The resistors are $10\pm 1\%$ M Ω 10 kV 2.5 W thick film type and the capacitors are $2.2\pm 20\%$ nF 6kV ceramic type. Great care was taken not to desolder the counter wire from the feedthrough during the electronics replacement. Stringing a thin proportional counter wire is a delicate process that requires enough tension on the wire to eliminate kinks, but not so much that the wire breaks.

After the signal exits the proportional counter it travels through a Kapton[®] shield coaxial cable, into a floating-shield vacuum feedthrough, and out of the chamber via standard 50 Ω coaxial cable. The signal is fed into an Ortec 142A charge-sensitive preamplifier at the usual input, inverted, amplified, and exits through the E terminal as positive voltage pulses. For 5.89 keV photons, the output pulses will be $V_0 = Q_D/C_f \approx 0.35$ V in height, where Q_D is the charge deposited in the detector wire by the incident photon, and $C_f \approx 1$ pF is the amplifier's feedback capacitance. In this equation $Q_D = EGe^-/\omega_{P10}$, where E is the energy of the incident photon and $G \approx 10^4$ is the gas gain. Figure 4.24 shows that we see 0.45 V pulses from the preamp on an oscilloscope. Since the HV bias had already been removed from the detector signal and the preamp's maximum bias voltage is 1 kV, we did not run the HV through the preamp. In this configuration, it was found that the preamplifier output will be extremely noisy unless the T and BIAS shields are well connected to the preamp's chassis. Since the chassis was painted, the paint had to be scraped off and creative taping methods were used to affix copper braid and make the electrical connection between the

shields. Typically, it is best to connect the preamplifier close to the detector to reduce input capacitance, microphonic (wire vibration) noise and radio frequency pickup. In our apparatus, it was not possible to make the amplifier and its power cable vacuum safe, so the unit had to be wired into the signal chain outside of the chamber. After exiting the preamplifier, the inverted, amplified signal was then fed into a NIM-BIN Tennelec 244 shaping amplifier with the gain set to 20, the pileup rejector turned off, and a peaking time of 12 μs . The signal was then fed into an Ortec 8k multi-channel analyzer (MCA) and recorded by Ortec's Maestro software running on a Windows XP PC. The data were collected in 256 channel mode. When tuning the proportional counter's electronics parameters, it is important to maximize proportional regime gas gain and use only enough shaping amplifier gain to fully utilize the 0-10 V input range of the MCA. This minimizes the width of the noise peak, allowing for the best low-energy sensitivity.

Commissioning data runs were taken with the MCA's internal high and low discriminators set to their default values of 0 and 255, respectively. However, it was found that running with this settings configuration caused a discrepancy between count rates measured with the MCA and count rates measured with single channel analyzer (SCA). I suspected that the problem had to do with dead time correction. Most generally, dead time is the short period of time following the detection of an event where the system is unable to detect new events. In proportional counters, there is a small dead time associated with the detector itself, where the electric field requires time to reconfigure after a pulse occurs in the wire. The MCA also has dead time because the input ADCs require $\sim 2 \mu\text{s}$ to convert an incoming analog pulse into a digital number. Note that the SCA has effectively no dead time, which is why I used it to make an unbiased comparison. Since the MCA's documentation contained insufficient detail on the subject of dead time and Ortec engineers adamantly, and incorrectly, assured me that changing the discriminator values would have no effect on dead time, I carried out my own investigation.

To perform the dead time test, the signal coming out of the preamplifier was split and routed to an Ortec 551 SCA and Ortec 715 counting module wired in series and the MCA so that the count rates could be compared directly. The SCA's lower discriminator was set below the oscilloscope-measured ^{55}Fe pulse heights and the upper discriminator to the 10 V maximum so that all ^{55}Fe pulses would make it

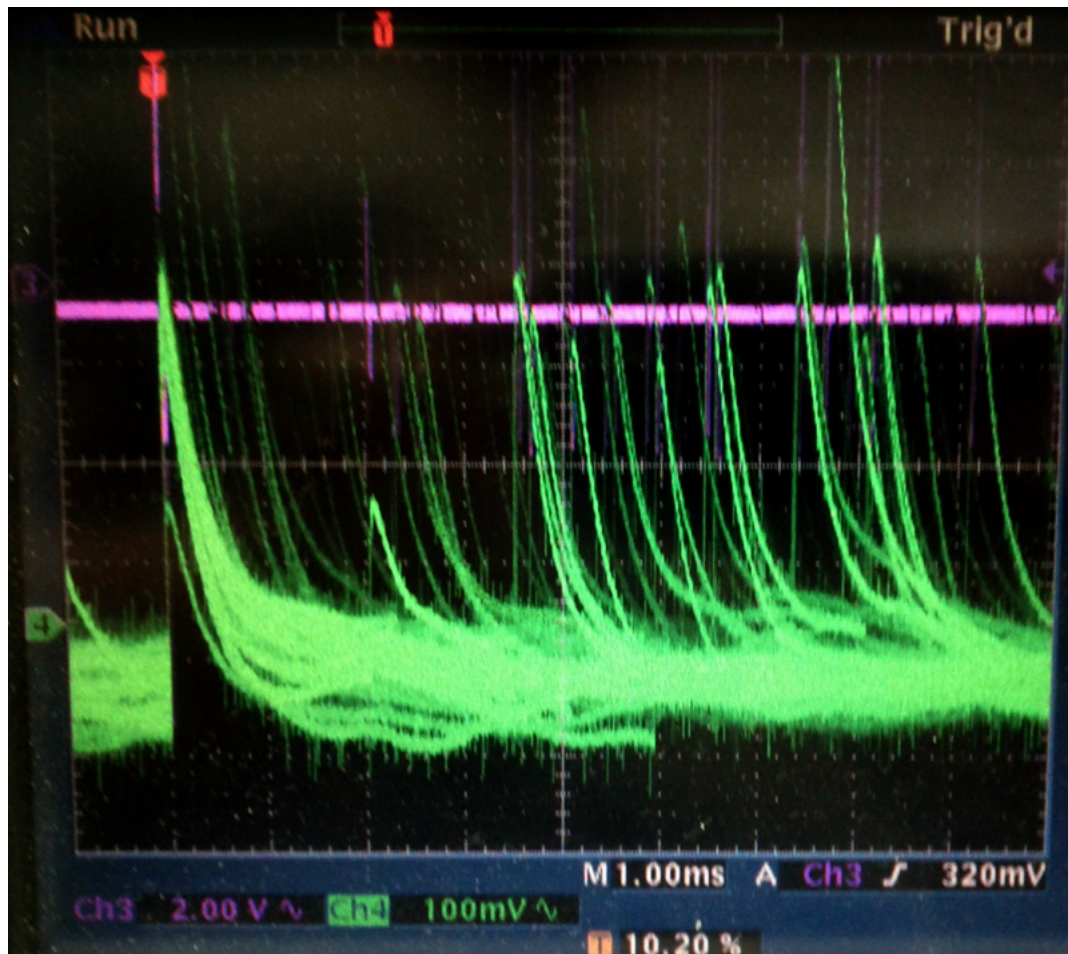


Figure 4.24: A photograph of oscilloscope output showing the proportional counter preamplifier output (positive, green pulses, bottom trace) and the shaping amplifier output (bipolar, purple pulses, upper trace). The green trace's scale is 100 mV/div. and the purple trace's scale is 2 V/div. The timing scale is 1 msec/div.

into the counting module and noise pulses would be filtered out. On the MCA, the dead time test data runs were taken with the lower discriminator level stepped from channel 0 to channel 27. The experiment proved to be very useful in interpreting the MCA's outputs. The counter outputs a two column energy spectrum in units of counts and channel number. It also reports real time and live time numbers for the data run. Real time is the time that a stopwatch would record for the length of time between the beginning and end of a data run. Live time is a number calculated by the MCA software that estimates the amount of time during the real time interval that the MCA was sensitive to new events. This is not trivial and

the MCA employs the Gedcke-Hale method [99] to make the estimate.

Figure 4.25 shows the results of our investigation. It was found that the MCA is outputting dead time corrected counts, not raw counts, evidenced by the counts/(real time) curve more closely approximating the SCA count rate than the counts/(live time) curve. For large dead times above 35%, the live time estimate begins to increasingly underestimate the count rate. It was found that increasing the MCA's internal lower level discriminator to channel 30 completely removes the low-energy noise peak, which was contributing to the vast majority of the dead time, without preventing the detection of any real X-rays.

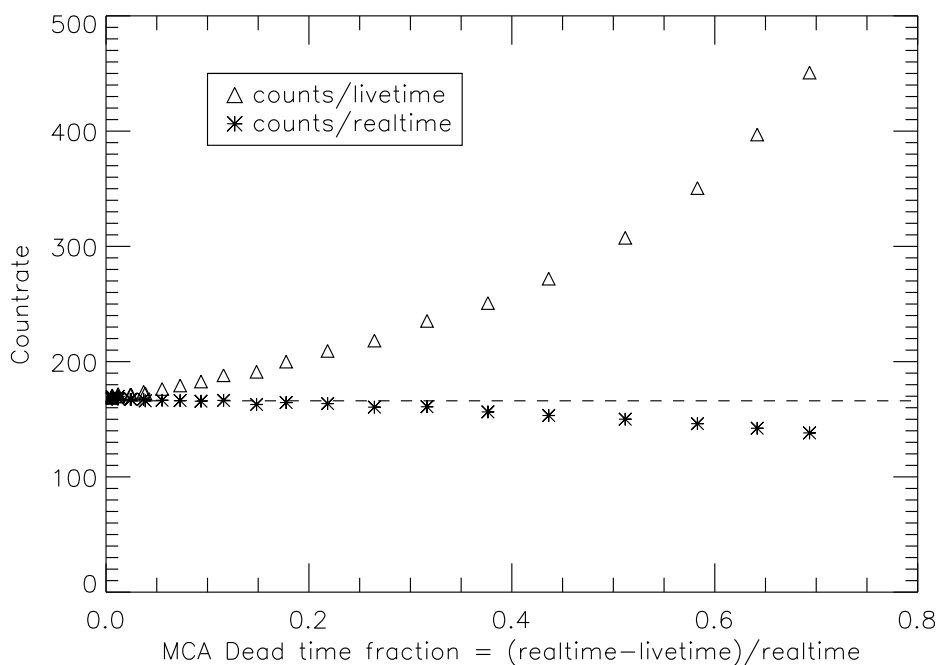


Figure 4.25: Results of the proportional counter dead time experiment. The SCA measured count rate was plotted with a dashed line to guide the eye.

As previously indicated, the proportional counter needed new windows. New window plates were fabricated from 0.25 inch aluminum plates that were carefully faced with a fly-cutter to produce a smooth surface finish. In previous window plate design iterations, it was found that a standard mill finish is not smooth enough to form a sealing surface with a Viton O-ring. The new plates' mounting hole pattern was simply designed to match the proportional counter body's blind tapped hole

pattern. The window cutout in the window plate, designed to be covered by the window and transmit X-rays, was centered on the proportional counter wire, where the interior electric field is most uniform, the energy resolution will be the best, and the response will be most predictable. In order to reduce systematic errors in the QE measurement due to the proportional counter and the H1RG having different active area geometries, the window cutout was sized to match the active area of the H1RG detector and approximate its square geometry with a rounded corner square. The cutout had straight edge to straight edge length l , that was easily machinable with a common $d = 0.125$ inch diameter end mill:

$$(18 \mu\text{m} \cdot 1024 \text{ pixels})^2 = 0.5265 \text{ inch}^2 \quad (4.27)$$

$$A = l^2 - [(d)^2 - \pi(d/2)^2] \quad (4.28)$$

Solving for l , the straight edge to straight edge length was 0.727 inches. A 0.0625 inch radius fillet was machined into the inside edge of the window cutout to increase the bend radius of, and reduce mechanical stresses on, the window when gas pressure inside the counter causes the window to bulge outwards during operation. A shallow (0.0625 inch) glue groove was machined into the interior surface of the window plate so that extra epoxy, used to attach the window to the window plate, would not puddle at the window's edge during curing. Detailed drawings can be found in Appendix A.1.

Moving on to the design of the window itself, the window had to be sturdy enough to withstand the 1 atmosphere (14.69 psi) of differential pressure between the inside of the counter and the chamber's vacuum space, but also as thin as possible so that it would transmit a large fraction of soft X-rays. The design iteration process was begun by building a previously tested design from the literature. It consisted of a $0.5 \mu\text{m}$ Mylar[®] film mechanically supported by a 0.001 inch thick, 0.01 inch pitch stainless steel mesh [100]. While 0.001 inch ($50 \mu\text{m}$) Mylar[®] films are extremely common as a result of their use in the food packing industry, thinner films are more difficult to purchase. I purchased 2.5, 3.5, and $6 \mu\text{m}$ films sold as X-ray fluorescence target holder films from Premier Lab supply. I purchased samples of 50 and 100 thread per inch (TPI) (0.02 inch and 0.01 inch pitch) stainless steel woven wire mesh from TWP Inc. that is sold for use as industrial filter ma-

terial. I chose Epo-tek[®] H20E silver filled, electrically conductive, low outgassing heat cure epoxy to bond the window to the window plate. Conductive epoxy was chosen to ensure good electrical contact between the window and the proportional counter body and therefore a uniform electric field inside the counter. In that vein, the inner surface of the Mylar[®] window needed to be made conductive to prevent charge accumulation and subsequent electric field distortion. A thin sputtered layer of aluminum or gold or a deposition of electroless nickel would have been ideal for meeting this requirement, but thin, metallized Mylar[®] was not commercially available and we did not have the capability to apply such a coating. The application of colloidal carbon (graphite) paint was investigated as a solution to the problem. Two types were tested: a brush-applied liquid paint, Dag[®] and an aerosol paint, Aero-Dag[®] G. The liquid paint was difficult to apply evenly, even after dilution as recommended by the manufacturer. The aerosol adhered well to the Mylar[®] and was used in the final build process. The optimal build procedure was:

1. Cut a large piece of heavy duty aluminum foil and taped a ~ 1 foot long sheet of the $6\ \mu\text{m}$ Mylar[®] to the foil sheet.
2. Applied ~ 50 very light coats of Aero-Dag[®] from a distance of ~ 15 inches to achieve the thinnest possible continuous-coverage conductive carbon layer on the Mylar[®] film. It was found that applying thick layers of the carbon paint caused it to pool up and drip very easily, resulting in uneven coverage. Coverage was verified in three ways: visible light penetration (check by eye with room lights), resistivity measurement ($\sim \text{k}\Omega$ with standard digital multimeter), and observation of static dissipation (film no longer clings to itself).
3. Surprisingly, the thin Mylar[®] was very difficult to cut with scissors. The coated Mylar[®] film was cut into 4 sections, ~ 1 inch by 2 inches each, using a new razor to cut through the Mylar[®] into the aluminum foil backing. This only worked when the angle between the knife and Mylar[®] is kept small, or else the Mylar[®] will tear. The 4 sections were used for the two active-use windows plus one spare for each.

4. According to company instructions, the H20E epoxy was prepared by pre-mixing each component individually, then mixing a minimum batch size of 3g (1.5g part A, 1.5g part B) on a piece of stainless steel foil, using stainless steel spatulas. According to the manufacturer, the epoxy can be removed by heating the epoxy to 500 °C (it will turn to ash) or soaking in a strong solvent such as dichloromethane (methylene chloride also known as Freon 30).
5. An epoxy syringe was used to fill the glue groove with mixed epoxy. The epoxy was thick and did not drip or wick at room temperature. However, its viscosity drops severely during the heat cure, enabling it to easily wick into places it should not be. Therefore, it is important to use the smallest amount necessary.
6. A scissor was used to cut \sim 1.5 inch by 1.5 inch sections of the 100 TPI stainless mesh.
7. Tweezers were used to position the mesh so that it symmetrically covered the window cutout. The 50 TPI mesh was difficult to handle because it bowed and required pre-clamping; the 100 TPI mesh did not.
8. The painted Mylar[®] sections were difficult to position on the window plate because they tended to roll up. Handling them from the edges with tweezers, the sections were positioned, carbon side up (facing the inside of the counter) in the center of the window plate.
9. In order to produce a good vacuum seal and mechanical bond around the perimeter of the window, a deformable material was needed to compress the Mylar[®]/mesh stack during the epoxy's oven cure. Polymer foams are deformable but most are made from either polystyrene or polyethylene. Polystyrene foam (Styrofoam[®]) begins to flow above 100°C and polyethylene foam melts at \sim 105°C, making them both unsuitable for this application. Silicone is a soft and strong elastomer that nominally retains its mechanical properties up to 400°F. Silicone sheet was procured and sample testing verified the material's suitability for use in the cure oven. For heat testing the sample was placed in the cure oven set at 160°C, 10 °C above the epoxy cure temperature,

for 4 hours, one hour longer than the total cure time. The material performed as expected.

10. The window plate, epoxy, mesh, painted Mylar[®], and silicone sheet stack were clamped between two aluminum plates using two C-clamps. The stack was stage cured by placing it in a room temperature oven and ramping the temperature up to 150C over the course of 3 hours. The staged cure helps to prevent the epoxy from wicking out of the glue groove by initiating a partial cure at low temperature, which raises epoxy viscosity, before the cure reaches its final high temperature.
11. Peeling open the stack revealed that the silicone cleanly peeled away from the carbon painted Mylar[®] and the bond looks good.
12. Using P-10, the proportional counter's fill gas, the windows were pressure tested by mounting them to the counter and slowly pressurizing it up to 1.5 atmospheres (22 psi) on the lab bench. During the pressure test, the window underwent a small amount of permanent deformation, forming a smooth spheroid shape.

Notable failures during the development of the working window design were the catastrophic (and loud) mechanical failure of both components in a nickel mesh and 2.5 μm Mylar[®] window and the failure of the mechanical support mesh in the nickel mesh and 6 μm Mylar[®] without an accompanying failure of the Mylar[®] layer (Figure 4.26). The tested nickel support mesh was an electro-formed 70 lines per inch grid, produced by the Buckbee-Mears company for cathode ray tubes. Also, in the 50 TPI SS mesh with 2.5 μm Mylar[®] test, the combination withstood pressure testing, as Priestly and Phelan reported, but the thin Mylar[®] was too permeable to the P-10 counter fill gas and caused the vacuum to rise to 10^{-3} mbar, which was unacceptable. Note that the final windows are not expected to have sufficient transmission to make measurements in the soft (< 1 keV) X-ray. A workable soft X-ray window could be fabricated with the 2.5 μm Mylar[®] paired with the 100 TPI stainless steel mesh. The Mylar's[®] inner surface would need to be made conductive with a thin metal film. Aluminum would be an ideal choice for the film because of its low density and low X-ray cross section.

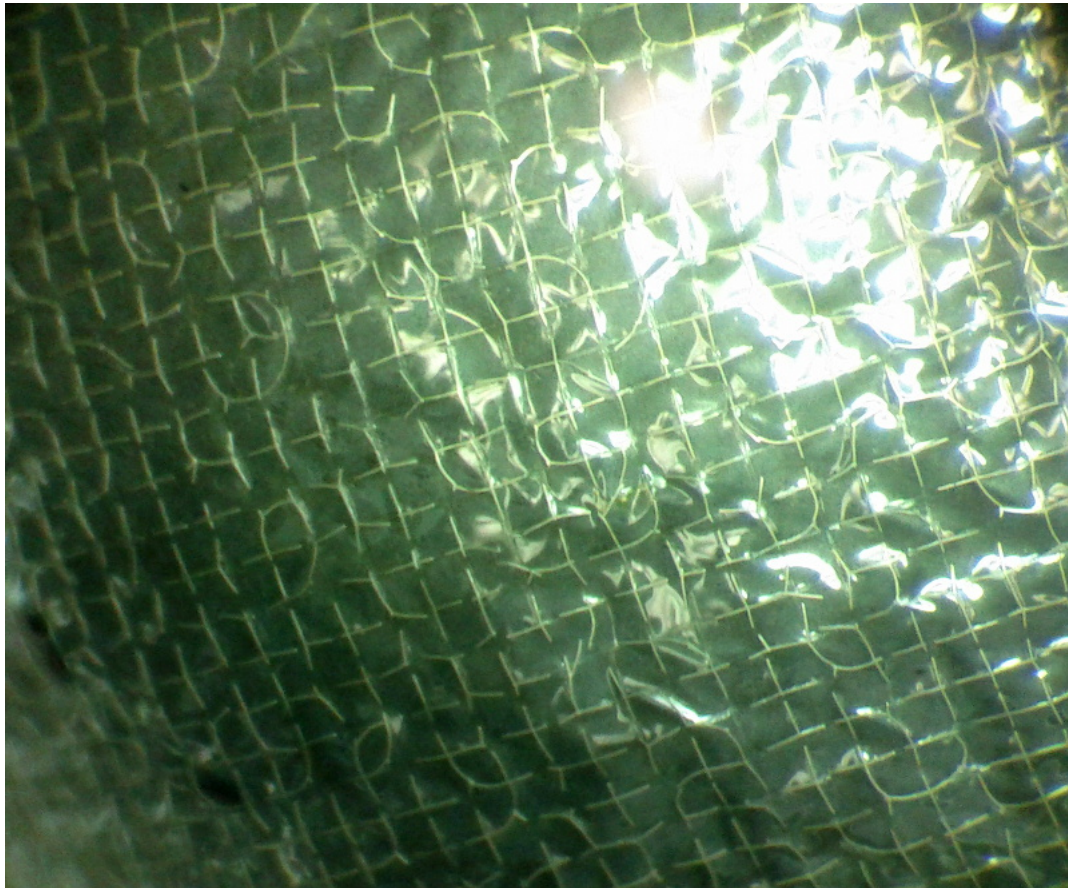


Figure 4.26: Microscope photograph of a pressure tested proportional counter window showing the mechanical failure of the electro-formed nickel mesh without a complete window blowout. Mylar[®] is a high tensile strength polymer.

The P-10 gas input and vent in the proportional counter were originally routed from 1/4 inch polyethylene tubes into the counter with NPT- Swagelok adapters. As in the previously discussed search for cryogenic tube fittings, it was found that Swagelok fittings can not produce a repeatable vacuum seal and the connectors were replaced with Ultra-torr[®] fittings. These fittings contain an O-ring that is compressed against the tube's outer surface, forming a repeatable high vacuum seal with no tools. The 1/4 inch tubes were replaced with similarly flexible, low-outgassing 1/8 inch copper tubes. The smaller tube diameter did not cause problems because the gas flow rate in this application is so low that the smaller diameter does not present a significant resistance to the gas flow. On the topic of vacuum seals, it was found that it is difficult to make a high vacuum seal with

national pipe taper (NPT) thread connections. NPT connections are an attractive design option because they're cheap to machine and easy to include in a design. However, despite a number of attempts using a varying number of PTFE tape wraps and varying amounts of torque, every NPT connection in the apparatus had to be semi-permanently sealed with Torr-Seal[®] in order to achieve a leak-free seal. Torr-Seal[®] has a consistency similar to toothpaste and it can be difficult to apply precisely without the epoxy finding its way into places that it should not be. I found it useful to mix the epoxy quickly (its viscosity increases noticeably within 10-15 minutes of mixing) and apply it with a syringe fitted with a large gauge needle.

Moving on to the absorption of X-rays in the proportional counter, a counter of this depth will allow a non-negligible fraction of incident X-rays to completely penetrate the gas and be absorbed by the chamber's back wall, without ever being detected. Since the detector had an absorption fraction less than unity, it had to be carefully calculated. The QE of the proportional counter is calculated with

$$QE(E) = T(E) \left(1 - \prod_{s=1}^S e^{-d\sigma_s(E)n_s}\right), \quad (4.29)$$

where $T(E)$ is the transmission of the window, s indexes the atomic species present in the counter gas, d is the depth of the gas, σ_s is the X-ray cross section of species s , and n_s is the number density of species s . The product of a sequence combines the transmission of each atomic species independently, and $(1 - T)$ is the total X-ray absorption fraction. Taking P-10 as an example, the counter QE equation takes the transmission through a depth of argon atoms and multiplies it by the transmission through an equivalent depth of methane, with the number densities adjusted according to the gas mixture fractions, to get the total transmission through the gas. Each atom acts like an opaque sphere with a projected area σ and the expression combines the effect of the total area presented by all of the atoms in the gas column. The total number density is solved for with the ideal gas law

$$n = \frac{P}{kT}, \quad (4.30)$$

where P is gas pressure, T is the gas temperature, and k is the Boltzmann constant. The number density of a particular atomic species, n_s , is solved for by multiplying the total number density by the fraction of atoms per gas particle, $n_s = n f_s$. P-10 gas is nominally 90% argon 10% methane (CH_4) by volume, which makes the number of atoms per gas particle 0.9, 0.1, and 0.4, for argon, carbon, and hydrogen, respectively. This notation accounts for varying gas mixtures and gas molecule composition at the same time. An equivalent method, used for the sake of brevity in the code, is to calculate an effective cross section,

$$\sigma = \sum_{s=1}^S \sigma_s f_s, \quad (4.31)$$

and use that to calculate the QE with

$$QE(E) = T(E)e^{-d\sigma(E)n}. \quad (4.32)$$

The X-ray cross section values were taken from Henke *et al.* [76], which is currently the standard source for elemental cross sections in the range of 10-30,000 eV. A package of IDL procedures and functions was written to perform these calculations for causal estimates, but, more importantly, to seamlessly perform the same calculations in the Monte Carlo error simulations that will be presented later in this chapter. The package is fully documented in Appendix C. The main components of the package are `muca1.pro`, which retrieves elemental cross sections from McMaster [101], `sb_henke.pro`, which retrieves elemental cross sections from Henke [76], and `filter_trans.pro/gas_trans.pro`, which calculate the transmission of a filter or gas volume using either the Henke or McMaster cross sections. Figure 4.27 shows the validation of the IDL package with the Lawrence Berkeley National Lab (LBNL) Center for X-ray Optics (http://henke.lbl.gov/optical_constants/) and National Institute for Standards and Technology (NIST) XCOM (<http://www.nist.gov/pml/data/xcom/index.cfm>) web applets. The discrepancy between our code and the LBNL code is negligible at the energies of our measurement, however we cannot explain the discrepancy between our cross sections and the NIST numbers.

Estimating the remaining parameters in the gas absorption expression amounts

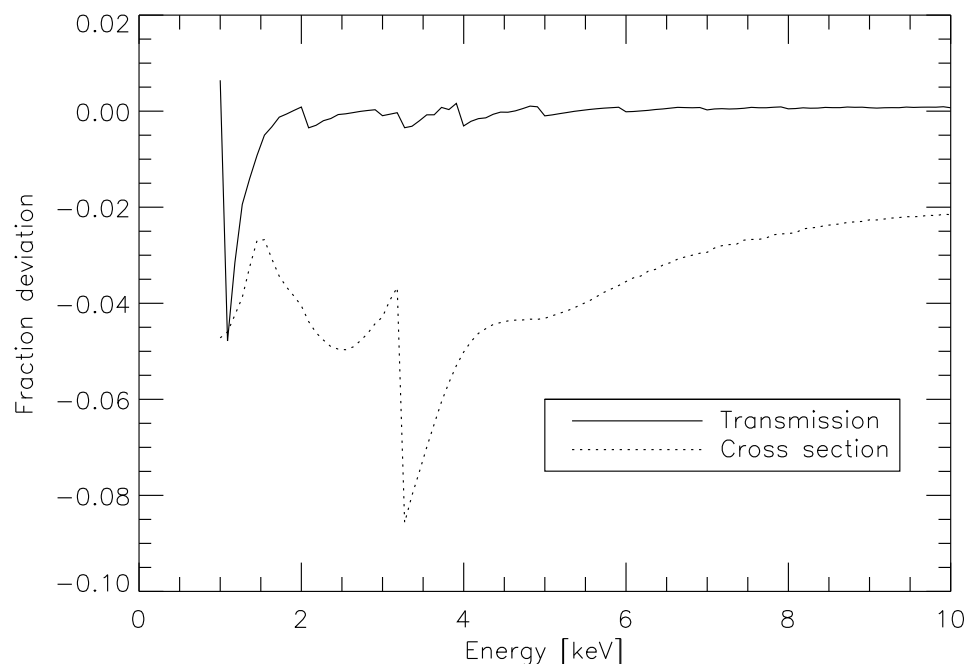


Figure 4.27: Comparing the output of our `sb_henke.pro` procedure, which accesses the Henke X-ray cross section database, to the photo-electric only X-ray cross sections reported in the NIST XCOM database. Over-plotted is a comparison between the gas transmission output value of our `gas_trans.pro` procedure and the LBNL gas transmission calculator for a 5.3975 cm thick section of $T = 291$ K, $P = 760$ torr, P-10 gas. Fractional deviation was calculated as the quantity of our value minus the external value divide by our value.

to knowing the number of absorbers present inside the proportional counter. Assayed P-10 was purchased and used for all reported data acquisition. The gas was certified to be $10.5 \pm 0.1\%$ methane by volume. Uncertified gas cylinders can vary by up to a few percent in the mixture composition, which will significantly alter the absorption fraction of the gas since argon and methane have different cross section values. The temperature of the counter gas was estimated before each data run, using the same platinum RTDs used to measure the detector and dewar temperature. These sensors are certified to have an absolute error of ± 1.7 K at 150 K according to the IEC-751 standard calibration. The pressure of the gas inside the proportional counter was measured before and after each data run using a Coastal Environmental Systems PDB-1 barometer borrowed from the local NOAA office.

Measuring the pressure of the gas in the counter is simple if the counter is operated with no gas flow. With the barometer connected to the gas system, the counter is filled, sealed off, and pressure measurements are taken while data are acquired. Despite this method's simplicity, I chose to run the counter in flow mode. Without gas flow, the fill gas mixture components will permeate the window at different rates, altering the gas composition, and thus the counter's QE, as a function of time. Also, outgassing from the counter interior and atmospheric gas contamination will accumulate and potentially change the counter's energy resolution over the course of an observation. In order to measure the pressure inside the chamber while gas was flowing, the length of the P-10 fill tube, d_1 , and vent tube, d_2 , were measured to be 251.0 cm and 207.1 cm, respectively. The pressure at the vent (room pressure, P_r) and at the fill line, P_l , were measured at the beginning and end of each data acquisition run. Assuming low-velocity flow, the pressure drop in a long narrow tube with fluid flowing through it scales linearly with the length of the tube. Accordingly, the pressure in the proportional counter was calculated with

$$P = P_l - (P_l - P_r) \frac{d_1}{d_1 + d_2}. \quad (4.33)$$

In addition to the non-unity gas absorption affecting the proportional counter QE, the window will transmit a non-unity fraction, $T(E)$, of incident X-ray photons. The window Mylar[®] is 6 μm thick, the Aero-Dag carbon paint forms an 8 μm film according to the manufacturer, and the woven mesh is 100 TPI 0.001inch stainless steel. While these parameters could be used to calculate the window transmission with reasonable precision, since the transmission was a measurable quantity, it was measured. The windows were designed so that they could be stacked on top of one another while attached to the proportional counter. While stacked, the two windows are separated by a set of stainless steel washers placed between the plates at each mounting screw. This prevents the top surface of the bottom window from contacting and marring the bottom surface of the top window plate, where the window has been epoxied. If all six screws or all six washers are not used, it has been found that the window plate will not seal. Calibration data were taken with window #1 attached to the counter, then with window #2 stacked

on top of window #1. For the observed count rates, C , $(C_{1\&2})/C_1 = T_2$, where T_2 is the transmission of window #2. Since transmission is a function of energy this calibration procedure has to be performed once for every new source used in the chamber. While this process may appear excessively time consuming, consider the uncertainties in estimating the effective thickness of a woven grid and a stack of thin films bulging under pressure. Additionally, for solids such as the window materials, X-ray transmission can be very difficult to predict near absorption edges due to X-ray absorption fine structure.

The double window calibration method is subject to error due to misalignment of the window stack. If the misalignment error were significant, strategies to precisely locate the plates with respect to one another could be considered. To place a rough upper limit on the misalignment error, I assume that all misalignment occurs due to the mounting bolts being off-center with respect to their slightly oversized mounting holes and that the plates remain parallel. Given that a 4-40 screw has a 0.112 inch OD and assuming that the holes have been reamed to their correct 0.116 inch specification, the bolt-hole error circle has a radius of $r = 0.002$ inches. The maximum decrease in total area occurs when the windows are maximally misaligned by $r/\sqrt{2}$ in the horizontal and vertical directions. Assuming, for simplicity, that the windows cutouts are squares with edge length $l = 0.727$, then the misaligned window stack will have $(l - r/\sqrt{2})^2/0.7279^2 = 99.6\%$ the open area of a perfectly aligned stack. This is small enough to be considered negligible.

During window construction, no effort was intentionally made to align the stainless mesh support grids with respect to the window plates. This ensures that the two mesh grids do not, by chance, during some assemblies of the window stack, accidentally align such that they overlap. Accidental alignment of this variety would skew the measured transmission too high during window calibration.

4.3.5 Detector Alignment

The solid angles subtended by the active areas of the proportional counter and the H1RG were designed to be equal. Alignment of the detectors and the measurement of their true positions in the caterpillar was performed with a Leica Disto D210XT handheld laser rangefinder. The rangefinder is designed to measure the distance

to a laser-illuminated region on an optically thick surface more than 5 cm and less than and 70 m from the device. Typically, it is used for building construction layout and not precision metrology, but the device's ± 1.5 mm precision was sufficient for the task of positioning detectors in the caterpillar. The rangefinder is built with flat surfaces on the chassis that are normal and parallel to the beam. Using these surfaces, the rangefinder was clamped to the proportional counter and the H1RG mounts. The observed position of the beam was then used to adjust the detectors' positions such that their center normals were in line with the X-ray source at the opposite end of the chamber. It is expected that with this method, the detectors were aligned to roughly within the 0.5 cm diameter of the rangefinder's laser beam, or 2 mrad at the 255 cm source-detector distance.

Next, the caterpillar's source flange was removed, the rangefinder mounted at the source position, and the distances to three points of known location on the front surface of each detector were ranged. These three ranging aim-points were arranged to form the vertices of a right triangle, making it more convenient to use their ranged distance to calculate both the source-detector distances and the angular deviation of each detector's central normal from alignment with the source. To increase the sensitivity of the angular measurement, the three points were spread out on each detector's respective surface to make the largest triangles possible. Table 4.4 summarizes the ranging results.

Coordinates (x, y) [inches]	Ranged distance [cm]
H1RG	
(0.00, 0.00)	254.8
(1.10, 0.00)	254.8
(0.00, 1.40)	254.8
Proportional Counter	
(0.00, 0.00)	256.9
(2.80, 0.00)	256.8
(0.00, 5.50)	256.9

Table 4.4: Alignment rangefinder data for both the H1RG and proportional counter. The rangefinder aim-point coordinates are in the planes of the detectors. The values listed under *Coordinates* will later be referred to as d_1 and d_2 and those under *Ranged distance* as l_1 , l_2 , and l_3 .

The three aim-points were used to calculate the angle, θ , between each detector's center surface normal, \vec{d}_n , and the vector that points from the source to the detector's center, \vec{l}_c . Reference Figure 4.28 for a definition of the angles and vectors.

$$l_{1,2,3} = l_c - d_{c1,2,3} \quad (4.34)$$

$$\theta = \sin^{-1} \left(\frac{l_{cy}^2 - l_{cx}^2}{\sqrt{l_{cx}^2 + l_{cy}^2 + l_{cz}^2}} \right) \quad (4.35)$$

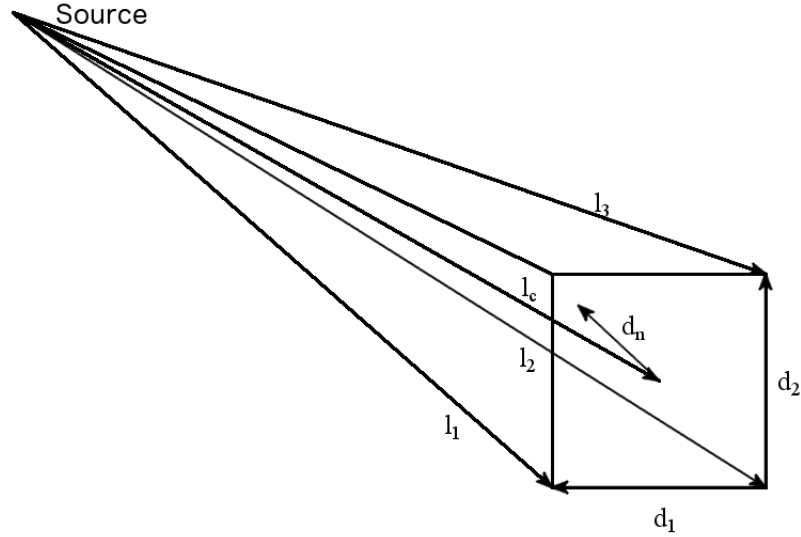


Figure 4.28: A vector diagram of the detector alignment parameters. The vectors \vec{l}_1, \vec{l}_2 , and \vec{l}_3 connect the source and the three range points on the detector. Vectors \vec{d}_1 and \vec{d}_2 connect the three range points on the detector and span the detector plane. The vector \vec{d}_n is the detector surface normal and \vec{l}_c connects the source and the detector center point.

4.4 Experimental Result

4.4.1 Window Calibration Result

The windows were calibrated with ^{55}Fe data acquired on December 7-8, 2012. The data are summarized in Table 4.5. Proportional counter X-ray energy spec-

tra were reduced by subtracting background spectra that were scaled by the ratio of data integration to background integration time. The total number of counts in the line was determined by summing all channel data inside the region where the line flux was distinctly separated from background noise. Measuring the combined transmission of windows #1 and #2, there were 560742 ± 755 background subtracted counts between channel 44 and channel 199 of the PC_2012-12-07_TIME_17_40.Spe and PC_2012-12-07_TIME_19_08.Spe calibration and background run. Given the data integration time of 4247 seconds, this yielded a count rate of 132.0 ± 0.18 counts per second. Measuring the transmission of window #2, there were 530789 ± 734 background subtracted counts between channel 49 and channel 207 of the PC_2012-12-08_TIME_22_28.Spe and PC_2012-12-08_TIME_21_33.Spe calibration and background run. Given the data integration time of 3210 seconds, this yielded a count rate of 165.35 ± 0.23 counts per second. Taking the ratio of these two count rates, window #1 was found to transmit $79.8 \pm 0.24\%$ of the ^{55}Fe energy X-rays incident on its surface.

Since modeling predicts that the window transmission is not appreciably different for the Mn $K\alpha$ and $K\beta$ line energies, this transmission value was assumed for both energies. Most of the window attenuation comes from the steel mesh, which is almost entirely opaque to X-rays. A back-of-the-envelope estimate for the 0.001 inch wire, 100 TPI mesh's open area yields $\left(\frac{1/100-0.001}{1/100}\right)^2 = 81\%$. The combined transmission of 6 μm of Mylar[®] on top of 8 μm of colloidal graphite at 5.89 and 6.49 keV is 96.6% and 97.5%, which, when weighted with the source line ratio and multiplied by the mesh open area, yields an expected transmission of 78.3%. The fact that this rough calculation leads to a value that is very close to our measured value bolsters our confidence in the measurement.

4.4.2 QE Data Acquisition

The QE measurement data were acquired for H1RG-167 over the course of an afternoon on December 17, 2012. This detector was chosen because it is representative of the lot of detectors, having standard read noise and dark current characteristics. Its half-aluminized OBF allowed for the opportunity to probe the filter's attenuation more directly than with QE measurements alone. In all of these data, the

Name	Real [s]	Live [s]	Dead %	Type	SCA [Counts]
Window 1&2					
PC_2012-12-07_TIME_15_30.Spe	3649	3660	0.30	⁵⁵ Fe	488,051
PC_2012-12-07_TIME_16_33.Spe	3660	3660	0.00	b.g.	6,348
PC_2012-12-07_TIME_17_40.Spe	4247	4260	0.30	⁵⁵ Fe	568,234
PC_2012-12-07_TIME_19_08.Spe	3779	3780	0.02	b.g.	6,255
Window 2					
PC_2012-12-08_TIME_20_28.Spe	1402	1407	0.35	⁵⁵ Fe	n.d.
PC_2012-12-08_TIME_20_54.Spe	744	746	0.26	⁵⁵ Fe	n.d.
PC_2012-12-08_TIME_21_33.Spe	3210	3222	0.37	⁵⁵ Fe	n.d.
PC_2012-12-08_TIME_22_28.Spe	4712	4713	0.02	b.g.	n.d.

Table 4.5: Summary of data taken to calibrate the proportional counter window. The *Real* and *Live* times represent the data-run’s stopwatch integration time and real time minus dead time, respectively. *Dead* is the dead time percent, $(\text{real time} - \text{live time})/(\text{real time})$, and is used to estimate the accuracy of the MCA’s live time estimate. For dead time percentages greater than 40%, the live time will be overestimated. *Type* indicates whether an X-ray source was exposed or the data are background (b.g.). *SCA* indicates the counts recorded by the SCA. No data (n.d.) were acquired with the SCA for the window #2 calibration because the MCA’s performance characteristics had already been verified. During the window #1 & #2 data acquisition, window #2 was mounted directly to the proportional counter, as in the window #2 acquisition. This was done to avoid a potential shift in the proportional counter’s response due to sealing it with different windows in the two sets of calibration runs.

^{55}Fe source was used to generate X-rays because of its stability and operational simplicity. Throughout the data acquisition, the HIRG was stabilized at 150 K and the proportional counter was sealed with window #1.

Three sets of data were taken, two sets with X-rays with one set with background in between the two X-ray data sets. Proportional counter and HIRG data were acquired simultaneously. Details of the data acquisition and results of the analysis (description to follow) are shown in Table 4.6 and 4.7.

Name	Type	Total	K α	K β
2012-12-17_TIME_17_03.fits	⁵⁵ Fe	1,170,712	966,700	158,746
2012-12-17_TIME_19_01.fits	b.g.	2,494	-	-
2012-12-17_TIME_20_39.fits	⁵⁵ Fe	1,171,860	970,745	154,620

Table 4.6: A summary of HIRG quantum efficiency data. As before *Type* identifies whether the X-ray source was exposed or the data are background (b.g.). *Total* is the unfiltered sum of all counts in the data set. *K α* and *K β* are the numerically integrated number of counts in the multi-gaussian least-squares fit of each respective line. For this table, the data sets were fit individually. The energy spectra are shown and the integration described in §4.4.3.

Name	Type	Live [s]	Dead [%]	SCA [c]·10 ³	MCA Rate [c s ⁻¹]	<i>P_{i,s}</i> [mbar]	<i>P_{i,e}</i> [mbar]	<i>P_r</i> [mbar]
PC_2012-12-17_TIME_17_03.Spe	⁵⁵ Fe	6815	0.37	163.8 ± 0.2	163.8±0.2	1,005.23	1,004.26	960.24
PC_2012-12-17_TIME_19_01.Spe	b.g.	3210	0.02	9.42±0.1	-	1,004.12	1,003.03	959.19
PC_2012-12-17_TIME_20_39.Spe	⁵⁵ Fe	10223	0.36	1,691±1	163.6±0.1	1,003.17	1,000.95	957.10

Table 4.7: A summary of proportional counter quantum efficiency data. As before, *Live*, *Dead*, and *SCA* are the live time, dead time percent, and the SCA counts recorded during the data run, respectively. *MCA Rate* is the background subtracted rate calculated for each run. The pressures *P_{i,s}*, *P_{i,e}*, and *P_r* represent the P-10 input line pressure at the start and end of the run and the ambient room pressure, respectively. Proportional counter energy spectra are shown and the emission line bounding described in §4.4.4

4.4.3 H1RG QE Data Reduction

The H1RG image data were acquired, archived, and reduced with the same IDL procedures discussed earlier in §3.3. During the creation of the event list data products, a primary event threshold of 500 DN was used to screen the images for potential X-ray events. This threshold is justified by the shape of the center pixel value distribution shown in Figure 4.29. The distribution of center pixel values determines the optimal primary threshold because it is this value that determines whether a pixel will be considered for event detection. The distribution was made by processing two ramps from the 2012-12-17_TIME_19_01 X-ray data set and two ramps from the 2012-12-17_TIME_17_03 background data set with `make_evtlist.pro`. The primary event detection threshold was set unusually low, at 40 DN, which is close to the 1σ noise floor. The center pixel value of each event was then used to calculate the plotted distributions. The figure shows that there is a clear boundary between the noise peak below 500 DN and the X-rays that begin to appear at 500 DN, indicating that the 500 DN primary event threshold is not filtering out a significant fraction of genuine X-ray events. The secondary threshold was set at the image median absolute deviation (39 DN) to balance photo-charge collection with unwanted noise pickup in each event. The count rate is unaffected by the choice of secondary threshold.

Figure 4.30 shows a spectrum of all X-rays detected in the summed 2012-12-17_TIME_19_01 and 2012-12-17_TIME_20_39 data sets with the insignificant 2012-12-17_TIME_17_03 background over-plotted. Interesting features to note in this spectrum are the large Mn $K\alpha$ and $K\beta$ peaks located at 2600 and 2800 DN respectively. The small peak at 1600 DN is the silicon escape peak. This signal is produced when the fluorescent silicon X-rays that are emitted by the de-excitation of the first silicon atoms to absorb and be ionized by incident X-rays escape the detector material. The silicon escape peak location $L_{\text{Si } esc.}$, compared to the location of the main peak associated with it L_{main} , will be $L_{main} - L_{\text{Si}}$, where L_{Si} is the location of the silicon $K\alpha$ emission line. In this case, the escape peak has components from both the Mn $K\alpha$ and the $K\beta$ peaks, but they are not resolvable. The peak at 5200 DN is a pileup peak where two $K\alpha/\beta$ X-rays were absorbed by the same pixel during a read-frame. The high-energy continuum between the $K\alpha/\beta$ peaks is likely due to pileup near misses, where two events are located close enough

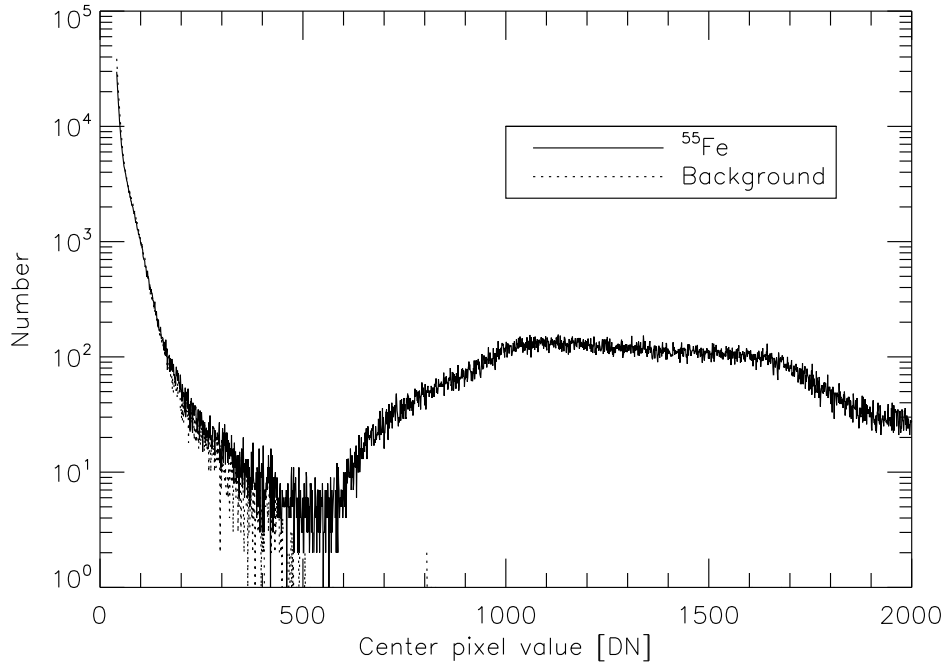


Figure 4.29: Pixel value distribution of the center (brightest) pixel of events detected with a primary threshold of 40 DN. With the primary threshold set this low, the algorithm will detect both noise (the large low level peak in the distribution) and true X-rays (the large, wide peak above 500 DN). The total distribution shows that the noise contribution cuts off and the X-ray distribution begins at 500 DN. The over-plotted background spectrum, which was produced with the same data reduction parameters, disappears above 500 DN indicating that the large distribution above 500 DN is X-rays.

that their signals contaminate one another. The observed rise in the continuum towards lower energy can be explained by the increased chance of two events landing near one another at larger separation distances. These large-distance near miss events exhibit lower total energy because the increased distance caused less signal to be summed with the 3×3 event detection region. The low-energy continuum below the $K\alpha/\beta$ peaks is the result of incomplete signal summing due to an event's extension beyond the 3×3 detection region. While this spectrum looks messy, all features outside of the main peaks total less than 3% of total events.

The number of events recorded in the H1RG spectrum will be defined in two ways. First, the *Total* number of events, listed in Table 4.6, is the number of events

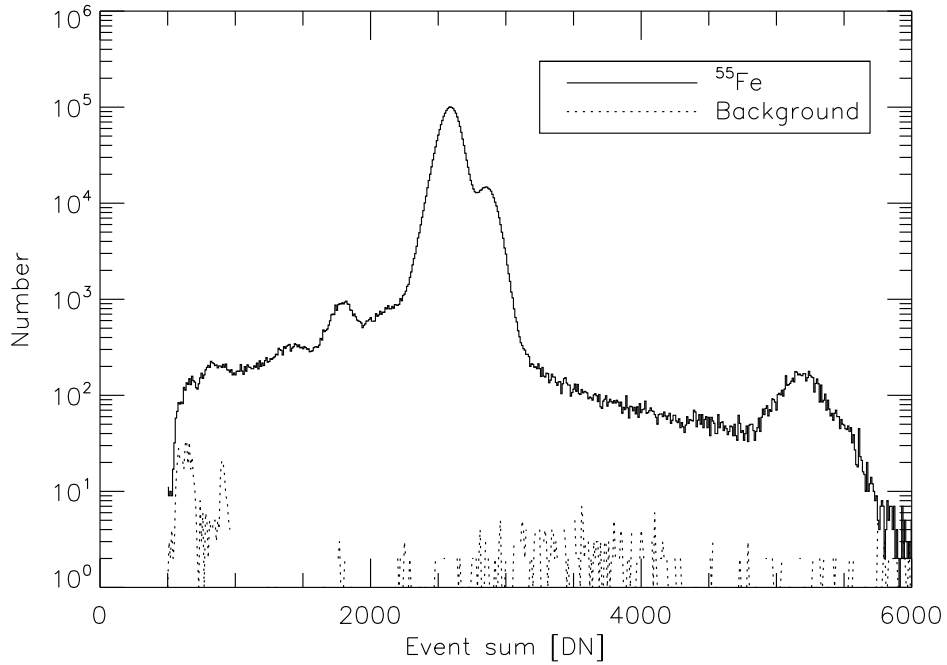


Figure 4.30: Energy spectrum of the total charge in events, summed using a 39 DN secondary threshold. The ^{55}Fe spectrum is a sum of the 2012-12-17_TIME_19_01 and 2012-12-17_TIME_20_39 data sets. The background data is from the 2012-12-17_TIME_20_39 data set.

with a summed signal greater than 750 and less than 6000 DN. This number will be used to calculate an average QE, a number that can be used to estimate detector layer thicknesses because it characterizes the detector's ability to simply detect a 5.89/6.49 keV photon. Second, the $K\alpha/\beta$ peaks were fit with a phenomenological peak function so that the blurry superposed peaks could be disentangled from one another and a QE calculated at both energies. The peak function, `multi_gauss3.pro` enables the creation of an arbitrary number of peaks, where each peak is the sum of an arbitrary number of Gaussian or skew-normal function components. After the first component, each subsequent component's amplitude and width are defined as a fraction of the first peak's amplitude and width, and the mean positions are defined absolutely with respect to the first peak's mean position. In the case of the ^{55}Fe spectrum, each peak was fit with a standard 3-parameter Gaussian (amplitude, mean, and width) plus a wider 4-parameter skew-normal function that helps account for the asymmetry and heavy tails observed in the

data. Least-squares fitting was performed with Craig Markwardt's excellent IDL package, MPFITFUN [102]. In the fit, the second component's parameters were tied together so that for both peaks, the smaller and wider skew-normal component was the same relative to the first peak, giving both peaks the same general shape. The result of numerically integrating these peaks individually is shown in Table 4.6 under $K\alpha$ and $K\beta$. When the two X-ray data sets were combined, there were 1,934,824 events in the $K\alpha$ peak and 317,549 events in the $K\beta$ peak. Figure 4.31 shows the result of the fit, which yielded a reduced chi-squared, $\chi_r^2 = 3.21$.

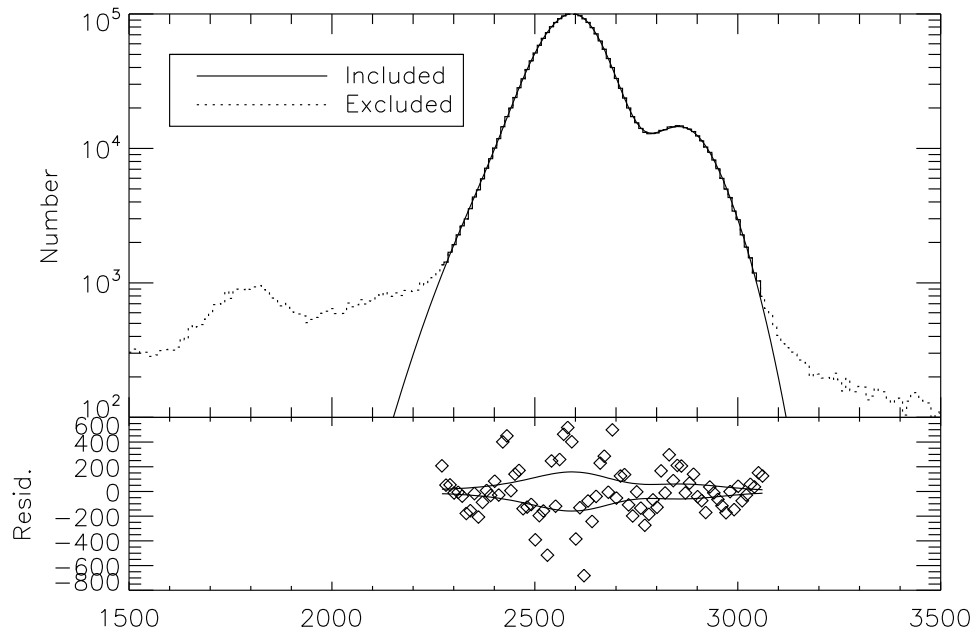


Figure 4.31: The top panel shows the combined H1RG data set. Data excluded from the fit are plotted with a dotted line and the included data are plotted with a solid line. The fit is over-plotted with a smooth, solid line. In the bottom panel, the fit residuals are shown, with a \sqrt{N} error contour over-plotted.

4.4.4 Proportional Counter Data Reduction

Following QE data acquisition, the proportional counter data were archived as spectra in ASCII text files so that they could be easily read by programs other than the MCA software that created them. The first step in turning the raw data into

a spectrum was to read the data and relevant parameters into memory. This was accomplished by the IDL procedure `pc_read_spectrum.pro`. Given a filename, the procedure will read raw spectral data (dead time corrected counts), live integration time, real integration time, and the MCA channel range into memory. Next, using the IDL procedure `pc_extract_counts.pro`, the scaled background spectrum was subtracted from the X-ray spectra. The scaling factor is the ratio of the live times. In the same procedure, a channel region that bounds the X-ray lines was chosen such that all counts in the line were included, but added noise was excluded. All background subtracted counts within the region were then summed, divided by the live time, and outputted as the count rate. The uncertainty in the count rate was calculated by first adding, in quadrature, the counting uncertainties from each channel of the X-ray spectrum to the scaled uncertainties from each channel of the background spectrum. The background subtracted uncertainties from all channels in the user-chosen bounding region were then summed in quadrature and divided by the live time to yield the uncertainty in the count rate.

In the `PC_2012-12-17_TIME_17_03/PC_2012-12-17_TIME_19_01` calibration and background data set, there were $1,116,418 \pm 1,064$ background subtracted counts between channel 41 and channel 212 of the spectrum. Given the data integration time of 6,815 seconds, this yielded a count rate of 163.8 ± 0.2 counts per second. In the `PC_2012-12-17_TIME_20_39/PC_2012-12-17_TIME_19_01` calibration and background data set, there were $1,673,336 \pm 1,303$ background subtracted counts between channel 43 and channel 215 of the spectrum. Given the data integration time of 10,223 seconds, this yields a count rate of 163.6 ± 0.1 counts per second. Figure 4.32 shows the two background-subtracted proportional counter spectra. Since there are no artifacts or a significant gain or count rate shift between the two spectra, the two were combined to increase signal to noise. To account for the barometric pressure change that occurred as the data were taken, the counter pressure before and after each run was averaged and taken in ratio, P_{c1}/P_{c2} , to yield a correction factor of 1.0026 for the second count rate. The combined count rate was $163.9 \pm 0.1 \text{ c s}^{-1}$.

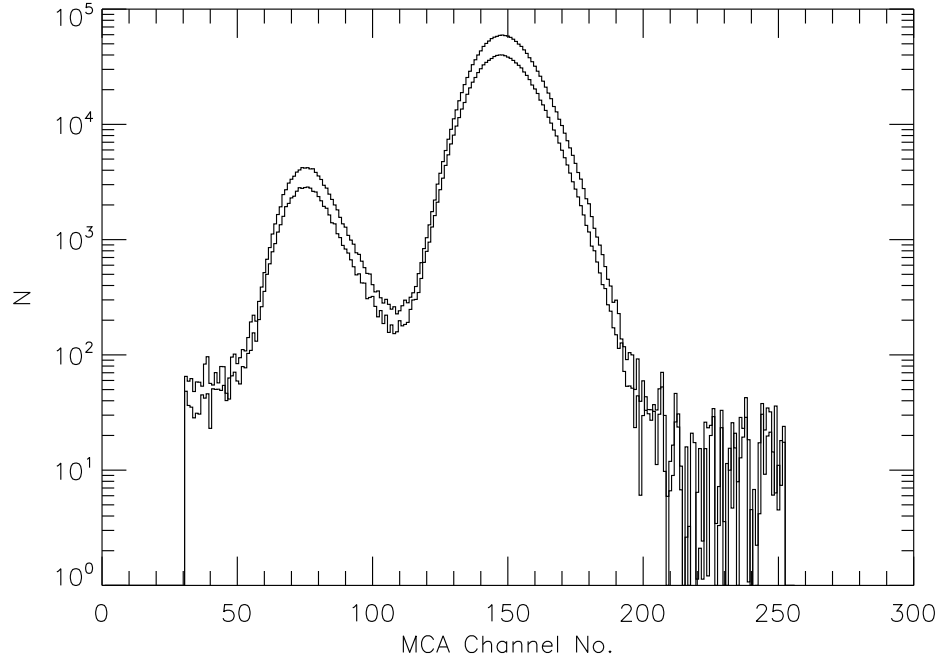


Figure 4.32: The two background subtracted proportional counter spectra acquired during QE data acquisition. The dominant features of the spectra are the large, combined ^{55}Mn $K\alpha/K\beta$ emission peak and the smaller argon escape peak.

4.4.5 QE Result

Given that both detectors are exposed to the same source, the H1RG's QE at a particular emission line energy was calculated by equating the source luminosity equations for each detector,

$$C_{\text{H1RG}}(E) \frac{4\pi}{\Omega_{\text{H1RG}}} \text{QE}_{\text{H1RG}}(E) = C_{\text{PC}}(E) \frac{4\pi}{\Omega_{\text{PC}}} \text{QE}_{\text{PC}}(E) \quad (4.36)$$

$$\text{QE}_{\text{H1RG}}(E) = \frac{\Omega_{\text{PC}}}{\Omega_{\text{H1RG}}} \frac{C_{\text{H1RG}}(E)}{C_{\text{PC}}(E)} \text{QE}_{\text{PC}}(E), \quad (4.37)$$

where Ω is the energy independent solid angle of the detector when viewed from the X-ray source, $C(E)$ is the measured count rate in an emission line, and $\text{QE}_{\text{PC}}(E)$ is the proportional counter QE, which was calculated in Equation 4.29. In the above equations, since the detector size is much smaller than the source-detector distance, solid angle has been approximated with $\Omega \approx \frac{A}{4\pi d^2}$. The QE of the proportional

counter is the product of the window transmission and the gas absorption. As discussed in §4.4.1, the window transmission is assumed to be the same for both ^{55}Fe energies. The energy dependent gas absorption is calculated following the method from §4.3.4.

In the above paragraph, note the careful use of language in the description of $C(E)$. These energy dependent count rate terms are not the same as the count rate as a function of energy, otherwise known as an energy spectrum. Instead it is the count rate in a line of energy E . To make a general argument where source emission is allowed to be broadband and $C(E)$ is treated as an energy spectrum, the detector's energy dependent response function would be included. That is an endeavor beyond the scope of this project and this analysis will only consider narrow-line emission. In the case of the $K\alpha$ line, the QE equation becomes

$$\text{QE}_{\text{H1RG } K\alpha} = \frac{\Omega_{\text{PC}}}{\Omega_{\text{H1RG}}} \frac{C_{\text{H1RG } K\alpha}}{C_{\text{PC } K\alpha}} \text{QE}_{\text{PC } K\alpha}. \quad (4.38)$$

However, a complication arises here in that we cannot directly measure $C_{\text{PC } K\alpha}$ since the proportional counter does not have sufficient energy resolution to distinguish between the source's two emission lines. We can only measure $C_{\text{PCFe}} = C_{\text{PC } K\alpha} + C_{\text{PC } K\beta}$, the count rate due to the two combined lines of the source. To solve for the proportional counter count rate in each line, we use the calculated line ratio from §4.3.3, to solve

$$\frac{\text{QE}_{\text{PC } K\beta}}{\text{QE}_{\text{PC } K\alpha}} \frac{C_{\text{PC } K\alpha}}{C_{\text{PC } K\beta}} = 6.79. \quad (4.39)$$

Solving the above equation for $C_{\text{PC } K\alpha}$ and substituting into Equation 4.38, the QE equation then becomes

$$\text{QE}_{\text{H1RG } K\alpha} = \frac{\Omega_{\text{PC}}}{\Omega_{\text{H1RG}}} \frac{C_{\text{H1RG } K\alpha}}{C_{\text{PCFe}} \left(1 + \frac{\text{QE}_{\text{PC } K\beta}}{6.79 \text{QE}_{\text{PC } K\alpha}}\right)^{-1}} \text{QE}_{\text{PC } K\alpha} \quad (4.40)$$

and the equation for $\text{QE}_{\text{H1RG } K\beta}$ similarly becomes

$$\text{QE}_{\text{H1RG } K\beta} = \frac{\Omega_{\text{PC}}}{\Omega_{\text{H1RG}}} \frac{C_{\text{H1RG } K\beta}}{C_{\text{PCFe}} \left(1 + \frac{6.79 \text{QE}_{\text{PC } K\alpha}}{\text{QE}_{\text{PC } K\beta}}\right)^{-1}} \text{QE}_{\text{PC } K\beta}. \quad (4.41)$$

The data show that, for events detected in the emission lines, $QE_{\text{H1RG } K\alpha} = 0.91 \pm 0.05$ and $QE_{\text{H1RG } K\beta} = 1.0 \pm 0.05$. The error analysis that lead to the quoted uncertainties will be explained in the following section. Such quantum efficiencies represent the probability that an incident X-ray of a certain energy will be detected in its line profile, as defined by the above fitting process, of the H1RG spectrum. These are useful quantities to know when considering the detector's spectroscopic performance in a science application. Note that it is not possible to use these QEs to meaningfully probe layer thicknesses in the detector itself. To do this would require a physical detector model that accounts for the complex factors like IPC, charge diffusion, and lattice traps, which remove signal from an event, or near-miss pileups which can add charge to it. Calculation of the emission line QEs incurs a systematic error due to the discrepancy between the fit emission line model and the data. Note that these QEs do not include events that are piled-up, in the escape peak, or poorly resolved.

To address this shortcoming of the emission line QE analysis, I calculated the average QE for the ^{55}Fe source using the total count rates from both detectors and solving for the H1RG's QE,

$$QE_{\text{H1RG Fe}} = \frac{\Omega_{\text{PC}}}{\Omega_{\text{H1RG}}} \frac{C_{\text{H1RG Fe}}}{C_{\text{PC Fe}}} QE_{\text{PC Fe}}, \quad (4.42)$$

where a weighted average of the proportional counter QE is calculated with

$$QE_{\text{PC Fe}} = QE_{\text{PC } K\alpha} \frac{6.79}{7.79} + QE_{\text{PC } K\beta} \frac{1}{7.79}. \quad (4.43)$$

Here, $C_{\text{PC Fe}}$ and $QE_{\text{H1RG Fe}}$ are the total count rates integrated over the entire spectrum of the respective detectors, while exposed to the iron source. The data show that the source-averaged QE is $QE_{\text{H1RG Fe}} = 0.97 \pm 0.05$. As with the emission line QEs, the error analysis that led to the quoted uncertainty will be explained in the next section. Unlike the emission line QEs, the averaged QE number can be meaningfully compared with the weighted average values of a detector QE model at 5.89 and 6.49 keV because it includes all detected X-rays. This comparison will be made in §4.5. Note that the average QE number is not simply an average of the two emission line QEs weighted with the line ratio. Since piled-up, poorly resolved, and escape peak events are included in the average QE, its value is a few

percent larger than the emission line QE weighted average.

4.4.6 QE Error Analysis

Since the detector QE is a complicated function of many parameters, a Monte Carlo simulation was designed to estimate the uncertainty in its measurement. A generalized Monte Carlo simulator, `sim_error.pro`, was written in IDL for this project. As input, the procedure takes nominal parameter values, parameter uncertainties, and a function that runs these values through the QE equations above (`h1rg_qe.pro`), and calculates the probability distribution function of the function's output. Table 4.8 lists all of the measured parameters that enter into the QE calculation and their estimated 1σ uncertainties. In the simulation, all input uncertainties are assumed to be normally distributed.

Parameter	Variable name	Value	Unit	Uncertainty (1σ)	Description
PC range point coord.	pc_xd	7.11	cm	0.025	RF pointing
PC range point coord.	pc_yd	13.97	cm	0.025	RF pointing
H1RG range point coord.	h1rg_xd	2.79	cm	0.025	RF pointing
H1RG range point coord.	h1rg_yd	3.55	cm	0.025	RF pointing
PC range dist.	pc_l1	256.8	cm	0.1	RF ranging
PC range dist.	pc_l2	256.8	cm	0.1	RF ranging
PC range dist.	pc_l3	256.9	cm	0.1	RF ranging
H1RG range dist.	h1rg_l1	254.8	cm	0.1	RF ranging
H1RG range dist.	h1rg_l2	254.8	cm	0.1	RF ranging
H1RG range dist.	h1rg_l3	254.8	cm	0.1	RF ranging
H1RG window width	h1rg_xwinsize	1.8432	cm	10^{-4}	μ -machining
H1RG window height	h1rg_ywinsize	1.8432	cm	10^{-4}	μ -machining
PC window width	pc_xwinsize	1.849	cm	0.0025	Machining
PC window height	pc_ywinsize	1.849	cm	0.0025	Machining
P-10 depth	gas_depth	5.398	cm	0.025	Machining
P-10 temperature	gas_t	291	K	1.7	IEC-751
P-10 pressure	gas_p	980.63	mbar	0.01	PDB-1 limit
P-10 gas fraction	gas_fraction	[0.895, 0.105, 0.42]	particle ⁻¹	[0.001, 0.001, 0.001]	Gas assay

Table 4.8: (Continued on the following page.)

Table 4.8: Summarized metrology of the measured parameters that enter into the H1RG QE calculation and their associated 1σ uncertainties. When applicable, the method of measurement and/or source of uncertainty is listed. *RF* abbreviates rangefinder. The gas fraction unit of particle^{-1} represents the fraction of a particular atomic species per gas particle in the mixture.

Error distributions were generated for the three measured QE values and are shown in Figure 4.33. The simulations show that, for events detected in the emission lines, $\text{QE}_{\text{H1RG K}\alpha} = 0.91 \pm 0.05$ and $\text{QE}_{\text{H1RG K}\beta} = 1.0 \pm 0.05$. The source-averaged number is $\text{QE}_{\text{H1RG Fe}} = 0.97 \pm 0.05$. While one might expect the higher intensity $\text{K}\alpha$ line's uncertainty to be lower than the $\text{K}\beta$ uncertainty, such is not the case because all of the errors are dominated by systematic errors. Counting error due to the number of X-rays in the data sets is a small component of the total uncertainty.

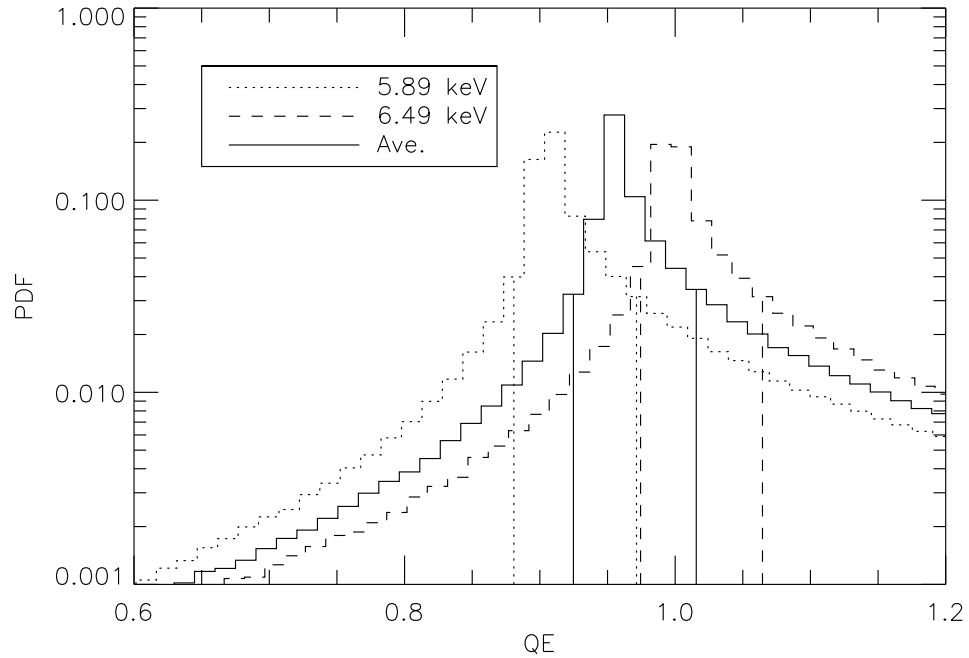


Figure 4.33: The three simulated probability density functions for the H1RG QE measured at 5.89 keV, 6.49 keV and an effective average QE that uses the 1:6.79 weighted average of incident photon flux. Even though the distributions are not Gaussian, the 68.26% confidence interval is plotted to provide a standard measure of the width.

4.5 Modeling HCD Quantum Efficiency

The QE as a function of energy was calculated with a one-dimensional slab absorption model. This assumes that the illumination is on-axis and collimated, the structures within each pixel of the HIRG's PIN diode array are uniform, and that the pixels are all identical. Given the detector 2 mrad detector alignment error, this translates into a negligible $2 \cdot 10^{-4}\%$ error in the projected detector layer thicknesses. Given the 2.6 cm HIRG diagonal, 1.25 cm source diameter, and the 255 cm source-detector distance, this corresponds to a maximum collimation error angle of 15 mrad which corresponds to a negligible layer thickness error of $10^{-2}\%$. The model assumes a $0.018\mu\text{m}$ Al OBF, a $0.025\mu\text{m}$ SiO_2 native oxide, an inactive $0.1\mu\text{m}$ n-doped layer (the top of the PIN diode), and a $100\mu\text{m}$ thick depletion region. The model calculates the QE with the following:

$$\text{QE} = (1 - e^{-\sigma_N n_N t_N}) c_N \prod_1^{N-1} e^{-\sigma_i n_i t_i} c_i \quad (4.44)$$

where N is the total number of layers in the slab model and the N^{th} layer is depleted silicon, where X-ray detection happens. The product of a series yields the total transmission through the detector's inactive top layers, while the $1 - \exp(-\sigma_N n_N t_N)$ term yields the absorption of the depleted silicon that produces a response in the detector. The model also assumes that sufficient bias voltage was used to fully deplete the diode's bulk.

Figure 4.34 shows the QE response, calculated with `sim_qe.pro`, for a variety of relevant parameter values. Choosing to vary the OBF thickness and the depletion depth at the same time is, in general, a bad idea because it conflates the two effects. However, in this case, the OBF only affects low-energy QE and the depletion depth only affects high-energy QE. Multiple parameter values were shown because throughout the development of the X-ray HCD, detectors with the shown OBF thicknesses were tested. Similarly, since detectors with varying depletion depth are available from TIS, three depletion depth thicknesses have been plotted to show this parameter's effect on high-energy QE. The 'No OBF'/ 180 \AA Al and $100\mu\text{m}$ curves apply to HIRG-167. The model predicts that for a 180 \AA aluminum

OBF and 100 μm of depleted silicon, the line ratio weighted QE average,

$$QE_{\text{H1RG Fe}} = QE_{\text{H1RG K}\alpha} \frac{6.79}{7.79} + QE_{\text{H1RG K}\beta} \frac{1}{7.79}, \quad (4.45)$$

for the two emission lines in our ^{55}Fe source will be 0.966, which is in excellent agreement with our $QE_{\text{H1RG Fe}} = 0.97 \pm 0.05$ measured estimate. This is the most meaningful comparison that can be made between the data and the model since the model does not predict which events will be detected in the line profile and which will not.

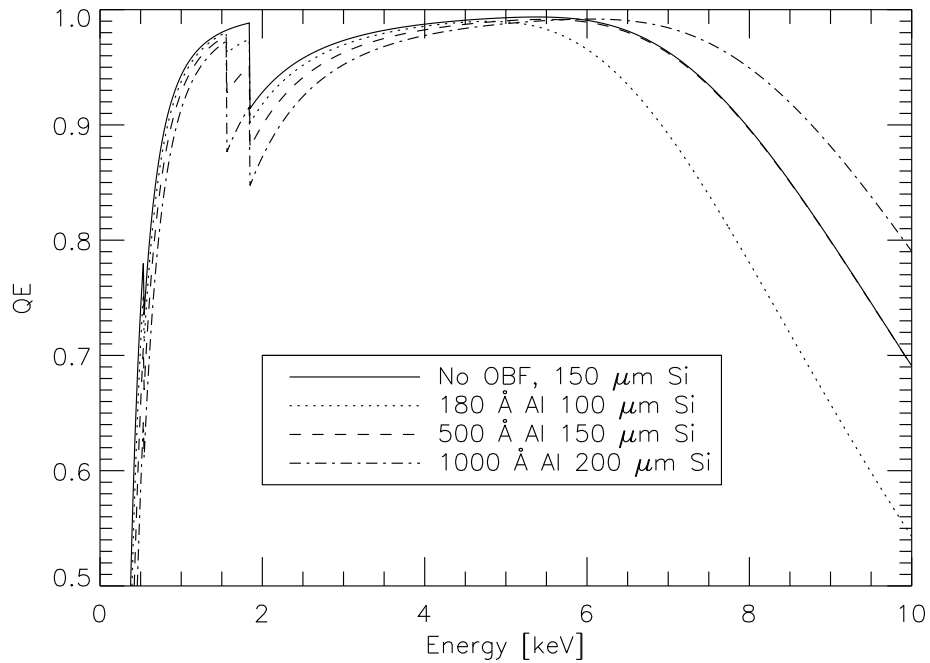


Figure 4.34: Slab 1-dimensional model of QE as a function of X-ray energy for variations of a nominal H1RG's OBF thickness and depletion layer depth. Notable features in all curves include the low-energy drop-off due to absorption from all of the overlying inactive layers, the O (0.5431 keV), Al (1.5596 keV, not present in 'No OBF' model), and Si (1.839 keV) absorption edges, and the high-energy drop-off due to the increasing over-penetration of high-energy X-rays through the depletion region.

4.6 Future QE Measurements

The depth of the absorption edges and the location of the high/low-energy rolloff feature in the HIRG QE models depend on the thickness of the layers that produce those features in the detector model. Variation of these layer thicknesses tends to affect the detector QE in localized energy regions, directly above the transition energy in the case of absorption edges, and above ~ 6 keV in the case of the 100 μm depletion depth. Accordingly, measuring the QE in these regions, where the QE tends to vary the most, is the most effective method for probing the detector layer thicknesses. Measuring QE with the 8.0 keV copper $K\alpha$ line would effectively probe the depletion depth of the detector. Measuring the QE at the 2.3 keV sulfur, 1.7 keV silicon, and 1.4 keV aluminum lines would be the best line choices for constraining the silicon and aluminum edge depths. Such measurements are planned to be included in future detector calibrations.

The future use of HCDs in X-ray astronomy

HCDs are currently poised to overtake CCDs as the prime focal plane array candidate on next-generation, X-ray space telescopes. In this chapter I will discuss how the competitive characteristics of HCDs have already enabled access to new science capabilities on smaller missions and are on track to do the same for large-aperture, focused X-ray telescopes as HCD technology develops.

5.1 Small Missions

The X-ray Coded Aperture Telescope (XCAT) [50] on the Joint Astrophysics Nascent Universe Satellite (*JANUS*) mission concept has shown that current-generation HyViSI™ HCDs are the superior FPA choice for a coded aperture mask X-ray telescope on a Small Explorer (SMEX) class mission. In order to achieve its baseline 3.9 sr field of view and monitor the X-ray sky for high-*z* gamma-ray bursts, the XCAT design required 40 detectors. HCDs were the optimal choice because of their extremely low power consumption compared to CCDs. Operating an equivalent number of CCDs would have dramatically increased the satellite's power budget, making the proposed design completely unfeasible with the budgetary limitations of a SMEX mission.

5.2 Large Missions

In addition to being viable for small missions, the current-generation of X-ray HyViSITM FPAs are also a stepping stone on a technology development path that is leading to more capable FPAs. Within the coming decade, this path will likely produce detectors that satisfy the mission requirements of next-generation large-aperture X-ray telescopes. Achieving International X-ray Observatory (*IXO*) science, which was prioritized in the 2010 Decadal Survey, will require a large aperture (several times 10^4 cm^2) X-ray telescope. Such a large aperture represents more than an order of magnitude increase in effective area compared with the current generation of telescopes, which will result in a similar increase in per pixel count rates at the focal plane, given similar plate scales. Mission concepts such as *SMART-X*, *ATHENA*, and the canceled *IXO* all included wide field imager instruments that required a soft X-ray imager with fast read speed, low noise, small pixel sizes, and moderately large format sizes.

Next-generation HCDs will eliminate the IPC of HyViSITM detectors with CTIA amplifiers. They will pioneer X-ray event-driven array readout, where in-pixel comparator circuitry will initiate pixel readout instead of the less efficient raster format that CCDs will always need to use. Smart readout schemes such as this will enable the detector to operate free of pile-up at significantly higher count rates and with higher time resolution, for a given pixel read speed. In-pixel CDS circuitry will reduce read noise. Fitting all of this circuitry into a small ($\sim 15 \mu\text{m}$) pixel pitch is feasible, but will require development work.

These capabilities will enable the spatial and temporal resolution of lower flux objects with moderate energy resolution. If these advanced missions are realized, black hole and active galactic nuclei surveys will probe deeper than ever before, spatially resolved spectra of clusters will advance precision cosmology on large scale structure, AGN iron lines will be time-resolved, the spin of black holes in the range $0 < z \lesssim 3$ will be measured, spectra will be obtained for black holes at $z \sim 10$, and the neutron star equation of state will be probed.

The X-ray Confirmation of HESS J0632+057 as a γ -ray Binary

6.1 Introduction

As discussed in Chapter 5, the HCD will soon become a competitive contender in the race to fulfill the FPA requirements set forth by next-generation X-ray telescopes. CCDs, however, are currently operating on all major X-ray satellite observatories. The *Swift* satellite has employed CCDs at the heart of its X-ray telescope for the past seven years with enormous success [103]. In this chapter I will present scientific work done using CCDs on the *Swift* X-Ray Telescope. The work has already been published [104] and has been reproduced by permission of the AAS.

There are currently three confirmed TeV gamma-ray binaries; PSR B1259-63 [105], LS 5039 [106], and LS I+61° 303 [107, 108, 109] as well as a fourth new GeV gamma-ray binary recently detected by *Fermi* [110] that could have associated TeV emission. Evidence at the 4.1σ level for Very High Energy (VHE) emission from the stellar mass black hole candidate Cyg X-1 has been reported by Albert *et al.* [111] during a single short flaring episode. Contained within each of these sources, a young and massive O or B star is orbited by a compact object, either a neutron star or a black hole. The VHE emission in TeV binary systems is powered either by pulsar winds driving shock acceleration or by mass accretion onto the compact

object driving a microquasar jet. The compact physical size of the emission region leads TeV binaries to be one of the few classes of Galactic VHE sources which appear point-like to TeV instruments. Following the discovery of several TeV objects with no identified counterparts, HESS J0632+057 was suggested to be a possible member of this exotic class of TeV/X-ray binaries [112, 113]. We are testing this hypothesis by using X-ray data to search for periodicity from orbital flux modulation.

HESS J0632+057 was first detected using 13.5 hr of data collected between 2004 March and 2006 March as part of the HESS Galactic Plane Survey [112]. In these data, the source has a peak significance of 7.1σ and a post-trials significance of 5.3σ , after accounting for trials associated with searching the entire field of view. Located on the edge of the Rosette Nebula within the Monoceros Loop region at R.A. 06h 32' 58.3", Dec. $+05^\circ 48' 20''$ ($\pm 28''$ stat., $20''$ sys.), the spatial distribution of the source is consistent with that of a point source (rms size $< 2'$ at 95% confidence) [112]. The source is located on the edge of the 99% contour of the EGRET unidentified object 3EG J0634+0521, but no object at the position of HESS J0632+057 is listed in the *Fermi* LAT point source catalog. MWC 148, a B0pe star, is positionally coincident with the centroid of the HESS position.

Hinton *et al.* [113] observed the region surrounding HESS J0632+057 on 2007 September 17 with *XMM*, obtaining 26 ks of good data. The observation resulted in the identification of point source XMMU J063259.3+054801, which is positionally coincident with both MWC 148 and HESS J0632+057, and within the 99% error circle of 1RXS J063258.3+054857. The source showed significant variability, declining from ~ 130 c/ksec to ~ 90 c/ksec over the course of the relatively short observation (≈ 7.2 hours). During this observation the source showed a mean deabsorbed flux of $(5.3 \pm 0.4) \cdot 10^{-13}$ erg cm $^{-2}$ s $^{-1}$ in the 1-10 keV range. The spectrum was well fit by an absorbed power-law model with a photon index of 1.26 ± 0.04 and a column density of $N_H = 3.1 \pm 0.3 \cdot 10^{21}$ cm $^{-2}$.

Beginning 2009 January 26, Falcone *et al.* [114] initiated a campaign to observe XMMU J063259.3+054801 with the *Swift* X-ray telescope (XRT; Burrows *et al.* [115]), reporting significant variability in 0.3-10 keV flux. While flux variability was measured on day to month-long timescales, Falcone *et al.* [114] found no evidence for periodicity and concluded that if periodicity was present, it was likely with

$P > 54$ days. Additionally, the X-ray source has shown no evidence of short timescale periodic or quasi-periodic variability in the range 0.005 - 800 Hz [116].

During December 2006 - January 2007 and December 2008 - January 2009 Acciari *et al.* [117] performed follow-up observations of HESS J0632+057 above 1 TeV with VERITAS, yielding flux upper limits well below the values published by HESS. Together, the VERITAS and HESS observations provide evidence for variability of the gamma-ray flux on time scales of months. More recently, both VERITAS and MAGIC have detected elevated TeV gamma-ray emission [118, 119] during the time period of elevated X-ray flux reported by Falcone *et al.* [120] in February 2011.

We find no report of optical flux modulation in the literature although Aragona *et al.* [121] report temporal variations in the $H\alpha$ emission line profile. HESS J0632+057 has shown a radio spectral index of $\alpha_r = 0.6 \pm 0.2$ and significant variability at 5 GHz on month-long time scales around a mean flux of 0.3 mJy [122], however no periodic variability could be detected in these data. This radio flux is much lower than the typical radio flux expected from a TeV blazar, making such a potential interpretation improbable. Recently, Moldon *et al.* [123] announced the 1.6 GHz detection of a milliarcsecond scale source coincident with MWC 148.

The point-like nature of the detected TeV source, the excellent positional coincidence with MWC 148 (chance coincidence of $\sim 10^{-4}$ according to Aharonian *et al.* [112]), the location on the Galactic plane with a low radio flux, the X-ray binary-like spectral index, and the variable X-ray and gamma-ray emission are all facts that argue in favor of an X-ray binary in association with MWC 148. Confirmation of HESS J0632+057/MWC 148 as a TeV binary would add a new member to this short list of objects; whereas, refutation of the binary hypothesis would establish an equally interesting class of TeV source. The most direct way to test this binary hypothesis is to search for periodic emission signatures. In this chapter, we report on recent monitoring data taken with *Swift*-XRT.

6.2 The Observations

The X-ray Telescope (XRT; Burrows *et al.* [115]) on the *Swift* observatory [124] was used to obtain sensitive observations in the 0.3-10 keV energy band. The typical

observation duration was ~ 5 ks with ~ 1 week spacing between most observations. The semi-regular cadence of the observations was due to *Swift*'s need to account for Gamma-ray burst and supernova targets of opportunity, spacecraft temperature, and Moon, Earth, and Sun constraints when scheduling science target pointings. This cadence worked very well for our science objective because it sampled, and therefore allowed us to probe, many different temporal periods in the source. From 16 May 2009 - 15 August 2009 and 10 May 2010 - 21 August 2010 the source was unobservable due to its close proximity to the Sun. The total *Swift*-XRT data set includes 463 ks of observations, extending from 2009 January 26 (MJD 54857.1) to 2011 March 27 (MJD 55647.6), representing a baseline of $T = 790.5$ days. All of the observations were obtained in photon counting (PC) mode. All observations beyond MJD 54965 are being reported here for the first time.

6.3 Analysis

We used the most recent versions of the standard *Swift* tools and the most recent calibration files available at the time of data processing. In particular, we utilized *Swift Software* version 3.7, *FTOOLS* version 6.10, and *XSPEC* version 12.6.0q. Light curves were generated using *xrtgrblc* version 1.5.

Source and background regions, bad CCD detector column correction, and point spread function corrections, and filtering of data were all performed as described in Falcone *et al.* [114]. Circular and annular regions are used to describe the source and background areas respectively, and the radii of both regions depend on the measured count rate. In order to handle cases where the sources land on bad CCD detector columns, point spread function correction is handled using *xrtlccorr*. Since these observations always resulted in XRT count rates ~ 0.01 – 0.08 c/s, there was no significant pile-up, which occurs in photon counting mode at count rates above ~ 0.5 c/s. The full light curves use a bin size of one observation per bin (observations were typically 4-6 ksec duration). In order to avoid systematics due to mode switching and to yield comparable photon statistics in all bins, we removed observations with integration times less than 700 seconds, which results in an inconsequential loss of 4 observations. All error bars are reported at the 1-sigma level, unless otherwise specified.

Spectral fitting was done with an absorbed power-law, with the N_H set to the value found by Hinton *et al.* [113] with *XMM*. Following the technique of Falcone *et al.* [114], we calculated rate-to-flux conversion factors for groups of observations, defining the groups such that they contained enough counts to enable good spectral fits and isolated a single flux state of the source. Following this temporal binning, each observation group was fit spectrally using a minimum energy binning ratio of 16 photons/bin, and in most cases the binning ratio was 20 photons/bin. Assuming that the observed energy spectrum does not change significantly while the source is in a particular flux state, the rate-to-flux conversion will apply for all observations in each group. Once the spectral fits were obtained, the flux was calculated. These flux values, which were calculated for each of the temporally binned data segments, were then used to calculate a flux-to-rate ratio during that time period. The time-dependent flux-rate ratio was then applied to the rate light curve, shown in Figure 6.1(a). We also fit the entire combined data set with an absorbed power law to obtain time averaged spectral parameters. Error bars represent the count-rate error scaled by the rate-to-flux conversion factor.

6.4 Results

A spectral fit of the combined data set finds that the data is well fit by an absorbed power-law spectrum with column density set to the *XMM* value ($N_H = 3.1 \pm 0.3 \cdot 10^{21} \text{ cm}^{-2}$). This results in an average spectral index of 1.58 ± 0.06 , a normalization constant of $2.4 \pm 0.1 \cdot 10^{-4}$, and $\chi^2 = 57.9$ with 39 degrees of freedom. This time averaged spectrum is consistent with the results of Falcone *et al.* [114] and other TeV binaries such as LS I+61° 303 [125]. The X-ray light curve, constructed from the entire data set, is shown in Figure 6.1. Given the observations, we define five different feature types in the variability; low level quiescent emission of $\sim 10^{-12} \text{ erg cm}^{-2} \text{ s}^{-1}$, large emission peaks, which are 4-5 times brighter than the quiescent emission, small precursor peaks, which are approximately 2 times brighter than the quiescent emission and precede each large peak, small mid-phase peaks, which are approximately 2.5 times brighter than quiescent emission and appear approximately half way between the large peaks, and dips, which succeed each large peak and represent a decrease in emission by a factor of $\sim 1/3$ below

quiescent. By eye, these emission features appear to be spaced at regular intervals, leading us to believe that their positions reveal an underlying periodicity in the source. To confirm the presence of periodic modulation, we apply an autocorrelation analysis. The period of the modulation is determined with a peak fitting method, and its statistical significance is established using Monte Carlo light curve simulations.

6.4.1 Peak Fitting

Peak fitting is a simple and robust method for measuring periodicities in data, such as these, where modulation is readily characterized by isolated peaks of enhanced and suppressed emission superimposed upon a quiescent state. We model the light curve with a sum of 10 Gaussians (one for each peak feature) and a constant (for the quiescent emission). This results in 31 free parameters. To obtain the best-fit parameter values, we perform chi-square minimization between the model and data. The final fit is shown as a solid line in Figure 6.1 and resulted in $\chi^2 = 207.5$ for 79 degrees of freedom. The large χ^2 is evidence that additional, small-scale variability is present in the light curve and/or that Gaussians do not ideally describe the flares. While the entire light curve is not ideally fit by this model, it provides a reasonable characterization of the variability and, more importantly, allows us to characterize the timing of the primary features in the light curve.

We propose that the large peaks (MJD 54966.2, 55283.3, and 55601.3) and the dips (MJD 55303.4 and 55630.0) most accurately characterize periodic behavior in the light curve. The small precursor peaks that precede each large peak are unsuitable for measuring the period because they are observed to have variable shape, position (with respect to the large peaks), and height and because their significance above quiescence is small. The small mid-phase peaks are also unsuitable for measuring the period because the second peak, centered at MJD 55431.8, is poorly sampled, yielding an unreliable peak position estimate. Averaging the separations between peak centers, using large peaks and dips, we calculate a period of 321 days. We conservatively estimate the error to be ± 5 days, the approximate average sampling rate during the large peaks and dips. Using this period, we have plotted the phase-folded light curve in Figure 6.4. This shows a strong similarity

between modulation observed during different phases, particularly during the large peaks and dips.

6.4.2 Lomb-Scargle

The Lomb-Scargle periodogram [126] is a standard tool used to search unevenly sampled, univariate data for periodic variation. The algorithm samples a predetermined grid of temporal frequencies, the test frequencies, and calculates the spectral power in the data at each frequency. Spectral power is the equivalent of an empirical reduction of the sum of the squared difference between the data and a sinusoid model of the sampled frequency. Therefore, peaks in a plot of spectral power as a function of test frequency, also called a periodogram, indicate potential periodicities in the data. In the special case of gaussian noise, sinusoidal data variation, and reasonably uniform sampling density, Horne & Baliunas [127] show that the periodogram height, z , is related to the likelihood that a peak is due to noise, F , as

$$F = 1 - [1 - e^{-z}]^{N_i}, \quad (6.1)$$

where N_i is the number of independent frequencies, found via Monte Carlo simulations to be related to the number of data points, N_0 as

$$N_i = -6.362 + 1.193N_0 + 0.00098N_0^2. \quad (6.2)$$

The normalized Lomb-Scargle periodogram of our X-ray light curve is shown in Figure 6.2. The periodogram is sampled N_i times between the inverse of the total time baseline for all observations and twice the mean Nyquist frequency, $\langle f_n \rangle$. The most significant peaks have periods of 300.3, 156.0, 75.9, and 63.9 days and false alarm probabilities of $4.11 \cdot 10^{-4}$, $1.61 \cdot 10^{-5}$, $9.19 \cdot 10^{-5}$, and $3.22 \cdot 10^{-5}$, respectively. The repetition of the unique, large peak dip structure in the light curve leads us to believe that the ~ 320 day period is the true binary modulation and that the higher frequency periodogram peaks are either, in the case of the 156.0 and 75.9 day periods, harmonics of the orbital frequency or, in the case of the 63.9 day period, the Lomb-Scargle algorithm triggering on the characteristic timescale defined by

the time between the middle of the large peak and the middle of the dip. Since the HESS J0632+057 light curve is highly non-sinusoidal, it is characterized better by the peak fitting method than by the Lomb-Scargle analysis. Furthermore, the non-sinusoidal light curve violates one of the assumptions of Horne & Baliunas [127] and the false alarm probability estimates calculated in this way should be viewed as upper limits presented to motivate further investigation of the period's significance. Due to these shortcomings we chose to disregard the Lomb-Scargle results and pursued a more appropriate algorithm for periodicity and periodicity significance estimation.

6.4.3 Autocorrelation

Instead of measuring the similarity of the light curve to some assumed, purely mathematical, periodic function (a sinusoid in the case of Lomb-Scargle), an alternative approach is to compare the data to other data. In general, this is known as correlation analysis. If one wishes to measure the degree of similarity between two different sets of data, cross correlation is used. If one wishes to measure a signal's similarity to itself, comparing its current behavior to past behavior in a search for repeating patterns, autocorrelation is used [128, 129]. The general procedure for both methods is to compare the data at two different points in time, separated by a time lag τ . For evenly sampled data, this is trivial, since all points in the data set align with one another. However, in the case of unevenly sampled data, additional steps must be taken to calculate the cross correlation function (CCF). One solution is to interpolate between data points and resample the data at locations necessary for calculating the CCF.

An autocorrelation analysis is often used as a test for repeating patterns in astronomical time series, as it requires no prior assumptions about the lightcurve profile [128, 129]. The Discrete Auto-Correlation Function (DACF), in particular, can be used to study the level of auto-correlation in unevenly sampled datasets without any interpolation or addition of artificial data points [130].

Figure 6.3 shows the result of applying the z -transformed DACF [131] to the *Swift*-XRT dataset. We show both the autocorrelation value, and the autocorrelation divided by its error, which provides an estimate of the significance of the

autocorrelation measurement. A clear peak is visible at a time lag of ~ 320 days, as well as the expected peak at twice this period.

6.4.4 Significance of the Period

To better estimate the significance of the 321 day periodicity, we performed Monte-Carlo simulations. By simulating many light curves with flare features similar in size and occurrence frequency to those seen in the observed light curve, we can estimate the probability that the light curve is generated by a source that exhibits the observed flaring pattern every 321 days, and not by a source that flares randomly in time. To characterize the flaring behavior in the observed light curve, we again fit the 10 Gaussian + constant model to the light curve. Since we see multiple repetitions of each feature type (large, small, and mid-phase peaks and dips) in the light curve, it is possible to measure not only each feature type's rate of occurrence in the data set, but also estimate the range of values of each type's height and width by using the mean and variance. We define the rate of feature type occurrence as the number of occurrences per total time where the feature type may have, potentially, been observed. Given our observation cadence, the only time intervals where peaks or dips could not have been detected were during the date ranges MJD 54970 - 55050 and MJD 55330 - 55424, where the source was too close to the Sun. During the entire period of *Swift* observations when peaks and dips could have been observed, we observed 3 large peaks, 3 small precursor peaks, 2 dips, and 2 small mid-phase peaks.

To generate the appropriate number of features of each type, we sample a random Poisson deviate corresponding to the calculated rate of occurrence. The shape of each feature is then created with a Gaussian peak of height and width generated by selecting a random deviate from a normal distribution with mean and variance measured in the corresponding feature type in the observed light curve. The mean position of each peak is generated by selecting a uniformly distributed random deviate on the observation baseline (MJD 54857 to MJD 55647). The peaks and dips are then combined with the best-fit value for the quiescent emission derived from data. The final simulated light curve is generated by sampling the model of superposed Gaussian peaks at the bin-center-times when *Swift* observed

HESS J0632+057. We then calculate the χ^2 between the simulated light curve and the model that best fit the observed data. The fraction of simulated light curves with calculated χ^2 less than that of the data represents the probability of generating the observed light curve with a source that is stochastically flaring (with flares having the observed size and rate of occurrence). In this way, we created 10^9 simulated light curves with randomly distributed flares and dips, none of which resulted in a χ^2 value less than that of the actual light curve, relative to the fit. Therefore, we find the false alarm probability for finding this periodic light curve from similar-sized stochastic flaring to be $P < 1 \cdot 10^{-9}$.

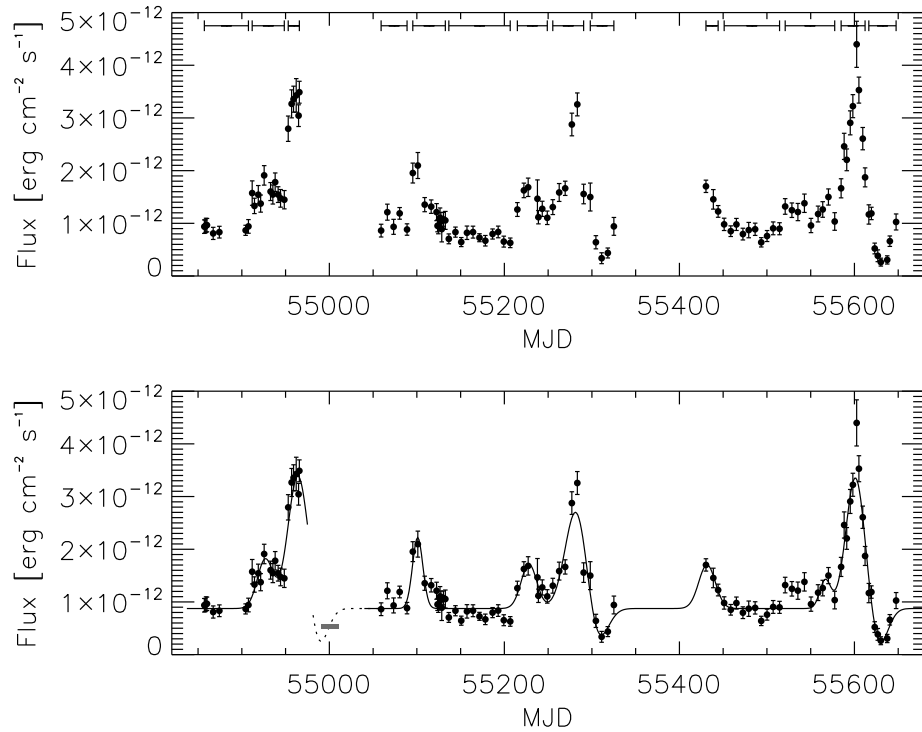


Figure 6.1: The background-subtracted X-ray light curve of XMMU J063259.3+054801 from the *Swift*-XRT observations in the 0.3-10 keV band. Figure 6.1(a) shows only the data and the time bin boundaries that were used for spectral fitting. Figure 6.1(b) shows the same data with the best fit of 10 Gaussians + constant model plotted as a solid line. Had the source been observable around MJD 55000, we hypothesize that it would have exhibited a dip state. To show this, we phase the best-fit model in the region of the MJD 55635 dip backwards by two periods and plot it as a dotted line. We also phase forward the *XMM* data taken on 2007 September 17 (MJD 54360) [113] by two periods and plot its error (dominated by period uncertainty) as a gray shaded box.

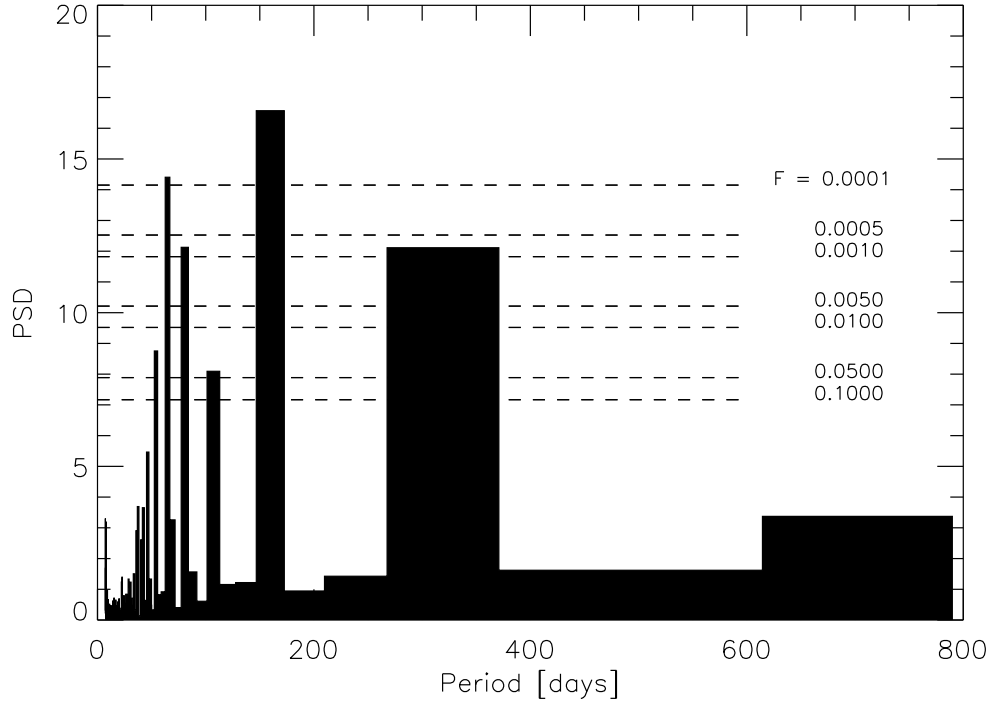


Figure 6.2: The Lomb-Scargle periodogram of *Swift*-XRT data sampled at N_i frequencies from $f_{min} = 1/T$ to $f_{max} = 2\langle f_n \rangle$. The horizontal dashed lines are a series of false alarm probability levels, $F = \{0.1, 0.05, 0.01, 0.005, 0.001, 0.0005, 0.0001\}$, representing the probability that a given peak is due to random fluctuation in the data and not a periodic signal. The most significant periodicities detected are the proposed 320 day period and its higher frequency harmonics. The peak at 60 days likely shows high significance because, as seen in the folded light curve (Figure 6.4), this is the characteristic timescale of the large peak followed by a small dip feature in the light curve.

6.5 Discussion & Conclusions

We have detected a 321 ± 5 day period in the 0.3-10 keV light curve of the unidentified TeV object HESS J0632+057. The observed periodicity has been shown to be significant by estimating the chance probability that the observed light curve periodicity is due to stochastic flaring of the source, resulting in a false alarm probability of $P < 1 \cdot 10^{-9}$. This implies a binary nature of HESS J0632+057, making it the fourth confirmed TeV binary (there are now 5 confirmed gamma-ray binaries, if one includes the recent announcement by Corbet *et al.* [110] of GeV

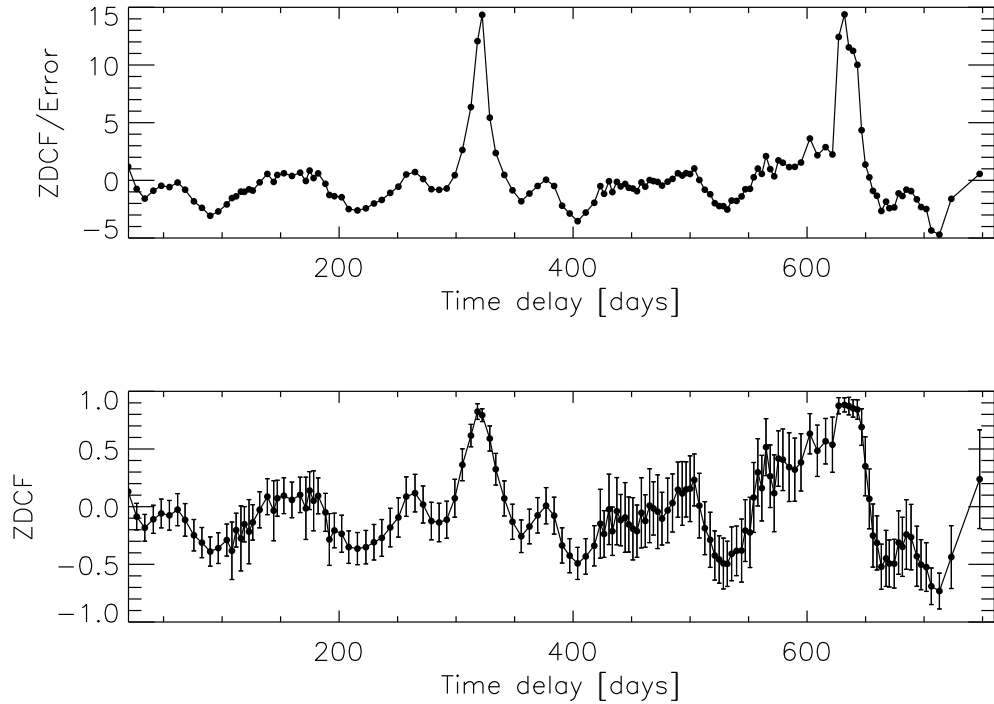


Figure 6.3: The z -transformed discrete correlation function as a function of time lag, plotted with error bars (bottom) and divided by error bars (top), to give an estimate of significance.

emission from 1FGL J1018.6-5856). The 321 ± 5 day period makes the system one of the longest period Be star TeV/X-ray binaries and observations by Skilton *et al.* [122] show that HESS J0632+057 may have an unusually low luminosity.

Figure 6.4 shows that the hardness does not vary significantly throughout most of the orbit, but it does reach a significant maximum when the light curve exhibits a dip feature. A constant line fit of the hardness data results in $\chi^2 = 55.4$ (with 7 dof), which shows that spectral variability is present, particularly during the flux dip. This is consistent with the harder photon index measured by Hinton *et al.* [113] at a time corresponding to a dip feature in the light curve, phased forward by two periods (Figure 6.1). This hardening of the X-ray spectrum during a flux decrease may be due to increased absorption of the soft X-rays in the source region, or it could be due to an orbital modulation of acceleration site parameters. If increased absorption due to a partial eclipse of the X-ray emission region is the origin of this

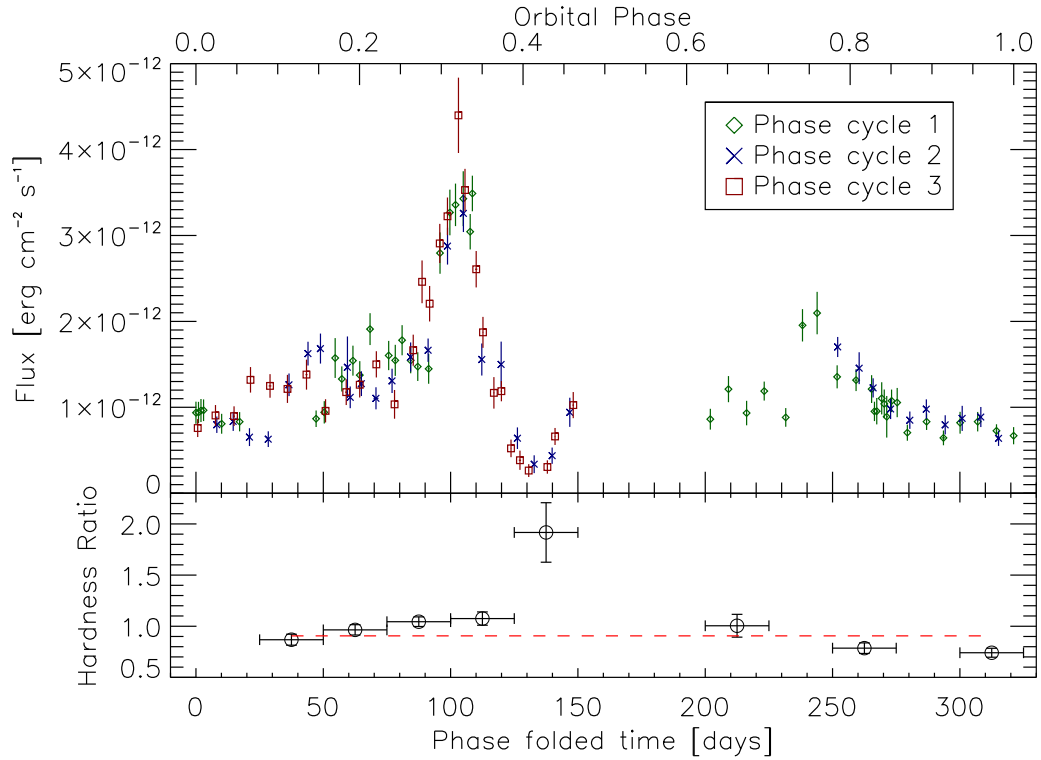


Figure 6.4: The X-ray light curve of XMMU J063259.3+054801 folded over the proposed period of 321 days. Zero phase has been arbitrarily defined as the date of first observation (MJD 54857). The three phase cycles that result from this folding are designated with diamond, X, and square symbols, respectively. The lower panel shows the hardness ratio (2.0-10.0 keV)/(0.3-2.0 keV), folded over the same period and binned at 25 day intervals to improve the signal to noise ratio. The shown hardness data were fit with a constant (red dashed line), resulting in $\chi^2 = 55.4$ for 7 degrees of freedom, thus confirming variability.

spectral hardening, then it argues for a geometry of the binary system that allows the Be star and/or its equatorial disk to pass between the X-ray emission region and our line-of-sight. This would imply that the binary orbit is highly inclined and that the emission region is small enough to be eclipsed. However, this would likely be associated with an increase in N_H , which is not observed in these data. An alternative, and more likely, explanation is that the spectral hardening during the flux dip is unrelated to absorption and instead caused by a change in acceleration site parameters, such as electron injection energies and cooling timescales, as a function of orbital phase.

In addition to the flux dip feature discussed above, the dominant features of the periodic phased X-ray light curve are a large flux peak with a factor of 5-6 flux increase over quiescent flux and a moderate flux peak with a factor of ~ 2.5 flux increase over quiescent flux. These peaks are separated in time by about one half period. The flux dip immediately follows the large flux peak. Each of these features lasts roughly ~ 4 weeks. The recent increase in TeV flux reported by Ong *et al.* [118] and Mariotti *et al.* [119] coincides with the time of the recent large X-ray peak, which could imply related mechanisms such as synchrotron and inverse Compton emission. By analogy with known X-ray binaries, it is reasonable to assert that the peaks are the result of orbital modulation, but the system geometry and X-ray generation mechanism are not well understood. If the spectral hardening discussed above is due to absorption from the Be star and the surrounding region, then the geometry would be most easily solved if the large flux peak were due to periastron passage. However, studies to-date have not found evidence for optical radial velocity shifts in the optical counterpart MWC 148 [121, 132]. Additional, radial velocity measurements are required to understand the system's geometry.

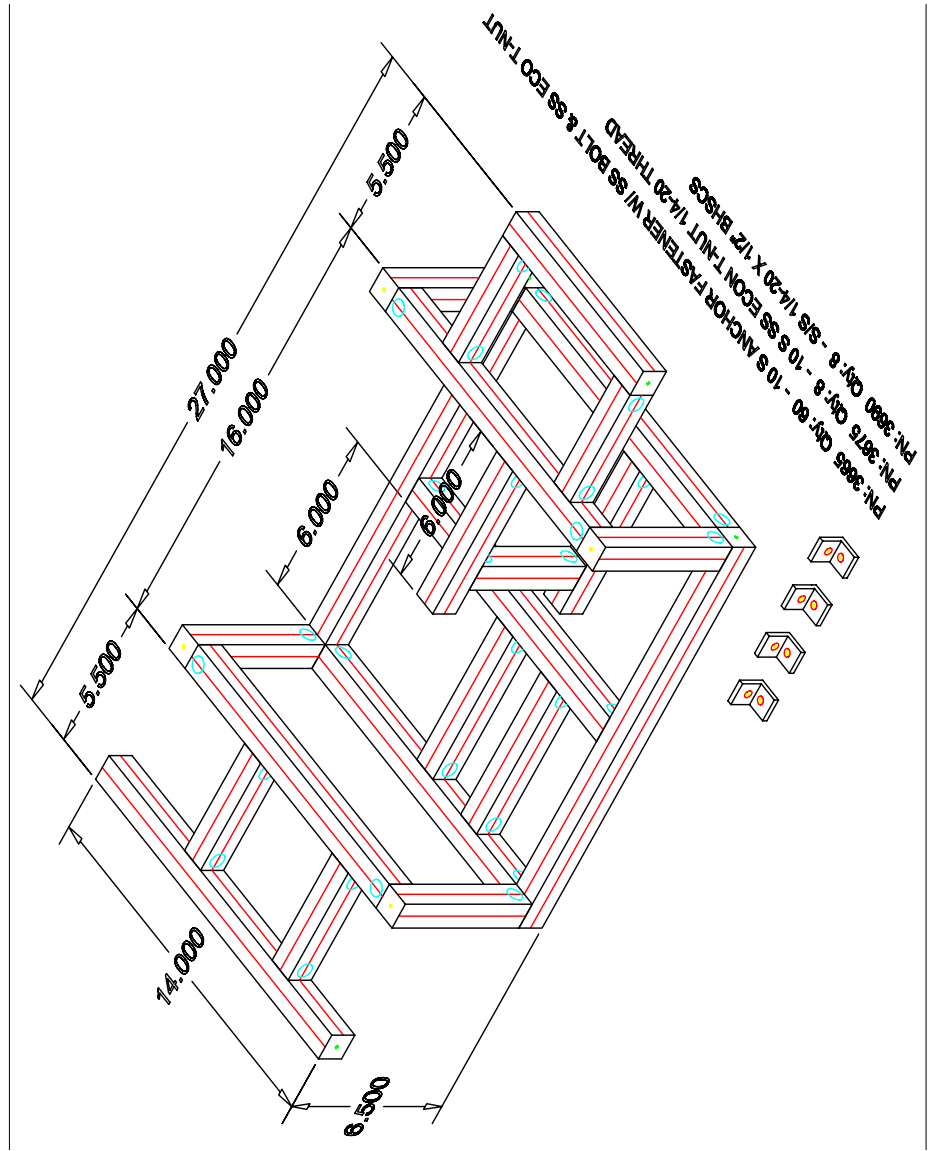
While the light curve is not sampled identically in each orbital cycle, making orbit-to-orbit variability difficult to assess, it appears that some variation exists, particularly in the regions preceding each large X-ray flare. This may indicate the presence of other variability timescales related to inhomogeneity in the Be star disk/wind. Other X-ray binaries, e.g., LS I+61° 303 [125, 133], show sporadic flaring behavior with a variety of timescales superposed on the binary orbit timescale, and this should be considered as a possible source of orbit-to-orbit variations for HESS J0632+057. Short timescale flaring analysis provides a way to probe the size of the emission region, as well as the power of the engine that must be feeding the associated acceleration site. If the dips indeed represent partial eclipses of the compact object by the donor star, this effect may also be used to constrain the size of the emission region and/or the size of a region of X-ray absorption. In principle, short timescale variability could also be used to probe different temporal signatures expected from Be star wind-driven shock models, binary interaction region models, and accretion-driven microquasar jet models.

Appendix **A**

Mechanical Drawings

A.1 Introduction

This appendix contains mechanical drawings of components that were fabricated for the QE teststand. All drawings except Figures A.1 and A.2 were produced with Solidworks 2012.



Frame Revised.pdf

Figure A.1: Carriage frame from Ralph A. Hiller Company. The joints were arranged in this way so that the carriage floor could be raised and/or the arm separation narrowed, if necessary.

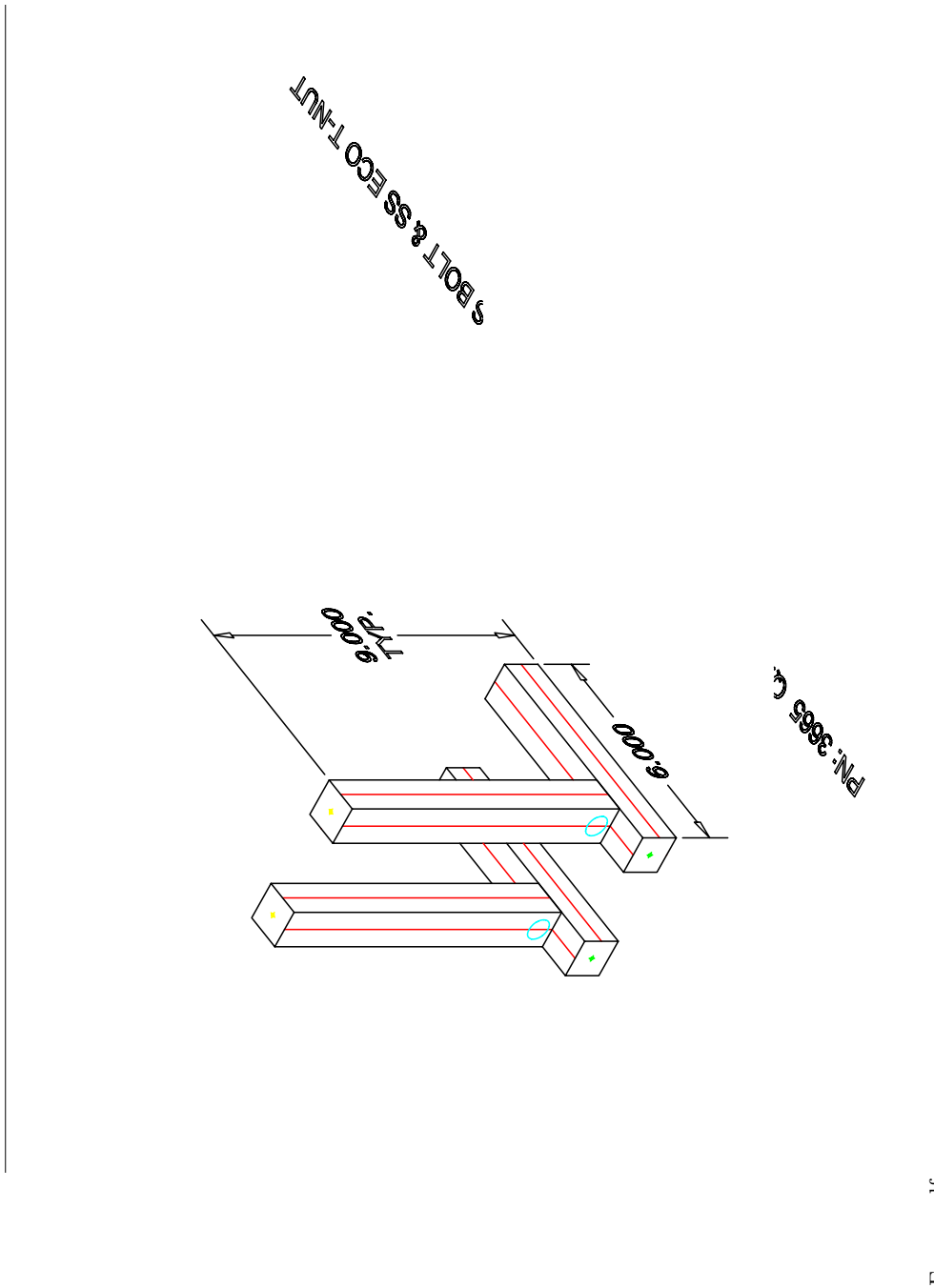


Figure A.2: Detector module frame from Ralph A. Hiller Company.

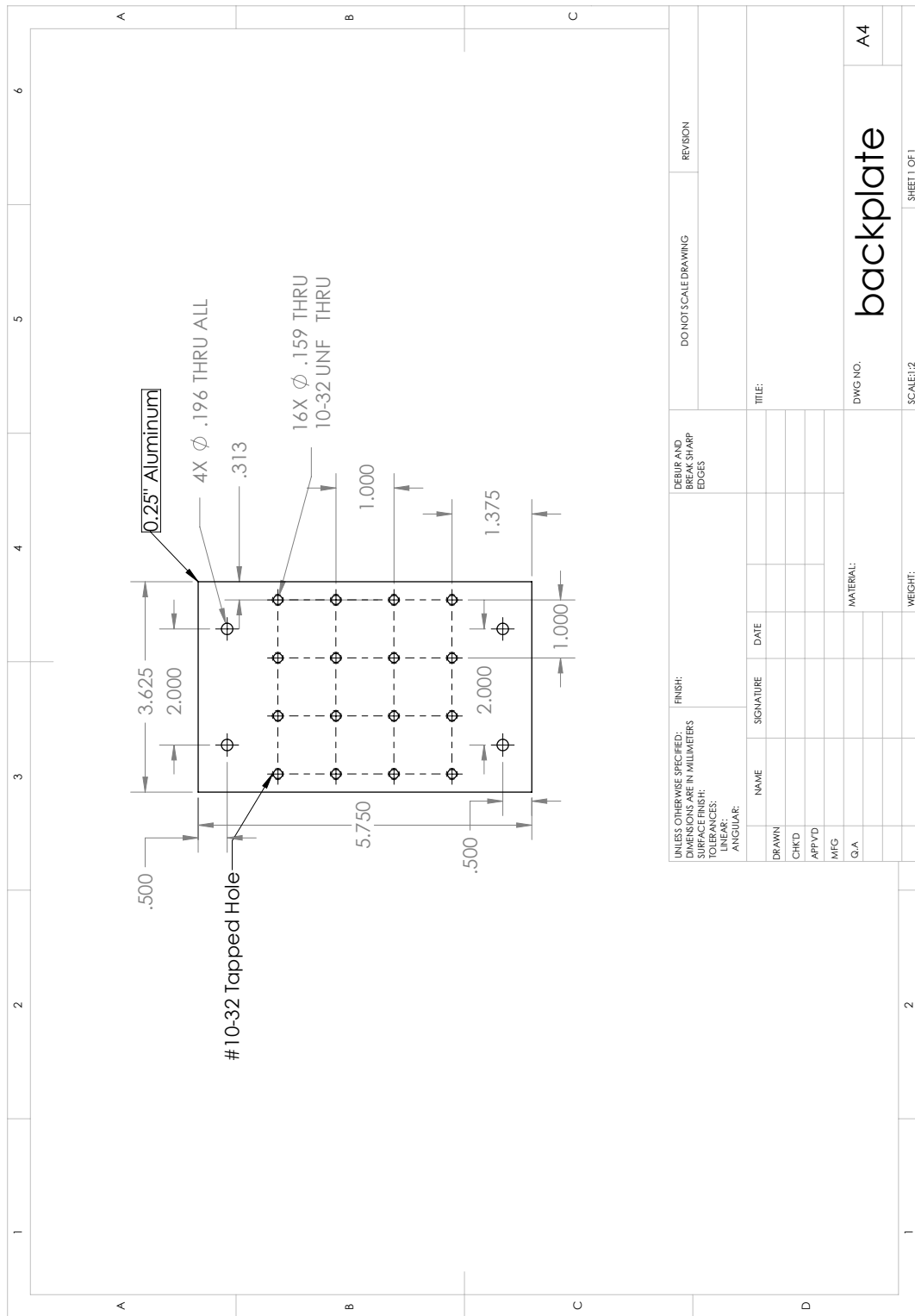


Figure A.3: Detector module breadboard.

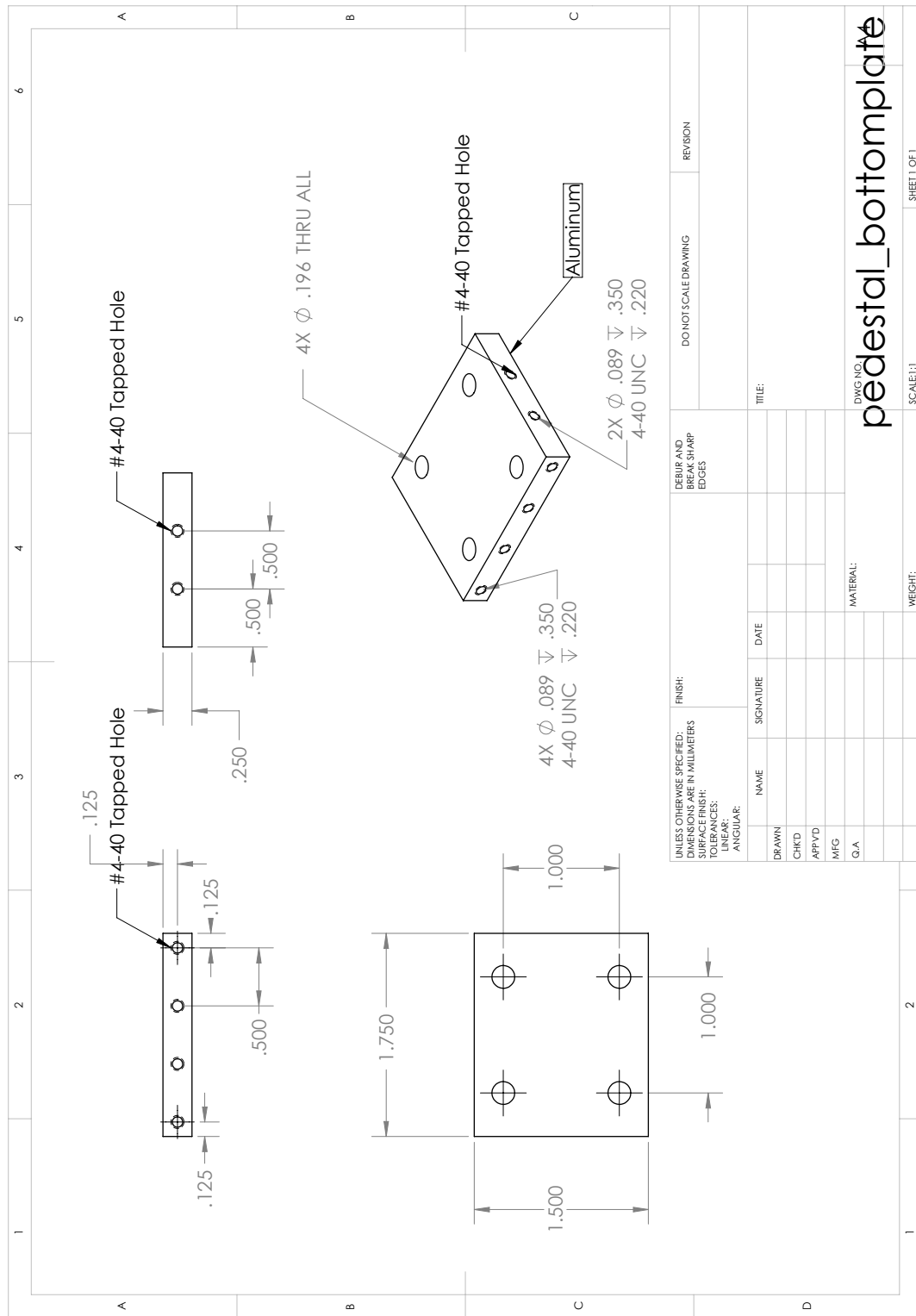


Figure A.4: Detector pedestal bottom plate.

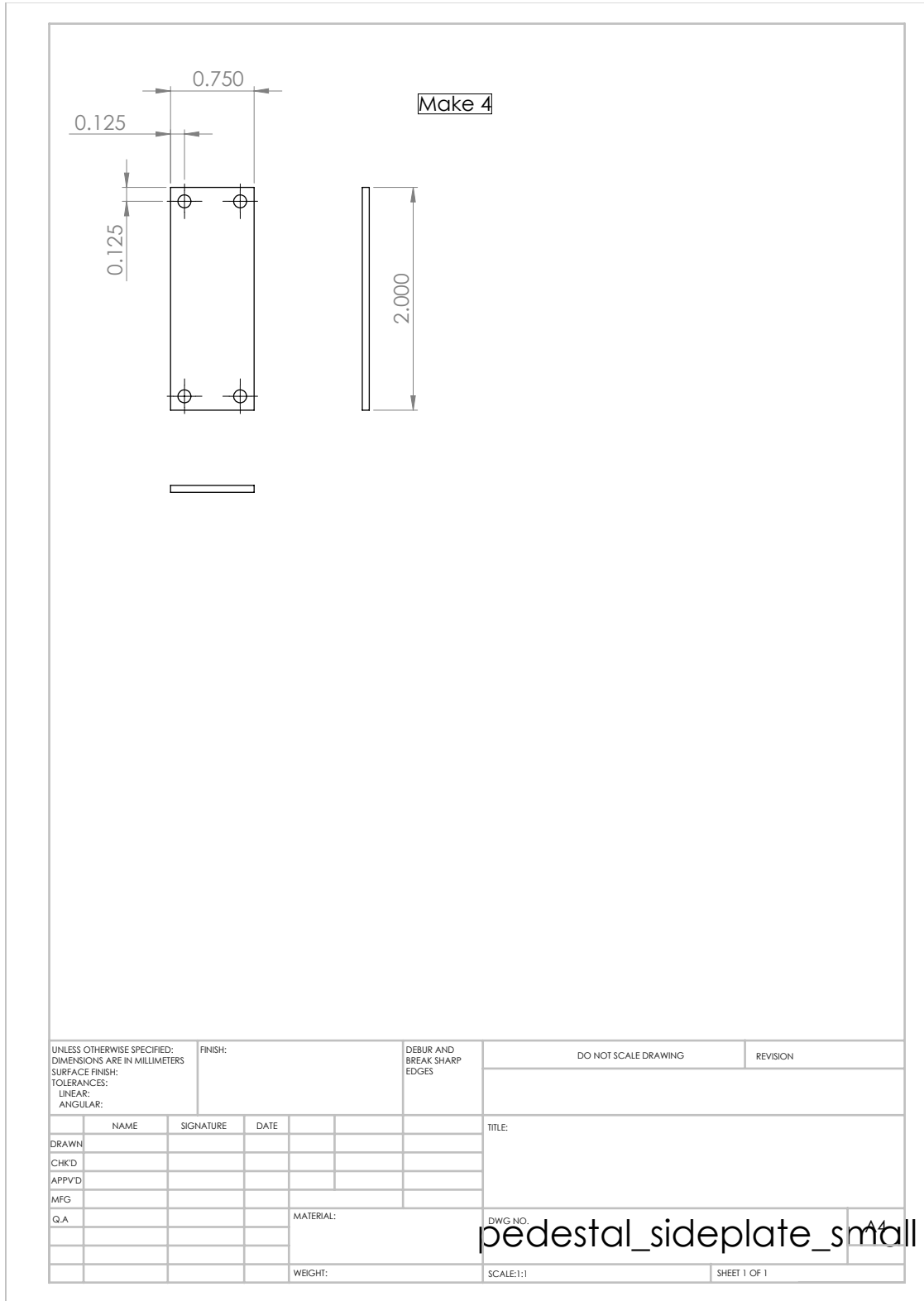


Figure A.5: Detector pedestal side strut.

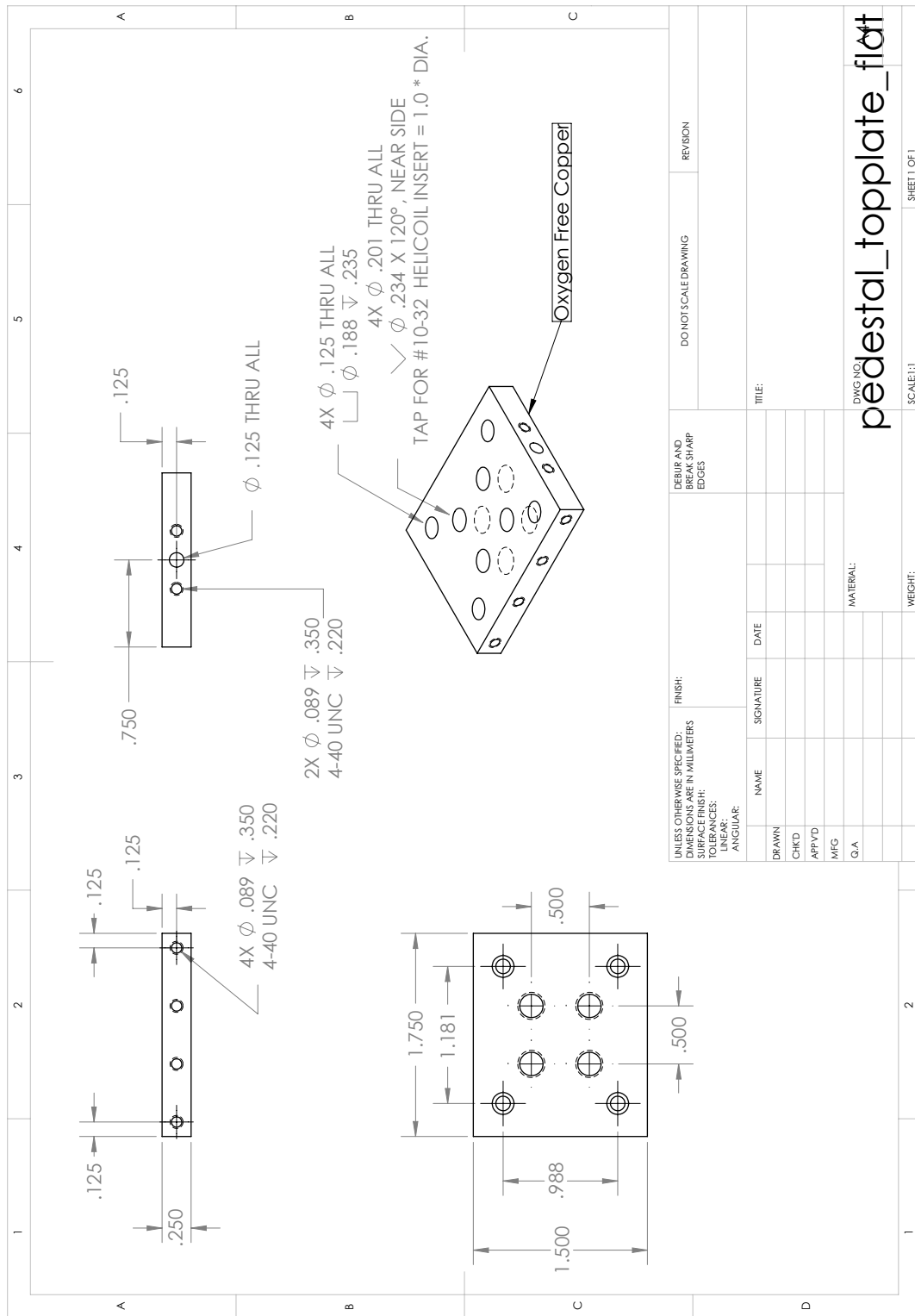


Figure A.6: Detector pedestal top plate.

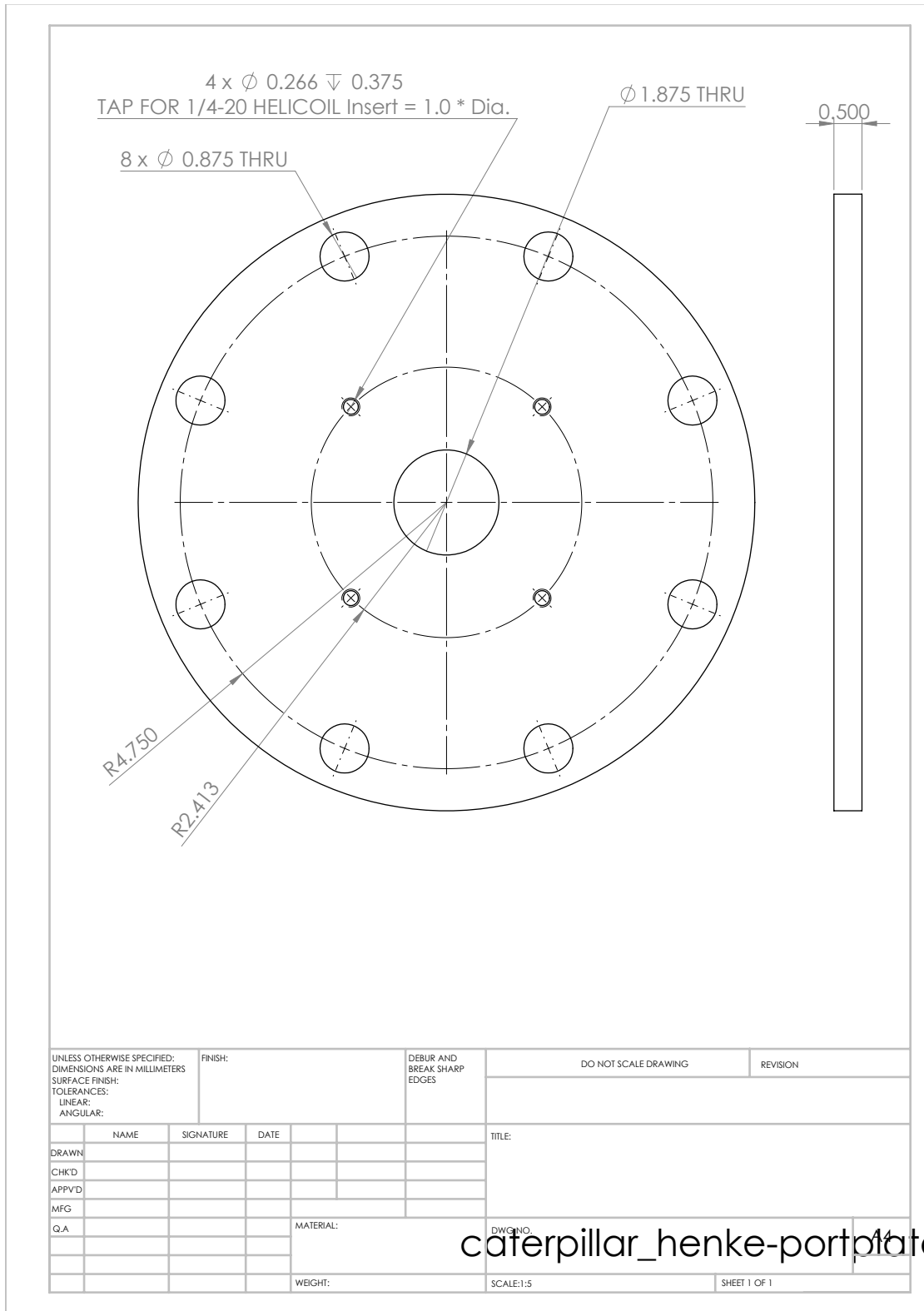


Figure A.8: Henke tube source port plate

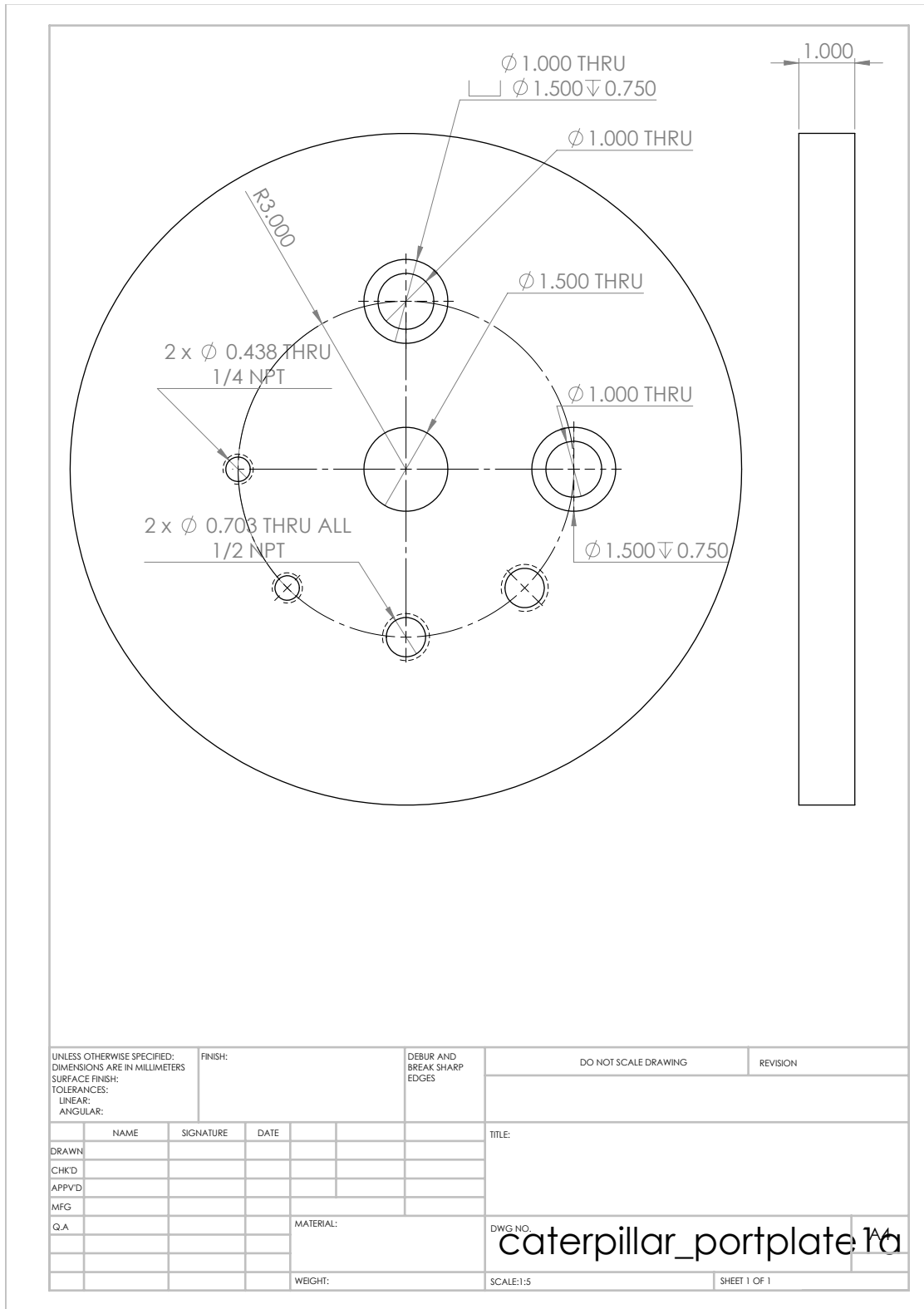


Figure A.9: (Continued on the following page.)

Figure A.9: Port plate containing all of the QE test stand feedthroughs. The two 1/2 inch NPT were used for the HV coaxial feedthrough that carried the proportional counter high voltage and the coaxial feedthrough that carried the proportional counter signal. The 1/4 inch NPTs are the proportional counter gas input and vent. The two large holes are for circular bayonet connectors.

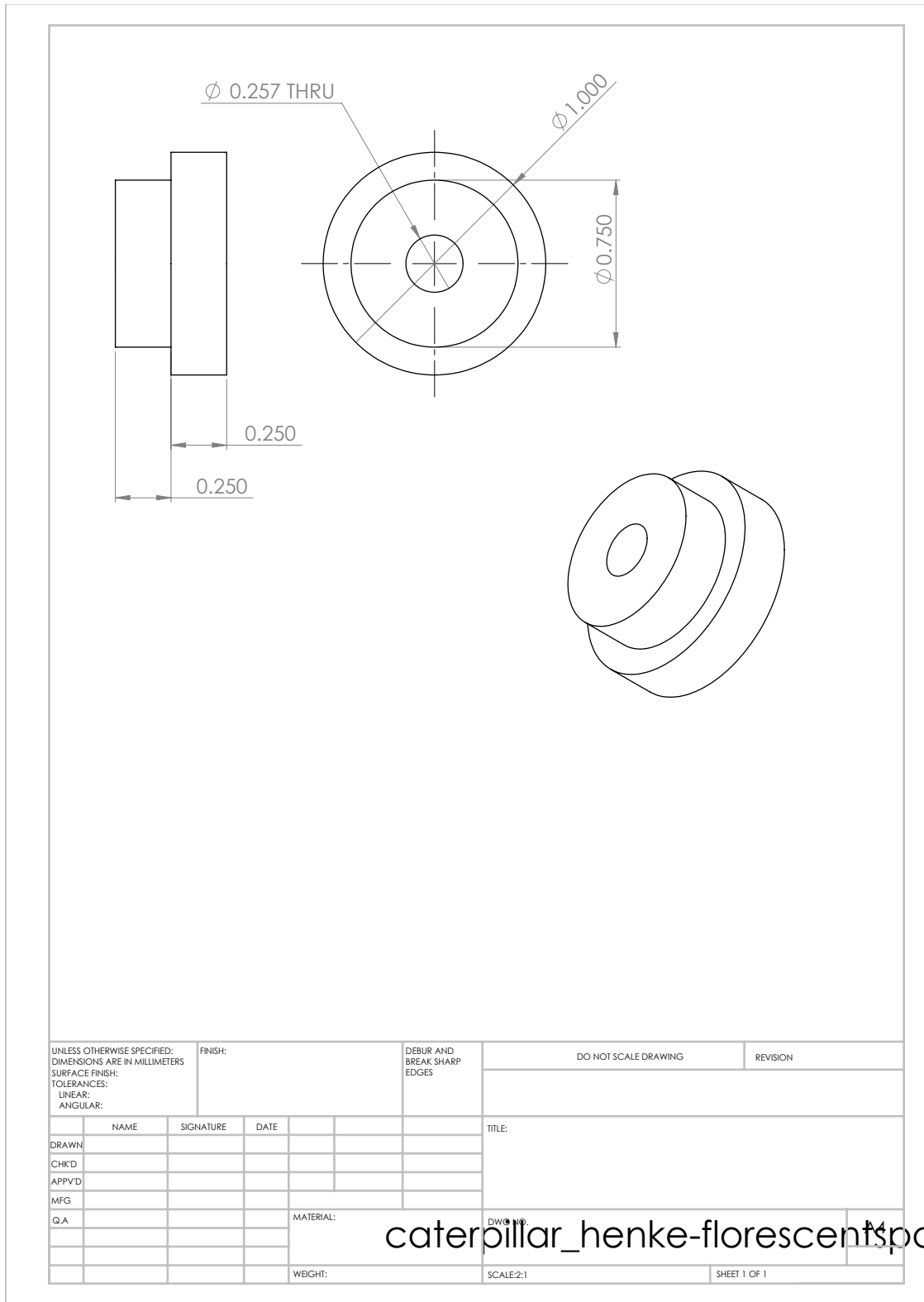


Figure A.10: Spacers that allow attaching the fluorescent target wheel to the Henke tube source port plate

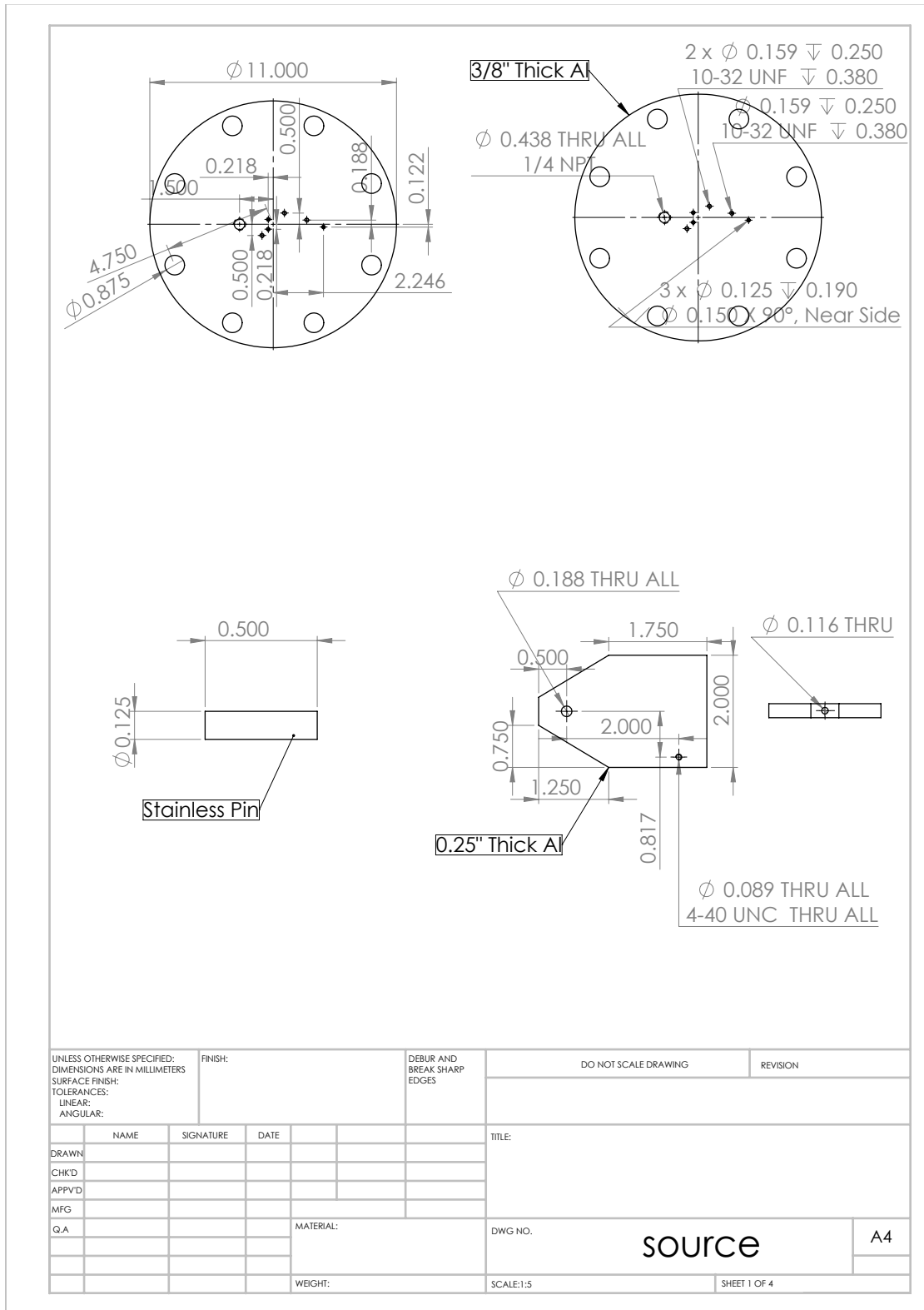


Figure A.11: Top, the source port plate. Bottom, the source shutter.

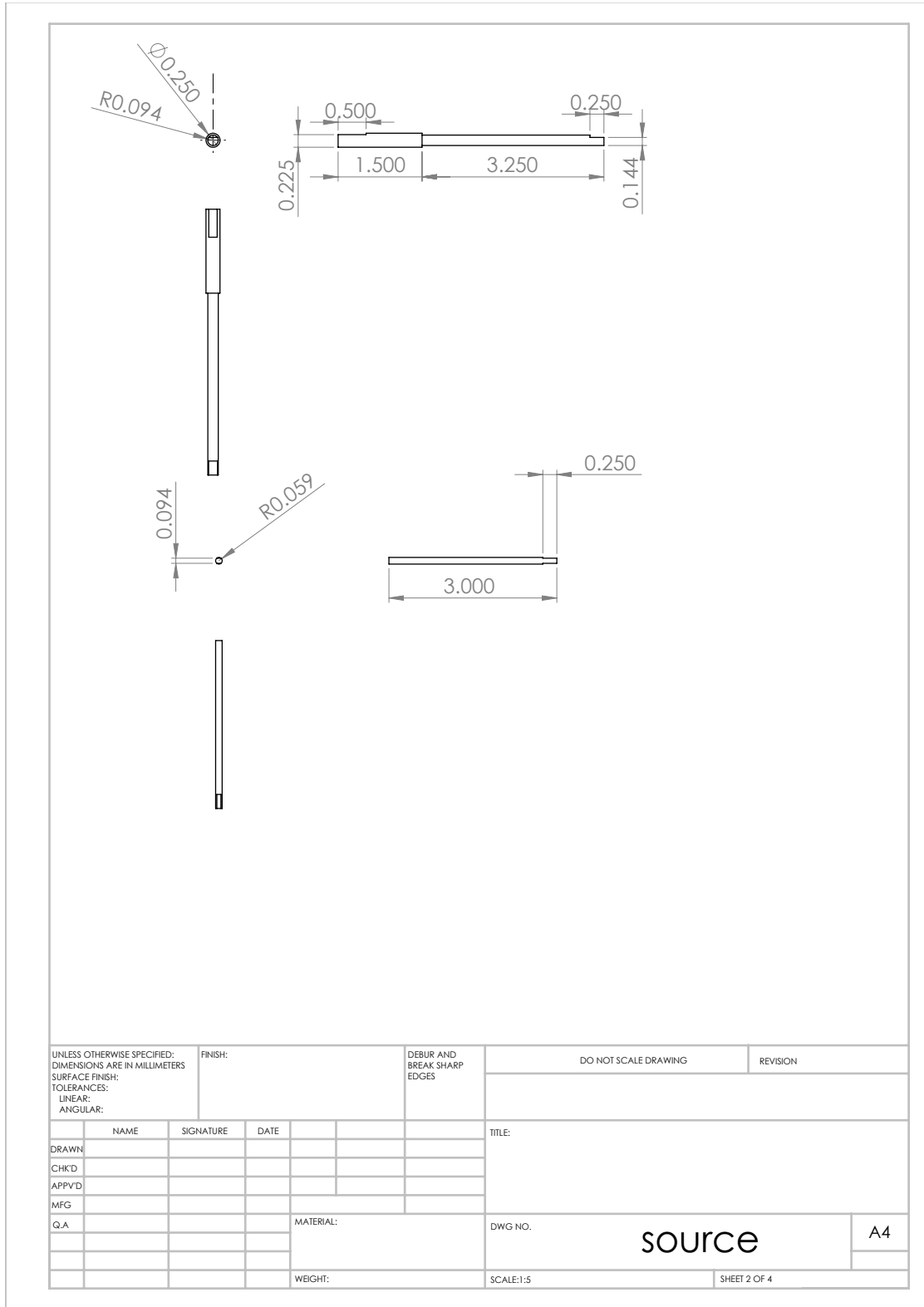


Figure A.12: The source holder rod and shutter rotational feedthrough shaft.

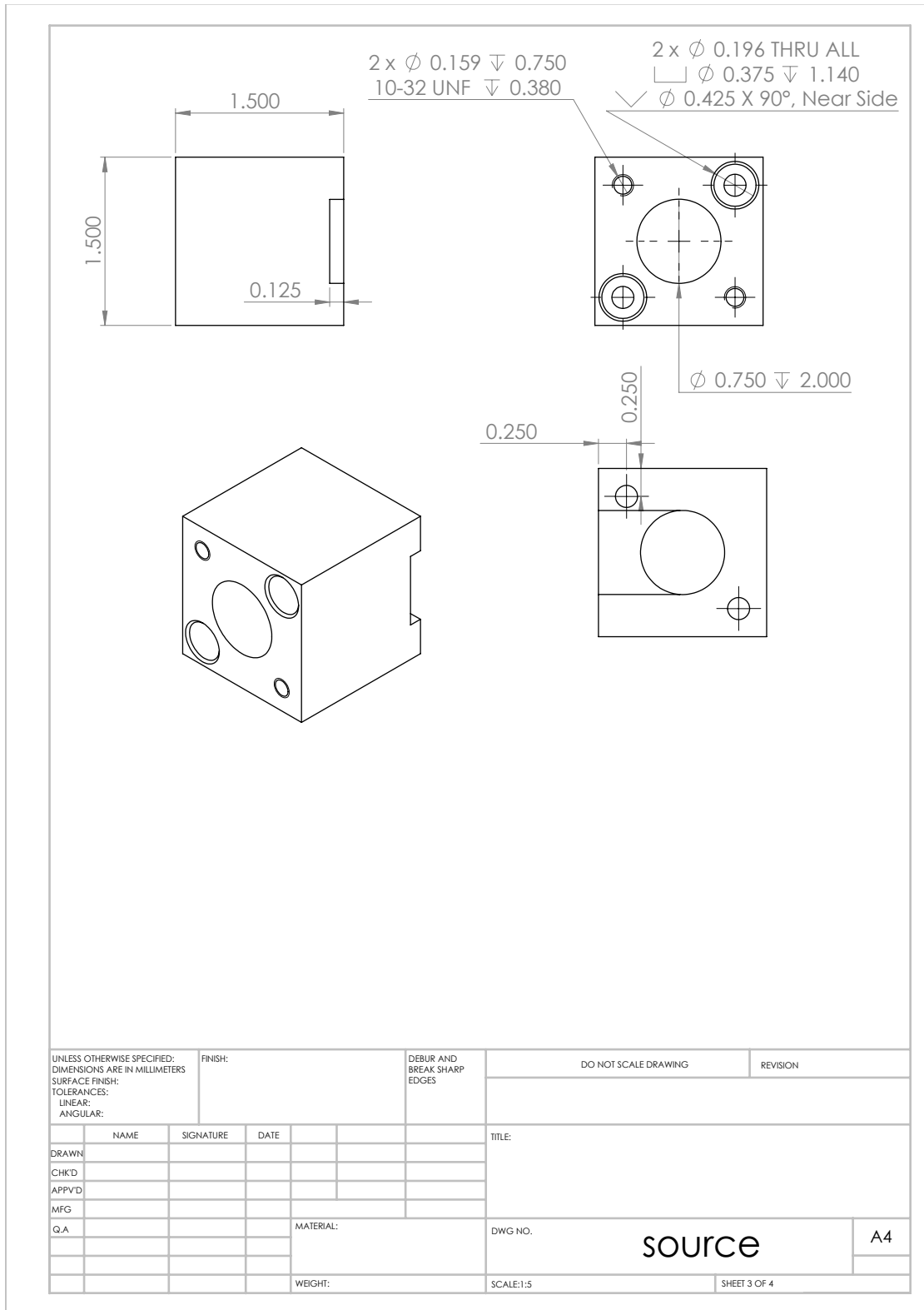


Figure A.13: The source shield.

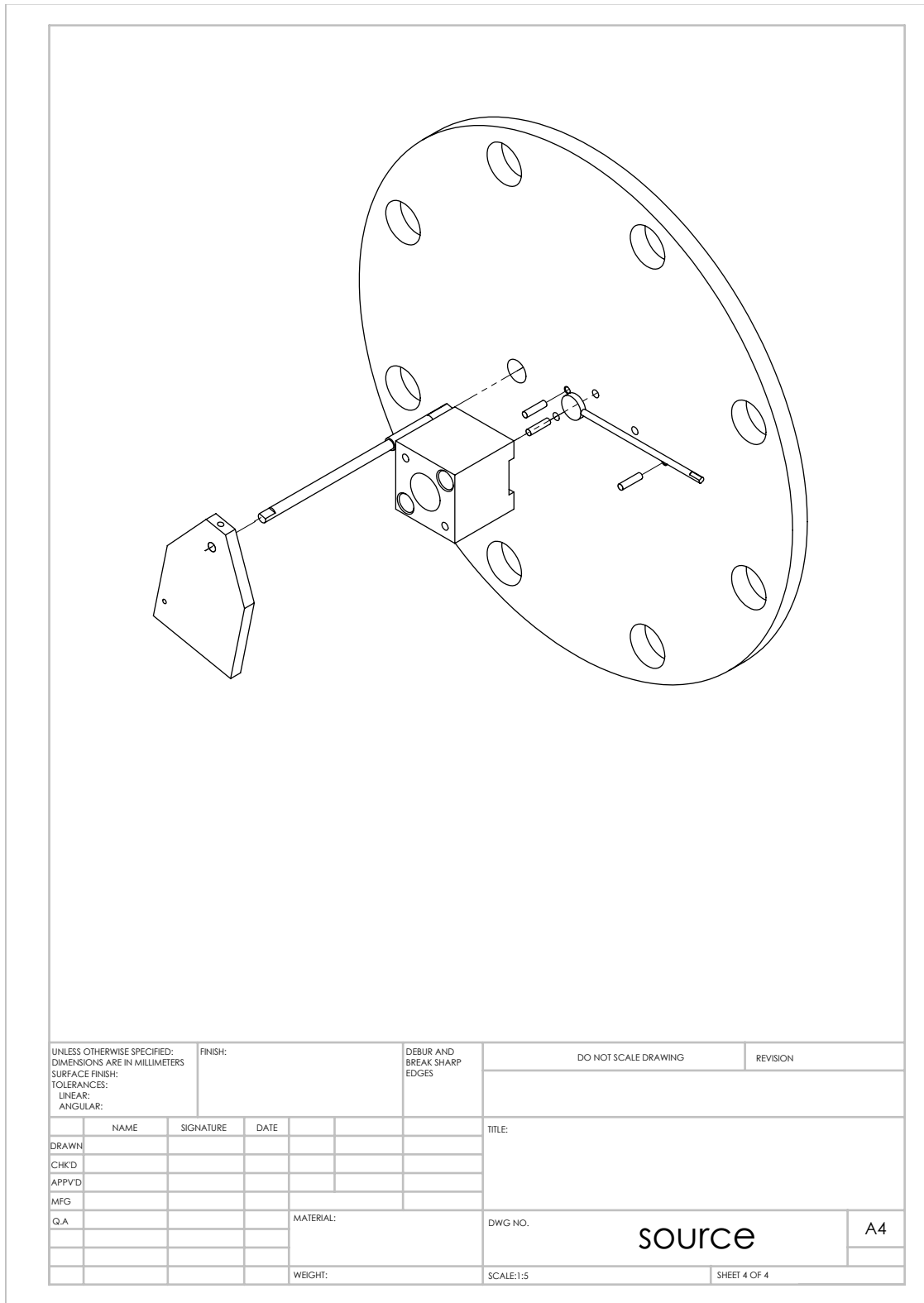


Figure A.14: An exploded view of the source plate.

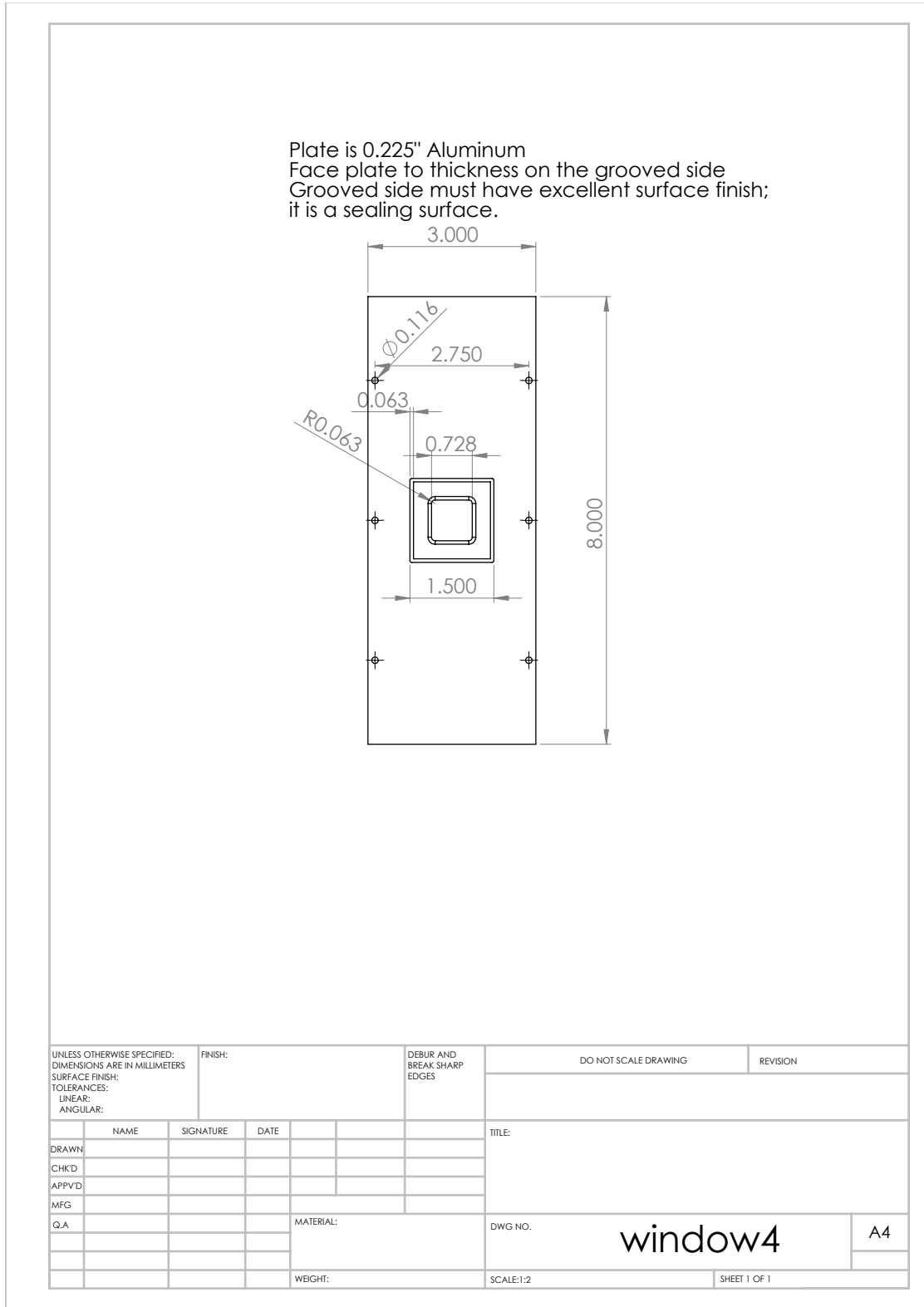


Figure A.15: Proportional counter window plate.

Appendix **B**

Electronics Schematics

B.1 Introduction

This appendix contains the schematics, layouts, and design notes for two electronics boxes that were designed and built for the QE test stand. The circuit boards are 4 layer boards designed with the proprietary software from and fabricated by www.expresspcb.com. Board layers are shown in the same order in which they are stacked in the board.

B.2 QE Test Stand

B.2.1 Heater Power Supply

The board takes four analog signals produced by the NI DAQ analog outputs (AOs) as input and outputs four lines that each power a Watlow Firerod 0.125 inch diameter by 1.25 inch long cartridge heater. The board is powered by an external +36 V and 0 V from a DC power supply. This circuit consists of four parallel, low-gain, high-power amplifiers, shown in Figure B.1. Each of the four amplifier circuits is built around an OPA 548 operational amplifier (opamp). Amplifiers are divided into classes A-D based on how they function. Class A-C amplifiers operate by using the input voltage to alter the rail voltage's conduction to the output. Class A are always on, making them low-distortion, high-frequency amplifiers that have very poor efficiency. Class B and C improve efficiency by turning the amplifier

off for portions of the input signal's cycle, but this results in increased distortion. The OPA 548 is the Class-D variety, which is also known as a switching amplifier. Such devices work by switching the rail's conduction to the output on and off very quickly with a duty cycle controlled by the input voltage. The output is passed through a low-pass filter removes the fast swings in the switched voltage, producing a smooth output. These amplifiers have high efficiency because the amplifier itself is either on or off and spends very little time in transition between the two states. Therefore they are useful for producing small, high power circuits, such as this heater power supply.

Although the OPA 548 is capable of producing 3 A when attached to an appropriately large heat sink, I limited the output near 2 A to add a margin of safety for the amplifiers. The current limit resistor, called R_{CL} in the OPA 548 application notes, was set at 20 k Ω so that each circuit would be current limited at approximately $I_{LIM} \approx 2.1$ A, according to

$$R_{CL} = \frac{15000 \cdot 4.75}{I_{LIM}} - 13750\Omega. \quad (\text{B.1})$$

The shown capacitors, known in this configuration as decoupling capacitors, conduct electromagnetic interference (EMI) and power supply noise to ground, leaving only the DC voltage. The capacitor values of $C_1 = 10 \mu\text{F}$, $C_2 = 0.1 \mu\text{F}$, and $C_3 = 0.01 \mu\text{F}$ were chosen according to the application note's suggestions and provide effective noise suppression over a range of frequencies.

On the advice of Fred Hearty, the heater was designed to operate in the range of 5 W, and I chose to overbuild it to a 25 W capability. The choice of $R_2 = 6$ k Ω and $R_1 = 1$ k Ω yields a gain, $G = 7$, according to

$$G = 1 + \frac{R_2}{R_1}. \quad (\text{B.2})$$

Given this gain, the intentionally restricted 0-5 V output swing of the DAQ AOs, and the heater (load) resistance of $R_L = 51 \Omega$, the heater is capable of generating between 0 and 25.4 W. Since the heaters are 0.125 inch diameter cylinders that are 1.25 inches long, this leads to a Watt density of $25.4/1.25 \cdot 0.1252\pi = 25.9$ W/in², which is far less than the heater's specified maximum Watt density of 400 W/in². However, these numbers are contingent on good thermal contact with the

material to be heated. I attempted to make a dry connection with high contact area between the cartridge heater and the detector mounting plate with a press fit. A Watlow[®] representative assured me that this was a good idea. Unfortunately, due to measured irregularities in the heater's outer diameter on the order of 0.0005 inches, and the relative fragility of the heaters, we destroyed one while trying to perform a press fit. Despite cooling the heater in LN2 and heating the block with a hot air heat gun, which added ~ 0.0005 inches of clearance, the press fit failed. We later drilled the heater hole in the detector mounting plate so that the heater freely fit, and made good thermal contact between the two components with Apiezon[®] N grease. Since the coefficient of thermal expansion of copper is larger than that of the heater's stainless steel sheath, the fit will get tighter at cryogenic temperatures. This eliminates the possibility of a runaway cooling scenario, where as the detector assembly cools, thermal contact between the heater and detector mounting plate decreases, reducing the heater's ability to transfer heat to the detector.

The amplifier's heat sink requirement was calculated according to

$$T_J = T_A + P_D \theta_{JA}, \quad (\text{B.3})$$

where $\theta_{JA} = \theta_{JC} + \theta_{CH} + \theta_{HA}$. In this equation T_J is the junction temperature ($^{\circ}\text{C}$), T_A is the ambient temperature ($^{\circ}\text{C}$), P_D is the power dissipated (W), θ_{JC} is the junction-to-case thermal resistance ($^{\circ}\text{C}/\text{W}$), θ_{CH} is the case-to-heat sink thermal resistance ($^{\circ}\text{C}/\text{W}$), θ_{HA} is the heat sink-to-ambient thermal resistance ($^{\circ}\text{C}/\text{W}$), and θ_{JA} is the junction-to-air thermal resistance ($^{\circ}\text{C}/\text{W}$). Interestingly, the power dissipated by the OPA 548 does not depend linearly on the output voltage, but instead goes as $P_D = I_L(V_S - V_O)$, where V_S is the supply voltage, V_O is the output voltage, and $I_L = V_O/R_L$ is the load (output) current. The power dissipation into the amplifier component starts low for low output, reaches a maximum of 5 W per amplifier when $V_O = 18$ (half of the supply), and then becomes small again when for large output. Choosing a maximum amplifier junction temperature $T_J < 125$ $^{\circ}\text{C}$ (150 $^{\circ}\text{C}$ minus a 25 $^{\circ}\text{C}$ safety margin), a maximum expected ambient air temperature of $T_A < 40$ $^{\circ}\text{C}$, known $\theta_{JC} = 2.5$ $^{\circ}\text{C}/\text{W}$, a typical value of $\theta_{CH} = 1$ $^{\circ}\text{C}/\text{W}$ for a TO-220 package, we can solve for the heat sink size, θ_{HA} . Given 4 amplifiers running at maximum P_D , $\theta_{HA} < 3$ $^{\circ}\text{C}/\text{W}$ is required. For heat sink

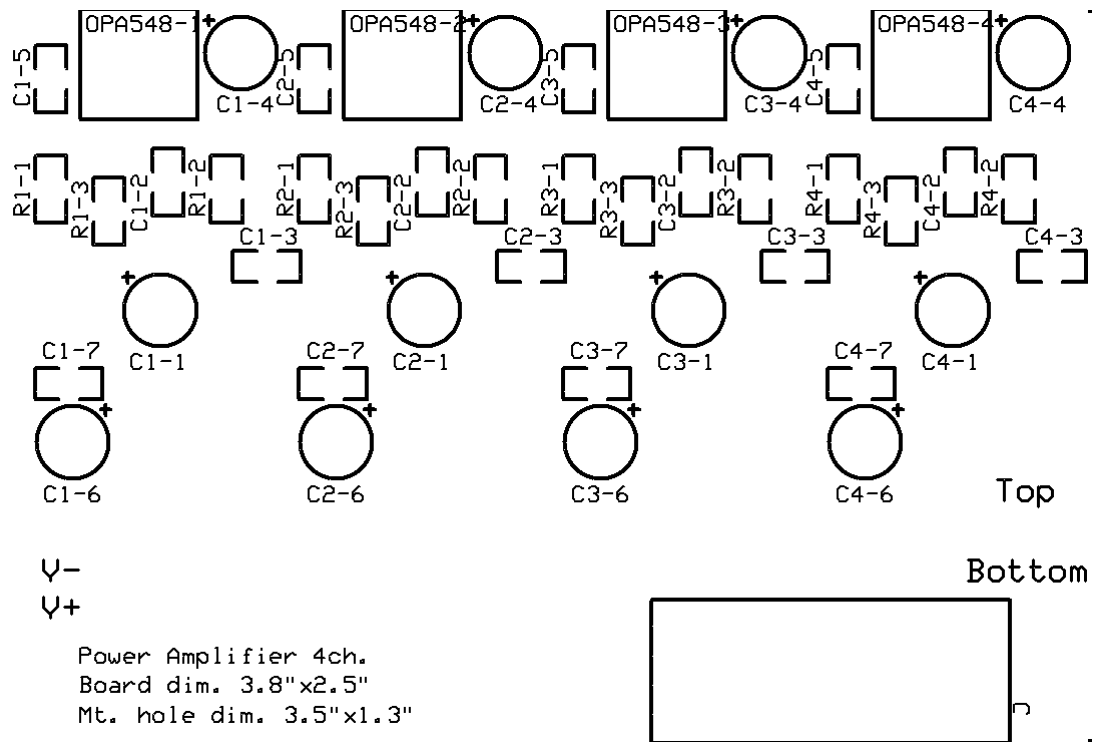


Figure B.2: Heater power amplifier top surface silk screen.

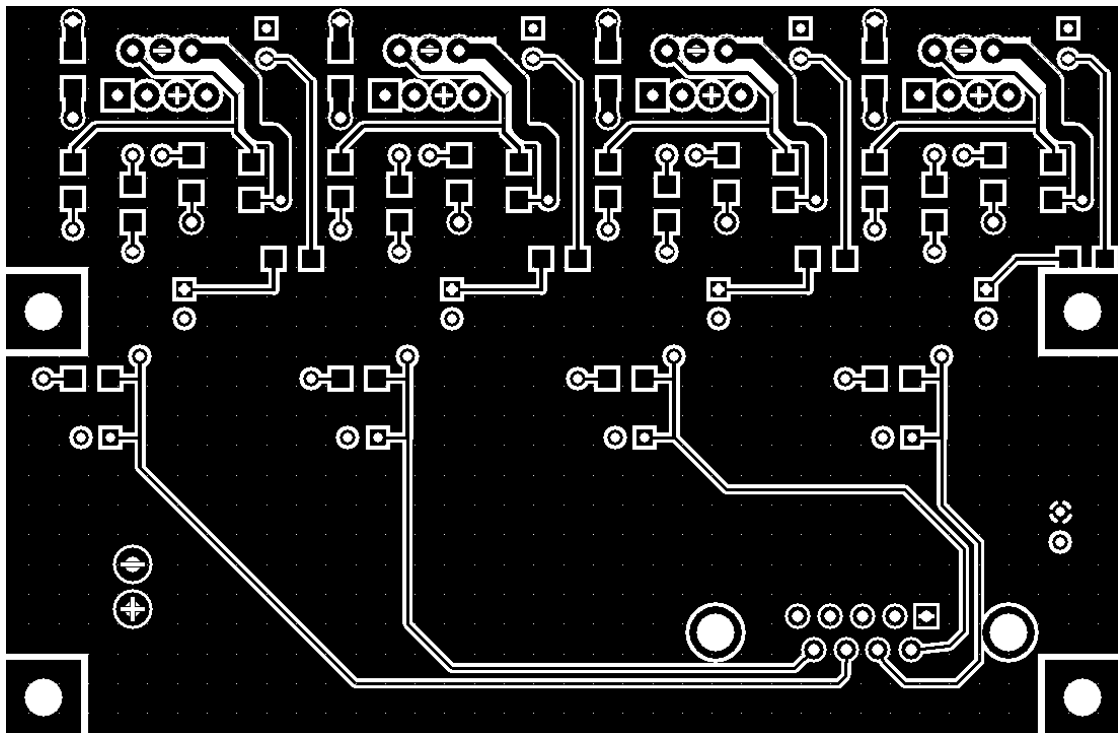


Figure B.3: Heater power amplifier top copper trace deposition.

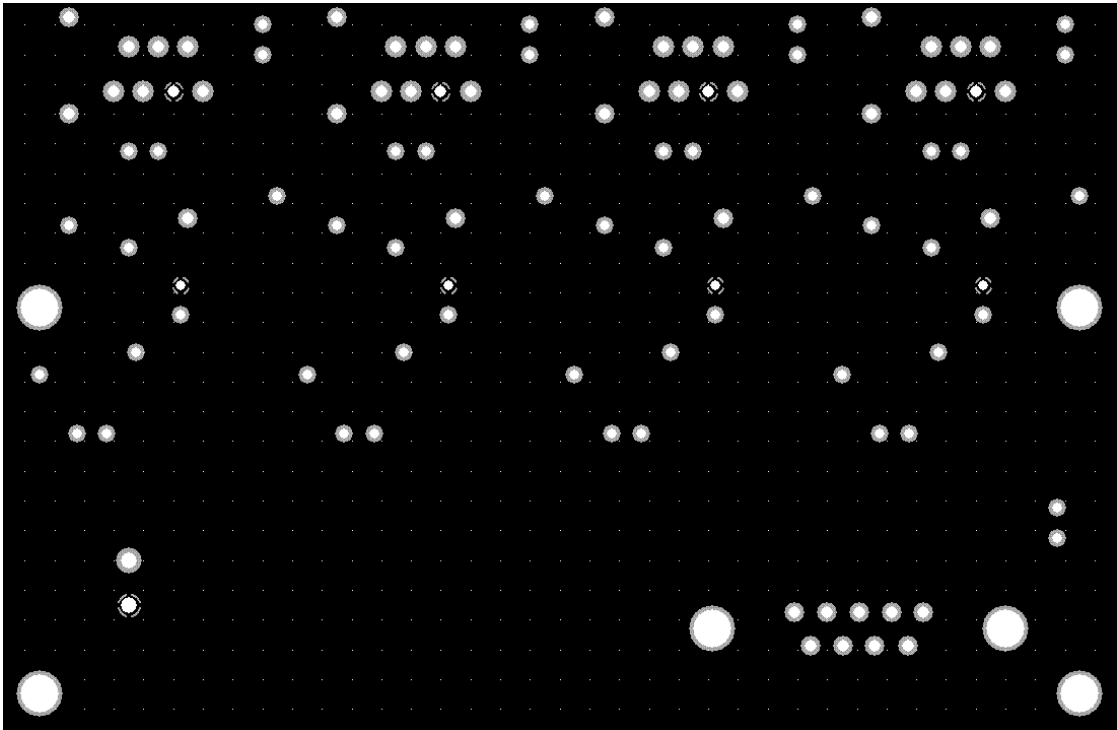


Figure B.4: Heater power amplifier upper inner power plane.

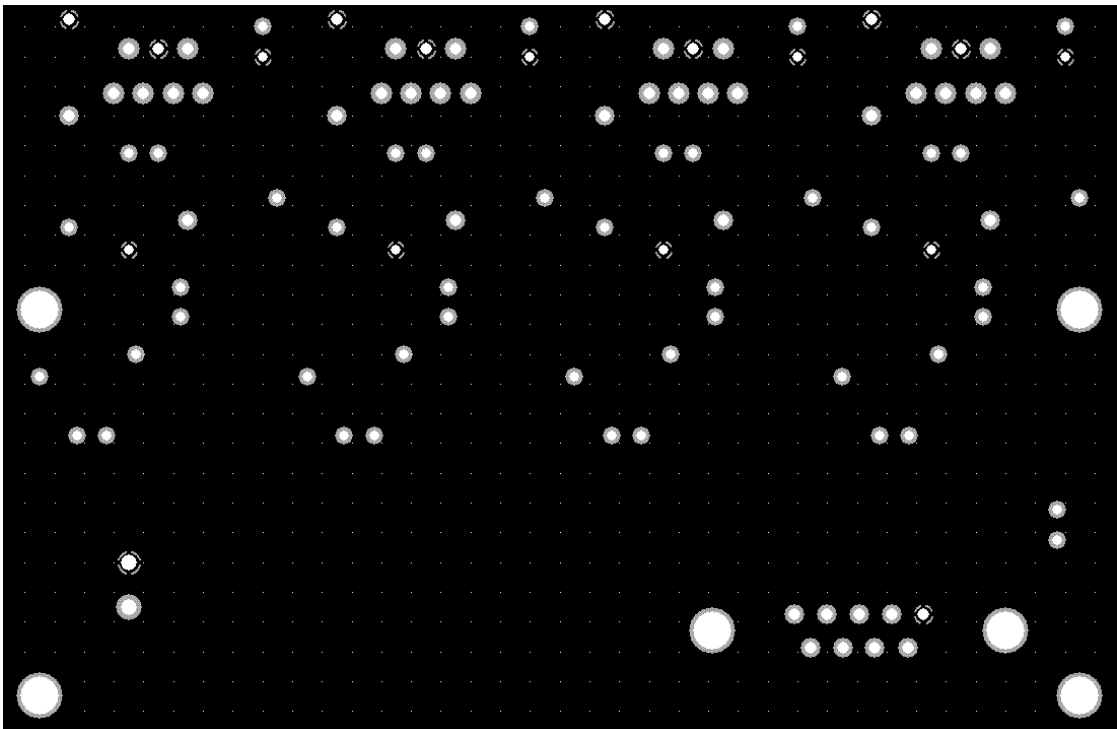


Figure B.5: Heater power amplifier lower inner ground plane.

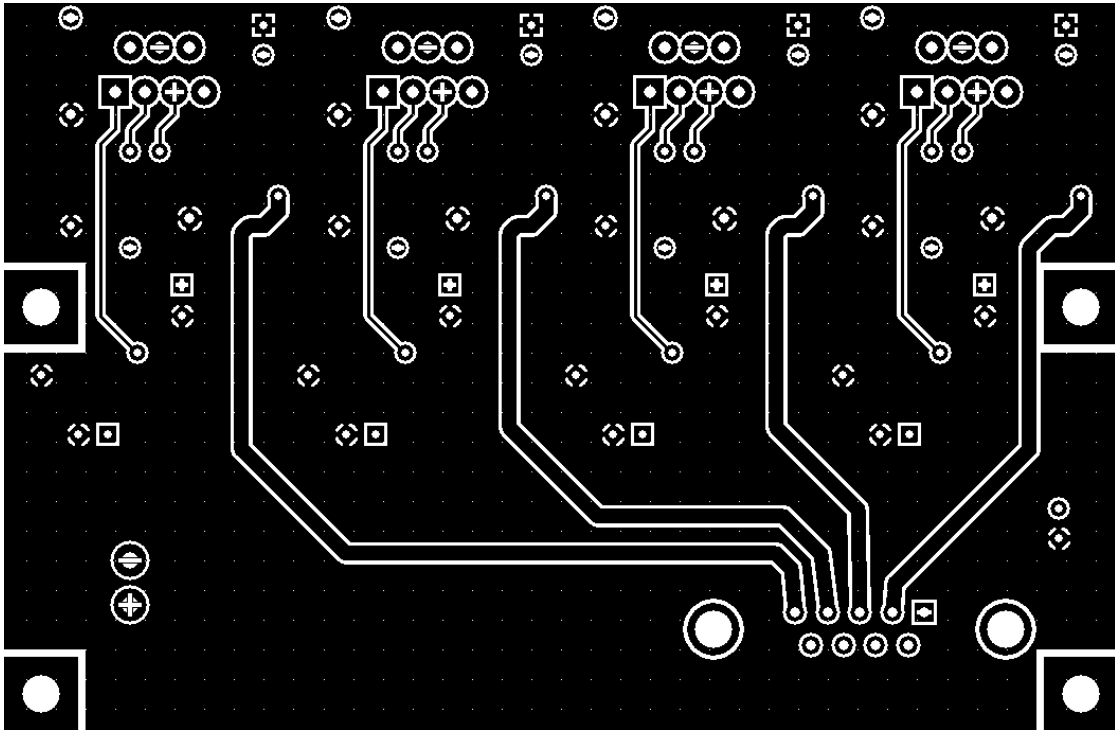


Figure B.6: Heater power amplifier bottom copper trace deposition.

USB port, or the NI DAQ digital out (DO) ports. A more serious design solution would digitally interface with the computer through one of the listed means, and use a digital to analog converter (DAC) to drive the power amplifier input.

B.2.2 RTD Current Source

This board outputs six constant current lines that each run to one of six PT-111 Lakeshore platinum RTD temperature sensors. Voltage probe lines from a NI DAQ enter the RTD current source box so that the voltage across the sensors can be measured. The current source circuit design, shown in Figure B.8 was adapted from an Analog Designs white paper [134]. The design uses a voltage reference as input to a difference amplifier circuit. An operational amplifier provides feedback into the difference amplifier. Components were chosen to get a continuous current near 1 mA, which is the sensor stimulation current recommended by Lakeshore, the temperature sensor manufacturer.

If I were to design this again, I would have the current be pulsed instead of

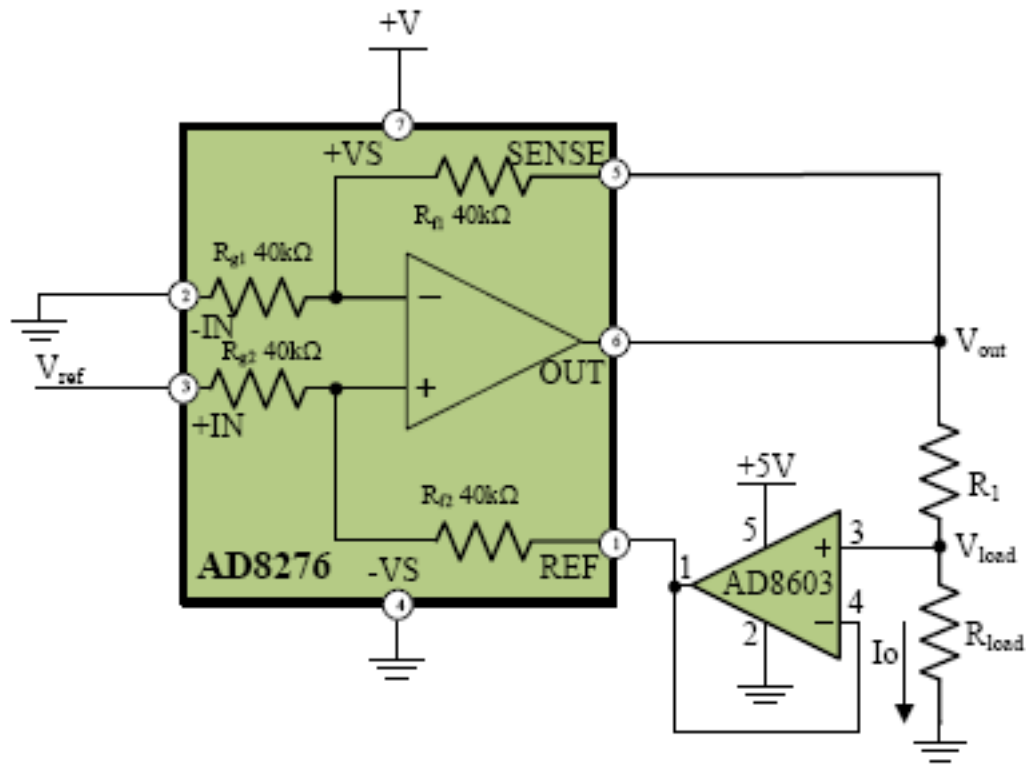


Figure B.7: The chosen difference amplifier configuration. This circuit creates an accurate current source for output currents less than 15 mA, the drive capability of the AD8276.

continuous. In the pulsed case, the average wattage deposited into the RTD can be kept the same as in the continuous current case ($0.988 \text{ mA } 50\Omega = 49 \text{ mW}$), but a higher current can be used. This will produce a larger voltage drop that will result in a higher S/N measurement at the DAQ. This could be implemented by generating a clock at a digital output of the DAQ with the temperature control VI. If the temperature clock were taken as an input to the current source, the DAQ's voltage measurement, which is controlled by the VI, and the current pulse could be synchronized.

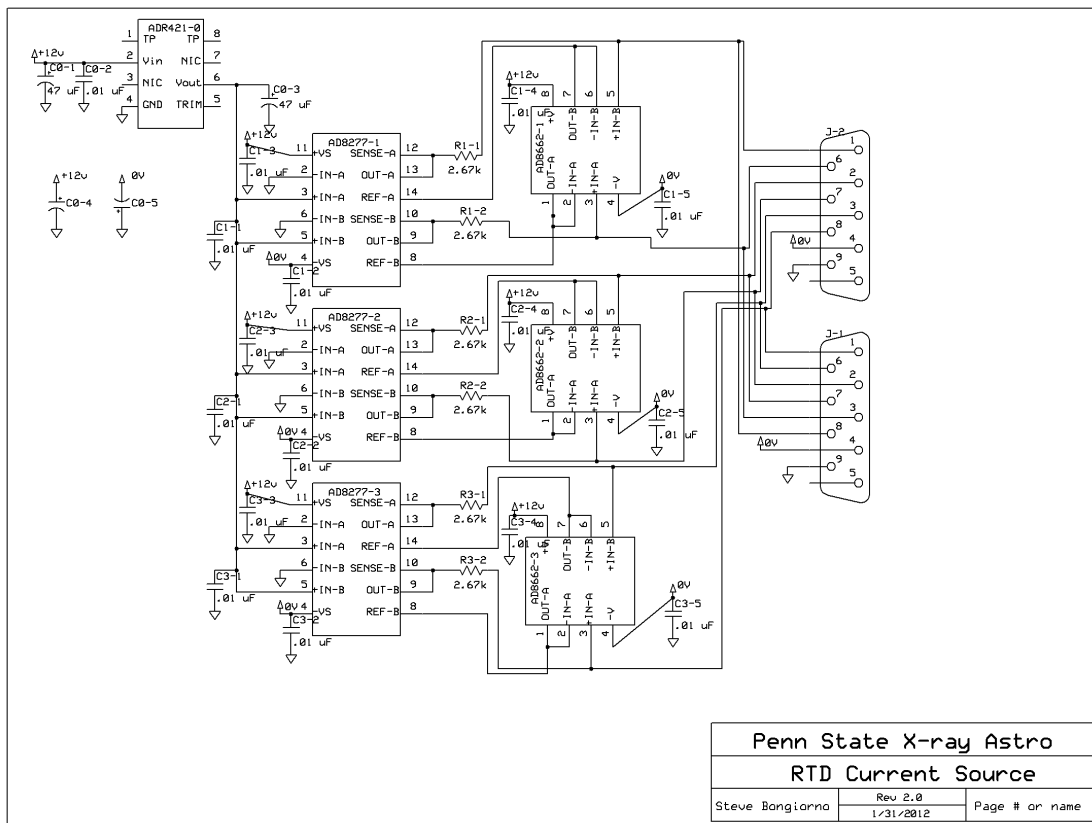


Figure B.8: Schematic of the 6-channel RTD current source.

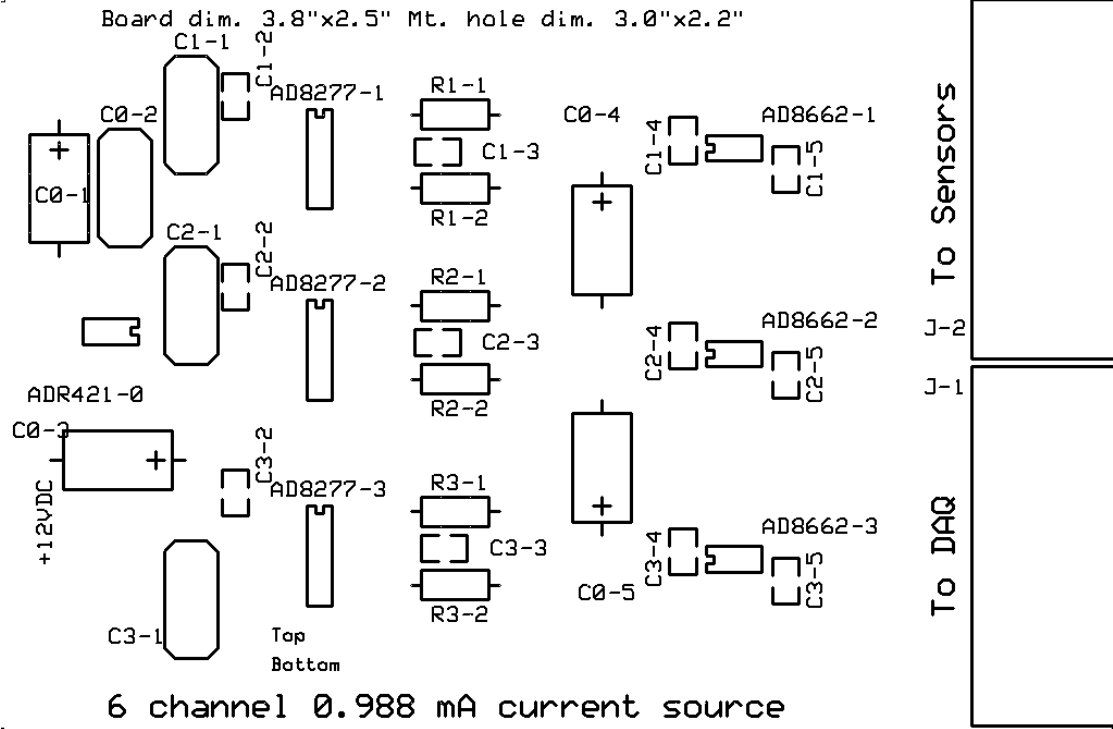


Figure B.9: Current source top surface silk screen.

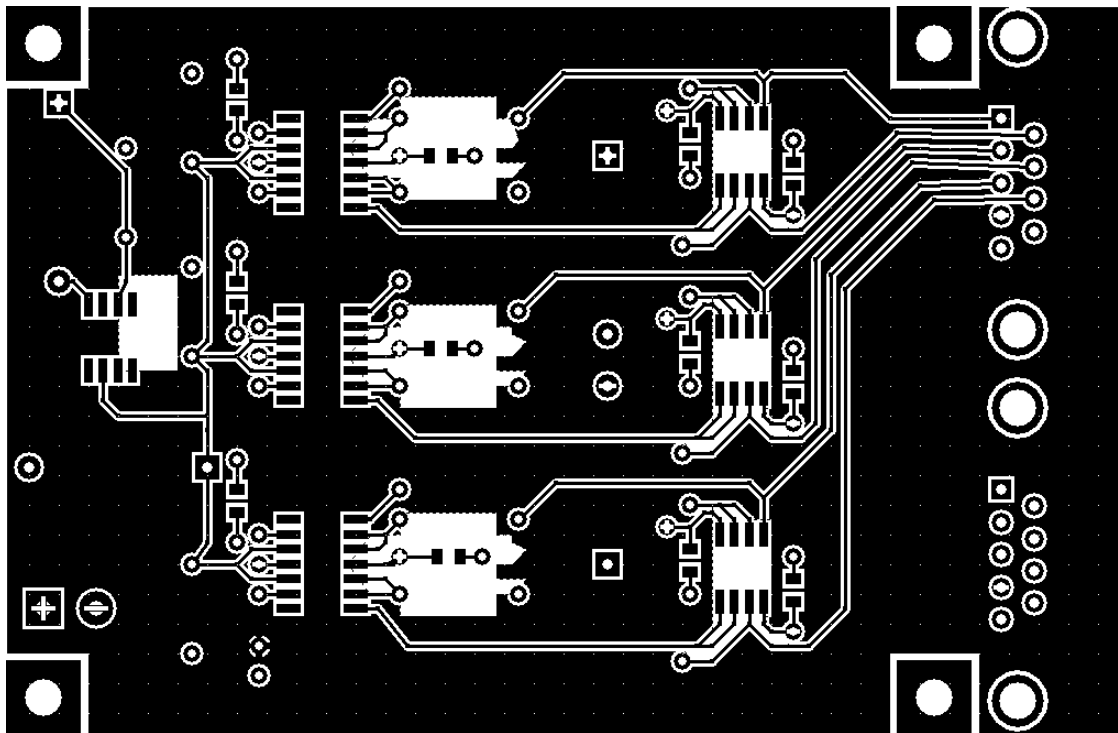


Figure B.10: Current source top layer copper deposition.

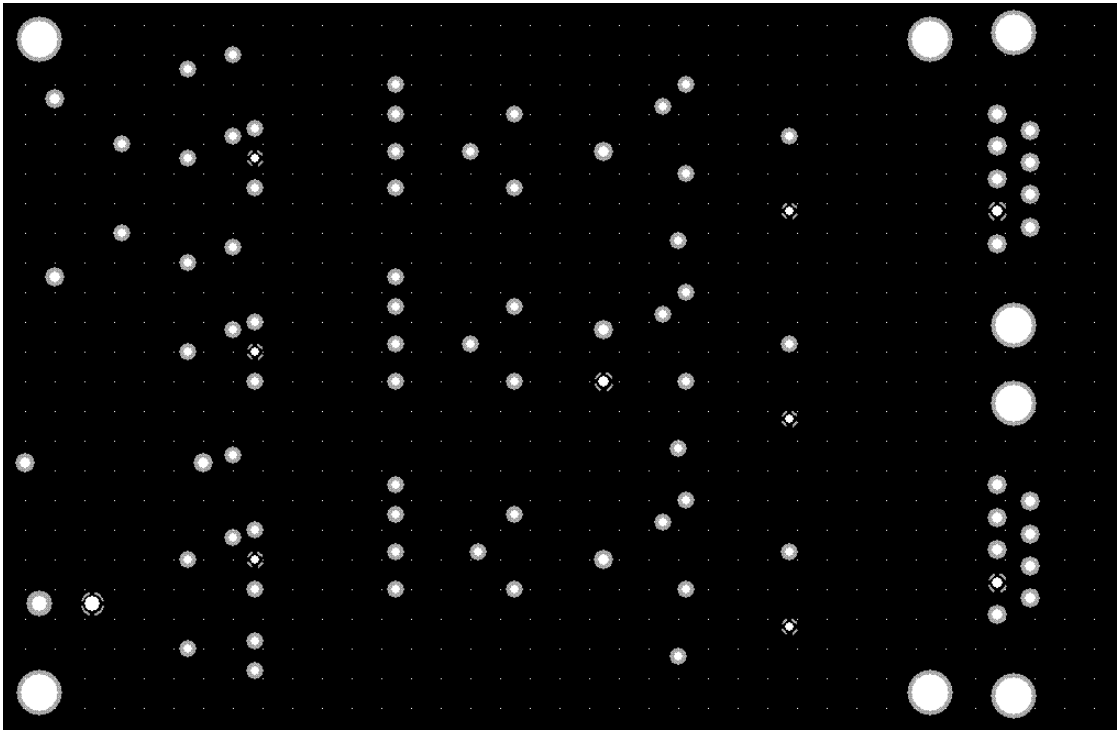


Figure B.11: Current source top inner copper layer.

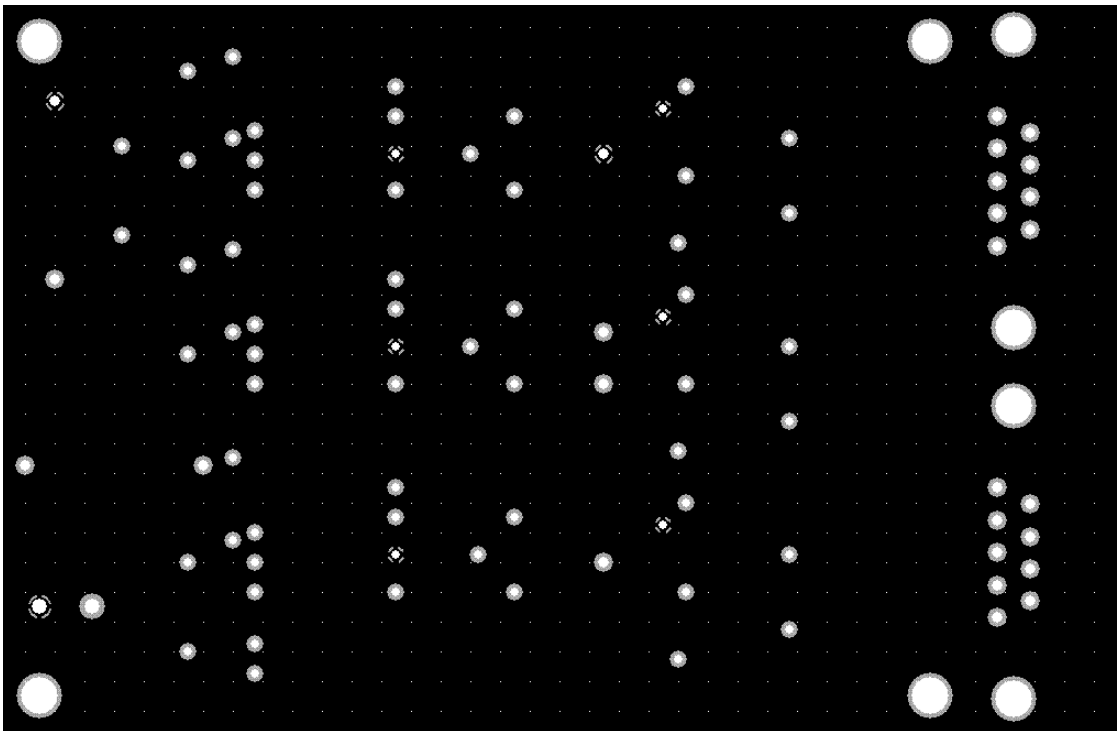


Figure B.12: Current source bottom inner copper layer.

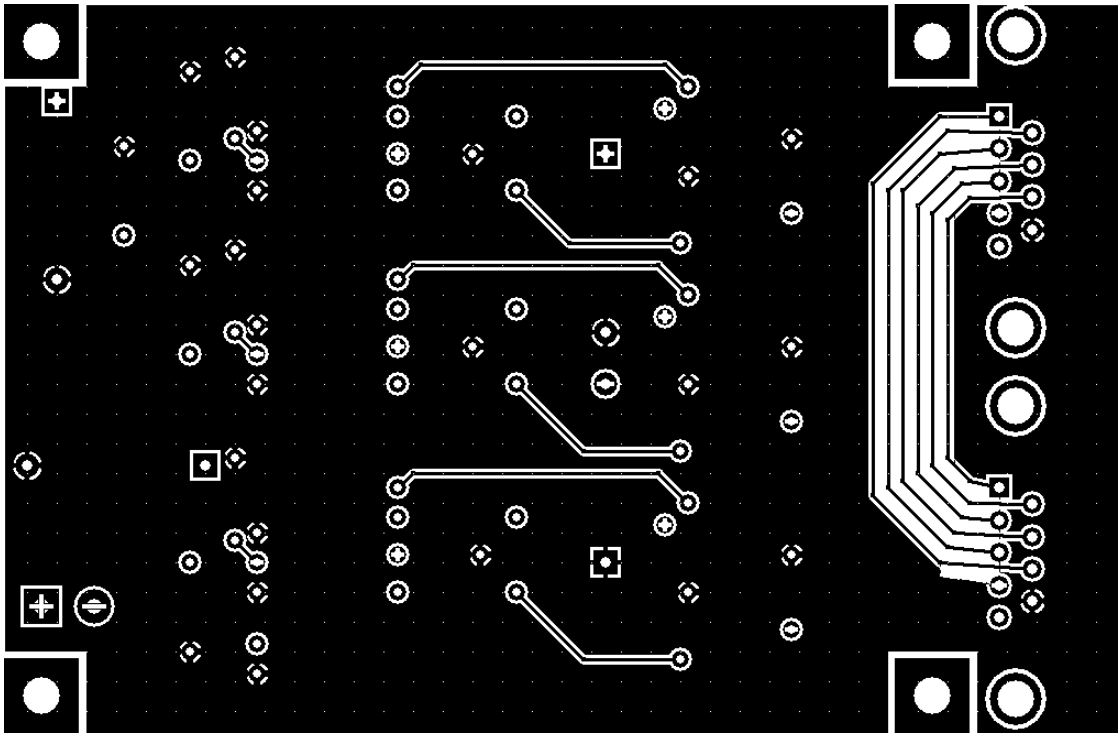


Figure B.13: Current source bottom layer copper deposition.

Appendix **C**

Code

C.1 Introduction

All original codes used in this thesis are listed here, grouped into three categories: *Data reduction* (Chapter 3), which were used to reduce and visualize X-ray HyViSI data, *QE Teststand* (Chapter 4), which were used to process and reduce data produced by the QE test stand, and *Thesis*, which were used to make demonstrative calculations presented in this thesis. In each section, the codes are listed in alphabetical order.

C.2 Data Reduction

- `calc_ipc.pro`
- `disp_evts.pro`
- `event_detect.pro`
- `evt_filter.pro`
- `grade_evts.pro`
- `make_evtlist.pro`
- `pixcal.pro`


```

;           save      :           saves plots to file. [not working]
;-
ntest = 100      ; number of points to test thresholds
events = evt_filter(events,cpixrange=[1200,4000]) ;only use iron data
           for IPC measurement

if not keyword_set(m1th) then m1th = 150      ; standard deviation
           threshold
if not keyword_set(m2th) then m2th = 60 ;constant 2nd brightest pix
           threshold
if not keyword_set(m3th) then m3th = 0.05 ;fraction 2nd brightest pix
           threshold
;;;;;;;;;;;;;;;;;;;;;;;;;;;;;;;;;;;;;;;;;;;;;;;;;;;;;;;;;;;;;;;;;;;;;;;;;;;;;;;;
print, "Calculating method 1-----"
ipc = dblarr(9,ntest)
m1th = dindgen(ntest)*m1th/(ntest-1) ; turning the max m1th into the
           array of m1th to test
n_evts = lindgen(ntest)
for j=0,ntest-1 do begin
           counter,j,ntest-1
           dev = dblarr(9,n_elements(events.x))
           sum=lonarr(n_elements(events.x))

           ; finding average of all secondary pixels in each event and
           storing it in vector 'ave'
           for i=0,8 do if i ne 4 then sum=sum+events.island[i] ; skipping
           center pix
           ave=sum/8.

           ; finding the squared deviation from average, summing, and taking
           square root. this is standard deviation.
           for i=0,8 do dev[i,*]=(events.island[i]-ave)^2
           sum=lonarr(n_elements(events.x))
           for i=0,8 do if i ne 4 then sum=sum+dev[i,*] ; skipping center
           pix
           standev=sqrt(sum/8.)

           ; for events with secondary pixel standard deviation less than
           the m1th, averaging all events
           index = where(standev lt m1th[j])
           for i=0,8 do ipc[i,j]=total(events[index].island[i])/n_elements(
           index)
           n_evts[j] = n_elements(index)
           ; normalizing the kernel to 1
           ipc[* ,j] = ipc[* ,j]/total(ipc[* ,j])
endfor

window,/free
plot, m1th,n_evts,xtitle='Standard Deviation Threshold [DN]',ytitle='
           Number of events used',/ylog,title='Method 1',ystyle=8,xmargin
           =[10,10]
axis, yrange=[0,1.1],yaxis=1,/save,ytitle='% charge outside center pix.'
oplot,m1th,sum/(sum+ipc[4,*])

```

```

window,/free
sum = ipc[0,*]
for i=1,8 do if i ne 4 then sum = sum+ipc[i,*]
plot, m1th,sum/(sum+ipc[4,*]),xtitle='Standard Deviation Threshold [DN]'
    ,ytitle='percent charge outside center pixel',title='Method 1'
read, 'What method 1 threshold do you want to use to calculate IPC? ',x
temp = min(abs(m1th-x),best) ;finding the m1th value closest to what the
    user typed into x
; printing the result
;;;;;;;;;;;;;;;;;;;;;;;;;;;;;;;;;;;;;;;;;;;;;;;;;;;;;;;;;;;;;;;;;;;;;;;;;;;;;;;;
print, "Method 1 - Secondary pixel standard deviation limit -----"
print, "Used "+strcompress(string(n_evts[best]))+" events to calculate:
print, ""
print, reform(ipc[*,best],3,3)
print, "The nodal capacitance calculated from this IPC kernel is: ",
print, "Up capacitance: ",
print, "Down capacitance: ",
print, "Left capacitance: ",
print, "Right capacitance: ",
print, "-----"

if keyword_set(save) then begin
    printplot
    set
    plot, m1th,n_evts,xtitle='Standard Deviation Threshold [DN]',
        ytitle='Number of events used',/ylog,title='Method 1'
    plot, m1th,sum/(sum+ipc[4,*]),xtitle='Standard Deviation
        Threshold [DN]',ytitle='percent charge outside center pixel',
        title='Method 1'
    printplot, /normal
endif

print, 'Calculating Method 2 -----'
ipc = dblarr(9,n_test)
m2th = dindgen(n_test)*m2th/(n_test-1) ; turning the max m1th into the
    array of m1th to test
n_evts = lindgen(n_test)

for j=0,n_test-1 do begin
    counter,j,n_test-1

    ;finding the brightest secondary pixel in each event
    brightest=events.island[0]
    island = events.island[[0,1,2,3,5,6,7,8]] ; skipping the center
        pixel
    for i=1,7 do begin
        pick = where(island[i,*] gt brightest,count)
        if count ne 0 then brightest[pick] = island[i,pick]
    endfor
    ; Do i use a constant DN threshold for m2th or should it be a
        fraction of the primary pixel?

```

```

; here I try a constant threshold. note it will only apply for
; one energy xray since a different energy primary will put a
; different amount of charge into the secondary pixels.

index = where(brightest lt m2th)
for i=0,8 do ipc[i,j]=total(events[index].island[i])/n_elements(
    index)
n_evts[j] = n_elements(index)
; normalizing the kernel to 1
ipc[* ,j] = ipc[* ,j]/total(ipc[* ,j])

endifor

window,/free
plot, m1th,n_evts,xtitle='2nd Brightest Pixel Threshold [DN]',ytitle='
    Number of events used',/ylog,title='Method 2'

window,/free
sum = ipc[0,*]
for i=1,8 do if i ne 4 then sum = sum+ipc[i,*]
plot, m1th,sum/(sum+ipc[4,*]),xtitle='2nd Brightest Pixel Threshold [DN]
    ',ytitle='percent charge outside center pixel',title='Method 2'
read, 'What method 2 threshold do you want to use to calculate IPC? ',x
temp = min(abs(m1th-x),best) ;finding the m1th value closest to where
    you clicked

; printing the result
print, "Method 2 - brightest secondary pixel limit -----"
print, "Used "+strcompress(string(n_evts[best]))+" events to calculate:
print, ""
print, reform(ipc[* ,best],3,3)
print, "-----"

if keyword_set(save) then begin
    printplot
    set
    plot, m1th,n_evts,xtitle='2nd Brightest Pixel Threshold [DN]',
        ytitle='Number of events used',/ylog,title='Method 1'
    plot, m1th,sum/(sum+ipc[4,*]),xtitle='2nd Brightest Pixel
        Threshold [DN]',ytitle='percent charge outside center pixel',
        title='Method 1'
    printplot, /normal
endif

print, "Calculating Method 3 -----"
ipc = dblarr(9,n_test)
m3th = dindgen(n_test)*m3th/(n_test-1) ; turning the max m1th into the
    array of m1th to test
n_evts = lindgen(n_test)

for j=0,n_test-1 do begin

```

```

counter, j, ntest-1

;finding the brightest secondary pixel in each event
brightest=events.island[0]
island = events.island[[0,1,2,3,5,6,7,8]] ; skipping the center
pixel
for i=1,7 do begin
    pick = where(island[i,*] gt brightest,count)
    if count ne 0 then brightest[pick] = island[i,pick]
endfor

; Do i use a constant DN threshold for m2th or should it be a
fraction of the primary pixel?
; Here I use the percentage. Like mark bautz said, i am biasing
the sample since i am saying what ipc is allowed into the
sample used for calculating ipc.

index = where(brightest lt m3th*events.island[4])

for i=0,8 do ipc[i,j]=total(events[index].island[i])/n_elements(
index)

; normalizing the kernel to 1
ipc[* ,j] = ipc[* ,j]/total(ipc[* ,j])
endfor

window,/free
plot, m1th,n_evts,xtitle='2nd Brightest % Pixel Threshold [DN]',ytitle='
Number of events used',/ylog,title='Method 3'

window,/free
sum = ipc[0,*]
for i=1,8 do if i ne 4 then sum = sum+ipc[i,*]
plot, m1th,sum/(sum+ipc[4,*]),xtitle='2nd Brightest % Pixel Threshold [
DN]',ytitle='percent charge outside center pixel',title='Method 3'
read, 'What method 3 threshold do you want to use to calculate IPC? ',x
temp = min(abs(m1th-x),best) ;finding the m1th value closest to where
you clicked

; printing the result
print, "Method 3 - brightest secondary % pixel limit -----"
print, "Used "+strcompress(string(n_evts[best]))+" events to calculate:
print, ""
print, reform(ipc,3,3)
print, "-----"

if keyword_set(save) then begin
    printplot
    set_plot, 'ps'
    device, filename=''
    plot, m1th,n_evts,xtitle='2nd Brightest % Pixel Threshold [DN]',
        ytitle='Number of events used',/ylog,title='Method 1'

```

```

device, /close
device, filename=', '
plot, m1th, sum/(sum+ipc[4,*]), xtitle='2nd Brightest % Pixel
      Threshold [DN]', ytitle='percent charge outside center pixel',
      title='Method 1'
device, /close
set_plot, 'x'
printplot, /normal
endif

; Method 4 -----
; myopic deconvolution

end



---


PRO disp_evts, events, index=index, evt_list=evt_list, output_name=
      output_name, quad=quad

; takes an IDL structure of events as input and produces a fits file
; showing the morphology of all of the events arranged for viewing
; index = [low index, high index] allows you to specify which events in
; the array you want to stick in the file.
; evt_list = an array of indices in events that you want to show with
; disp_evts
; output_name = the name given to the output fits file.
; quad = a switch that causes the use of 5x5 event regions instead of
; the usual 3x3

;;;;;;;;;;;;;;;;;;;;;;;;;
; initializing stuff
;;;;;;;;;;;;;;;;;;;;;;;;;

IF KEYWORD_SET(index) THEN events = events[index(0):index(1)]

IF KEYWORD_SET(evt_list) THEN events = events[evt_list]

num_evts = N_ELEMENTS(events.x)
PRINT, num_evts

num_width = FLOOR(SQRT(num_evts))

;;;;;;;;;;;;;;;;;;;;;;;;;
; assigning event islands into the image array
;;;;;;;;;;;;;;;;;;;;;;;;;
IF KEYWORD_SET(quad) THEN BEGIN

      array = FLTARR(num_width*6+1, (num_width+2)*6+1)
      FOR i=0L, num_evts-1 DO BEGIN
            temp = DBLARR(5,5)
            temp[*,0] = events[i].reef[0:4]
            temp[0,1] = events[i].reef[5]
            temp[1:3,1] = events[i].island[0:2]
            temp[4,1] = events[i].reef[6]

```

```

temp[0,2] = events[i].reef[7]
temp[1:3,2] = events[i].island[3:5]
temp[4,2] = events[i].reef[8]
temp[0,3] = events[i].reef[9]
temp[1:3,3] = events[i].island[6:8]
temp[4,3] = events[i].reef[10]
temp[*,4] = events[i].reef[11:15]

array[6*(i MOD num_width)+2-2:6*(i MOD num_width)+2+2,6*
      FLOOR(i/num_width)+2-2:6*FLOOR(i/num_width)+2+2] = temp
ENDFOR
ENDIF ELSE BEGIN
array = FLTARR(num_width*4+1,(num_width+2)*4+1)
FOR i=0L,num_evts-1 DO array[4*(i MOD num_width)+2-1:4*(i MOD
      num_width)+2+1,4*FLOOR(i/num_width)+2-1:4*FLOOR(i/num_width)
      +2+1] = events[i].island
ENDELSE

;;;;;;;;;;;;;;;;;;;;;;;;;;;;;;;;;;;;;;;;;;;;;;;;;;;;;;;;;;;;;;;;;
; figuring out business with the filename, whether or not to overwrite
; an existing file and whatnot
;;;;;;;;;;;;;;;;;;;;;;;;;;;;;;;;;;;;;;;;;;;;;;;;;;;;;;;;;;;;;;;;;
IF KEYWORD_SET(output_name) THEN BEGIN
splitname = STRSPLIT(output_name, '.',/extract)
output_name_noext = STRJOIN(splitname[0:N_ELEMENTS(splitname)-2],
      '.')
ENDIF ELSE BEGIN
output_name_noext = 'disp_evts'
output_name = 'disp_evts.fits'
ENDELSE

SPAWN, 'ls '+output_name,temp
WHILE temp EQ output_name DO BEGIN
response1=''
READ, response1, PROMPT = 'The event list ' + output_name + '
      already exists. Choose (o) to overwrite it, (a) to append
      something to the new filename, or (s) to stop running: '
IF response1 EQ 'o' THEN BEGIN
SPAWN, 'rm -rf '+output_name
temp = ''
ENDIF
IF response1 EQ 'a' THEN BEGIN
response2 = ''
READ, response2, PROMPT = 'Type what you want to append to
      the filename so that it becomes unique: '
output_name = output_name_noext + response2 + '.fits'
SPAWN, 'ls ' + output_name,temp
ENDIF
IF response1 EQ 's' THEN BEGIN
PRINT, "Ok fine, then I am going to stop running."
temp = ''
STOP

```



```

; Generating the array of event pixel locations
;;;;;;;;;;;;;;;;;;;;;;;;;;;;;;;;;;;;;;;;;;;;;;;;;;;;;;;;;;;;;;;;;

j=0L ; counter to see how many elements get inserted into local_max_pix
IF N_p_thresh_pix GT 0 THEN BEGIN
  FOR i=0L,N_ELEMENTS(p_thresh_pix)-1 DO BEGIN
    IF TOTAL(image(BOX1D(p_thresh_pix[i],chipx)) GT image(
      p_thresh_pix[i])) EQ 0. THEN BEGIN ; testing for a
      local maxima
      local_max_pix[j,0] = p_thresh_pix[i]
      IF (LONG(side)/2 EQ LONG(side)/2.) THEN BEGIN ; if
        side is even you have to do this stuff to
        determine which way the event will shift
        local_max_pix[j,1] = CHOOSE_SHIFT(image[
          BOX1D(local_max_pix[j,0],chipx)])
      ENDIF
      j=j+1
    ENDIF
  ENDFOR
  local_max_pix = local_max_pix[0:j-1,*]
; trimming local_max_pix down to the correct size. this should be faster
; than concatenating each step of the way
;;;;;;;;;;;;;;;;;;;;;;;;;;;;;;;;;;;;;;;;;;;;;;;;;;;;;;;;;;;;;;;;;

ENDIF ELSE BEGIN

  PRINT, 'Event detect found no pixels greater than th1 in this
  image'

ENDELSE

; Initializing the structure for storing the event list
; num_evts = N_ELEMENTS(local_max_pix[*,0])
events = REPLICATE({x:0, y:0, island:DBLARR(side^2), reef:DBLARR((side
+2)^2-side^2), sum:DOUBLE(0), grade_asca:0, grade_acis:0, event_num
:0, noise_sigma:0, image_num:0}, num_evts)

; Assigning values to the event list
; FOR i=0L,num_evts-1 DO BEGIN
  events[i].x = local_max_pix[i,0] MOD chipx ; event x coord.
  events[i].y = FLOOR(local_max_pix[i,0]/chipx) ; event y coord.
  events[i].island = image[BOX1D(local_max_pix[i,0],chipx,/center,
    quadrant=local_max_pix[i,1],side=side)] ; all of the pixel
    values in the event

```

```

events[i].reel = image[ELEMENT(BOX1D(local_max_pix[i,0],chipx,/
    center,quadrant=local_max_pix[i,1],side=side+2)
    ,[0,1,2,3,4,5,9,10,14,15,19,20,21,22,23,24])]
events[i].event_num = i ; event index. starts at 0
events[i].noise_sigma = noise_sigma
ENDFOR

RETURN, events
END

```

```

FUNCTION evt_filter, events, evt_list=evt_list, xrange=xrange, yrange=
    yrange, cpixrange=cpixrange, sumrange=sumrange,$
    spixrange=spixrange, asca=asca, acis=acis, grade_include=grade_include,
    grade_reject=grade_reject, splitrangle=splitrangle, negs=negs, old_th2=
    =old_th2,$
new_th2=new_th2,no_corners=no_corners,imrange=imrange,sp_reject=
    sp_reject

;takes an event list structure as input and returns an index list or new
    event structure containing events with specified properties.
;note that each of the filtering methods are ANDed with one another

;evt_list - takes an existing event index list as input so that it can
    be further pared down.
;xrange yrange - a range of the form [low,high] that removes events
    outside of a specified pixel range on the chip.
;cpixrange - a range of the form [low,high] that removes events with a
    center pixel value outside of the specified range.
;sumrange - a range of the form [low,high] that removes events outside
    of a specified range of event sum. This corresponds to a range on the
    spectrum.
;spixrange - a range of the form [low,high] that removes events with
    secondary threshold pixels outside of the specified range.
;grade_include/reject - an array containing grade numbers to be included
    or rejected in the returned structure.
;asca/acis - specifies the grade number format. acis is default.
;splitrangle - a range of the form [low%,high%] that removes events with
    a second brightest pixel that is not within a specified range
    percentage of the primary event pixel
;negs - in non-deconvolved data all pix should be above zero. Specifying
    this keyword filters out those that, for some reason, are not.
;th2 - lets you respecify a secondary event threshold for quick plotting
.
;no_corners = when doing splitrangle filtering, set this keyword to
    exclude corners of a 3x3 event since IPC should never put charge in
    these pixels.
;imrange - a range of the form [low,high] that removes events outside of
    a specified range of image_num (image numbers.

new_events=events

num_evts = N_ELEMENTS(new_events.x)

```

```

IF KEYWORD_SET(asis) and KEYWORD_SET(asca) THEN BEGIN
    print, "You cannot use acis and asca grade formats at the same
        time."
    stop
ENDIF

IF NOT KEYWORD_SET(asis) and NOT KEYWORD_SET(asca) THEN acis=1

IF KEYWORD_SET(evt_list) THEN BEGIN
    evt_list_bool = REPLICATE(0,num_evts)
    evt_list_bool[evt_list] = 1
ENDIF ELSE evt_list_bool = REPLICATE(1,num_evts)

IF KEYWORD_SET(xrange) THEN evt_list_bool = evt_list_bool AND ((
    new_events.x GT xrange[0]) AND (new_events.x LT xrange[1]))

IF KEYWORD_SET(yrange) THEN evt_list_bool = evt_list_bool AND ((
    new_events.y GT yrange[0]) AND (new_events.y LT yrange[1]))

IF KEYWORD_SET(cpixrange) THEN evt_list_bool = evt_list_bool AND ((
    new_events.island[4] GT cpixrange[0]) AND (new_events.island[4] LT
    cpixrange[1]))

IF KEYWORD_SET(imrange) THEN evt_list_bool = evt_list_bool AND ((
    new_events.image_num GE imrange[0]) AND (new_events.image_num LE
    imrange[1]))

IF KEYWORD_SET(old_th2) THEN BEGIN
    grades = INTARR(num_evts)
    rosetta = [32,64,128,8,0,16,1,2,4]
    FOR i=0L,num_evts-1 DO BEGIN
        new_events[i].sum = TOTAL(new_events[i].island[WHERE(
            new_events[i].island GE old_th2)])
        new_events[i].grade_acis = TOTAL(rosetta[WHERE(new_events[
            i].island GT old_th2)])
        new_events[i].grade_asca = acis2asca(new_events[i].
            grade_acis)
    ENDFOR
ENDIF

IF KEYWORD_SET(new_th2) THEN BEGIN
    new_events.grade_acis = transpose((new_events.island GT new_th2)
        ##[32,64,128,8,0,16,1,2,4])
    new_events.sum = total((new_events.island GT new_th2)*new_events.
        island,1)
ENDIF

IF KEYWORD_SET(sumrange) THEN evt_list_bool = evt_list_bool AND ((
    new_events.sum GT sumrange[0]) and (new_events.sum LT sumrange[1]))

IF KEYWORD_SET(asca) THEN BEGIN
    temp_evt_list_bool = REPLICATE(0,num_evts)
    IF KEYWORD_SET(grade_include) THEN BEGIN

```

```

        FOR i=0,N_ELEMENTS(grade_include)-1 DO temp_evt_list_bool
            = temp_evt_list_bool OR (new_events.grade_asca EQ
                grade_include[i])
            evt_list_bool = evt_list_bool AND temp_evt_list_bool
        ENDFOR
    ENDFOR
    IF KEYWORD_SET(grade_reject) THEN BEGIN
        FOR i=0,N_ELEMENTS(grade_reject)-1 DO temp_evt_list_bool =
            temp_evt_list_bool OR (new_events.grade_asca EQ
                grade_reject[i])
            evt_list_bool = NOT ((NOT evt_list_bool) OR
                temp_evt_list_bool)
        ENDFOR
    ENDFOR
ENDIF

IF KEYWORD_SET(akis) THEN BEGIN
    temp_evt_list_bool = REPLICATE(0,num_evts)
    IF N_ELEMENTS(grade_include) GT 0 THEN BEGIN
        FOR i=0,N_ELEMENTS(grade_include)-1 DO temp_evt_list_bool
            = temp_evt_list_bool OR (new_events.grade_acis EQ
                grade_include[i])
            evt_list_bool = evt_list_bool AND temp_evt_list_bool
        ENDFOR
    ENDFOR
    IF KEYWORD_SET(grade_reject) THEN BEGIN
        FOR i=0,N_ELEMENTS(grade_reject)-1 DO temp_evt_list_bool =
            temp_evt_list_bool OR (new_events.grade_acis EQ
                grade_reject[i])
            evt_list_bool = NOT ((NOT evt_list_bool) OR
                temp_evt_list_bool)
        ENDFOR
    ENDFOR
ENDIF

IF KEYWORD_SET(splitrange) THEN BEGIN
    IF KEYWORD_SET(no_corners) THEN sort_evts = DBLARR(5,num_evts)
    ELSE sort_evts = DBLARR(9,num_evts)
    FOR i=0L,num_evts-1 DO BEGIN
        IF KEYWORD_SET(no_corners) THEN BEGIN
            temp_island = new_events[i].island[[1,3,4,5,7]]
            sort_evts[* ,i] = REVERSE(temp_island[ SORT(
                temp_island)])
        ENDFOR ELSE BEGIN
            sort_evts[* ,i] = REVERSE(new_events[i].island[ SORT(
                new_events[i].island)]) ;sort() outputs lowest
                to highest, but reverse() turns this highest to
                lowest so that i can conveniently subscript
                with 0 and 1 to get highest and second highest
                elements.
        ENDFOR
    ENDFOR
    ENDFOR
    evt_list_bool = evt_list_bool AND ( ((sort_evts[1,*]/sort_evts
        [0,*]) GT splitrange[0]/100.) AND ((sort_evts[1,*]/sort_evts
        [0,*]) LT splitrange[1]/100.))
ENDIF

```

```

IF KEYWORD_SET(negs) THEN BEGIN
    no_negs = INTARR(num_evts)
    FOR i=0L,num_evts-1 DO no_negs[i] = TOTAL(new_events[i].island LE
        0) EQ 0
    evt_list_bool = evt_list_bool AND no_negs
ENDIF

IF KEYWORD_SET(sp_reject) THEN BEGIN
salt = bytarr(1)
FOR i = 0, MAX(new_events.image_num)-1
    ;get indices of all events in the left column and all events in
    the right column
    left_evt_list_index = WHERE(new_events.x LT 512 AND new_evts.
        image_num EQ i)
    right_evt_list_index = WHERE(new_events.x GE 512 AND new_evts.
        image_num EQ i)

    ;get number of events in each list. should be roughly equal
    n_left = n_elements(left_evt_list_index)
    n_right = n_elements(right_evt_list_index)

    ;magic
    something = $
    rebin(fix(new_events[left_evt_list_index].image_num),n_left,
        n_right) eq rebin(transpose(fix(new_events[
        right_evt_list_index].image_num)),n_left,n_right) $
and $
    rebin(fix(new_events[left_evt_list_index].y),n_left,n_right) eq
    rebin(transpose(fix(new_events[right_evt_list_index].y)),
        n_left,n_right)$
and $
    rebin(fix(new_events[left_evt_list_index].x),n_left,n_right) eq
    rebin(transpose(1024 - fix(new_events[left_evt_list_index].x))
        ,n_left,n_right)

    ;the answer
    answer = array_indices([n_left,n_right],where(something),/
        dimensions)
    salt = bytarr(n_elements(answer[0,*]))
    salt[[answer[0,*],answer[1,*]]] = 1

    evt_list_bool = evt_list_bool and salt
ENDIF

PRINT, 'There were '+STRCOMPRESS(STRING(num_evts))+ ' new_events pre-
    filtering and '+STRCOMPRESS(STRING(N_ELEMENTS(WHERE(evt_list_bool))))
    +' events post-filtering. This is a '+STRCOMPRESS(STRING(DOUBLE(
    N_ELEMENTS(WHERE(evt_list_bool)))/num_evts*100.))+ ' % cut.'

RETURN, new_events[WHERE(evt_list_bool)]

```

END

```

PRO grade_evts, filename, th2=th2, quad=quad,deconvolve=deconvolve,iter=
  iter

; procedure grades filename according to thershold procedures or
  settings. it fills in the grade column of a fits table or overwrites
  it if it exists.
; if no filename is specified, grade_evts looks for an event table with
  the default name scheme
; it adds threshold tags to the fits file.
; quad = a switch that, when set, compares pixel information in "island"
  and in "reef" against the given th2 to find a summed total event
  energy. this is like setting side=5 but I never made that work. The
  event grades will be wrong but who cares we do not use those anyway.
; deconvolve = a switch that performs deconvolution on every event.
  average the low split thresh events to get a kernel. use gaussian
  noise mode in max_likelihood because it should be correct AND because
  it should conserve flux. insert new fields into event binary table.
; iter = number of LR iterations to perform (10 is standard)

; the speed of this pro can be improved by doing the vectorized grading
  like in evt_filter

t1 = LONG(STRSPLIT(ELEMENT(STRSPLIT(SYSTIME(0),/extract),3),':',/extract
))

IF KEYWORD_SET(deconvolve) AND NOT KEYWORD_SET(iter) THEN iter=10 ;
  default number of LR iterations.
IF NOT KEYWORD_SET(filename) THEN BEGIN
  SPAWN, 'pwd', dirname
  filename = STRMID(dirname,STRPOS(dirname,'/',/reverse_search)+1,
    STRLEN(dirname)-STRPOS(dirname,'/',/reverse_search)-1)+'.fits'
  events = MRDFITS(filename,1,phheader)
ENDIF ELSE BEGIN
  events = MRDFITS(filename,1,phheader)
ENDELSE

IF KEYWORD_SET(deconvolve) THEN BEGIN
  filename_noext = STRSPLIT(filename,'.fit',/extract,/regex)
  filename_noext = filename_noext[0]+'_deconv'+'_iter'+STRING(iter,
    format='(I02)')
  filename = filename_noext+'.fits'
  ;;;;;;;;;;;;;;
  ; deleting the event file if it's already there.
  ;;;;;;;;;;;;;;

  SPAWN, 'ls '+filename,temp
print, temp, filename
  WHILE temp EQ filename DO BEGIN
    response1=''
    READ, response1, PROMPT = 'The event list ' + filename + '
      already exists. Choose (o) to overwrite it, (a) to

```

```

        append something to make the filenames unique, or (s)
        to stop running: '
IF response1 EQ 'o' THEN BEGIN
    SPAWN, 'rm -rf '+filename+'.fits'
    temp = ''
ENDIF
IF response1 EQ 'a' THEN BEGIN
    response2 = ''
    READ, response2, PROMPT = 'Type what you want to
        append to the filenames so that it becomes
        unique: '
    filename = + filename_noext + response2 + '.fits'
    SPAWN, 'ls ' + filename,temp
ENDIF
IF response1 EQ 's' THEN BEGIN
    PRINT, "Ok fine, then I am going to stop running."
    temp = ''
    STOP
ENDIF
IF ((response1 NE 'o') AND (response1 NE 'a') AND (
    response1 NE 's')) THEN PRINT, 'Hey buddy, type o for
    overwrite, a for append, or s to stop running.'
ENDWHILE
ENDIF

side = FXPAR(pheader, 'SIDE')

IF side EQ 3 THEN rosetta = [32,64,128,8,0,16,1,2,4]
IF side EQ 4 THEN rosetta =
    [2048,4096,8192,16348,128,256,512,1024,8,16,32,64,0,1,2,4] ; matrix
    used for assigning event events

; use the noise array in the events structure to do the calculation

; find thresholds
IF NOT KEYWORD_SET(th2) THEN BEGIN
    th2 = 3*events[1].noise_sigma
    print, 'Secondary threshold calculated to be ', th2
ENDIF

; reading grade translation file into memory
; old path on linux machine '/astro/grads/sdb210/abe_research/analysis/
    hcd_reduce/grade_translation.txt'
; i need to make this work on any machine. this will work so long as
    there's a copy of grade_translation.txt in the same dir as every copy
    of grade_evts.pro. there should be only one copy though.'
findpro, 'grade_evts',/noprint,dirlist=dirlist
grade_trans_path = dirlist[0]+'grade_translation.txt'
READCOL, grade_trans_path,acis_grades,ac0,ac1,ac2,ac3,ac4,ac5,ac6,ac7,
    ac8,$
asca_grades,as0,as1,as2,as3,as4,as5,as6,as7,as8,delimiter=',',comment='';
    ',format='I,I,I,I,I,I,I,I,I,I,I,I,I,I,I,I,I',/silent
as_island=intarr(3,3,n_elements(asca_grades))

```

```

ac_island=intarr(3,3,n_elements(asca_grades))
FOR i=0,N_ELEMENTS(asca_grades)-1 DO BEGIN
    as_island[0:2,0:2,i] = [[as0[i],as1[i],as2[i]], [as3[i],as4[i],as5
        [i]], [as6[i],as7[i],as8[i]]]
    ac_island[0:2,0:2,i] = [[ac0[i],ac1[i],ac2[i]], [ac3[i],ac4[i],ac5
        [i]], [ac6[i],ac7[i],ac8[i]]]
ENDFOR

```

```

FXADDPAR, pheader, 'TH2', th2

```

```

num_evts = N_ELEMENTS(events.x)

```

```

IF KEYWORD_SET(deconvolve) THEN BEGIN
    print, 'Filtering events to produce the kernel...'
    kernel_events = evt_filter(events,splitrange=[10,20])
    kernel_data = [[[events.ref[0:4]], [[TRANPOSE(events.ref[5]),
        events.island[0:2],TRANPOSE(events.ref[6])]], [[TRANPOSE(
        events.ref[7]),events.island[3:5],TRANPOSE(events.ref[8])
        ]], [[TRANPOSE(events.ref[9]),events.island[6:8],TRANPOSE(
        events.ref[10])]], [[events.ref[11:15]]]] ; i should not use
    the mean here. the ipc distribution in each non central pixel
    (what i am after) will be skewed towards higher counts because
    of real charge splitting. maybe the mode (hist peak) is a
    better distribution central tendency estimator. With the mode
    you must do avepixcal during make_evtlist because otherwise
    the zero peak will always be the mode.
    kernel = lonarr(5,5)

    print, 'Creating the kernel...'
    FOR i=0,4 DO BEGIN
        FOR j=0,4 DO BEGIN
            hist = HISTOGRAM(kernel_data[i,*,j],locations=
                locations,min=-100,max=2000)
            hist[WHERE(locations eq 0)] = hist[WHERE(locations
                eq 0)+1] ; patching the zero peak with the
                histogram element to the right of zero.
            temp = MAX(hist,max_subscript)
            kernel[i,j] = locations[max_subscript]
            ;kernel[i,j] = MODE(DOUBLE(kernel_data[i,*,j])) ;
                this way would work great if the zero peak was
                not a problem with medpixcal3
        ENDFOR
    ENDFOR
    kernel = DOUBLE(kernel)/total(kernel)
    print, 'Performing deconvolution and grading...'
    FOR i=0L,num_evts-1 do begin
        FOR j=0,iter-1 DO MAX_LIKELIHOOD, [[events[i].ref[0:4]], [
            events[i].ref[5],events[i].island[0:2],events[i].ref[
            6]], [events[i].ref[7],events[i].island[3:5],events[i]
            ].ref[8]], [events[i].ref[9],events[i].island[6:8],
            events[i].ref[10]], [events[i].ref[11:15]]],kernel,
            deconv, Re_conv,/gaussian ; do deconv with 4x4 event

```

```

        region
        events[i].reef = [deconv[0:5],deconv[9:10],deconv[14:15],
            deconv[19:24]]
        deconv = deconv[1:3,1:3]      ; cut the event down to a 3x3
            region after it has been deconvolved for event
            characterization
        events[i].grade_acis = TOTAL(rosetta[WHERE(deconv GE th2)
            ])
        events[i].grade_asca = asca_grades[WHERE(acis_grades EQ
            events[i].grade_acis)]
        events[i].sum = TOTAL(deconv * as_island[*,*,WHERE(
            acis_grades EQ events[i].grade_acis)]) ; using proper
            detouched corner rejection
        events[i].island = deconv[0:8]
    ENDFOR
    FXADDPAR, pheader, 'DECONV', 'yes'
ENDIF ELSE BEGIN
    print, 'Performing grading...'
    FOR i=0L,num_evts-1 DO BEGIN
        events[i].grade_asca = acis2asca(TOTAL(rosetta[WHERE(
            events[i].island GE th2)])) ; acis2asca(TOTAL(grade[
            WHERE(image[BOX1D(second(i,0),chipx,/center,quadrant=
            second(i,1),side=4)] GT th2)])) ; event grade
        events[i].grade_acis = TOTAL(rosetta[WHERE(events[i].
            island GE th2)]) ; TOTAL(grade[WHERE(image[BOX1D(second[
            i,0],chipx,/center,quadrant=second[i,1],side=4)] GT th2
            )])
        IF NOT KEYWORD_SET(quad) THEN events[i].sum = TOTAL(events[i].
            island[WHERE(events[i].island GE th2)])
        IF KEYWORD_SET(quad) THEN BEGIN
            events[i].sum = TOTAL(events[i].island[WHERE(events[i].
            island GE th2)])
            IF ELEMENT(WHERE(events[i].reef GE th2),0) NE -1 THEN
                events[i].sum = events[i].sum + TOTAL(events[i].reef[
                WHERE(events[i].reef GE th2)])
        ENDIF
    ENDIF

; the old stuff...TOTAL( image[WHERE( image[BOX1D(local_max_pix[i,0],
    chipx,side=side,/center,quadrant=local_max_pix[i,1])] GT th2 ) +
    local_max_pix[i,0] - FLOOR(side^2/2.) + (LONG(side)/2 EQ LONG(side)
    /2.)*((local_max_pix[i,1] GE 2)*(side/2+local_max_pix[i,1]-2) + (
    local_max_pix[i,1] LT 2)*(-side/2-local_max_pix[i,1]+1) - 1)] ) ; you
    need to add all of this fucking shit to make it work with an off-
    center, even-sided event box. it all equals 4 when side=3

    ENDFOR
ENDELSE
print, 'Writing fits file...'
IF KEYWORD_SET(deconvolve) THEN BEGIN
    MWRFITs, events, filename, pheader
ENDIF ELSE BEGIN
    SPAWN, 'rm -rf ' + filename
    MWRFITs, events, filename, pheader

```

ENDELSE

```
t2 = LONG(STRSPLIT(ELEMENT(STRSPLIT(SYSTIME(0),/extract),3),':',/extract
))
dt = (t2[0]*3600+t2[1]*60+t2[2])-(t1[0]*3600+t1[1]*60+t1[2])
dt = LONG([FLOOR(dt/3600.), FLOOR((dt/3600.-FLOOR(dt/3600.))*60), ((dt
/3600.-FLOOR(dt/3600.))*60-FLOOR((dt/3600.-FLOOR(dt/3600.))*60))*60])
print, 'This took '+STRCOMPRESS(STRING(dt[0]))+'h '+STRCOMPRESS(STRING(
dt[1]))+'m '+STRCOMPRESS(STRING(dt[2]))+'s to run.'
END
```

```
; $Id: make_evtlist.pro,v 1.1 2011/01/23 sdb210 $
PRO make_evtlist, th1=th1, side=side, ramps=ramps, ramprange=ramprange $
, output_fname=output_fname, smoothing_func=
smoothing_func
;+
; NAME : make_evtlist
; CATEGORY: HCD X-ray data reduction
; SYNTAX: make_evtlist,
;
; RUN make_evtlist FROM INSIDE THE DIRECTORY CONTAINING ALL OF THE
IMAGES OF THE RUN YOU WANT TO REDUCE. IT WILL GENERATE A FITS EVENT
LIST.
; deconvolve - set keyword to deconvolve the images
; th1 - the primary event threshold to use for event detection
; side - the width (in pixels) of the event detection box
; ramps - set keyword to treat data taken in ramp style.
; if ramp keyword is set then keyword ramprange can be used to specify
which ramps are used in reduction.
; output_name = the desired output evtlist filename
; smoothing_func - a scalar string naming the function to be used in row
noise correction. robust_mean is default. used in non-ramp (cds)
style data acquisition since the data has not yet been pseudo cds
subtracted or rownoise corrected yet
; salt_reject - keyword that prevents grade zeros from making it into the
event list. these are spurious salt noise events and only clog up
the dataset.
iter=15 ; number of ML deconvolution iterations

IF NOT KEYWORD_SET(side) THEN side=3
IF KEYWORD_SET(deconvolve) THEN kernel = DOUBLE(READFITS('/users/grads/
sdb210/abe_research/analysis/redux/psf_hyvisi_fixed.fits'))

;;;;;;;;;;;;;;;;;;;;;;;;;;;;;;;;;;;;;;;;;;;;;;;;;;;;;;;;;;;;;;;;;;;;;;;;;;;;;;;;
; generate image directory list and check to see if you are in a run
directory with image directories inside of it. works for ramps and
CDS
;;;;;;;;;;;;;;;;;;;;;;;;;;;;;;;;;;;;;;;;;;;;;;;;;;;;;;;;;;;;;;;;;;;;;;;;;;;;;;;;

IF KEYWORD_SET(ramps) THEN BEGIN
    SPAWN, 'ls image*.fits',filenames
    IF STRLEN(filenames[0]) EQ 0 THEN BEGIN
```

```

PRINT, "You are not in a directory with Janus ramp style
      CDS subtracted images. I am going to stop, you are
      gonna go into a directory with image directories, and
      then we will try again."
STOP
ENDIF
n_files = N_ELEMENTS(filenamees)

;;;;;;;;;;;;;;;;;;;;;;;;;;;;;;;;;;;;;;;;;;;;;;;;
; Parsing the filenames string array
;;;;;;;;;;;;;;;;;;;;;;;;;;;;;;;;;;;;;;;;;;;;;;;;

fname_st = {prefix:'' ,rstr:'' ,R:0,mstr:'' ,M:0,nstr:'' ,N:0,suffix:
           ''} ; filenames structure
fname_st = REPLICATE(fname_st,n_files)

FOR i=0,n_files-1 DO BEGIN
  r_pos = STRPOS(filenamees[i],'_R')
  m_pos = STRPOS(filenamees[i],'_M')
  n_pos = STRPOS(filenamees[i],'_N')
  suf_pos = STRPOS(filenamees[i],'.fits')
  len = STRLEN(filenamees[i])
  fname_st[i].prefix = STRMID(filenamees[i],0,r_pos)
  fname_st[i].rstr = STRMID(filenamees[i],r_pos,m_pos-r_pos)
  fname_st[i].r = FIX(STRMID(filenamees[i],r_pos+2,m_pos-
    r_pos-2))
  fname_st[i].mstr = STRMID(filenamees[i],m_pos,n_pos-m_pos)
  fname_st[i].m = FIX(STRMID(filenamees[i],m_pos+2,n_pos-
    m_pos-2))
  fname_st[i].nstr = STRMID(filenamees[i],n_pos,suf_pos-n_pos
    )
  fname_st[i].n = FIX(STRMID(filenamees[i],n_pos+2,suf_pos-
    n_pos-2))
  fname_st[i].suffix = STRMID(filenamees[i],suf_pos,5)
ENDFOR

;;;;;;;;;;;;;;;;;;;;;;;;;;;;;;;;;;;;;;;;;;;;;;;;
; ordering the parsed string structure
;;;;;;;;;;;;;;;;;;;;;;;;;;;;;;;;;;;;;;;;;;;;;;;;
good_forder = SORT(fname_st.r*LONG(10000)+fname_st.m*LONG(100)+
  fname_st.n*LONG(1))
fname_st = fname_st[good_forder]
filenamees = filenamees[good_forder]

; generating ramp number parameters
n_ramps = LONG(N_ELEMENTS(UNIQ(fname_st[ SORT(fname_st.r) ].r))) ;
  number of unique numbers in the ramp number array. input to
  uniq() must be sorted for it to work. this allows for skipped
  run numbers

; generating frame number parameters
n_frames = LONG(N_ELEMENTS(UNIQ(fname_st[ SORT(fname_st.n) ].n)))

```

```

; allowing only ramps specified with ramprange
IF KEYWORD_SET(ramprange) THEN filenames = filenames[WHERE(
    fname_st.r GE ramprange[0] AND fname_st.r LE ramprange[1])]

ENDIF ELSE BEGIN
    SPAWN, 'ls -d */',filenames
    IF STRMID(filenames[0],11,4) NE 'TIME' THEN BEGIN ; this checks
        to see if the string TIME is in the first element of filenames
        which should be the directories with files.
        PRINT, "You are not in a directory with CDS image
            directories that I know how to read. I am going to stop
            , you are going to go into a directory with image
            directories, and then we will try again."
        STOP
    ENDIF
ENDELSE

;;;;;;;;;;;;;;;;;;;;;;;;;;;;;;;;;;;;;;;;;;;;;;;;;;;;;;;;;;;;;;;;;
; generate output_name, the name of the output fits file
;;;;;;;;;;;;;;;;;;;;;;;;;;;;;;;;;;;;;;;;;;;;;;;;;;;;;;;;;;;;;;;;;
IF NOT KEYWORD_SET(output_name) THEN BEGIN
    SPAWN, 'pwd',current_path
    current_path = STRSPLIT(current_path,'/',/EXTRACT)
    current_dir = current_path[N_ELEMENTS(current_path)-1]
    filename_noext = current_dir
    IF KEYWORD_SET(deconvolve) THEN filename_noext = filename_noext +
        '_deconv'
    output_name = filename_noext + '.fits'
ENDIF

;IF KEYWORD_SET(deconvolve) AND KEYWORD_SET(output_name) THEN
    filename_noext = STRSPLIT(filename,STRPOS(output_name,'.fit'))
    ;;;;;;;;;;;;;;;;;;FIX THIS!!!!!!!!!!!!

;;;;;;;;;;;;;;;;;;;;;;;;;;;;;;;;;;;;;;;;;;;;;;;;;;;;;;;;;;;;;;;;;
; deleting the event file if it is already there.
;;;;;;;;;;;;;;;;;;;;;;;;;;;;;;;;;;;;;;;;;;;;;;;;;;;;;;;;;;;;;;;;;

SPAWN, 'ls '+output_name,temp
WHILE temp EQ output_name DO BEGIN
    response1=''
    READ, response1, PROMPT = 'The event list ' + output_name + '
        already exists. Choose (o) to overwrite it, (a) to append
        something to make the filenames unique, or (s) to stop running
        : '
    IF response1 EQ 'o' THEN BEGIN
        SPAWN, 'rm -rf '+output_name
        temp = ''
    ENDIF
    IF response1 EQ 'a' THEN BEGIN
        response2 = ''

```



```

        image = LONG(READFITS(filenamees[i])) ; note this data has
            already had ramp_cds run on it.
        IF KEYWORD_SET(smoothing_func) THEN FXADDPAR, pheader, '
            PIXCAL', smoothing_func ELSE FXADDPAR, pheader, 'PIXCAL
            ', 'robust_mean'
    ENENDIF ELSE BEGIN
        CD, filenamees[i]
        IF KEYWORD_SET(smoothing_func) THEN BEGIN
            image = PIXCAL(LONG(READFITS('SCAH1RG-C001-IR25-SC2
                -B-010-JWST_R01_M01_N02.fits')))-LONG(READFITS('
                SCAH1RG-C001-IR25-SC2-B-010-JWST_R01_M01_N01.
                fits')),smoothing_func=smoothing_func)
            FXADDPAR, pheader, 'PIXCAL', smoothing_func
        ENENDIF ELSE BEGIN
            image = PIXCAL(LONG(READFITS('SCAH1RG-C001-IR25-SC2
                -B-010-JWST_R01_M01_N02.fits')))-LONG(READFITS('
                SCAH1RG-C001-IR25-SC2-B-010-JWST_R01_M01_N01.
                fits')),smoothing_func='robust_mean')
            FXADDPAR, pheader, 'PIXCAL', 'robust_mean'
        ENELSE
        CD, '..'
    ENELSE

    IF KEYWORD_SET(deconvolve) THEN BEGIN
        PRINT, 'deconvolving '+filenamees(i)
        FOR j=0,iter DO MAX_LIKELIHOOD,image,kernel,deconv,FT_PSF=
            psf_ft
        image = deconv
    ENENDIF

    PRINT, 'grading '+filenamees[i]
    old_events = events
    new_events = EVENT_DETECT(image,th1=th1,side=side)
    new_events.image_num = REPLICATE(i,N_ELEMENTS(new_events.
        image_num))

    num_evts = N_ELEMENTS(new_events.x)+N_ELEMENTS(old_events.x)
    events = REPLICATE({x:0, y:0, island:DBLARR(side^2), reef:DBLARR
        ((side+2)^2-side^2), sum:DOUBLE(0), grade_asca:0, grade_acis
        :0, event_num:0, noise_sigma:0, image_num:0}, num_evts)

    events.x = [old_events.x,new_events.x]
    events.y = [old_events.y,new_events.y]
    events.island = [[old_events.island],[new_events.island]]
    events.reef = [[old_events.reef],[new_events.reef]]
    events.sum = [old_events.sum,new_events.sum]
    events.grade_asca = [old_events.grade_asca,new_events.grade_asca]
    events.grade_acis = [old_events.grade_acis,new_events.grade_acis]
    events.event_num = [old_events.event_num,new_events.event_num]
    events.noise_sigma = [old_events.noise_sigma,new_events.
        noise_sigma]
    events.image_num = [old_events.image_num,new_events.image_num]

```

```
ENDFOR
```

```

;;;;;;;;;;;;;;;;;;;;;;;;;;;;;;;;;;;;;;;;;;;;;;;;;;;;;;;;;;;;;;;;;;;;;;;;;;;;;;;;
; Removing the first row of each tag used to initialize the structure
; and writing some header stuff and the structure to a fits table
;;;;;;;;;;;;;;;;;;;;;;;;;;;;;;;;;;;;;;;;;;;;;;;;;;;;;;;;;;;;;;;;;;;;;;;;;;;;;;;;

```

```
events = events[1:*
```

```

FXADDPAR, pheader, 'CHIPX', N_ELEMENTS(image[*,0])
FXADDPAR, pheader, 'CHIPY', N_ELEMENTS(image[0,*])
FXADDPAR, pheader, 'FRAMES', N_ELEMENTS(filenamees)
MWRFITS, events, output_name, pheader

```

```
END
```

```

FUNCTION pixcal, image, width=width,cal_frame=cal_frame,smoothing_func=
    smoothing_func,forecast=forecast
;uses boxcar robust_mean filter

; width - integer specifying the number of points used in boxcar
; filtering
; smoothing_func - scalar string naming the function to use for rownoise
; subtraction, default is robust_mean but other possibilities are
; median, mean, medave, ref_pix_mean, ref_pix_med
; cal_frame - set this keyword to a variable name that will contain the
; number that gets subtracted off of the data frame. this can be used
; for testing
; forecast - a keyword that tells the boxcar filter to use time series
; forecasting (does not apply to reference pixel subtraction options)

imsize = SIZE(image)

IF NOT KEYWORD_SET(smoothing_func) THEN BEGIN
    smoothing_func='robust_mean'
    print, 'Using robust_mean smoothing by default.'
ENDIF

IF smoothing_func EQ 'robust_mean' THEN param_string='3' ; sigma cutoff
; for outlier rejection
IF smoothing_func EQ 'medave' THEN param_string='10' ;ave window size in
; pixels
IF smoothing_func EQ 'robust_mean' OR smoothing_func EQ 'mean' OR
; smoothing_func EQ 'medave' OR smoothing_func EQ 'ref_pix_mean' THEN
; image2 = DOUBLE(image)
IF smoothing_func EQ 'ref_pix_med' OR smoothing_func EQ 'median' THEN
; image2 = image

IF KEYWORD_SET(cal_frame) THEN cal_frame = DBLARR(imsize[1],imsize[2])
IF NOT KEYWORD_SET(width) THEN width = 21; & print, 'Using a boxcar
; width of '+STRING(width,format='(I03)'),' pixels by default.'

```

```

FOR i=4,imsize[2]-5 DO BEGIN ;goes from row to row
  IF smoothing_func EQ 'ref_pix_mean' OR smoothing_func EQ '
    ref_pix_med' THEN BEGIN
    image2[5:imsize[1]/2-1,i] = image2[5:imsize[1]/2-1,i] -
      mean(image[0:4])
    image2[imsize[1]/2:imsize[1]-5,i] = image[imsize[1]/2:
      imsize[1]-5,i] - mean(image[imsize[1]-6:imsize[1]-1])
  ENDIF
  IF smoothing_func EQ 'robust_mean' OR smoothing_func EQ 'mean' OR
    smoothing_func EQ 'median' OR smoothing_func EQ 'medave' THEN
  BEGIN
    left_cal = BOXCAR(image[5:imsize[1]/2-1,i],width,
      smoothing_func,param_string=param_string,poly_forecast=
      forecast)
    right_cal = BOXCAR(image[imsize[1]/2:imsize[1]-5,i],width,
      smoothing_func,param_string=param_string,poly_forecast=
      forecast)
    image2[5:imsize[1]/2-1,i] = image[5:imsize[1]/2-1,i] -
      left_cal ;left channel
    image2[imsize[1]/2:imsize[1]-5,i] = image[imsize[1]/2:
      imsize[1]-5,i] - right_cal ;right channel
    IF KEYWORD_SET(cal_frame) THEN BEGIN
      cal_frame[5:imsize[1]/2-1,i] = left_cal
      cal_frame[imsize[1]/2:imsize[1]-5,i] = right_cal
    ENDIF
  ENDIF
ENDIF
ENDFOR

RETURN, image2
END

```

```

PRO ramp_cds, smoothing_func=smoothing_func,append=append,cal_frame=
  cal_frame,noforecast=noforecast,everyother=everyother
; program produces cds subtracted data from data read in a ramp style. e
; .g. reset-read read read...x(n-frames)
; n_frames = the number of dataframes after the initial reset-read frame
  taken in the ramp
; run this program inside the directory containing the ramp fits files
; dc_pixcal - if you are going to use the run to calculate dark current,
  then pixcal will completely take out the dark current signal and the
  cds will make for non pretty ramps. specify this keyword to use
  dcpixcal
; also in normal mode the algorithm will subtract frame 2-1,3-2,4-3 etc
  to produce the final images. in dc_pixcal mode it will subtract
  2-1,3-1,4-1 etc
; smoothing_func - scalar string naming the function to use for rownoise
  subtraction, default is robust_mean but other possibilities are
  median, mean, medave, ref_pix_mean, ref_pix_med
; append - a scalar string that will be added to filenames right before
  the .fits. this is for saving multiple sets of reduced images with
  different medpixcal settings.
; cal_frame - a keyword switch to indicate that you want ramp_cds to
  produce an additional set of images containing the numbers that

```

```

    pixcal subtracts off of each data image pixel.
; everyother - a keyword switch that activates contracting the images by
    deleting every other pixel. added on 2010_11_29 to reduce h2rg-122
    data.
; 2010_06_19 - added header copying.

IF NOT KEYWORD_SET(append) THEN append = ''
IF NOT KEYWORD_SET(noforecast) THEN forecast=1
IF NOT KEYWORD_SET(smoothing_func) THEN smoothing_func='robust_mean'

filename = FILE_SEARCH('SCA*.fits')
n_files = N_ELEMENTS(filename)

IF n_files EQ 0 THEN BEGIN ; this checks to see if the first element of
    filename had anything written to it. if not then there were no ramp
    files found.
    PRINT, "You are not in a directory with ramp images that I know
        how to read. I am going stop, you are going to go into a
        directory with ramp images, and then we will try again."
    STOP
ENDIF

;;;;;;;;;;;;;;;;;;;;;;;;;;;;;;;;;;;;;;;;;;;;;;;;;
; Parsing the filename string array
;;;;;;;;;;;;;;;;;;;;;;;;;;;;;;;;;;;;;;;;;;;;;;;;;

fname_st = {prefix:'',rstr:'',R:0,mstr:'',M:0,nstr:'',N:0,suffix:''} ;
    filename structure
fname_st = REPLICATE(fname_st,n_files)

FOR i=0,n_files-1 DO BEGIN
    r_pos = STRPOS(filename[i],'_R')
    m_pos = STRPOS(filename[i],'_M')
    n_pos = STRPOS(filename[i],'_N')
    suf_pos = STRPOS(filename[i],'.fits')
    len = STRLEN(filename[i])
    fname_st[i].prefix = STRMID(filename[i],0,r_pos)
    fname_st[i].rstr = STRMID(filename[i],r_pos,m_pos-r_pos)
    fname_st[i].r = FIX(STRMID(filename[i],r_pos+2,m_pos-r_pos-2))
    fname_st[i].mstr = STRMID(filename[i],m_pos,n_pos-m_pos)
    fname_st[i].m = FIX(STRMID(filename[i],m_pos+2,n_pos-m_pos-2))
    fname_st[i].nstr = STRMID(filename[i],n_pos,suf_pos-n_pos)
    fname_st[i].n = FIX(STRMID(filename[i],n_pos+2,suf_pos-n_pos-2))
    fname_st[i].suffix = STRMID(filename[i],suf_pos,5)
ENDFOR

;;;;;;;;;;;;;;;;;;;;;;;;;;;;;;;;;;;;;;;;;;;;;;;;;
; ordering the parsed string structure
;;;;;;;;;;;;;;;;;;;;;;;;;;;;;;;;;;;;;;;;;;;;;;;;;

```

```

good_forder = SORT(fname_st.r*LONG(10000)+fname_st.m*LONG(100)+fname_st.
    n*LONG(1))
fname_st = fname_st[good_forder]
filename = filename[good_forder]

; generating ramp number parameters
n_ramps = LONG(N_ELEMENTS(UNIQ(fname_st[ SORT(fname_st.r) ] .r))) ; number
    of unique numbers in the ramp number array. input to uniq() must be
    sorted for it to work. this allows for skipped run numbers

; generating frame number parameters
n_frames = LONG(N_ELEMENTS(UNIQ(fname_st[ SORT(fname_st.n) ] .n)))

; manually setting bitpix fits header keyword to avoid warning messages.
IF smoothing_func EQ 'robust_mean' OR smoothing_func EQ 'mean' OR
    smoothing_func EQ 'medave' OR smoothing_func EQ 'ref_pix_mean' THEN
    bitpix = -64
IF smoothing_func EQ 'ref_pix_med' OR smoothing_func EQ 'median' THEN
    bitpix = 32

;;;;;;;;;;;;;;;;;;;;;;;;;
; doing the subtractions
;;;;;;;;;;;;;;;;;;;;;;;;;

FOR i=0,n_ramps-1 DO BEGIN
    FOR j=1,n_frames-1 DO BEGIN
        z = LONG(i*n_frames+j)
        image2 = LONG(READFITS(fname_st[z].prefix+fname_st[z].rstr
            +fname_st[z].mstr+fname_st[z].nstr+fname_st[z].suffix,
            header2))
        image1 = LONG(READFITS(fname_st[z-1].prefix+fname_st[z-1].
            rstr+fname_st[z-1].mstr+fname_st[z-1].nstr+fname_st[z-
            1].suffix,header1))
        acqtime = SXPARG(header1,'ACQTIME')
        new_acqtime = TENV(long(strmid(acqtime,0,2)),long(strmid(
            acqtime,3,2)),long(strmid(acqtime,6,6)))+TENV
            (0,0,5.28384/2.)
        new_acqtime = SIXTY(new_acqtime)
        new_acqtime = string(new_acqtime[0],format='(I02)')+':'+
            string(new_acqtime[1],format='(I02)')+':'+string(
            new_acqtime[2],format='(F06.3)')
        SXADDPAR,header1,'ACQTIME',new_acqtime ;UTC time at the
            end of each read frame. this makes the ramp cds acqtime
            halfway between the 2nd exposure.
        inttime = SXPARG(header1,'INTTIME')
        new_inttime = STRING(inttime+5.28384/2.,format='(F10.5)')
        SXADDPAR,header1,'INTTIME',new_inttime ;total integration
            time during a ramp at the end of an exposure. this
            makes the ramp cds inttime half way through the second
            exposure
        SXADDPAR,header1,'BITPIX',bitpix
        IF smoothing_func NE 'ref_pix_med' AND smoothing_func NE '
            median' THEN BEGIN ; removing these two keywords for

```

```

cases where the values pixel values will be integers.
they cause every pixel to be offset by 32,768.
Documented in wiki on 100908
      SXDELPAR,header1,'BSCALE'
      SXDELPAR,header1,'BZERO'
ENDIF
IF keyword_set(everyother) then image3=CONTRACT_OLD(image2
-image1,offset=[1,1]) else image3=image2-image1
WRITEFITS, 'image'+fname_st[z].rstr+fname_st[z].mstr+
fname_st[z].nstr+append+fname_st[z].suffix,PIXCAL(
image3,cal_frame=cal_frame,smoothing_func=
smoothing_func,forecast=forecast),header1
IF KEYWORD_SET(cal_frame) THEN WRITEFITS, 'cal_frame'+
fname_st[z].rstr+fname_st[z].mstr+fname_st[z].nstr+
append+fname_st[z].suffix,cal_frame,header1
print, 'I used '+smoothing_func
print, 'i did ' + fname_st[z].prefix+fname_st[z].rstr+
fname_st[z].mstr+fname_st[z].nstr+fname_st[z].suffix +
' minus '+fname_st[z-1].prefix+fname_st[z-1].rstr+
fname_st[z-1].mstr+fname_st[z-1].nstr+fname_st[z-1].
suffix + ' and called it ' + 'image'+fname_st[z].rstr+
fname_st[z].mstr+fname_st[z].nstr+fname_st[z].suffix

      ENDFOR
ENDFOR

END

```

```

PRO spectrum, events=events, xrange=xrange, yrange=yrange, xtitle=xtitle
, xstyle=xstyle, ytitle=ytitle, ystyle=ystyle, title=title,xlog=xlog,
ylog=ylog, binsize=binsize, output_name=output_name, error=error,
save=save,$
cross=cross, brightest=brightest, fraction=fraction, ecal=ecal, fitgauss
=fitgauss,spectrum_y=spectrum_y,spectrum_x=spectrum_x,n_events=
n_events,min=min,max=max,unfiltered_events=unfiltered_events,thick=
thick,xthick=xthick,ythick=ythick,charthick=charthick, multi_parinfo=
multi_parinfo, multi_funcargs=multi_funcargs

; takes an IDL event structure as input and plots the energy spectrum.

; xrange = x axis range of the output plot
; yrange = y axis range of the output plot
; xtitle = x axis title of the output plot
; ytitle = y axis title of the output plot
; title = title of the output plot
; binsize = the binsize, in DN, used when computing the spectra
  histogram
; output_name = name of the output postscript file if keyword /save is
  set
; error = keyword set to include poisson error bars in the output plot
; save = keyword set to save a postscript copy of the plot
; brightest = integer ranging from 1-9 indicating which indicates the
  number of brightest pixels in each event to include in the event sum.
  ex. brightest = 2

```

```

; indicates to plot the two brightest pixels in each event.
; fraction = make the y axis in units of fraction of total events
      instead of number of events.
; to plot spectra of a certain grade of event, use evt_filter.pro to the
      event structure that gets input to spectrum.pro.
; ecal = set this keyword to do an interactive energy calibration.
      spectrum.pro uses gain units of keV/DN to convert the x axis to
      energy
; fitgauss = a range in abccissa coordinates over which to fit a single
      gaussian. this is for doing accurate peak width and center
      measurement. if you want to fit multiple peaks, specify the abccissa
      ranges like [[low1,high1],[low2,high2],[low3,high3]]
; multi_parinfo = fill this keyword with a parinfo structure that will
      be passed to mpfitfun if you want to do a multipeak fit with
      multi_gauss3.
; multi_funcargs - funcargs array to pass to multi_gauss3.
; spectrum_x = keyword set to variable that you want to contain the
      spectrum histogram. use this for fitting with mpfitfun or making
      composite spectra.
; spectrum_y = keyword set to variable taht you want to contain the
      spectrum histograms locations. use this for fitting with mpfitfun or
      making composite spectra.
; n_events = set to a variable that will contain the number of events in
      the output plot.
; min = min value to be considered in the histogram used to create the
      spectrum
; max = max value to be considered in the histogram used to create the
      spectrum

;;;;;;;;;;;;;;;;;;;;;;;;;;;;;;;;;;;;;;;;;;;;;;;;;;;;;;;;;;;;;;;;;;;;;;;;;;;;;;;;
; accepts an IDL event structure into keyword events and plots the
      spectrum
; if keyword events not is not supplied, spectrum looks for an event
      list in the current directory
;;;;;;;;;;;;;;;;;;;;;;;;;;;;;;;;;;;;;;;;;;;;;;;;;;;;;;;;;;;;;;;;;;;;;;;;;;;;;;;;

;SPAWN, 'pwd', dirname
CD, Current=dirname ;this is doing a pwd. for some reason spawn pwd
      started giving a syntax error on 20101212...

IF NOT KEYWORD_SET(events) THEN BEGIN
      events = MRDFITS(STRMID(dirname,STRPOS(dirname,'/'),/
          reverse_search)+1,STRLEN(dirname)-STRPOS(dirname,'/'),/
          reverse_search)-1)+'.fits',1,header)
ENDIF

num_evts = N_ELEMENTS(events.x)

IF NOT KEYWORD_SET(title) THEN title = STRMID(dirname,STRPOS(dirname,'/'),/
      /reverse_search)+1,STRLEN(dirname)-STRPOS(dirname,'/'),/
      reverse_search)-1)+'.fits'
IF NOT KEYWORD_SET(xtitle) AND NOT KEYWORD_SET(ecal) THEN xtitle = 'DN'

```

```

IF NOT KEYWORD_SET(xtitle) AND KEYWORD_SET(ecal) THEN xtitle = 'Energy [
  keV]'
IF NOT KEYWORD_SET(ytitle) AND KEYWORD_SET(fraction) THEN ytitle = 'Frac
  . tot. evts.'
IF NOT KEYWORD_SET(ytitle) AND NOT KEYWORD_SET(fraction) THEN ytitle = '
  N_events.'
IF NOT KEYWORD_SET(xrange) THEN xrange=[0,3000]

IF KEYWORD_SET(brightest) THEN BEGIN
  ;sorted = DBLARR(9,num_evts)
  new_events=events
  sorted = sort_nd(new_events.island,1)
  new_events.sum = total(new_events.island[sorted[9-brightest
    :8,*]])
  ;FOR i=0L,num_evts-1 DO BEGIN
  ;   new_events=events
  ;   sorted[* ,i] = SORT(new_events[i].island)
  ;   new_events[i].sum = TOTAL(new_events[i].island[sorted[9-
    brightest:8,i]])
  ;END
ENDIF

IF KEYWORD_SET(new_events) THEN hist = HISTOGRAM(new_events.sum, binsize
  =binsize,locations=locations,min=min,max=max) $
ELSE hist = HISTOGRAM(events.sum, binsize=binsize,locations=locations,
  min=min,max=max)

IF KEYWORD_SET(ecal) THEN BEGIN
  i=0 ; while loop counter
  WHILE N_ELEMENTS(response_coef) EQ 0 DO BEGIN
    PLOT, locations,hist,psym=10, xtitle='DN', xrange
      =[0,3500], ytitle='Num. Evts.', title=title
    IF i EQ 0 THEN BEGIN
      PRINT,"You chose to do energy calibration. Click on
        the peak of the lowest energy line that you
        would like to include in the calibration..."
      cursor,x,y,4,/data
      line_coef = MPFITFUN('gaussian',locations,hist,sqrt
        (hist)+1.,[y,x,70.],yfit=yfit,/quiet)
      oplot, locations,yfit,thick=2
      READ, "What is the energy of the line that you just
        clicked in keV? ",energy
    ENDIF ELSE BEGIN
      answer=''
      READ,'Would you like to add another line to the
        energy calibration (a) or perform the
        calibration (p): ',answer
      CASE answer OF
        'a':BEGIN
          PRINT, "Click on the peak of the line that
            you would like to add to the calibration
            ..."
          cursor,x,y,4,/data

```

```

line_coef = [[line_coef],[MPFITFUN('gaussian
',locations,hist,sqrt(hist)+1.,[y,x
,70.],yfit=yfit,/quiet)]]
oplot, locations,yfit,thick=2
read, "What is the energy of the line that
you just clicked in keV? ",temp
energy=[energy,temp]
END
'p':BEGIN
    IF i EQ 0 THEN response_coef=linfit
        ([0,line_coef[1]],[0,energy],yfit
        =yfit) ELSE response_coef=linfit(
        line_coef[1,*],energy,yfit=yfit)
    END
ELSE: PRINT, "You did not type in 'a' or 'p'."
ENDCASE
ENDELSE
    i=i+1
ENDWHILE
;window,3
;plot, [coef1[1],coef2[1]],[answer1,answer2],psym=5,xtitle='DN',ytitle='
Energy',title='Linearity'
;oplot, dindgen(100)*3500./99.,dindgen(100)*3500./99.*(answer2-answer1)
/(coef2[1]-coef1[1])+(answer1-coef1[1]*(answer2-answer1)/(coef2[1]-
coef1[1]))
;window,4
;locations=locations*(answer2-answer1)/(coef2[1]-coef1[1])+(
answer1-coef1[1]*(answer2-answer1)/(coef2[1]-coef1[1]))
locations=locations*response_coef[1]+response_coef[0]
WINDOW,/free

PLOT, line_coef[1,*],energy[*],xtitle='DN',ytitle='Energy',title=
'Linearity',psym=5
OPLOT, line_coef[1,*],yfit
print, 'Conversion gain linear fit paramters: ',response_coef

ENDIF

IF KEYWORD_SET(fraction) THEN hist = hist/DOUBLE(num_evts)
window,/free
PLOT, locations,hist,psym=10,xrange=xrange, yrange=yrange, xtitle=xtitle
, ytitle=ytitle, title=title,xstyle=xstyle,ystyle=ystyle,xlog=xlog,
ylog=ylog

n_events = TOTAL(hist[WHERE(locations GT xrange[0] AND locations LT
xrange[1])])
PRINT, 'There are ' + STRCOMPRESS(STRING(n_events)) + ' events shown in
this plot.'

IF KEYWORD_SET(unfiltered_events) and KEYWORD_SET(fitgauss) THEN BEGIN ;
    taking a stab at calculating how many events were filtered out of a
given line.

```

```

n_gauss = N_ELEMENTS(fitgauss)/2.
unfiltered_hist = HISTOGRAM(unfiltered_events.sum, binsize=
    binsize,locations=unfiltered_locations,min=min,max=max)
FOR i=0,n_gauss-1 DO BEGIN
    unfiltered_gauss_locations = unfiltered_locations[WHERE(
        unfiltered_locations GE fitgauss[0,i] AND
        unfiltered_locations LE fitgauss[1,i])]
    unfiltered_gauss_hist = unfiltered_hist[WHERE(
        unfiltered_locations GE fitgauss[0,i] AND
        unfiltered_locations LE fitgauss[1,i])]
    unfiltered_yfit = GAUSSFIT(unfiltered_gauss_locations,
        unfiltered_gauss_hist,unfiltered_coef,nterms=5,sigma=
        unfiltered_sigma)
    n_unfiltered_events = total(GAUSSIAN(unfiltered_locations,
        unfiltered_coef[0:2]))
ENDFOR

ENDIF

IF n_elements(multi_parinfo) gt 0 and n_elements(multi_functargs) gt 0
    THEN BEGIN
print, multi_parinfo.fixed
    multifit = mpfitfun('multi_gauss3', locations, hist, weights=1./((
        double(hist)+1d-1), parinfo=multi_parinfo, yfit=yfit,
        functargs=multi_functargs)
;dof=dof, bestnorm=bestnorm
    oplot, locations, yfit, thick=2
print, chisq
print, 'integral of each line'
print, 'This fit missed ',total(hist-yfit),' counts. This is ',
    total(hist-yfit)/double(hist)*100., ' percent of the total
    number of the events.'
ENDIF

IF KEYWORD_SET(fitgauss) THEN BEGIN
    n_gauss = N_ELEMENTS(fitgauss)/2.
    FOR i=0,n_gauss-1 DO BEGIN
        gauss_locations = locations[WHERE(locations GE fitgauss[0,
            i] AND locations LE fitgauss[1,i])]
        gauss_hist = hist[WHERE(locations GE fitgauss[0,i] AND
            locations LE fitgauss[1,i])]
        yfit = GAUSSFIT(gauss_locations,gauss_hist,coef,nterms=5,
            sigma=sigma)
        n_filtered_events = total(GAUSSIAN(locations,coef[0:2]))
        OPLOT, gauss_locations,yfit
        PRINT, 'Gaussian fit number ' + STRING(i,FORMAT='(I02)') +
            ' results: Amplitude = '+STRCOMPRESS(STRING(coef[0]))+'
            +/-'+STRCOMPRESS(STRING(sigma[0]))+' mu = '+
            STRCOMPRESS(STRING(coef[1]))+' +/-'+STRCOMPRESS(STRING(
            sigma[1]))+' sigma = '+STRCOMPRESS(STRING(coef[2]))+'
            +/-'+STRCOMPRESS(STRING(sigma[2]))
        PRINT, '          '+STRCOMPRESS(STRING(sigma[2]))
            '+ Delta E/E = '+
            STRCOMPRESS(STRING(coef[2]*2.354/coef[1]))
    ENDFOR
ENDIF

```

```

        IF KEYWORD_SET(unfiltered_events) THEN PRINT, '
                    '+' Approximate fraction of true
                    X-rays in this line remaining after filtering: '+
                    STRCOMPRESS(STRING(n_filtered_events/
                    n_unfiltered_events))
    ENDFOR
ENDIF

IF KEYWORD_SET(error) THEN ERRPLOT, locations,hist-SQRT(hist)/2.,hist+
    SQRT(hist)/2.

IF KEYWORD_SET(save) THEN BEGIN
    set_plot, 'ps'
    IF NOT KEYWORD_SET(output_name) THEN device, filename='spectrum'+
        STRMID(dirname,STRPOS(dirname,'/',/reverse_search)+1,STRLEN(
        dirname)-STRPOS(dirname,'/',/reverse_search)-1)+'.ps' ELSE
        device, filename=output_name
    printplot

    PLOT, locations,hist,psym=10,xrange=xrange, yrange=yrange, xtitle
        =xtitle, ytitle=ytitle, title=title,xstyle=xstyle,ystyle=
        ystyle,thick=thick,xthick=xthick,ythick=ythick,charthick=
        charthick

    IF KEYWORD_SET(fitgauss) THEN BEGIN ; the refitting needs to be
        here so that more than one line fit can be oplotted. you could
        always save the fits to an array but this is simpler.
        n_gauss = N_ELEMENTS(fitgauss)/2.
        FOR i=0,n_gauss-1 DO BEGIN
            gauss_locations = locations[WHERE(locations GE
                fitgauss[0,i] AND locations LE fitgauss[1,i])]
            gauss_hist = hist[WHERE(locations GE fitgauss[0,i]
                AND locations LE fitgauss[1,i])]
            yfit = GAUSSFIT(gauss_locations,gauss_hist,coef,
                nterms=5,sigma=sigma)
            OPLOT, gauss_locations,yfit
        ENDFOR
    ENDFIT
    IF KEYWORD_SET(error) THEN ERRPLOT, locations,hist-SQRT(hist)/2.,
        hist+SQRT(hist)/2.
    DEVICE, /close

    set_plot, 'x'
    printplot, /normal

ENDIF

spectrum_y = hist
spectrum_x = locations

END

```

C.3 QE Teststand

- gas_trans.pro
- h1rg_qe.pro
- mucal.pro
- multi_gauss3.pro
- pc_extract_counts.pro
- pc_read_spectrum.pro
- sb_henke.pro
- sb_read_henke.pro
- sim_error.pro
- sim_qe.pro

```
function gas_trans, energy, gas_depth, gas_temperature, gas_pressure, z=
    z, fraction=fraction, en_weights=en_weights, xsec=xsec, use_mucal=
    use_mucal

; behavior

; (dtp - depth temperature pressure)
; when en is a scalar and dtp are scalars, returns a single transmission
.

; It is not recommended to use gas_trans in this way inside of a loop
. This will be slow. Take advantage of the vectorization features.
; when en is a scalar, and #dtp gt 1, returns #dtp of results in a
vertical vector

; Useful for a source with one energy and many variants of dtp.
; when en is a vector, and #dtp gt 1, returns #dtp of results and
assumes that you want each energy to apply to each dtp. #en and #dtp
must be the same.

; Useful for different energies and different dtp states
; when en is a vector and #dtp eq 1, returns # en results.

; Useful for constructing an energy transmission spectrum.
; when en is a vector and en_weights is set, assumes that energies are
from a single source and should be averaged together.
```

```

; Useful for a source with multiple energies.
; when z is a scalar, one element is used for all iterations.
; when z is a horizontal array, it is assumed that all elements are
  present in all iterations.

; when xsec is set, mucal/henke are bypassed and the specified cross
  sections are used instead. if #en=1 then x dimension of xsec must
  equal #z and #fraction. if #en >1 and #z or #fraction >1 then
  xdimension of xsec is for z and y dimension is for en. if #en >1 and
  #z or #fraction =1 then x dimension of xsec must equal #z and #
  fraction. XSEC MUST BE INPUT IN UNITS OF BARNES PER ATOM!!!

; Note that at the moment, mucal cannot deal with a new set of z values
  for each iteration but eventually i'd like to use the vertical
  direction of the z array to enable this capability.
; outputs the fraction x-ray transmission through a volume of gas

; en - x-ray photon energy in [keV]
; depth - depth of absorbing gas in [cm]
; temperature - temperature of absorbing gas in [kelvin]
; pressure - pressure of absorbing gas in [atm]
; z - atomic number of absorbing gas species
; fraction - the number of each species PER GAS PARTICLE. Note that this
  is weird. p10 is z=[18,6,1] and fraction=[.9,.1,.4]. Nitrogen would
  be [5] [2] because it is diatomic. Pure argon would be [18] [1]. Pure
  methane would be [6,1] [1,4].
; en_weights - a keyword that needs to be used if there is more than one
  energy X-ray photon entering the gas. It specifies the ratio of the
  energies.
; use_mucal - keyword switch that uses mucal.pro to look up x-ray cross
  secitons instead of the default henke.pro

en=energy      ; do this so that the changed energy array does not get
  passed back out of the function and mess up the standard idl session.
depth = gas_depth
temperature = gas_temperature
pressure = gas_pressure

;ERROR CHECKING
if keyword_set(en_weights) then begin
  if n_elements(en) ne n_elements(en_weights) then begin
    print, 'gas_trans.pro says that the number of energies and
      the number of energy weights must agree.'
    stop
  endif
  if total(en_weights) ne 1. then begin
    print, 'gas_trans.pro says that the energy weights were
      not normalized so I normalized them.'
    en_weights = en_weights/total(en_weights)
  endif
endif
endif

```

```

n_depth = n_elements(depth)
n_temperature = n_elements(temperature)
n_pressure = n_elements(pressure)
if (n_depth ne n_temperature and lnot(n_depth eq 1 or n_temperature eq 1
    )) or (n_depth ne n_pressure and lnot(n_depth eq 1 or n_pressure eq
    1)) then begin
    print, "gas_trans.pro says that the number of elements in depth,
        temperature, and pressure either need to be the same or the
        non identical arrays number of elements must be equal to one."
    stop
endif

k= 1.3806488d-16 ; boltzman constant in cgs
; if energy is a scalar, then just make it a 1 element 1d vector to make
    idl happy.
if (size(en))(0) eq 0 then en = [en]
n_en = n_elements(en) ;number of elements in the energy array
if keyword_set(z) then n_el = n_elements(z) else n_el = n_elements(
    fraction) ;number of elements present in the gas
n_iter = n_elements(depth) ; number of 'dtp iterations' of the system
    to calculate

; convert pressure from atm to the cgs unit bayre (not bar!!!)
pressure = pressure * 1013250.

;fixing arrays to always be a horizontal array. vertical vs horizontal
    usually does not matter when doing array manipulations but it matters
    here because of the array inflation
p_size = size(pressure)
t_size = size(temperature)
d_size = size(depth)
if p_size[0] eq 2 then pressure = transpose(pressure)
if t_size[0] eq 2 then temperature = transpose(temperature)
if d_size[0] eq 2 then depth = transpose(depth)

if not keyword_set(xsec) then begin
    ; looking up cross sections using mucal.
    if not keyword_set(fraction) then begin
        if not keyword_set(z) then begin
            print, 'gas_trans.pro says that if you do not set
                xsec, I need to know the element(s)'
            stop
        endif
        if n_elements(z) gt 1 then begin
            print, 'gas_trans.pro says that if you do not set
                xsec, I need to know element fractions.'
            stop
        endif
        if n_elements(z) eq 1 then fraction =[1.]
    endif
    if n_elements(z) ne n_elements(fraction) then begin

```

```

        print, 'gas_trans.pro says that the number of elements and
              the number of element fractions must agree.'
        stop
    endif
; took out normalizing because it is wrong. this prevents there
    from being more than one atom per gas particle.
; if total(fraction) ne 1. then begin
;     print, 'gas_trans.pro says that the element fractions were
        not normalized so I normalized them.'
;     fraction = fraction/total(fraction)
; endif

if keyword_set(use_mucal) then begin
print, en, z
    ; using my mucal code
    mucal, en, z, xsec
endif else begin
    ; using my henke code
    sb_henke, en, z, xsec
; chris jacobsens henke.pro is not vectorized for energy,
    z, or density so we have to feed it one at a time.
; f2_out = dblarr(n_elements(z), n_en)

; for i = 0, n_en-1 do begin
;     for j = 0, n_elements(z)-1 do begin
;         density = 1 ; dummy density. the f1 f2
            will be accurate but delta and beta will not.
;         energy = en*1000.
;         henke, z2element(z[j]), density, energy[i], f1,
            f2, delta, beta
;         ; beta and delta can be easily used to
                calculate the abs coef using abs_coef =
                    4.*!dpi*beta*en/(h*c), but it is a pain
                    to go backwards to the xsec. it is
                    easier to go from f1 and f2 to the xsec,
                    which will then be used to go to the
                    abs coef.
;         f2_out[j, i] = f2
;     endfor
; endfor
; h = 6.62606957d-27
; c = 2.99792458d10
; EVperERG = 6.2414503832469d11
; ANGperCM = 1d8
; RE = 2.817938070d-13 ; radius of the electron in cm
; xsec = 2*f2_out*RE*1d-16*h*c*(EVperERG*ANGperCM)^2/rebin(
    reform(energy, 1, n_en), 3, n_en)
endif else
; print, xsec
endif else begin
; using the specified cross sections
if (size(xsec))(0) eq 1 and n_elements(en) eq 1 and n_elements(
    xsec) ne n_elements(fraction) then begin

```

```

        print, 'gas_trans.pro says that the number of elements in
              fraction array must be equal to the number of rows in
              xsec array.'
        stop
    endif
    if (size(xsec))(0) eq 1 and n_elements(xsec) ne n_elements(en)
        then begin
            print, 'gas_trans.pro says that the number of elements in
                  en array must be equal to the number of rows in xsec
                  array.'
            stop
        endif
    endif

    if keyword_set(xsec) and (size(xsec))(0) eq 2 then begin
        print, 'xsec is being interpreted with species in the
              first dimension and energies in the second dimension.'
    endif

; if cross sections are supplied as a sum for multiple species we
    need to expand xsec to match the output from mucal, which
    lists xsec vertically by energy and horizontally by individual
    species. When you supply xsec this way, you are supplying
    total cross section at a given energy.
    if keyword_set(xsec) and (size(xsec))(0) eq 1 and n_en gt 1 then
        begin
            xsec = [transpose(xsec),dblarr(n_el-1,n_en)]
        endif
    if keyword_set(xsec) and (size(xsec))(0) eq 1 and n_el gt 1 then
        begin

    endif
;if #en=1 then x dimension of xsec must equal #z and #fraction.
    if #en >1 and #z or #fraction >1 then xdimension of xsec is
    for z and y dimension is for en. if #en >1 and #z or #fraction
    =1 then x dimension of xsec must equal #z and #fraction.
endelse

; figure out the partial pressures (pressure*fraction) to get the
    respective n numbers of each species n = P/(kT)
;n = rebin([pressure],n_iter,n_en,n_el)*rebin(transpose(reform(fraction,
    n_el,1,1),[2,1,0]),n_iter,n_en,n_el)/(k*rebin([temperature],n_iter,
    n_en,n_el))

; NEW!!!!!!!!!!!!this method does not use partial pressures
n = rebin([pressure],n_iter,n_en,n_el)/(k*rebin([temperature],n_iter,
    n_en,n_el))

depth = rebin([depth],n_iter,n_en,n_el)

; had problems multiplying this rebinned n array by other arrays when it
    is only one element in size. when en was an array, it would only
    multiply the first element of en. this necessitates the following
    line

```

```

if n_elements(n) eq 1 then begin
    n = n[0]
    depth = depth[0]
endif

;index = reform(indgen(n_el,n_en),n_en,n_el)
xsec = rebin(transpose(reform(xsec,n_el,n_en,1),[2,1,0]),n_iter,n_en,
    n_el)

; NEWW!!!!!!!!!!!!!!!!!!!!!!alculatate an effective cross section based on the
    element species present. This should yield a cross section per gas
    particle.
xsec = total(xsec*rebin(transpose(reform(fraction,n_el,1,1),[2,1,0]),
    n_iter,n_en,n_el),3)

; the absorption coefficient (cm^-1) used in formula I=I_0*exp(-xsec
    [5]*1d-24*n*thickness)
; obviously xsec[5] is only correct for one energy. This is for xsec in
    units of barnes/atom. For cm^2/g, the formula should be I_0*exp(-xsec
    [5]*density*thickness)

;I/I_0 = exp(-(total xsec [cm^2/gm]) * converstion factor [gm barn /
    atom cm^2] * [cm^2/barn] * [1/cm^3] * [cm] )
; note: absorption coefficients should be in units of barns per atom by
    default.
; use IDLs built in product of a sequence function product() to
    multiplicativly combine the effects of the different species

if keyword_set(en_weights) then begin
    ; perform a weighted average of the transmission with the
        en_weights (combining the action from different photons to get
        the average transmission.)
    ; perform a product of a sequence to combine terms from different
        species (these are acting at the same time on the same photon
        and get multiplied to combine their effect)
    ;return, total(product(exp(-xsec*1d-24*n*depth),3)*rebin(reform(
        en_weights,1,n_en),n_iter,n_en),2)
    ; new!!!!!!!!!!!!!!!!!!!!!!!!!!!!!!
    return, total(exp(-xsec*1d-24*n*depth)*rebin(reform(en_weights,1,
        n_en),n_iter,n_en),2)

    endif else begin
        ;return, product(exp(-xsec*1d-24*n*depth),3)
        ; new!!!!!!!!!!!!!!!!!!!!!!!!!!!!!!
        ; do not need to do the product thing because you've calculated
            an effective cross section for all species.
        return, exp(-xsec*1d-24*n*depth)
    endif
endif

end



---


function h1rg_qe, $

```

```

pc_d1, pc_d2, h1rg_d1, h1rg_d2, pc_l1, pc_l2, pc_l3, h1rg_l1, h1rg_l2,
  h1rg_l3,$
h1rg_xwinsize, h1rg_ywinsize, pc_xwinsize, pc_ywinsize, $
pc_countrate, h1rg_counts, n_frames, $
countrate_twowin, countrate_onewin, $
gas_depth, gas_t, gas_p, gas_fraction=gas_fraction, gas_z=gas_z, energy=
  energy, en_weights=en_weights,$
p_results=p_results, nominal=nominal

; there are 25 random variables
; PURPOSE
; function takes the QE test stand's many parameters as input and
  outputs the h1rg's qe

;KEYWORDS
; pc and h1rg d1 and d2 - these are the distances between the
  measurement points on the proportional counter and H1rg, respectively
  . There are three points in the shape of a right triangle and d1 and
  d2 measure the length of the legs. Error in the position of these
  points is assumed to be machining error (~0.001") which is negligible
  .

; pc and h1rg l1, l2, and l3 - these are the distances from the source
  to the three measurement points on the proportional counter and h1rg,
  respectively.
; h1rg and pc x and y winsize - the x and y size of the of the h1rg
  detector and the pc window.
;l1 and l2 span d2. l2 and l3 span d1.

; pc_countrate - the deadtime corrected countrate recorded during a data
  run in the proportional counter
; h1rg_counts - number of counts recorded during the data run in the
  H1rg detector
; n_frames - the number of h1rg data frames in the data run (used to
  calculate total h1rg live time)
; energy - the line energy(ies) of the photons in keV
; en_weights - the fraction of photons that the current source produces
  at the corresponding energy. when there are multiple line energies
  things get weird. If there are multiple energies present and you
  assume nothing about the smoothness of the QE(E) function, which we
  probably shouldn't since this function can be jagged and weird, all
  that we can do is calculate a weighted average of the QE at the given
  energies. If the proportional counter had enough energy resolution
  to separate the energies and produce a countrate within each given
  line, then we could calculate a QE value at each energy.
  Unfortunately, the PC has terrible energy resolution and it's
  physically impossible to separate the Mn kalpha and kbeta lines.
; a better way to do this would be to take a calibrated PC spectrum, as
  opposed to simple countrates, as input. this could help account for
  low energy bremsstrahlung from a Henkey tube.
; UPDATE I HAVE DEACTIVATED THIS KEYWORD - i'll take care of this when i
  generate the random input to this function using sim_error.pro

```

```

; as it is, right now what this program will output is the weighted mean
    of the qe at both energies. this is not the qe in between, and it's
    not possible to resolve the qe at a single energy. it's just a
    weighted average of the two. lets just quote that and move on.

; countrate_twowin - the countrate measured with two windows in front of
    the proportional counter (calibrating the outer filter)
; countrate_onewin - the countrate measured with one window in front of
    the proportional counter (baseline measurement)

; gas_depth - proportional counter gas volume depth (cm)
; gas_temp - proportional counter gas temperature (K)
; gas_p - proportional counter gas pressure (bar)

; p_results - prints results to the screen for debugging.
; nominal - keyword switch that, when set, prints a bunch of ratios to
    help you see where the qe took a hit during the calculation

; VECTOR MATH
; the distance measurement from the source to the three points (a right
    triangle of known size) on the detectors are vectors. Nominally,
    these are all the same distance but with measurement error, they will
    vary. Calculate the vector from the source to the center of the
    detector in terms of the right triangle distances and the three
    distance measurements.
; cross multiply the two right triangle vectors to get the vector
    perpendicular to the plane of the detector
; use the cross product between this norm vector and the source-
    detectorcenter vector to get the angle between them
; multiply the detector area by cos of this angle to get the area of the
    shifted detector plane projected onto the xy plane.
; see wiki for the algebra

;d1 and d2 are the distances, in the detector plane, between the
    measurement points
;l1, l2, and l3 are the distances from the source to the measurement
    points
; in practice, these are
;the nominal l values can be calculated using c_dist and the measured d
    values

h1rg_lcx = -(h1rg_l2^2 - h1rg_l3^2)/(2.*h1rg_d1)
h1rg_lcy = (h1rg_l1^2 - h1rg_l2^2)/(2.*h1rg_d2)
h1rg_lcz = sqrt(h1rg_l1^2 - h1rg_lcx^2 + h1rg_lcx*h1rg_d1 - h1rg_d1^2/4.
    - h1rg_lcy^2 + h1rg_lcy*h1rg_d2 - h1rg_d2^2/4.)
; i think the below line is wrong...
;h1rg_theta = asin(sqrt((h1rg_lcy^2 - h1rg_lcx^2)/(h1rg_lcx^2 + h1rg_lcy
    ^2 + h1rg_lcz^2)))
; it should be the following...
h1rg_theta = asin((h1rg_lcy^2 - h1rg_lcx^2)/sqrt(h1rg_lcx^2 + h1rg_lcy^2
    + h1rg_lcz^2))

```

```

h1rg_c_dist = sqrt(h1rg_lcx^2 + h1rg_lcy^2 + h1rg_lcz^2); this is just
    the combination of the xyz components that we just calculated
h1rg_eff_area = cos(h1rg_theta)*h1rg_xwinsize*h1rg_ywinsize

pc_lcx = -(pc_l2^2 - pc_l3^2)/(2.*pc_d1)
pc_lcy = (pc_l1^2 - pc_l2^2)/(2.*pc_d2)
pc_lcz = sqrt(pc_l1^2 - pc_lcx^2 + pc_lcx*pc_d1 - pc_d1^2/4. - pc_lcy^2
    + pc_lcy*pc_d2 - pc_d2^2/4.)
; i think the below line is wrong...
;pc_theta = asin(sqrt((pc_lcy^2 - pc_lcx^2)/(pc_lcx^2 + pc_lcy^2 +
    pc_lcz^2)))
pc_theta = asin((pc_lcy^2 - pc_lcx^2)/sqrt(pc_lcx^2 + pc_lcy^2 + pc_lcz
    ^2))
pc_c_dist = sqrt(pc_lcx^2 + pc_lcy^2 + pc_lcz^2)
pc_eff_area = cos(pc_theta)*pc_xwinsize*pc_ywinsize

; this is the general way to do the filter calculation
;supportive mesh
;pc_countrate = pc_countrate / filter_trans(energy, thickness1, density1
    , composition1 = composition1) * blocked_fraction1 + (1.-
    blocked_fraction1)
;window material
;pc_countrate = pc_countrate / filter_trans(energy, thickness2, density2
    , composition2 = composition2) * blocked_fraction2 + (1.-
    blocked_fraction2)
;gas detection medium

; this is the easy, empirical way to do the filter transmission
    calculation
; countrate_twowin/countrate_onewin is the transmission fraction through
    the window that was present in one of the calibration runs. Note, it
    's probably better if the same window is on the inside in both runs
    to keep any electric field effects from the inner surface of the
    window constant
pc_countrate_win = pc_countrate / (countrate_twowin/countrate_onewin)
; P-10 is 90% argon 10% methane by volume. Methane's chemical formula is
    CH4. Therefore, the number fraction of the gas is [90/(90+10*5),
    10/140, 40/140] = [0.642857, 0.0714286, 0.285714] (% by volume is the
    same as number percentage of gas particles due to PV = nkT. Imagine
    two plastic bags filled to the same volume with different gasses. The
    bags are not taut so P = 1atm, the volume is the same by design, and
    T is the same because the systems are allowed to equilibrate.
    Therefore n is the same inside the bags. The only thing different is
    that the heavier gas atoms will be moving slower.) and the z numbers
    are [18, 6, 1]

;gas_fraction = [0.642857, 0.0714286, 0.285714]
;gas_z = [18, 6, 1]

gas_transmission = gas_trans(energy, gas_depth, gas_t, gas_p, z=gas_z,
    fraction=gas_fraction, en_weights=en_weights)

```

```

; (1-gas_trans) is the absorption fraction. true counts * absorption =
;   detected counts. therefore detected counts / ( 1-transmission) = true
;   counts
pc_countrate_trans = pc_countrate_win / (1- gas_transmission)

luminosity = pc_countrate_trans * (4.*!dpi*(pc_c_dist)^2) / pc_eff_area

;h1rg_counts is the total number of counts in a ramp. n_frames is the
;   number of frames in the ramp
h1rg_countrate = h1rg_counts/(n_frames*5.24288)

qe = h1rg_countrate/(luminosity*(h1rg_eff_area/(4.*!dpi*h1rg_c_dist^2)))

if keyword_set(p_results) then begin
    print, 'h1rg_theta',h1rg_theta
    print, 'h1rg_c_dist',h1rg_c_dist
    print, 'h1rg_eff_area',h1rg_eff_area
    print, 'pc_theta',pc_theta
    print, 'pc_c_dist',pc_c_dist
    print, 'pc_eff_area',pc_eff_area
    print, 'gas_transmission',gas_transmission
    print, 'pc_countrate',pc_countrate
    print, 'h1rg_countrate',h1rg_countrate
endif

if keyword_set(nominal) then begin
    print, 'PC gas transmission = ', gas_transmission
    print, 'Detector projected area ratios = ', h1rg_eff_area/
        pc_eff_area
    print, 'Detector flux ratio due to different distance = ',(
        h1rg_c_dist/pc_c_dist)^2
endif

return, qe
end

```

```

pro mucal, en, z, xsec, unit=unit, output=output, er=er, print_er=
    print_er

;   input:
;   en=energy at which we need the x-section (in keV)
;   unit=units to be output.'C' for cm**2/gm,'B' for barns/atom |
;   cross sections
;   output=choose between photoelectric abs.(p), coherent scattering |
;   (c), incoherent scattering (i), and total cross section (t). |
;   Total is default.
;   z=atomic number of the elements
;   print_er=set keyword to print errors to screen
;
;   returned values:
;   xsec(0)=photoelectric x-section cm^2/gm
;   xsec(1)=coherent x-section cm^2/gm
;   xsec(2)=incoherent x-section cm^2/gm

```

```

;   xsec(3)=total x-section cm^2/gm
;   xsec(4)=conversion factor unitless barns/atom = C * (cm^2/gm) |
;           barn = 10^-24 cm^2
;   xsec(5)=absorption coefficient cm^-1
;   xsec(6)=atomic weight gm/mol
;   xsec(7)=density gm/cm^3
;   xsec(8)=l2-edge jump
;   xsec(9)=l3-edge jump
;
;   energy(0)=k-edge energy
;   energy(1)=l1-edge energy
;   energy(2)=l2-edge energy
;   energy(3)=l3-edge energy
;   energy(4)=m-edge energy
;   energy(5)=k-alpha1
;   energy(6)=k-beta1
;   energy(7)=l-alpha1
;   energy(8)=l-beta1
;
;   fly(0)= k fluorescence yield
;           |
;   fly(1)= l1 fluorescence yield
;           |
;   fly(2)= l2 fluorescence yield
;           |
;   fly(3)= l3 fluorescence yield
;           |
;
;   er=error code
;
;   error codes:
;   er=1: energy input is zero
;   er=3: no documentation for given element (z<94)
;   er=4: no documentation for given element (z>94)
;   er=5: l-edge calculation may be wrong for z<30 as mcmaster |
;         uses l1 only.
;   er=6: energy at the middle of edge
;   er=7: no z supplied
;
; HOW THIS THING IS VECTORIZED
; if en is an array, the output will be cross sections for different
  energies
; if z is a horizontal array, it's assumed that it specifies the output
  will be cross sections for different z
; if both are arrays, the output will be cross sections for different e
;   on the y axis and z on the x axis of the array.
; NOTE: this means that right now you can only calculate for one set of
  z's at a time
;   eventually i'd like to allow for submitting a 2d z array where
  the x axis is different elements, and the
;   y axis is for different energies

```

```

; READ THAT MCMASTER DATA FROM FILE
read_data, '/Users/sdb210/code/mucal/datafile.txt', data

if not keyword_set(output) then output = 't'
if output ne 't' and output ne 'c' and output ne 'i' and output ne 'p'
  then begin
    print, 'Output was not specified correctly. Enter either
    photoelectric abs. (p), coherent scattering (c), incoherent
    scattering (i), or total cross section (t).'
  stop
endif

; MAKE THE UNIT UPPERCASE IF IT ISN'T ALREADY UPPERCASE
if keyword_set(unit) then unit = strupcase(strcompress(unit,/remove_all)
) else unit = 'B'

;ERROR CHECKING TIME
er = 0
if n_elements(z) eq 0 then begin
  er = 7
  if keyword_set(print_er) then print, '**no z, what do you want?**'
  stop
endif

if where(en le 0) ne -1 then begin
  er = 1
  if keyword_set(print_er) then print, '**can not calculate for
  zero (or negative) energy**'
  stop
endif else begin
  e = en
endif

if where(z eq 84 or z eq 85 or z eq 87 or z eq 88 or z eq 89 or z eq 91
or z eq 93) ne -1 then begin
  er = 3
  if keyword_set(print_er) then print, '**sorry no documents Z
  =84,85,87-89,91,93**'
  stop
endif

if where(z gt 94 or z lt 1) ne -1 then begin
  er = 4
  if keyword_set(print_er) then print, '**no documents for Z > 94
  or no elements with Z < 0**'
  stop
endif

; getting the ELEMENTS INDEX array that we're interested in
el_ind = z-1
n_el_ind = n_elements(el_ind)

; checking to see if an energy is in the middle of an edge

```

```

if total((e lt data[el_ind].ek and e gt data[el_ind].ek - 0.001) or $
  (e lt data[el_ind].el and e gt data[el_ind].el - 0.001) or $
  (e lt data[el_ind].em and e gt data[el_ind].em - 0.001)) gt 0 then
  begin

    er = 6
    if keyword_set(print_er) then print, '**at least one energy is at the
      middle of an edge. using pre-edge fit results may be wrong.**'
  endif

; STARTING THE CALCULATION

n_e = n_elements(en)

;INITIALIZE vars

bsum = dblarr(1,n_e,n_el_ind)
sum = bsum
chs = bsum
csum = bsum
cis = bsum
cisum = bsum

; inflating the exponents array
exponents = rebin(indgen(4),4,n_e,n_el_ind)

; inflating the energy array
e = rebin(reform(en,1,n_e),4,n_e,n_el_ind)

;which energies to include in this calculation
;calc = where(e ge rebin(reform(data[el_ind].ek,1,1,n_el_ind),4,n_e,
  n_el_ind),count)
calc2d = where(e[0,*,*] ge rebin(reform(data[el_ind].ek,1,1,n_el_ind),1,
  n_e,n_el_ind),count) ; i think that i need this 2d index to use
  after total has been used to go from 3 to 2d.
;summing...
if count gt 0 then sum[calc2d] = sum[calc2d] + (total(rebin(reform(data[
  el_ind].ak[0:3],4,1,n_el_ind),4,n_e,n_el_ind)*alog(e)^exponents,1))(
  calc2d)

;calc = where(e lt rebin(reform(data[el_ind].ek,1,1,n_el_ind),4,n_e,
  n_el_ind) and e ge rebin(reform(data[el_ind].l3,1,1,n_el_ind),4,n_e,
  n_el_ind),count)
calc2d = where(e[0,*,*] lt rebin(reform(data[el_ind].ek,1,1,n_el_ind),1,
  n_e,n_el_ind) and e[0,*,*] ge rebin(reform(data[el_ind].l3,1,1,
  n_el_ind),1,n_e,n_el_ind),count)
if count gt 0 then sum[calc2d] = sum[calc2d] + (total(rebin(reform(data[
  el_ind].al[0:3],4,1,n_el_ind),4,n_e,n_el_ind)*alog(e)^exponents,1))(
  calc2d)

;calc = where(e lt rebin(reform(data[el_ind].l3,1,1,n_el_ind),4,n_e,
  n_el_ind) and e ge rebin(reform(data[el_ind].em,1,1,n_el_ind),4,n_e,

```

```

    n_el_ind),count)
calc2d = where(e[0,*,*] lt rebin(reform(data[el_ind].l3,1,1,n_el_ind),1,
    n_e,n_el_ind) and e[0,*,*] ge rebin(reform(data[el_ind].em,1,1,
    n_el_ind),1,n_e,n_el_ind),count)
if count gt 0 then begin
    sum[calc2d] = sum[calc2d] + (total(rebin(reform(data[el_ind].am
    [0:3],4,1,n_el_ind),4,n_e,n_el_ind)*alog(e)^exponents,1))(
    calc2d)
    if total(z le 29) gt 0 then begin
        er = 5
        if keyword_set(print_er) then print, '**WARNING:McNaster
        uses L1 edge results. May be imprecise for Z < 30 **'
    endif
endif
endif

;calc = where(e lt rebin(reform(data[el_ind].em,1,1,n_el_ind),4,n_e,
    n_el_ind),count)
calc2d = where(e[0,*,*] lt rebin(reform(data[el_ind].em,1,1,n_el_ind),1,
    n_e,n_el_ind),count)
if count gt 0 then sum[calc2d] = sum[calc2d] + (total(rebin(reform(data[
    el_ind].an[0:3],4,1,n_el_ind),4,n_e,n_el_ind)*alog(e)^exponents,1))(
    calc2d)

bax = exp(sum)

calc = z gt 29
if total(calc) gt 0 then begin
    calc1 = e ge rebin(reform(data[el_ind].l3,1,1,n_el_ind),4,n_e,
        n_el_ind) and e lt rebin(reform(data[el_ind].l2,1,1,n_el_ind)
        ,4,n_e,n_el_ind)
    if total(calc and calc1) gt 0 then bax[where(calc and calc1)] =
        bax[where(calc and calc1)]/(lj1*lj2)
    calc2 = e ge rebin(reform(data[el_ind].l2,1,1,n_el_ind),4,n_e,
        n_el_ind) and e lt rebin(reform(data[el_ind].el,1,1,n_el_ind)
        ,4,n_e,n_el_ind)
    if total(calc and calc2) gt 0 then bax[where(calc and calc2)] =
        bax[where(calc and calc2)]/lj1
endif

;calc = e eq 1
calc2d_bin = e[0,*,*] eq 1.
calc2d = where(calc2d_bin)
calc2dnot_bin = lnot(e[0,*,*] eq 1.)
calc2dnot = where(calc2dnot_bin)
if total(calc2d) gt 0 then chs[calc2d] = chs[calc2d] + (total(rebin(
    reform(data[el_ind].coh[0:3],4,1,n_el_ind),4,n_e,n_el_ind),1))(calc2d
    ) $
else chs[calc2dnot] = chs[calc2dnot] + (total(rebin(reform(data[el_ind].
    coh[0:3],4,1,n_el_ind),4,n_e,n_el_ind)*alog(e)^exponents,1))(
    calc2dnot)

bcx = exp(chs)

```

```

;calc = e eq 1.
calc2d_bin = e[0,*,*] eq 1.
calc2d = where(calc2d_bin)
calc2dnot_bin = lnot(e[0,*,*] eq 1.)
calc2dnot = where(calc2dnot_bin)
if total(calc2d) gt 0 then cis[calc2d] = cis[calc2d] + (total(rebin(
    reform(data[el_ind].coh[0:3],4,1,n_el_ind),4,n_e,n_el_ind),1))(calc2d
) $
else cis[calc2dnot] = cis[calc2dnot] + (total(rebin(reform(data[el_ind].
    coh[0:3],4,1,n_el_ind),4,n_e,n_el_ind)*alog(e)^exponents,1))(
    calc2dnot)

binx = exp(cis)

btox = bax + bcox + binx

; in the below section, reforming the btox matrix puts the array in the
    correct size, but the elements are in the wrong order.
; i need to create a new array (named index) to rearrange them
index = transpose(indgen(n_e,n_el_ind))

; choose which type of output you want.
case output of
    ; my new output variable
    't':begin
        case unit of
            'C': xsec = (reform(btox,n_el_ind,n_e))(index)*
                rebin(data[el_ind].den,n_el_ind,n_e)/rebin(data
                    [el_ind].cf,n_el_ind,n_e)
            'B': xsec = (reform(btox,n_el_ind,n_e))(index)
        endcase
    end
    'p':begin
        case unit of
            'C': xsec = (reform(bax,n_el_ind,n_e))(index)*
                rebin(data[el_ind].den,n_el_ind,n_e)/rebin(data
                    [el_ind].cf,n_el_ind,n_e)
            'B': xsec = (reform(bax,n_el_ind,n_e))(index)
        endcase
    end
    'c':begin
        case unit of
            'C': xsec = (reform(bcox,n_el_ind,n_e))(index)*
                rebin(data[el_ind].den,n_el_ind,n_e)/rebin(data
                    [el_ind].cf,n_el_ind,n_e)
            'B': xsec = (reform(bcox,n_el_ind,n_e))(index)
        endcase
    end
    'i':begin
        case unit of
            'C': xsec = (reform(binx,n_el_ind,n_e))(index)*
                rebin(data[el_ind].den,n_el_ind,n_e)/rebin(data

```

```

                                [el_ind].cf,n_el_ind,n_e)
                                'B': xsec = (reform(binx,n_el_ind,n_e))(index)
                                endcase
                                end
                                endcase
                                end

```

```

FUNCTION multi_gauss3, x, input_pars, npeaks=npeaks, nterms=nterms,
ncomponents=ncomponents

; calculates a sum of multiple gaussians to make a multi peaked output.
; Each peak can be composed of a sum of gaussian components, each with
; a variable number of terms

; F = par(0)*EXP(-Z^2/2) + par(3) + par(4)*X + par(5)*X^2
; Z = (X-par(1))/par(2)
; par 0 - A
; 1 - mu
; 2 - sigma
; 3 - skewnormal factor
; 4 - continuum offset
; 5 - continuum linear slope
; 6 - continuum parabolic curvature

; x is the independent variable
; pars is an array filled with all of the gaussian parameters with the
; parameters from subsequent gaussian components and subsequent peaks
; concatenated end to end.
; npeaks is a scalar, the number of peaks that will be generated in the
; output
; ncomponents is a vector with one element for each peak produced in
; the output. It determines the number of gaussians components that
; will be summed to make up the final peak. The first gaussian has
; standard units. The subsequent gaussian amplitudes and widths are
; specified as ratios with respect to the first gaussian in the peak.
; All mu parameters for components after the first should be specified
; in units with respect to the first component's mu.
; nterms is a vector with one element for each gaussian used in the
; function. that element specifies the number of terms to used in that
; gaussian.

; examples:
; x = dindgen(500)/499*40-20
; plot, x, multi_gauss3(x, [5,0,1,0,0,0,-1, 4,2,1, .5,-1,1.5,
; 7,1,2,0,6], npeaks=3,nterms=[7,3,3,5], ncomponents=[1,2,1]) ;produces
; 3 peaks, one with two components, each with a different number of
; terms.
; plot, x, multi_gauss3(x, [10,-10,2, .5,2,2, .25,4,2, 10,10,2, .5,2,2,
; .25,4,2], npeaks=2,nterms=[3,3,4, 3,3,4], ncomponents=[3,3]) ;
; showcases that all component parameter values after the first are
; relative to the first one.

```

```

;pars =      [      - - - - -      - - -      - - -      - - - - -      ]
;nterms =    [      6      3      3      5      ]
;ncomponents = [      1      2      1      ]
;npeaks =     [      3      ]

; calculating the gaussian causes benign floating point underflow errors
; that cause mpfitfun to stop. david fanning provides this solution
; for ignoring them in only this function.
currentExcept = !Except
!Except = 0

pars=input_pars

if not keyword_set(npeaks) and keyword_set(nterms) then npeaks =
    n_elements(nterms)
if not keyword_set(npeaks) then npeaks=1
if not keyword_set(ncomponents) then ncomponents = intarr(npeaks) + 1
if not keyword_set(nterms) then nterms = intarr(npeaks) + 3

if (size(npeaks))(0) ne 0 and total((size(npeaks))(0:1) eq [1,1]) eq 2
    then npeaks = (npeaks)(0)
if (size(npeaks))(0) ne 0 and total((size(npeaks))(0:1) eq [1,1]) ne 2
    then begin
        print, 'npeaks should be a scalar.'
        stop
    endif

if total(nterms lt 3) gt 0 then begin
    print, 'no elements of nterms can be less than 3. You need at
        least 3 terms to define a gaussian!'
    stop
endif

if npeaks ne n_elements(ncomponents) then begin
    print, 'npeaks must be the same as the number of elements in
        ncomponents.'
    stop
endif

if total(ncomponents) ne n_elements(nterms) then begin
    print, 'nterms needs to be an array with the same number of
        elements as the total number of components.'
    stop
endif

if total(nterms) ne n_elements(pars) then begin
    print, 'pars needs to have the same number of elements as the
        total number of terms specified in nterms.'
    stop
endif

npoints = n_elements(x)

```

```

y = dblarr(npoints)
for i=0,npeaks-1 do begin
    for j=0,ncomponents[i]-1 do begin

        par0 = total(nterms[0:total(ncomponents[0:i])-ncomponents[
            i]+j])-nterms[total(ncomponents[0:i])-ncomponents[i]+j]
        if j eq 0 then comp0par0 = par0 ; when you pass the first
            component, save it's par0 so that you can use it later
            when you calculate subsequent components parameter
            values relative to the first's

        ;par0 = (total(nterms[0:])-nterms[])*ncomponenets[0:i-1])
            ; the index of par 0 inside pars for the current term.

        if j gt 0 then begin ; need to adjust pars so that they'
            re relative to first component in the peak.
            pars[par0] = pars[comp0par0]*pars[par0]
            pars[par0+1] = pars[comp0par0+1]+pars[par0+1]
            pars[par0+2] = pars[comp0par0+2]*pars[par0+2]
        endif

        if pars[par0+2] ne 0.0 then begin ; make sure that sigma
            isn't zero
            z = (x-pars[par0+1])/pars[par0+2] ; then calculate
                z
            ez = exp(-z^2/2.) ; and gaussian part as normal.
        endif else begin
            ez = dblarr(npoints) ; This condition prevents a
                division by zero explosion and just returns all
                zeros instead of the less useful nan.
        endelse

        case nterms[total(ncomponents[0:i])-ncomponents[i]+j] of
            ; this mess just gets a steadily increasing index for
            nterms
            3: f = pars[par0]*ez
            4: f = pars[par0]*ez*(1.+erf(pars[par0+3]*z/sqrt
                (2.)))
            5: f = pars[par0]*ez*(1.+erf(pars[par0+3]*z/sqrt
                (2.))) + pars[par0+4]
            6: f = pars[par0]*ez*(1.+erf(pars[par0+3]*z/sqrt
                (2.))) + pars[par0+4] + pars[5]*x
            7: f = pars[par0]*ez*(1.+erf(pars[par0+3]*z/sqrt
                (2.))) + pars[par0+4] + pars[5]*x + pars[6]*x^2
        endcase
        ;f[where(y+f eq y)] = 0d ; this is an attempt to
            remove underflow error
        y = y + f

    endifor
endfor
endfor

```

```

; this block of code reports any non floatingpoint underflow math errors
  and turns math error reporting back on before exiting the function.
floating_point_underflow = 32
status = Check_Math()      ; Get status and reset accumulated math error
  register.
;IF(status AND NOT floating_point_underflow) NE 0 THEN Message, 'IDL
  Check_Math() error: ' + StrTrim(status, 2)
!Except = currentExcept

return, y
end

```

```

PRO pc_extract_counts, spec_data, spec_bg, data_int_time, bg_int_time,
  data_range, extract_range=extract_range, countrate=countrate,
  err_countrate=err_countrate, counts=counts, err_counts=err_counts

```

```

;spec_data - vector containing spectrum data
;spec_bg - vector containing spectrum background (use as long of a
  background as possible)
;data_int_time - scalar double indicating the integration time of the
  data spectrum. use the live time.
;bg_int_time - scalar double indicating the integration time of the
  background. use the live time.
;data_range - a two element vector that indicates how many bins are in
  the data. this gets extracted from the .spe data file.
;extract_range - a two element vector keyword with elements indicating
  the left and right MCA bins to bound the data that will be extracted.
  If this keyword is not set, the program will prompt you to enter the
  values by clicking on the plot.
;countrate - output keyword
;err_countrate - output keyword
;counts - output keyword
;err_counts - output keyword

```

```

; takes MCA spectra as input, removes background and
; it might be valuable to implement a "flat fielding" function. From the
  look of the spectrum, it seems that some channels might be "narrower
  " than others. I say narrower because i do not think channels with
  low counts are have a lower gain; that would imply that counts are
  being missed. I think that the range of pulse heights that fall into
  that bin might be slightly smaller so it will register fewer counts.
  This would throw off a spectral analysis but I am not concerned with
  that. All I hvae to do is add up counts in a large range. One could
  calibrate this out with a pulse generator or by taking a very high
  count data run and fitting the data with a spline. As the number of
  counts per bin increases, the signal to noise should increase,
  however if the bins are unevenly spaced, there will be a source of
  noise that grows linearly with the signal instead of as sqrt(signal).
  Divide the spline fit by the data to determine the relative bin
  width. Then use this to define your non uniform bin widths. It should
  be possible to resample the histogram to arrive at a uniform bin
  spacing.

```

```

ndata = n_elements(spec_data)

scale_factor = double(data_int_time)/double(bg_int_time)

mca = indgen(ndata)+1 ; an array of the mca channel numbers

cutoff = floor(25/255.*data_range[1]) ; a cutoff defined to avoid
      plotting the noise peak. UPDATE: the noise peak should not exist in
      the data. Use the discriminator built into the MCA. I usually use a
      lower level cutoff of 30 in 255 bin mode.

; plot the data, ignoring the noise peak
window, 1
plot, mca, spec_data, psym=10, title = 'Data and background', xtitle='MCA
      Channel No.', ytitle='No. Counts', yrange = [1,max(spec_data[cutoff:
      ndata-1])],/ylog
oplot, spec_bg *scale_factor, psym=10

err_data = sqrt(spec_data)
err_bg = sqrt(spec_bg)

; subtract the background

spec_bgsub = spec_data-spec_bg*(scale_factor)

; plot the background subtracted data, ignoring the noise peak.
window,2
plot, mca, spec_bgsub, psym=10, title='Background subtracted spectrum',
      xtitle='MCA Channel No.', ytitle='No. Counts', /ylog, yrange=[1,max(
      spec_bgsub[cutoff:ndata-1])]

; calculate error by summing in quadrature and scaling by the same scale
      factor as with the data
err_bgsub = sqrt(err_data^2 + (scale_factor)*err_bg^2)

if n_elements(extract_range) eq 0 then begin
      print, "Click a left bound on the background subtracted plot to
      define the range of counts that you would like to sum"

      cursor,x_1, y_1,4,/data

      print, "Click a right bound on the background subtracted plot to
      define the range of counts that you would like to sum"

      cursor,x_2, y_2,4,/data
endif else begin
      if n_elements(extract_range) ne 2 then begin
              print, 'extract_range is supposed to be a 2 element vector
              .',
              stop
      endif
      x_1 = extract_range[0]

```

```

        x_2 = extract_range[1]
    endelse

    ; if left and right are backwards, swap them
    if x_1 gt x_2 then begin
        x_temp = x_1
        x_1 = x_2
        x_2 = x_temp
    endif

    if x_2 gt data_range[1] then x_2 = data_range[1]

    ; the x value returned by cursor will be a number between 0 and
    ; datarange[1]. All we have to do is convert that number to an integer
    ; to get the index.

    x_1 = floor(x_1)
    x_2 = floor(x_2)

    counts = total(spec_bgsub[x_1:x_2])
    ; sum the errors in quadrature
    err_counts = total(err_bgsub[x_1:x_2]^2)^.5

    countrate = counts/data_int_time
    err_countrate = (countrate)*sqrt((err_counts/counts)^2+(.5/data_int_time
    )^2)

    print, 'There are'+strcompress(string(counts))+ ' +/-'+strcompress(string
    (err_counts))+ ' background subtracted counts between channel'+
    strcompress(string(x_1))+ ' and channel'+strcompress(string(x_2))+ ' of
    the spectrum. Given the data integration time of'+strcompress(string
    (data_int_time)) + ' seconds, this yields a countrate of'+strcompress(
    string(countrate)) + ' +/-'+strcompress(string(err_countrate)) + '
    counts per second.'

    ; error is calculated by using the usual division error propagation rule
    ; to combine the poisson error in the number of counts with the timing
    ; error of 0.5 seconds. (counts/data_int_time) * sqrt((err_counts/
    counts)^2+(.5/data_int_time)^2)

    ;if you need to distinguish overlapping peaks, you need to do a
    ; multigauss fit instead of the simple left right ranging. if the peaks
    ; do not have to be separated, just use a simple sum. it will not add
    ; in any non gaussianity fitting error.

    ;result = mpfitfun('multi_gauss', indgen(npoints), spec_peakbgsub,
    ; err_peakbgsub, parinfo = {tied:1}, functargs = {ngauss:k, nterms:3})

end

```

```

PRO pc_read_spectrum, filename, spec_data, live_time=live_time,
    real_time=real_time, data_range=data_range

; Reads a spectrum file (*.Spe format), generated by the Ortec MCA, into
; memory.
; filename - the name of the file to be read.
; spec_data - output containing the spectrum data, which is in units of
; counts THAT ALREADY DEADTIME CORRECTED.
; live_time - optional output containing the estimated total time that
; the MCA spent sensitive to pulses. Time is in seconds.
; real_time - optional output containing the time elapsed between the
; start and end of the data run. real_time = live_time + dead_time Due
; to the MCA outputting deadtime corrected counts, this is nominally
; used as the integration time. WARNING: if the dead time percentage is
; high, this will be wrong.
; data_range - the channel (bin) range of the data file.
; note that in the data file $MEAS_TIM is the integration time, in
; seconds. the two numbers represent the stopwatch integration time and
; the actual live time (stopwatch time minus deadtime)

nlines = FILE_LINES(filename)

spec_data = lonarr(nlines)
data_range = lonarr(2)
openr, lun, filename, /get_lun

for i=0,nlines[0]-1 do begin
    temp = ' '
    readf, lun, temp

    case 1 of
        (i eq 9):times = long(strsplit(temp,' ',/extract))
        (i eq 11):data_range = long(strsplit(temp,' ',/extract))
        (i ge 12 and i le data_range[1]+12):spec_data[i-12] = long
            (temp)
    else:
        endcase
endcase
endfor
live_time = times[0]
real_time = times[1]
spec_data = spec_data[0:data_range[1]]

close,/all

if (real_time-live_time)/real_time gt .4 then print, 'WARNING: Dead time
    percentage is larger than 40%. There will be error in the countrate
    estimate.'

end
; before i realized the case statement is faster.
; if i eq 9 then times = long(strsplit(temp,' ',/extract))
; if i eq 11 then data_range = long(strsplit(temp,' ',/extract))

```

```

;      if i ge 12 and i le data_range[1]+12 then spec_data[i-12] = long(
temp)

```

```

pro sb_henke, input_energy, input_z, xsec, unit=unit, sum=sum, quadratic
=quadratic

; energy - incident photon energy in keV.
; z - atomic number. Can be a scalar or vector.
; xsec - output variable for the cross section(s).
; unit - specify either 'b' for barns/atom or 'c' for cm^2/g.
; sum - sums the contributions from multiple elements instead of
outputting multiple cross sections.

if n_elements(input_energy) le 0 then begin
    print, 'sb_henke.pro says that the energy array needs to have
more than zero elements'
    stop
endif

en = input_energy*1000 ; converting to eV to match Henke data tables.
Do the variable change so that the changed energy array doesn't get
passed back out of the function and mess up the standard idl session.
if not keyword_set(unit) then unit= 'b' ; barns/atom is the default
output unit
if unit ne 'b' and unit ne 'c' then begin
    print, 'You specified some illegal value for unit'
    stop
endif

restore, '/Users/sdb210/code/qe_teststand/sb_henke_data.sav' ; restoring
variables: table_z, table_name, table_symbol, table_atwt,
table_density, energy, f1, and f2 arrays from file for ALL elements.
This file was created by sb_henke_read.pro

h = 6.62606957d-27 ; plancks constant in cgs
c = 2.99792458d10 ; speed of light in cm/s
r_electron = 2.8179403267d-13 ; classical electron radius in cm
n_avogadro = 6.02214129d23 ; avogadro's constant
ergev = 1.602176565d-12 ; erg per ev

;CRC constants

ind = input_z-1 ; indices of the elements that you want returned
energy = energy[* ,ind]
f2 = f2[* ,ind]

; summing together the contributions from various elements
if keyword_set(sum) then f2 = total(f2,2)

f2_interpol = dblarr(n_elements(f2[0,*]),n_elements(en))

for i=0,n_elements(f2[0,*])-1 do begin

```

```

        f2_interpol[i,*] = interpol(f2[where(finite(f2[* ,i])),i],energy[
            where(finite(f2[* ,i])),i],en,quadratic=quadratic)
    endfor
case unit of
    'b': xsec = 2*f2_interpol*r_electron*h*c/(rebin(transpose(en),
        n_elements(f2_interpol[* ,0]),n_elements(en))*ergev)*1d24 ;
        calculating xsec in barns/atom
    'c': xsec = 2*n_avogadro/rebin(table_atwt[ind],n_elements(
        f2_interpol[* ,0]),n_elements(en))*f2_interpol*r_electron*h*c/(
        rebin(transpose(en),n_elements(f2_interpol[* ,0]),n_elements(en)
        ))*ergev) ; calculating xsec cm^2/g
endcase

end



---


pro sb_henke_read

;this program uses the henke 93 ascii data files available on the LBNL
website to create a sb_henke.sav file that contains element z, name,
symbol, atomic weight, density, an energy grid (in eV) and the f1 and
f2 values at each energy.

cd, '/Users/sdb210/code/qe_teststand'
readcol, 'periodic_table.txt',table_name,table_symbol,table_z,table_atwt
,table_density,delimiter=', ',format='A,A,I,D,D'

sort_ind = sort(table_z) ; the z sorted indices for the full periodic
table

table_z = table_z[sort_ind]
table_name = table_name[sort_ind]
table_symbol = table_symbol[sort_ind]
table_atwt = table_atwt[sort_ind]
table_density = table_density[sort_ind]

henke_sort_ind = sort((table_z[where(table_z le 92)])(sort(table_symbol[
where(table_z le 92)]))) ; the symbol alphabetized indices for
elements 1-92 (ie the henke list)

prefix = '/Users/sdb210/code/xrdata/henke_data/'

filenames = ['ac.nff', 'ag.nff', 'al.nff', 'ar.nff', 'as.nff', 'at.nff',
'au.nff', 'b.nff', 'ba.nff', 'be.nff', 'bi.nff', 'br.nff', 'c.nff',
'ca.nff', 'cd.nff', 'ce.nff', 'cl.nff', 'co.nff', 'cr.nff', 'cs.nff',
'cu.nff', 'dy.nff', 'er.nff', 'eu.nff', 'f.nff', 'fe.nff', 'fr.nff',
'ga.nff', 'gd.nff', 'ge.nff', 'h.nff', 'he.nff', 'hf.nff', 'hg.nff',
'ho.nff', 'i.nff', 'in.nff', 'ir.nff', 'k.nff', 'kr.nff', 'la.nff',
'li.nff', 'lu.nff', 'mg.nff', 'mn.nff', 'mo.nff', 'n.nff', 'na.nff',
'nb.nff', 'nd.nff', 'ne.nff', 'ni.nff', 'o.nff', 'os.nff', 'p.nff', '
pa.nff', 'pb.nff', 'pd.nff', 'pm.nff', 'po.nff', 'pr.nff', 'pt.nff',
'ra.nff', 'rb.nff', 're.nff', 'rh.nff', 'rn.nff', 'ru.nff', 's.nff',
'sb.nff', 'sc.nff', 'se.nff', 'si.nff', 'sm.nff', 'sn.nff', 'sr.nff',
'ta.nff', 'tb.nff', 'tc.nff', 'te.nff', 'th.nff', 'ti.nff', 'tl.nff']

```

```

, 'tm.nff', 'u.nff', 'v.nff', 'w.nff', 'xe.nff', 'y.nff', 'yb.nff', '
zn.nff', 'zr.nff']

; sort list by z
filenames = prefix + filenames[henke_sort_ind]
nfiles = n_elements(filenames)

nen = 1000 ; there are a variable number of data points for each
           element so lets just make the energy array larger and fill the rest
           in with nans.
energy = dblarr(nen,nfiles) + !values.d_nan
f1 = dblarr(nen,nfiles) + !values.d_nan
f2 = dblarr(nen,nfiles) + !values.d_nan

for i=0,nfiles-1 do begin
    print, 'Reading '+filenames[i]+'...'
    readcol,filenames[i],energy_temp,f1_temp,f2_temp,delimiter=' ',
        format='D,D,D'
    energy[0:n_elements(energy_temp)-1,i] = energy_temp
    f1[0:n_elements(f1_temp)-1,i] = f1_temp
    f2[0:n_elements(f2_temp)-1,i] = f2_temp
endfor

f1[where(f1 eq -9999)] = !values.d_nan
f2[where(f2 eq -9999)] = !values.d_nan

save,table_z,table_name,table_symbol,table_atwt,table_density,energy,f1,
    f2,filename='/Users/sdb210/code/qe_teststand/sb_henke_data.sav'

end

```

```

pro sim_error, myfunc,ind_var=ind_var, pars=pars, parerrors=parerrors,
    parnames=parnames, spars=spars, spar_positions=spar_positions,
    spar_ratios=spar_ratios, parinfo=parinfo,$
input_percentiles=input_percentiles, input_confint=input_confint, n_iter
    =n_iter, pdf_min=pdf_min, pdf_max=pdf_max, n_bins=n_bins, lotsoplots=
    lotsoplots, method=method,$
pdf_dist=pdf_dist, pdf_locations=pdf_locations, exact_soln=exact_soln,
    dist_med=dist_med, output_confint=output_confint, output_percentiles=
    output_percentiles, cdf = cdf, cor = cor, slope=slope, u_slope=
    u_slope, ind_slope=ind_slope, u_ind_slope=u_ind_slope,$
keyword1=keyword1, keyword2=keyword2, keyword3=keyword3, keyword4=
    keyword4, keywordnames=keywordnames,$
save_plots=save_plots

; MANDATORY INPUTS
; myfunc - a string containing the name of the function for which you
           will be calculating simulated errors. Do not include the ".pro"
           extension. Parameters must be passed as variables, not keywords, or
           arrays of parameters. The function must be able to take vectors as
           inputs.

```

```

; ind_var - a vector of the independent variable. Essentially one batch
  of simulations will be performed for each independent variable point.
  If there is no independent variable in the function that you are
  using, then set ind_var equal to any scalar number. The independent
  variable is something like time in an RV curve. In other applications
  there may be no independent variable so this loop will only run once
  . Instead of generating a 2d contour plot, we can simply generate a 1
  d plot of the PDF.
; pars - the exact parameters for the function. These values will be
  perturbed.
; parerrors - the one sigma error for pars

;the following spars crap should eventually all be lumped into parinfo.
  doing it this way is stupid and just a quick fix. shuffling is not
  really different than the gaussian distributed parameters, it is a
  random number selected from a distribution with discrete values with
  specified weights, rather than a continuous set of values with
  continuously varying gaussian weights.
; spars - shuffle parameters. make the horizontal axis of this array
  different parameters and the vertical axis, the possible values that
  these parameters can take. If there are multiple parameters with
  different possible values, make the empty array elements !VALUES.
  F_NAN. For example, I created this to generate arrays of Fe55 photon
  energy values. The array needed to contain a randomly shuffled
  assortment of 6.4 and 5.9 keV photon energies in a 1:~8 ratio.
; spar_positions - the position in the gaussian par array to insert the
  shuffle parameter
; spar_ratios - same array format as spars array, horizontal axis is for
  separate parameters, vertical axis corresponds to the ratio in which
  the different possible values should occur.

; parinfo - NOT FUNCTIONAL YET. Will enable extra options for each
  parameter.

; OPTIONAL INPUTS - the program will only calculate these if you specify
  them.
; input_percentiles - the desired percentile locations (in units of
  fraction. one needs only specify the left set of percentiles ie 5%
  and not 5% and 95%). The 20th percentile is the location below which
  20% of the measurements fall. This measurement has no regard for the
  shape (peaks, tails, etc.) of the distribution.
;input_confint - the desired confidence interval locations (in units of
  fraction). These values represent the probability that a value will
  be contained within the interval.

; OPTIONAL PDF/BOOTSTRAP RELATED INPUTS
; n_iter - the number of iterations for each call to the function. This
  number should be higher when there are more parameters. One must
  adequately sample all permutations of the randomly distributed
  parameters.
; pdf_min - minimum sampled PDF value. It is desirable to tightly bound
  the PDF with pdf_max and pdf_min so that the number of bins samples
  the montecarloed points somewhat optimally.

```

```

; pdf_max - maximum sampled PDF value
; n_bins - the number of bins to use when making the PDF from
    montecarloed points

; OUTPUTS
; pdf_dist - insert a variable here that will contain the probability
    density function upon output... aka the distribution. has do change
    this from pdf to pdf_dist because idl thought it was an ambiguous
    keyword.
; pdf_locations - insert a variable here that will contain the pdf x-
    axis.
; exact_soln - insert a variable here that will contain the exact
    solution.
; output_percentiles - the location of the desired percentiles (on both
    the left and right sides of the distribution)
; output_confint - the location of the desired confidence intervals
; dist_med - the median of the distribution. whether this is relevant or
    not is up to you.
; cor - NOT WORKING YET. the correlation coefficients.

; KEYWORD SWITCHES
; lotsoplots - set this keyword to include a 1d plot of the PDF at each
    independent variable value.
; method - set this keyword to either 'old', 'new', or 'pinfo' to choose
    a method for running the MC.
; ADD THIS FEATURE!!!! if variance is zero then sim_error should skip
    over the variable and pass only the nominal value

; keyword1...2...3...4 - keywords to pass onto the function. their
    values will not be randomized. more keywords can be added if
    necessary. make sure to modify the line where n_key is defined so
    that it counts the new keywords.
; keywordnames - string array defining the names of the keywords to pass
    .

; PARINFO STRUCTURE TAGS
; parinfo.pars
; parinfo.parerrors
; parinfo.type - gaussian or discreet. maybe poisson too?
; parinfo.prate - if i implement poisson, this is the poisson rate.
; parinfo.dvalues - discrete values. if multiples, they must be the same
    size array. pad with !VALUES.F_NAN
; parinfo.dweights - discrete weights. if multiples, they must be the
    same size array. pad with !VALUES.F_NAN

; TROUBLESHOOTING
; if there is noise in the distribution or the distribution is shaped
    strangely, this code does not do well at finding confidence intervals
    .

; Written by Steve Bongiorno 1/16/2012 - Pat Broos helped with deciding
    on the execute() function instead of call_function.

```

```

if n_elements(ind_var) eq 0 then begin
    ind_var = [0]
    ind_var_name = 'XX'
endif else begin
    ind_var_name = string(ind_var,format = '(E8.2)')
endif
endif

if n_elements(parinfo) eq 0 and (n_elements(pars) eq 0 or n_elements(
    parerrors) eq 0) then begin
    print, 'You have to set either parinfo or (pars and parerrors)'
    stop
endif

if n_elements(method) eq 0 then method = 'new'
if n_elements(parinfo) ne 0 and method ne 'parinfo' then begin
    print, 'You set parinfo but chose a method other than parinfo.
        WTF man? I am going to use parinfo.'
    method = 'pinfo'
endif

;if not keyword_set(input_percentiles) then begin
;    input_percentiles = [.001, .021, .136]
;    print, "You did not supply any input percentiles or confidence
        intervals so I am going to use 1, 2, and 3 sigma."
;endif

;if keyword_set(input_confint) then begin
;    input_confint = [.5,.95,.99]
;    print, "You did not supply any input confidence intervals so I am
        going to use 50, 95, and 99 percent. By the way the 50th percentile
        is the median."
;endif

if n_elements(n_bins) eq 0 then n_bins=100
if n_elements(n_iter) eq 0 then n_iter=10000L
if keyword_set(pars) then n_pars = n_elements(pars) else n_pars = 0
if keyword_set(spars) then n_spars = n_elements(spars[*],0) else n_spars
    = 0
if keyword_set(keywordnames) then n_key = n_elements(keywordnames) else
    n_key = 0 ; the number of keywords that have been set

result = dblarr(n_iter)
n_ind_var = n_elements(ind_var)
ind_result = dblarr(n_pars+n_spars,long(n_iter/10))

; initializing the arrays. These will contain one column for each
    independent variable and two rows for each percentile/confidence
    interval.
if n_elements(input_percentiles) gt 0 then begin
    if n_elements(ind_var) gt 0 then begin
        output_percentiles = dblarr(n_elements(ind_var),n_elements
            (input_percentiles)*2)
    endif else begin

```

```

        output_percentiles = dblarr(1,n_elements(input_percentiles
        )*2)
    endwhile
endif
if n_elements(input_confint) gt 0 then begin
    if n_elements(ind_var) gt 0 then begin
        output_confint = dblarr(n_elements(ind_var),n_elements(
        input_confint)*2)
    endif else begin
        output_confint = dblarr(1,n_elements(input_confint)*2)
    endwhile
endif
pdf = dblarr(n_ind_var,n_bins)
cdf = dblarr(n_ind_var,n_bins)

; For some reason FSC_COLOR is no longer working. Error message says
; some license issue.
;lineColor = FSC_COLOR("Red", !D.Table_Size)
;contourColor = FSC_COLOR("Green", !D.Table_Size)

; Looping through each X-axis (independent variable) index
for j=0L,n_ind_var-1 do begin

    case method of
        'old':begin
            ; The old method Monte-Carlo loop
            for i=0L,n_iter-1 do begin
                thrown_pars = pars+randomn(j*n_ind_var+i,n_pars)*
                parerrors
                result[i] = call_function(myfunc, ind_var[j],
                thrown_pars)
            endfor
        end
        'new':begin
            ; The new method Monte-Carlo loop
            thrown_pars = rebin(pars,n_pars,n_iter) + randomn(seed,
            n_pars,n_iter)*rebin(parerrors,n_pars,n_iter)
            ; This is a n_pars x n_iter size array filled with thrown
            pars. Note that sequential permutations of this 2d
            thrown_pars matrix are also valid, new random sets of
            parameters. Unfortunately I do not know how to
            sequentially shift this matrix without a for loop. In
            this case I think it is faster to generate more random
            numbers and hold them in memory than to use some
            processor to efficiently reuse the random numbers that
            have already been generated and are already in memory.

            ;result = call_function(myfunc, ind_var[j], thrown_pars)
            ; If sim_error was vectorized like this, the functions you
            use must be written to accept parameters in this funny
            way. It would be faster than looping, but it is not
            very general due to the way that the functions must be
            written.

```

```

; this is a crappy way to code the shuffle thing . will
; have to be more elegant later when i implement parinfo
if n_elements(spars) gt 0 then begin
    for i=0,n_elements(spars[*],0)-1 do begin
        values = spars[i,where(finite(spars[i,*]))];
        strip the nans
        weights = spar_ratios[i,where(finite(
            spar_ratios[i,*]))]
        ; concatenate the new array into the thrown
        ; pars array in the correct position
        thrown_pars = [thrown_pars[0:spar_positions[
            i]-2,*],transpose(randomd(seed,values,
            weights,n_iter)),thrown_pars[
            spar_positions[i]-1:*,*]]
    endfor
endif

```

```

; Generating the string input to the execute function.
if n_ind_var gt 1 then begin
    exstring = 'result = ' + myfunc + '(replicate(
        ind_var[j],n_iter)'
    for i=0,n_pars+n_spars-1 do exstring = exstring + '
        ,thrown_pars[' + strcompress(string(i,format='(
        I)'),/remove_all) + ',*]'
    ; creates a string that looks like:
    ; result = myfunc(ind_var[j],thrown_pars[0,*],
        thrown_pars[1,*])

    ; creating the independent exstring where only one
    ; par is tweaked at a time. (I AM TESTING THE
    ; IDEA OF USING A SCALAR FOR THE IND_VAR INSTEAD
    ; OF USING REPLICATE LIKE I DO IN THE LINES ABOVE
    .

```

```

ind_exstring = strarr(n_pars+n_spars)
for k=0,n_pars+n_spars-1 do begin
    ind_exstring[k] = 'ind_result['+strcompress(
        string(k,format='(I)'),/remove_all)+' ,*]'
        = ' +myfunc + '(ind_var[j],
    for i=0,k-1 do ind_exstring[k] =
        ind_exstring[k] + 'transpose(replicate(
        pars[' + strcompress(string(i,format='(I
        )'),/remove_all) + '],long(n_iter/10))),
        ,

    ind_exstring[k] = ind_exstring[k] + '
        thrown_pars[' + strcompress(string(i,
        format='(I)'),/remove_all) + ',0:long(
        n_iter/10)-1],'
    for i=k+1,n_pars+n_spars-1 do ind_exstring[k
    ] = ind_exstring[k] + 'transpose(
        replicate(pars[' + strcompress(string(i,
        format='(I)'),/remove_all) + '],long(

```

```

        n_iter/10))),'
; remove the trailing comma
ind_exstring[k] = strmid(ind_exstring[k],0,
    strlen(ind_exstring[k])-1)
endfor

endif else begin
    exstring = 'result = ' + myfunc + '('
    for i=0,n_pars+n_spars-2 do exstring = exstring + '
        thrown_pars[' + strcompress(string(i,format='(I)
        )'),/remove_all) + ',*],'
    exstring = exstring + 'thrown_pars[' + strcompress(
        string(n_pars+n_spars-1,format='(I)'),/
        remove_all) + ',*]'
; this creates a string that looks like:
; result = myfunc(thrown_pars[0,*],thrown_pars
    [1,*])

    ind_exstring = strarr(n_pars+n_spars)
    for k=0,n_pars+n_spars-1 do begin
        ind_exstring[k] = 'ind_result['+strcompress(
            string(k,format='(I)'),/remove_all)+',*]
            = ' +myfunc + '('
        for i=0,k-1 do ind_exstring[k] =
            ind_exstring[k] + 'transpose(replicate(
            pars[' + strcompress(string(i,format='(I)
            )'),/remove_all) + '],long(n_iter/10))),
            '
        ind_exstring[k] = ind_exstring[k] + '
            thrown_pars[' + strcompress(string(i,
            format='(I)'),/remove_all) + ',0:long(
            n_iter/10)-1],'
        for i=k+1,n_pars+n_spars-1 do ind_exstring[k
            ] = ind_exstring[k] + 'transpose(
            replicate(pars[' + strcompress(string(i,
            format='(I)'),/remove_all) + '],long(
            n_iter/10))),'
        ;remove the trailing comma
        ind_exstring[k] = strmid(ind_exstring[k],0,
            strlen(ind_exstring[k])-1)
    endfor

endelse
;add on the keyword business, if needed.
if n_key gt 0 then begin
    for i = 0,n_key-1 do begin
        exstring = exstring + ', ' + keywordnames[i]+
            '=keyword'+strcompress(string(i+1,format
            ='(I)'),/remove_all)
        ind_exstring = ind_exstring + ', ' +
            keywordnames[i]+'=keyword'+strcompress(
            string(i+1,format='(I)'),/remove_all)
    endfor
endfor

```

```

endif

exstring = exstring + ')'
ind_exstring = ind_exstring + ')'

; starting the calculation
status = execute(exstring)

if status eq 0 then begin
    print, 'The normal execute command did not compile
    or run properly'
    print, 'The execute string when a failure occurred
    was: '
    print, exstring
    what
    stop
endif
if keyword_set(lotsoplots) then begin
    for i=0,n_pars+n_spars-1 do begin
        print, 'Calculating result'+strcompress(
            string(i))+'....'
        status = execute(ind_exstring[i])
        if status eq 0 then begin
            print, 'The independent par.
            analysis execute command did not
            compile or run properly'
            stop
        endif
    endfor
endif
endif
end
;endelse
'pinfo':begin
; PUT THE PARINFO STUFF HERE
;for i

end
else:begin
print, 'You specified an unknown method'
stop
end
endcase
; remove nans and print the number of them
not_nans = where(result ne !values.d_nan and result ne -!values.
    d_nan and result ne !values.d_infinity and result ne -!values.
    d_infinity)
print, 'There were: ',n_iter-n_elements(not_nans),' nans or infs
    in the Monte Carlo result out of', n_iter,' iterations. I have
    taken them out because IDL can not handle them on its own.'
result = result[not_nans]
; histograms location array elements define the left edge of each
    bin. The left edge of the first bin starts at min and the

```

```

    right edge of the last bin stops at max + binsize. binsize = (
    max-min)/(nbins-1)
if not keyword_set(pdf_max) then pdf_max = max(result,/nan)
if not keyword_set(pdf_min) then pdf_min = min(result,/nan)
binsize = (pdf_max-pdf_min)/double(n_bins-1)

; calculating the PDF
pdf[j,*] = double(histogram(result,locations=pdf_locations,min=
    pdf_min, max=pdf_max,nbins=n_bins,/nan))
dist_med = median(result)
; normalizing the PDF
pdf[j,*] = pdf[j,*]/total(double(pdf[j,*]))
; calculating the cumulative distribution function
cdf[j,*] = total(pdf[j,*],/cumulative)

; This finds the locations that correspond to given percentiles. This
    also does an array concatenation to generate the complimentary
    set of percentiles; ie .05, .10, .50 will result in .05, .10,
    .50, .95, .90, and .50.
if keyword_set(input_percentiles) then output_percentiles[j,*] =
    pdf_locations[value_locate(cdf,[input_percentiles,1.-
    input_percentiles])]

if keyword_set(input_confint) then begin
    ; This section of code finds the locations that correspond
        to the input confidence interval.

    ; Sorting the pdf array and reversing the result so that
        we get an array that starts with the indices of the pdf
        peak(s) and then goes into the wings simultaneously (
        and evenly).
    inv_ind = reverse(sort(pdf))
    ; using the inverse indices to get the pdf and location
        values in this special "starting at the peak and going
        down the slope" ordering.
    inv_pdf = pdf[inv_ind]
    inv_loc = pdf_locations[inv_ind]

    ; calculating the cumulative distribution function using
        this "peak down" ordering
    cum_inv_pdf = total(inv_pdf,/cumulative)

    ; looping through the input confidence intervals one at a
        time.
    for i=0,n_elements(input_confint)-1 do begin
        ; Find all of the locations in confidence interval
            i.
        conf_int_loc = inv_loc(where(cum_inv_pdf lt
            input_confint[i]))
        ; These points are out of order so we sort them.
        conf_int_loc = conf_int_loc[sort(conf_int_loc)]
        ; If the distribution is noisy or has more than one
            peak we will have identified multiple groups

```

of points in the previous lines. The following line finds any x axis (locations) gap larger than the expected binsize, which is known and calculated above. This gets rid of multiple groups due to noise but not due to multiple large scale peaks in the distribution. (shift -1 means moving to the left)

```

;NEW lets try to find the boundaries of the large
chunk of elements in conf_int_ind that are
equal to binsize. These correspond to the
confidence interval. This line checks to make
sure that there are three values in a row equal
to binsize, which should correspond to the
center of the peak. Noise on the outside of the
peak will only have one or two elements in a
row where the conf_int_ind is equal to binsize.
;interval = where(conf_int_ind eq binsize and shift
(conf_int_ind,-1) eq binsize and shift(
conf_int_ind,-2) eq binsize)

conf_int_dif = (conf_int_loc-shift(conf_int_loc,1))
(1:*) lt 1.01*binsize
;NEW
interval = dblarr(2)
interval[0] = conf_int_loc[(where(conf_int_dif and
shift(conf_int_dif,-1) and shift(conf_int_dif
,-2)))(0)]
n_conf_int = n_elements(where(conf_int_dif and
shift(conf_int_dif,1) and shift(conf_int_dif,2)
))
interval[1] = conf_int_loc[(where(conf_int_dif and
shift(conf_int_dif,1) and shift(conf_int_dif,2)
))(n_conf_int-1)]
; NEW assume that the distribution has one peak and
pick off the first and last element. I add 2
to the second part to adjust the location to
the actual right edge due to the two shifts in
the above statement.
;interval = interval[0,n_elements(interval)-1]
;interval[1] = interval[1] + 2
output_confint[j,i*2:i*2+1] = interval
endfor
endif

if keyword_set(exact_soln) then begin
if n_ind_var gt 1 then begin
exact_soln = call_function(myfunc, ind_var[j], pars
)
endif else begin
exact_soln = call_function(myfunc,pars)
endif
endif
endif

```

```

if keyword_set(lotsoplots) then begin
  if (n_ind_var gt 1) then begin
    window,j
    plot, pdf_locations, pdf[j,*]
    oplot, pdf_locations, pdf[j,*],psym=4
    if keyword_set(exact_soln) then oplot, [exact_soln,
      exact_soln], [0,1],thick=2;; color=lineColor
    if keyword_set(input_confint) then for k=0,
      n_elements(output_confint)-1 do oplot, [
      output_confint[j,k],output_confint[j,k]], [0,pdf
      [value_locate(pdf_locations,output_confint[j,k]
      )]]]
    if keyword_set(input_percentiles) then for k=0,
      n_elements(output_percentiles)-1 do oplot, [
      output_percentiles[j,k],output_percentiles[j,k]
      ]],[0,1];;color=contourColor, thick=2
  endif
  if n_elements(parnames) eq 0 then begin
    print, 'Parameter names were not set so I auto
      named them by their numbers in the plot'
    parnames = 'Par. No. '+strcompress(string(indgen(
      n_pars)),/remove_all)
  endif
  for m = 0,n_pars-1 do begin
    print, 'Plotting result'+strcompress(string(m))+
      ...'

    cd, '.',current=current_dir
    printplot
    set_plot, 'ps'
    device, filename=current_dir+timestamp(12)+'/'
      ind_par_'+parnames[m]+'plot_ind_var_'+
      ind_var_name[j]+'.ps'

    ; calculate the 2d density function of the
      scatterplot points
    mx1 = max(thrown_pars[m,*],min=mn1,/nan)
    mx2 = max(result,min=mn2,/nan)
    er = 0
    bn1 = fd_binsize(thrown_pars[m,*],er=er1)
    bn2 = fd_binsize(result,er=er2)
    n1 = floor((mx1-mn1)/bn1)
    n2 = floor((mx2-mn2)/bn2)
    ; if the er flag is flipped, do not try to
      calculate a contour because it will have zero
      size.
    if er1 eq 0 and er2 eq 0 then begin
      finite_index = where(finite(result))
      result_hist = hist_2d(thrown_pars[m,
        finite_index],result[finite_index],bin1=
        bn1,bin2=bn2,min1=mn1,min2=mn2,max1=mx1,

```

```

        max2=mx2)
; calculate locations of the 100 hist_2d bin
  centers
locations1 = (dindgen(n1+1)+.5)*bn1 + mn1
locations2 = (dindgen(n2+1)+.5)*bn2 + mn2
; the levels, in percent of total points, to
  contour on the plot. contour requires
  that the input levels are low to high so
  that means these values must be high to
  low.
levels = [90,75,50,25]
; sort the 2d hist, reverse this so that it
  is big to small
sort_result_hist = result_hist[reverse(sort(
  result_hist))]
; create a 1-d cumulative distribution
  function, then use value_locate to see
  where the desired percentages fall on
  this cdf. then use this to index the
  sorted histogram. this will give the
  hist value at which the percentage
  occurs.
levels_values = sort_result_hist[
  value_locate(total(sort_result_hist,/
  cumulative)/total(result_hist),levels
  /100.)]
x_index = where(result_hist > levels[0])
  mod n_elements(result_hist[:,0]) ;not
  used right now
y_index = floor(where(result_hist >
  levels_values[0]) / n_elements(
  result_hist[:,0]))
yrange = [min(locations2[y_index])*(1-.1),
  max(locations2[y_index])*(1+.1)]
contour,result_hist,locations1,locations2,
  levels=levels_values,yrange=yrange,
  ytitle='Ind. Var.',xtitle=parnames[m]
; overplot the original huge and messy data
;oplot, thrown_pars[m,*],result,psym=3

endif else begin
  oplot, thrown_pars[m,*],result,psym=2
endif
; calculate the slope of the independent data
fit_ind_result = linfit(thrown_pars[m,where(finite(
  ind_result[m,*]))],ind_result[m,where(finite(
  ind_result[m,*]))],sigma=sig,yfit=yfit)
; oplot the fit to the independent result so that
  it is underneath the data
xrange = [min(thrown_pars[m,*],/nan),max(
  thrown_pars[m,*],/nan)]
oplot, xrange,fit_ind_result[1]*xrange +
  fit_ind_result[0],linestyle=2

```

```

; oplot the result with all other pars held
  constant.
oplot, thrown_pars[m,*],ind_result[m,*],psym=3
xyouts, .175,.86,'Contours encircle '+strjoin(
  string(levels,format='(I2)'),', ') + ' percent
  of the points.',/normal,charsize=.5
xyouts, .175,.84,'Independent result linear fit has
  a slope of '+string(fit_ind_result[1])+ ' +/- '
  +string(sig[1]),/normal, charsize=.5
xyouts, .175,.82,'Given the '+parnames[m]+'
  uncertainty of ' +string(parerrors[m])
device, /close
set_plot, 'x'
printplot, /normal
endfor
endif
endifor

; calculating and printing the slope and correlation coefficient for each
  parameter wrt the QE.

cor = dblarr(n_pars+n_spars)
slope = dblarr(n_pars+n_spars)
u_slope = dblarr(n_pars+n_spars)
ind_slope = dblarr(n_pars+n_spars)
u_ind_slope = dblarr(n_pars+n_spars)

for i=0,n_elements(throw_pars[*],0)-1 do begin
  ;print, [throw_pars[i,*],result]
  ; had a problem where sometimes the result would be NaN due to a
    semi-gaussian parameter receiving a random result that is out
    of its range. Getting rid of the NaNs is a way to essentially
    truncate the parameter to its allowable range. To do better
    parameter ranging, finish the parinfo keyword.
  index = where(finite(result))
  cor[i] = correlate(throw_pars[i,index],result[index])
  fit_result = linfit(throw_pars[i,index],result[index],sigma=sig)
  slope[i] = fit_result[1]
  u_slope[i] = sig[1]
  index = where(finite(ind_result[i,*]))
  fit_ind_result = linfit(throw_pars[i,index],ind_result[i,index],
    sigma=sig)
  ind_slope[i] = fit_ind_result[1]
  u_ind_slope[i] = sig[1]
endifor

if (n_ind_var gt 1) and keyword_set(lotsoplots) then begin
  window,j+1
  plot, ind_var, exact_soln, color=lineColor, thick=2
  for i=0,n_elements(output_percentiles)-1 do oplot, ind_var,
    output_percentiles[i,*];, color=contourColor, thick=2
endif

```

```

pdf_dist = pdf ; needed to call this pdf_dist instead of pdf because idl
    said it was an ambiguous keyword when i call sim_error with it
end

```

```

function sim_qe, energy, thickness, density, amu=amu, coverage =
    coverage, xsec=xsec, z=z, use_mucal=use_mucal, saveplots=saveplots

; returns qe as a function of energy.

; This is a 1d quantum efficiency calculator that only accounts for
    total attenuation from top layers and photoelectric absorption in the
    depletion region.
; For a more effective estimation, the pixel must be simulated in full 3
    d and semiconductor effects (especially electric field shapes) taken
    into account.
; It is assumed that all photoelectric absorption that happens in the
    depleted layer results in a detected X-ray.

; right now the code does not work for compounds. a kludgy way to make
    it do compounds is to split the compound up into a layer for each
    species. use the same thickness and density and effective, summed amu
    for each level, so that the number density ends up the same, but
    specify a different z for each layer.

; energy - in keV, the independent variable. can be scalar or vector
; thickness - array containing thickness of each layer (microns)
; density - array containing density of each layer (g cm-3)
; amu - the atomic weight of the element in each layer
; coverage - array of coverage fraction for each attenuating layer (
    fraction).
; xsec - if you want to bypass the automatic cross section lookup, then
    specify cross sections here. xsec must contain the same number of
    elements as energy.
; z - the atomic number of the element in each layer.
; saveplots - save the plots to file
; use_mucal - keyword switch that uses mucal.pro instead of sb_henke.pro
    for cross sections.
; it is assumed that the last layer in the stack is the depleted silicon
    that does the charge generation.

; xsec - for specifying the cross section of each layer (barns/atom)
; z - for specifying the atomic number of the species in each layer.

n_a = 6.02214129d23 ; avagadros number

nlayers = n_elements(thickness)

if not keyword_set(coverage) then coverage = dblarr(nlayers)+1.
if total(coverage lt 1 or coverage lt 0) gt 0 then begin
    print, "Coverage numbers must be fractions less than 1 and
        greater than 0."
    stop
endif
endif

```

```

if nlayers ne n_elements(coverage) or nlayers ne n_elements(density)
  then begin
    print, 'coverage, density, and thickness must all have the same
    number of elements. ie the number of layers in this detector.'
    stop
  endif
if keyword_set(xsec) then begin
  if n_elements(xsec) ne n_elements(energy) then begin
    print, 'Number of elements in xsec must equal number of
    elements in energy.'
    stop
  endif
endif
if total(energy eq 0) gt 0 then begin
  print, 'The energy cannot be zero.'
  stop
endif

if keyword_set(xsec) then use_mucal = 0 else use_mucal = 1

if keyword_set(saveplots) then begin
  penergy = dindgen(1000)/999.*9.8+.2
  pqe = sim_qe(penergy,thickness,density,amu=amu, coverage =
  coverage, xsec=xsec, z=z, use_mucal=use_mucal)
  plot, penergy, pqe, xtitle='Energy [keV]',ytitle='QE'
  set_plot, 'ps'
  device, filename='sim_qe.eps',/encapsulated
  printplot
  plot, penergy, pqe, xtitle='Energy [keV]',ytitle='QE'
  printplot, /normal
  device, /close
  set_plot, 'x'
endif

n = n_a/amu*density
qe = dblarr(n_elements(energy))+1.

; add up total transmission from all layers except the last one
for i=0,nlayers-2 do begin
  if keyword_set(use_mucal) then begin
    mucal,energy,z[i],xsec,output='t'
  endif else begin
    sb_henke,energy,z[i],xsec
  endelse

  qe = qe*exp(-xsec*1d-24*n[i]*thickness[i]*1d-4)*coverage[i]
endifor

; calculate photoelectric absoption from the last layer
if keyword_set(use_mucal) then begin
  mucal,energy,z[i],xsec,output='p'

```

```

endif else begin
    sb_henke,energy,z[i],xsec
endelse

qe = qe*(1.-exp(-xsec*1d-24*n[i]*thickness[i]*1d-4))*coverage[i]

return, qe

end

;h1rg-167
; ALUMINUM NATIVE OXIDE? probably too thin to matter at all.

; ALUMINUM BLOCKING FILTER
; .0180 um aluminum = 180 Angstroms
; 2.70 g/cm^3
; atomic weight is 26.9815386

; SILICON NATIVE OXIDE
; .025-.028 um SiO2 (word of mouth from Yibin via Dave)
; 2.648 g/cm^3
; atomic weight is 15.9994*2+28.0855

; N DOPED SILICON
; fraction of um Si n doped layer
; 2.3290 g/cm^3
; atomic weight is 28.0855

; DEPLETION REGION
; 150 um Si depletion depth
; 2.3290 g/cm^3
; atomic weight is 28.0855

;          [Al   Si   O     O     Si(n) Si(i)]
;thickness = [0.018, 0.025, 0.025, 0.025, 1d-1, 150] ;    took guesses
;          for n doped depth based on yibins estimate of a "fraction of a micron
;          "

;density = [2.7, 2.648,2.648,2.648, 2.3290, 2.3290]
;amu = [26.9815386, 15.9994*2+28.0855,
;       15.9994*2+28.0855,15.9994*2+28.0855, 28.0855, 28.0855]
;z = [13, 14, 8, 8, 14, 14]
; energy = dindgen(1001)/1000.*9.8+.2
; qe=sim_qe(energy,thickness, density,z=z, amu=amu)

;daves thicknesses
;talfil = 1000. ; aluminum optical blocking filter
;tsigat = 0.   ; Poly silicon gate
;tsio2g = 0.   ; sio2 intergate insulator
;tsiogp = 0.   ; sio2 intergate insulator 2
;tsi3n4 = 0.   ; nitride insulator (si3n4)
;tsio2 = 200.  ; oxide insulator (siO2)
;tsi = 200.   ; silicon depletion depth

```

```

;tsio2p = 0.

; some of daves constants that I do not need
;pixsyz = 18. ; pixel size (microns)
;rms = 50.0 ; readnoise RMS
;fano = 0.12 ; fano factor for silicon
;conv = 3.65 ;

; fwhm of energy resolution at 5.9 keV (eV)
;fwhm = conv*2.354*sqrt((fano*5890/conv)+rms*rms)
; readnoise floor (eV)
;floor = rms*conv*2.354

```

C.4 Thesis

- pumpspeed.pro
- solve_ipc.pro

```

function spfunc,vars
pult = vars[0]
sp = vars[1]

v = 1.2d6 ; volume in cubic cm
t=86.4d3 ;time in seconds
pinit=1000.*1d3 ; atmospheric initial pressure in mbar converted to
    barye
pc =1d-6*1d3 ; chamber pressure at time t in mbar converted to barye
q = 3d-2*1d3*1d3 ; caterpillar water gas load mbar l/s converted to
    barye cm^3/s

k = 1.38064d-16 ; boltzmann's constant in cgs
m = 28.014*1.6605d-24 ; atomic mass of n2 in grams
temp = 291 ; temperature in kelvin
nu = sqrt(8*k*temp/(!dpi*m)) ; mean particle velocity cm/s

area = (8*2.54/2)^2*!dpi; pump entrance orifice area 8" ID in cm^2
c = nu/4.*area; conductance to from chamber to pump cc/s

return, [ ( ( -(v/t) * alog((pc-pult)/(pinit-pult)) )^(-1) + (1/c) )
    ^(-1) - sp, pult-q/sp]
end

pro pumpspeed

pult = 1d-7*1d3; ultimate pressure guess in mbar converted to barye
sp = 800*1d3; pumping speed guess in cc per second

```

```

result = newton([pult,sp], 'spfunc')

print, 'Given the guesses pult='+strcompress(pult)+ ' barye and sp='+
      strcompress(sp)+' cc per second, the results were pult='+strcompress(
      result[0])+ ' barye and sp=' strcompress(result[1]) + ' barye per
      second.'

end

```

```

function ipc_newton, c
q = 2.4113d-16
v = [3.93160,0.381382, 0.263602, 0.426251, 0.274819]; 0.244729,
      0.395732, 0.255143]

return, [-v[0] + q/(total(c[0]*c[1:4]/(c[1:4]+c[0]))+c[0]),$
-v[1] + (q*c[1]/(c[0]+c[1]))/(total(c[0]*c[1:4]/(c[1:4]+c[0]))+c[0]),$
-v[2] + (q*c[2]/(c[0]+c[2]))/(total(c[0]*c[1:4]/(c[1:4]+c[0]))+c[0]),$
-v[3] + (q*c[3]/(c[0]+c[3]))/(total(c[0]*c[1:4]/(c[1:4]+c[0]))+c[0]),$
-v[4] + (q*c[4]/(c[0]+c[4]))/(total(c[0]*c[1:4]/(c[1:4]+c[0]))+c[0])]

end

pro solve_ipc

c = [2.2d-14, 3.2d-15,2.3-15,3.2d-15,2.3d-15]

result = newton(c, 'ipc_newton',/double,itmax=10000,stepmax=10)
print, 'The initial capacitance values are ', c
print, 'The solved capacitances are ', result

end

```

Bibliography

- [1] KITCHIN, C. R. (2003) *Astrophysical Techniques*, Taylor and Francis Group.
- [2] ROGALSKI, A. (2012) “Progress in focal plane array technologies,” *Progress in Quantum Electronics*, **36**, pp. 342 – 473.
URL <http://www.sciencedirect.com/science/article/pii/S0079672712000183>
- [3] GEIST, J. and C. S. WANG (1983) “New calculations of the quantum yield of silicon in the near ultraviolet,” *Phys. Rev. B*, **27**, pp. 4841–4847.
URL <http://link.aps.org/doi/10.1103/PhysRevB.27.4841>
- [4] HOLLAND, A. D., A. D. T. SHORT, G. W. FRASER, and M. L. J. TURNER (1995) “The X-ray polarization sensitivity of CCDs,” *NIM Phys. Res. A*, **355**, pp. 526–531.
- [5] FRASER, G., A. ABBEY, A. HOLLAND, K. MCCARTHY, A. OWENS, and A. WELLS (1994) “The X-ray energy response of silicon Part A. Theory,” *Nuclear Instruments and Methods in Physics Research Section A: Accelerators, Spectrometers, Detectors and Associated Equipment*, **350**, pp. 368 – 378.
URL <http://www.sciencedirect.com/science/article/pii/0168900294911851>
- [6] FANO, U. (1947) “Ionization Yield of Radiation. II. The Fluctuations of the Number of Ions,” *Phys. Rev.*, **72**, pp. 26–29.
- [7] OWENS, A., G. W. FRASER, and K. J. MCCARTHY (2002) “On the experimental determination of the Fano factor in Si at soft X-ray wavelengths,” *Nuc. Inst. and Meth. in Phys. Res. A*, **491**, pp. 437–443.
- [8] (2013), “,” <http://www.securitycameraworld.com/images/Technical-Articles/ccdconcept.gif>.

- [9] (2013), “CMOS PRIMER,” <http://www.siliconimaging.com/ARTICLES/CMOS%20PRIMER/image015.jpg>.
- [10] BOYLE, W. and G. SMITH (1970) “Charge Coupled Semiconductor Devices,” *Bell System Technical Journal*, **49**, pp. 587–593.
- [11] AMELIO, G., M. TOMPSETT, and G. SMITH (1970) “Experimental Confirmation of the Charge Coupled Device Concept,” *Bell System Technical Journal*, **49**, pp. 593–600.
- [12] KOPPEL, L. N. (1977) “Direct soft x-ray response of a charge-coupled image sensor,” *Review of Scientific Instruments*, **48**(6), pp. 669–672.
URL <http://link.aip.org/link/?RSI/48/669/1>
- [13] BURROWS, D. N., J. A. NOUSEK, G. D. BERTHIAUME, and G. P. GARMIRE (1989) “Search for soft X-ray emission from SN 1987A with a CCD X-ray imaging spectrometer,” *ApJ*, **347**, pp. 1114–1118.
- [14] JANESICK, J. R. (2001) *Scientific Charged Coupled Devices*, SPIE Press, Bellingham, Washington.
- [15] HARKINS, W. (1999) “Space Radiation Effects on Electronic Components in Low-Earth Orbit,” *NASA Public Lessons Learned*, **0824**.
URL <http://www.nasa.gov/offices/oce/llis/0824.html>
- [16] MCKELVEY, M. E., K. A. ENNICO, R. R. JOHNSON, P. W. MARSHALL, R. E. McMURRAY, JR., C. R. MCCREIGHT, J. C. PICKEL, and R. A. REED (2004) “Radiation environment performance of JWST prototype FPAs,” in *Society of Photo-Optical Instrumentation Engineers (SPIE) Conference Series* (T. J. Grycewicz and C. R. McCreight, eds.), vol. 5167 of *Society of Photo-Optical Instrumentation Engineers (SPIE) Conference Series*, pp. 223–234.
- [17] SHORT, A. “Swift XRT: proton environment and CCD degradation,” *Swift project document*, **SWIFT-LUX-RE-001/1**.
- [18] PAGANI, C., A. P. BEARDMORE, A. F. ABBEY, C. MOUNTFORD, J. P. OSBORNE, M. CAPALBI, M. PERRI, L. ANGELINI, D. N. BURROWS, S. CAMPANA, G. CUSUMANO, P. A. EVANS, J. A. KENNEA, A. MORETTI, K. L. PAGE, and R. L. C. STARLING (2011) “Recovering Swift-XRT energy resolution through CCD charge trap mapping,” *AAp*, **534**, A20, 1108.5049.
- [19] DAVIS, J. E. (2001) “Event Pileup in Charge-coupled Devices,” *The Astrophysical Journal*, **562**(1), p. 575.
URL <http://stacks.iop.org/0004-637X/562/i=1/a=575>

- [20] VAUGHAN, S., M. R. GOAD, A. P. BEARDMORE, P. T. OBRIEN, J. P. OSBORNE, K. L. PAGE, S. D. BARTHELMY, D. N. BURROWS, S. CAMPANA, J. K. CANNIZZO, M. CAPALBI, G. CHINCARINI, J. R. CUMMINGS, G. CUSUMANO, P. GIOMMI, O. GODET, J. E. HILL, S. KOBAYASHI, P. KUMAR, V. L. PAROLA, A. LEVAN, V. MANGANO, P. MSZROS, A. MORETTI, D. C. MORRIS, J. A. NOUSEK, C. PAGANI, D. M. PALMER, J. L. RACUSIN, P. ROMANO, G. TAGLIAFERRI, B. ZHANG, and N. GEHRELS (2006) “Swift Observations of the X-Ray-Bright GRB 050315,” *The Astrophysical Journal*, **638**(2), p. 920.
URL <http://stacks.iop.org/0004-637X/638/i=2/a=920>
- [21] NOUSEK, J. (2013), “HRMA/ACIS Effective Area and Energy Resolution: Analysis technique,” http://www2.astro.psu.edu/xray/docs/cal_report/node200.html.
- [22] FOR SWIFT, M. O. C. (2013), “Swift XRT Software: Read out modes,” <http://www.swift.psu.edu/xrt/software.html>.
- [23] AGENCY, E. S. (2013), “XMM-Newton Users’ Handbook: 3.3.2 Science modes of the EPIC cameras,” http://xmm.esac.esa.int/external/xmm_user_support/documentation/uhb_2.2/node28.html#2800.
- [24] FOSSUM, E. (1995) “Low power camera-on-a-chip using CMOS active pixel sensor technology,” in *Low Power Electronics, 1995., IEEE Symposium on*, pp. 74–77.
- [25] SCHUSTER, M. and G. STRULL (1965) “A monolithic mosaic of photon sensors for solid state imaging applications,” in *Electron Devices Meeting, 1965 International*, vol. 11, pp. 20–21.
- [26] ——— (Dec) “A monolithic mosaic of photon sensors for solid-state imaging applications,” *Electron Devices, IEEE Transactions on*, **13**(12), pp. 907–912.
- [27] WECKLER, G. (1967) “Operation of p-n Junction Photodetectors in a Photon Flux Integrating Mode,” *Solid-State Circuits, IEEE Journal of*, **2**(3), pp. 65–73.
- [28] AHOUIE, M. and S. KLEINFELDER (2006) “Monolithic Sensors for Charged-Particle Imaging using Per-Pixel Correlated Double Sampling,” in *Nuclear Science Symposium Conference Record, 2006. IEEE*, vol. 1, pp. 54–58.
- [29] KLEINFELDER, S., L. JIN, and X. NGUYEN-HUU (2009) “A high-performance charged-particle CMOS image sensor with per-column A/D conversion,” in *Nuclear Science Symposium Conference Record (NSS/MIC), 2009 IEEE*, pp. 37–41.

- [30] KLEINFELDER, S., Y. CHEN, K. KWIATKOWSKI, and A. SHAH (2004) “High-speed CMOS image sensor circuits with in situ frame storage,” *Nuclear Science, IEEE Transactions on*, **51**(4), pp. 1648–1656.
- [31] BELETIC, J. W., R. BLANK, D. GULBRANSEN, D. LEE, M. LOOSE, E. C. PIQUETTE, T. SPRAFKE, W. E. TENNANT, M. ZANDIAN, and J. ZINO (2008) “Teledyne Imaging Sensors: infrared imaging technologies for astronomy and civil space,” in *Society of Photo-Optical Instrumentation Engineers (SPIE) Conference Series*, vol. 7021 of *Society of Photo-Optical Instrumentation Engineers (SPIE) Conference Series*.
- [32] KENTER, A. T., R. KRAFT, and S. S. MURRAY (2012) “Development of monolithic CMOS detectors as x-ray imaging spectrometers,” in *Society of Photo-Optical Instrumentation Engineers (SPIE) Conference Series*, vol. 8453 of *Society of Photo-Optical Instrumentation Engineers (SPIE) Conference Series*.
- [33] VAILLANT, J. and F. HIRIGOYEN (2004) “Optical simulation for CMOS imager microlens optimization,” in *Society of Photo-Optical Instrumentation Engineers (SPIE) Conference Series* (B. Culshaw, A. Mignani, and R. Riesenber, eds.), vol. 5459 of *Society of Photo-Optical Instrumentation Engineers (SPIE) Conference Series*.
- [34] MARQUET, L. and J. HARDY (1978) “Historical Review Of Adaptive Optics Technology,” in *Society of Photo-Optical Instrumentation Engineers (SPIE) Conference Series*, vol. 0141, pp. 2–10.
URL [+http://dx.doi.org/10.1117/12.956505](http://dx.doi.org/10.1117/12.956505)
- [35] THOM, R. (1977) “High density infrared detector array,” *US Patent 4039833*.
- [36] BAI, Y., W. TENNANT, S. ANGLIN, A. WONG, M. FARRIS, M. XU, E. HOLLAND, D. COOPER, J. HOSACK, K. HO, T. SPRAFKE, R. KOPP, B. STARR, R. BLANK, J. W. BELETIC, and G. A. LUPPINO (2012) “4K x 4K format 10 micron pixel pitch H4RG-10 hybrid CMOS silicon visible focal plane array for space astronomy,” in *Society of Photo-Optical Instrumentation Engineers (SPIE) Conference Series*, vol. 8453 of *Society of Photo-Optical Instrumentation Engineers (SPIE) Conference Series*.
- [37] BAI, Y., G. BERND, J. R. HOSACK, M. C. FARRIS, and J. T. BAJAJ (2004) “Hybrid CMOS Focal Plane Array with Extended UV and NIR Response for Space Applications,” vol. 5167 of *Proc. SPIE*, p. 83.

- [38] BAI, Y., M. C. FARRIS, A. K. PETERSEN, and J. W. BELETIC (2007) “Inter-Pixel Capacitance in Fully-Depleted Silicon Hybrid CMOS Focal Plane Arrays,” in *Society of Photo-Optical Instrumentation Engineers (SPIE) Conference Series*, vol. 6690 of *Proc. SPIE*.
- [39] SIMMS, L. (2007) *HYBRID CMOS SIPIN DETECTORS AS ASTRONOMICAL IMAGERS*, Ph.D. thesis, Stanford University.
- [40] NAVE, R. (2013), “P-N Energy Bands,” <http://hyperphysics.phy-astr.gsu.edu/hbase/solids/pnjun2.html#c1>.
- [41] WARREN, P., S. DEWALT, and M. BLOUKE (2005) “Total ionizing dose response of the Hawaii-2RG focal plane array,” in *Society of Photo-Optical Instrumentation Engineers (SPIE) Conference Series*, vol. 5902 of *Society of Photo-Optical Instrumentation Engineers (SPIE) Conference Series*, pp. 59020N–59020N–9.
URL [+http://dx.doi.org/10.1117/12.621736](http://dx.doi.org/10.1117/12.621736)
- [42] BAI, Y., J. T. BAJAJ, J. W. BELETIC, M. C. FARIS, A. JOSHI, S. LAUXTERMANN, A. PETERSEN, and G. WILLIAMS (2008) “Teledyne Imaging Sensors: Silicon CMOS imaging technologies for X-ray, UV, Visible and Near Infrared,” vol. 7021 of *Proc. SPIE*.
- [43] ROBBINS, M., P. MISTRY, and P. JORDEN (2011) “Detailed characterisation of a new large area CCD manufactured on high resistivity silicon,” in *Society of Photo-Optical Instrumentation Engineers (SPIE) Conference Series*, vol. 7875, pp. 787507–787507–12.
URL [+http://dx.doi.org/10.1117/12.876627](http://dx.doi.org/10.1117/12.876627)
- [44] BAGNASCO, G., M. KOLM, P. FERRUIT, K. HONNEN, J. KOEHLER, R. LEMKE, M. MASCHMANN, M. MELF, G. NOYER, P. RUMLER, J.-C. SALVIGNOL, P. STRADA, and M. TE PLATE (2007) “Overview of the near-infrared spectrograph (NIRSpec) instrument on-board the James Webb Space Telescope (JWST),” in *Society of Photo-Optical Instrumentation Engineers (SPIE) Conference Series*, vol. 6692 of *Society of Photo-Optical Instrumentation Engineers (SPIE) Conference Series*.
- [45] PRIESKORN, Z., C. V. GRIFFITH, S. D. BONGIORNO, A. D. FALCONE, and D. N. BURROWS (2013) “Characterization of Si Hybrid CMOS Detectors for use in the Soft X-ray Band,” *ArXiv e-prints*, 1303.6666.
- [46] KITAMOTO, S., T. KOHMURA, N. YAMAMOTO, H. TAKANO, H. SAITO, K. SUGA, H. SEKIGUCHI, S. CHIBA, I. OKAMOTO, K. HAYASHIDA, H. KATAYAMA, T. ENOYUCHI, Y. NAKASHIMA, T. SHIROSHOUJI,

- Y. TAWARA, A. FURUZAWA, and T. TANAKA (2004) “Soft x-ray transmission of optical blocking filters for x-ray CCD camera onboard Astro-E2,” in *Society of Photo-Optical Instrumentation Engineers (SPIE) Conference Series* (O. Citterio and S. L. O’Dell, eds.), vol. 5168 of *Society of Photo-Optical Instrumentation Engineers (SPIE) Conference Series*, pp. 376–385.
- [47] TOWNSLEY, L. K., F. R. POWELL, J. F. MACKAY, M. G. LAGALLY, J. A. NOUSEK, and G. P. GARMIRE (1996) “Transmission maps of the ACIS UV/optical blocking filters,” in *Society of Photo-Optical Instrumentation Engineers (SPIE) Conference Series* (R. B. Hoover and A. B. Walker, eds.), vol. 2805 of *Society of Photo-Optical Instrumentation Engineers (SPIE) Conference Series*, pp. 134–145.
- [48] BONGIORNO, S. D., A. D. FALCONE, D. N. BURROWS, and R. COOK (2009) “Measurements of Si hybrid CMOS x-ray detector characteristics,” vol. 7435 of *Proc. SPIE*.
- [49] ——— (2010) “Measurements of Si hybrid CMOS x-ray detector characteristics,” vol. 7742 of *Proc. SPIE*.
- [50] FALCONE, A. D. and D. N. BURROWS (2010) “The X-ray coded aperture telescope on the JANUS Mission,” in *Society of Photo-Optical Instrumentation Engineers (SPIE) Conference Series*, vol. 7732 of *Proc. SPIE*.
- [51] FINGER, G., R. DORN, M. MEYER, and L. MEHRGAN (2006) “Interpixel Capacitance in Large Format CMOS Hybrid Arrays,” vol. 6276 of *Proc. SPIE*.
- [52] MORI, K., H. TSUNEMI, E. MIYATA, C. J. BALUTA, D. N. BURROWS, G. P. GARMIRE, and G. CHARTAS (2001) “Improvement of the Chandra ACIS Spatial Resolution by Selecting the Split Pixel Events,” in *New Century of X-ray Astronomy* (H. Inoue and H. Kunieda, eds.), vol. 251 of *Astronomical Society of the Pacific Conference Series*, p. 576.
- [53] GRIFFITH, C. V., S. D. BONGIORNO, D. N. BURROWS, A. D. FALCONE, and Z. R. PRIESKORN (2012) “Characterization of an x-ray hybrid CMOS detector with low interpixel capacitive crosstalk,” in *Society of Photo-Optical Instrumentation Engineers (SPIE) Conference Series*, vol. 8453 of *Society of Photo-Optical Instrumentation Engineers (SPIE) Conference Series*, 1207–6317.
- [54] CONAN, J.-M., T. FUSCO, L. M. MUGNIER, E. KERSALE, and V. MICHAU (1999) “Deconvolution of Adaptive Optics Images with Imprecise Knowledge of the Point Spread Function: Results on Astronomical Objects,” in *European Southern Observatory Conference and Workshop Proceedings*

- (D. Bonaccini, ed.), vol. 56 of *European Southern Observatory Conference and Workshop Proceedings*, p. 121.
- [55] DORN, R. J., S. ESCHBAUMER, G. FINGER, L. MEHRGAN, M. MEYER, and J. STEGMEIER (2006) “A CMOS visible silicon imager hybridized to a Rockwell 2RG multiplexer as a new detector for ground based astronomy,” in *Society of Photo-Optical Instrumentation Engineers (SPIE) Conference Series*, vol. 6276 of *Society of Photo-Optical Instrumentation Engineers (SPIE) Conference Series*.
- [56] CHELIKOWSKY, J., D. J. CHADI, and M. L. COHEN (1973) “Calculated Valence-Band Densities of States and Photoemission Spectra of Diamond and Zinc-Blende Semiconductors,” *Phys. Rev. B*, **8**, pp. 2786–2794.
URL <http://link.aps.org/doi/10.1103/PhysRevB.8.2786>
- [57] GREEN, M. A. (2008) “Self-consistent optical parameters of intrinsic silicon at 300 K including temperature coefficients,” *Solar Energy Materials and Solar Cells*, **92**(11), pp. 1305 – 1310.
URL <http://www.sciencedirect.com/science/article/pii/S0927024808002158>
- [58] MCCULLOUGH, P. R., M. REGAN, L. BERGERON, and K. LINDSAY (2008) “Quantum Efficiency and Quantum Yield of an HgCdTe Infrared Sensor Array,” *Publications of the Astronomical Society of the Pacific*, **120**, pp. 759–776.
- [59] MELVIN, M. A. (1955) “Blackbody Radiation and Lambert’s Law,” *American Journal of Physics*, **23**, pp. 508–510.
- [60] ROGALSKI, A. (2005) “HgCdTe infrared detector material: history, status and outlook,” *Reports on Progress in Physics*, **68**, pp. 2267–2336.
- [61] DAVIS, M. W., T. K. GREATHOUSE, K. D. RETHERFORD, G. S. WINTERS, Y. BAI, and J. W. BELETIC (2012) “Far ultraviolet sensitivity of silicon CMOS sensors,” in *Society of Photo-Optical Instrumentation Engineers (SPIE) Conference Series*, vol. 8453 of *Society of Photo-Optical Instrumentation Engineers (SPIE) Conference Series*.
- [62] DANZMANN, K., M. GÜNTHER, J. FISCHER, M. KÜHNE, and M. KOCK (1988) “High current hollow cathode as a radiometric transfer standard source for the extreme vacuum ultraviolet,” *Applied Optics*, **27**, pp. 4947–4951.

- [63] IDZOREK, G. C. and R. J. BARTLETT (1997) “Silicon photodiode characterization from 1 eV to 10 keV,” in *Society of Photo-Optical Instrumentation Engineers (SPIE) Conference Series* (O. H. Siegmund and M. A. Gummin, eds.), vol. 3114 of *Society of Photo-Optical Instrumentation Engineers (SPIE) Conference Series*, pp. 349–356.
- [64] KEISTER, J. W. (2007) “Silicon photodiodes for absolute soft x-ray radiometry,” in *Society of Photo-Optical Instrumentation Engineers (SPIE) Conference Series*, vol. 6689 of *Society of Photo-Optical Instrumentation Engineers (SPIE) Conference Series*.
- [65] CURRAN, S. C. (1958) “The Proportional Counter as Detector and Spectrometer,” *Handbuch der Physik*, **45**, pp. 174–221.
- [66] FAILOR, B. H., E. M. GULLIKSON, N. G. LINK, J. C. RIORDAN, and B. C. WILSON (2012) “Sensitivity of an image plate system in the XUV (60 eV < E < 900 eV),” *Journal of Instrumentation*, **7**, p. 4011, 1202.1197.
- [67] BOOTSMA, T. M. V., E. J. VAN ZWET, A. C. BRINKMAN, J. W. DEN HERDER, L. DE JONG, P. DE KORTE, and S. M. OLSHOORN (2000) “Synchrotron calibration and response modelling of back-illuminated XMM-RGS CCDs,” *Nuclear Instruments and Methods in Physics Research A*, **439**, pp. 575–581.
- [68] BAUTZ, M. W., M. J. PIVOVAROFF, S. E. KISSEL, G. Y. PRIGOZHIN, T. ISOBE, S. E. JONES, G. R. RICKER, R. THORNAGEL, S. KRAFT, F. SCHOLZE, and G. ULM (2000) “Absolute calibration of ACIS x-ray CCDs using calculable undispersed synchrotron radiation,” in *Society of Photo-Optical Instrumentation Engineers (SPIE) Conference Series* (J. E. Truemper and B. Aschenbach, eds.), vol. 4012 of *Society of Photo-Optical Instrumentation Engineers (SPIE) Conference Series*, pp. 53–67.
- [69] MARTY, P. and J.-P. BERNARD (2001) “EPIC/XMM calibrations,” *X-ray Astronomy: Stellar Endpoints, AGN, and the Diffuse X-ray Background*, **599**, pp. 750–753.
- [70] ASCHENBACH, B. (1988) “Design, construction, and performance of the Rosat high-resolution X-ray mirror assembly,” *Applied Optics*, **27**, pp. 1404–1413.
- [71] ITOH, K., H. KUNIEDA, Y. MAEDA, K. MISAKI, P. J. SERLEMITSOS, R. SHIBATA, B. BUDAU, W. BURKERT, M. J. FREYBERG, G. HARTNER, K.-W. CHAN, Y. HABA, A. HAYAKAWA, R. IIZUKA, C. INOUE, H. INOUE, M. ISHIDA, A. ITOH, J. P. LEHAN, H. MORI, M. NAITOU, S. OKADA,

- T. OKAJIMA, T. SHIMIZU, Y. SOONG, and Y. YOKOYAMA (2004) “Ground-based x-ray calibration of the Astro-E2 x-ray telescope: II. With diverging beam at PANTER,” in *Society of Photo-Optical Instrumentation Engineers (SPIE) Conference Series* (G. Hasinger and M. J. L. Turner, eds.), vol. 5488 of *Society of Photo-Optical Instrumentation Engineers (SPIE) Conference Series*, pp. 85–92.
- [72] TAGLIAFERRI, G., A. MORETTI, S. CAMPANA, A. F. ABBEY, R. M. AMBROSI, L. ANGELINI, A. P. BEARDMORE, H. W. BRÄUNINGER, W. BURKERT, D. N. BURROWS, M. CAPALBI, G. CHINCARINI, O. CITTERIO, G. CUSUMANO, M. J. FREYBERG, P. GIOMMI, G. D. HARTNER, J. E. HILL, K. MORI, D. C. MORRIS, K. MUKERJEE, J. A. NOUSEK, J. P. OSBORNE, A. D. T. SHORT, F. TAMBURELLI, D. J. WATSON, and A. A. WELLS (2004) “Swift XRT effective area measured at the Panter end-to-end tests,” in *Society of Photo-Optical Instrumentation Engineers (SPIE) Conference Series* (K. A. Flanagan and O. H. W. Siegmund, eds.), vol. 5165 of *Society of Photo-Optical Instrumentation Engineers (SPIE) Conference Series*, pp. 241–250.
- [73] RUPP, B. (2005) *Biomolecular Crystallography: Principles, Practice, and Application to Structural Biology*, Garland Science.
- [74] KENTER, A. T., R. KRAFT, S. NULSEN, G. MEEHAN, and S. S. MURRAY (2005) “Rockwell CMOS hybrid imager as a soft x-ray imaging spectrometer,” in *Society of Photo-Optical Instrumentation Engineers (SPIE) Conference Series* (O. H. W. Siegmund, ed.), vol. 5898 of *Society of Photo-Optical Instrumentation Engineers (SPIE) Conference Series*, pp. 479–489.
- [75] VENTURA, V. and L. RISEGARI (2007) *The Art of Cryogenics*, Elsevier.
- [76] HENKE, B. L., E. M. GULLIKSON, and J. C. DAVIS (1993) “X-Ray Interactions: Photoabsorption, Scattering, Transmission, and Reflection at $E = 50\text{--}30,000$ eV, $Z = 1\text{--}92$,” *Atomic Data and Nuclear Data Tables*, **54**, pp. 181–342.
- [77] DYLLA, H. F. (2006) “The Development of UHV and XHV for Physics Research,” CERN Accelerator School, Platja D’Aro, Spain.
URL [\url{http://cas.web.cern.ch/cas/Spain-2006/PDFs/Dylla-3.pdf}](http://cas.web.cern.ch/cas/Spain-2006/PDFs/Dylla-3.pdf)
- [78] WAGNER, A., W. AND SAUL and P. A. (1994) “International Equations for the Pressure Along the Melting and Along the Sublimation Curve of Ordinary Water Substance,” *Journal of Physical and Chemical Reference Data*, **23**(3), pp. 515–527.
URL <http://link.aip.org/link/?JPR/23/515/1>

- [79] O'HANLON, J. (2003) *A User's Guide to Vacuum Technology*, Wiley-Interscience.
- [80] JACQUOT, B. C., S. P. MONACOS, M. E. HOENK, F. GREER, T. J. JONES, and S. NIKZAD (2011) "A system and methodologies for absolute quantum efficiency measurements from the vacuum ultraviolet through the near infrared," *Review of Scientific Instruments*, **82**(4), 043102.
URL <http://link.aip.org/link/?RSI/82/043102/1>
- [81] LI, M. and H. F. DYLLA (1993) "Model for the outgassing of water from metal surfaces," vol. 11, AVS, pp. 1702–1707.
URL <http://link.aip.org/link/?JVA/11/1702/1>
- [82] INC., S. (2013), "Stirling Coolers," <http://www.sunpower.com/>.
- [83] TE TECHNOLOGY INC. (2013), "Multi-Stage Modules," <http://www.tetech.com/Peltier-Thermoelectric-Cooler-Modules/Multi-Stage.html>.
- [84] LBNL (2013), "Viewing the Periodic Table of the Elements with X-rays," <http://ie.lbl.gov/xray/xrf.htm>.
- [85] THOMPSON, A. C. and D. VAUGHAN (2001) "X-ray Data Booklet," *Lawrence Berkeley National Laboratory, University of California*.
URL <http://xdb.lbl.gov>
- [86] PRESTON, A. (1970) "Iron-55 in fish from the North Atlantic," *Marine Biology*, **6**, pp. 345–349.
- [87] HAYNES, W. (2013) *Handbook of Chemistry and Physics*, 93 ed., CRC.
- [88] SCOFIELD, J. H. (1974) "Relativistic Hartree-Slater Values for K and L X-ray Emission Rates," *Atomic Data and Nuclear Data Tables*, **14**, pp. 121–137.
- [89] LANGMUIR, I. (1934) "Thoriated tungsten filaments," *Journal of the Franklin Institute*, **217**(5), pp. 543 – 569.
URL <http://www.sciencedirect.com/science/article/pii/S0016003234903483>
- [90] HENKE, B. L. (1961) "Ultra-soft X-ray Source," *US Patent 3138729*.
- [91] YANG, Y., Z. SHI, Z. FEI, X. JIN, J. XIAO, R. HUTTON, and Y. ZOU (2011) "Configuration and calibration of a flat field grating spectrometer in the wavelength range 760Å with a Manson ultrasoft x-ray source," *Physica Scripta*, **2011**(T144), p. 014064.

- [92] LARRABEE, R. D. (1957) "The Spectral Emissivity and Optical Properties of Tungsten," *MIT Research Laboratory of Electronics*, (328).
- [93] SCHMIDT, J. and M. MOLDOVER (2003) "Dielectric Permittivity of Eight Gasses Measured with Cross Capacitors," *International Journal of Thermophysics*, **24**.
- [94] WITTKKE, J. H. (2013), "3.5.5.2 Detector Theory," <http://www4.nau.edu/microanalysis/microprobe/WDS-DetectorTheory.html>.
- [95] MAZZIOTTA, M. (2008) "Electron-hole pair creation energy and Fano factor temperature dependence in silicon," *Nuclear Instruments and Methods in Physics Research Section A: Accelerators, Spectrometers, Detectors and Associated Equipment*, **584**(2-3), pp. 436 – 439.
URL <http://www.sciencedirect.com/science/article/pii/S0168900207022668>
- [96] DOKE, T., N. ISHIDA, and M. KASE (1992) "Fano factors in rare gases and their mixtures," *Nuclear Instruments and Methods in Physics Research Section B: Beam Interactions with Materials and Atoms*, **63**(4), pp. 373 – 376.
URL <http://www.sciencedirect.com/science/article/pii/0168583X92952078>
- [97] TAWARA, H., N. ISHIDA, J. KIKUCHI, and T. DOKE (1987) "Measurements of the W values in argon, nitrogen, and methane for 0.93 to 5.3 MeV alpha particles," *Nuclear Instruments and Methods in Physics Research Section B: Beam Interactions with Materials and Atoms*, **29**(3), pp. 447 – 455.
URL <http://www.sciencedirect.com/science/article/pii/0168583X87900553>
- [98] KASE, M., T. AKIOKA, H. MAMYODA, J. KIKUCHI, and T. DOKE (1984) "Fano factor in pure argon," *Nuclear Instruments and Methods in Physics Research Section A: Accelerators, Spectrometers, Detectors and Associated Equipment*, **227**(2), pp. 311 – 317.
URL <http://www.sciencedirect.com/science/article/pii/0168900284901396>
- [99] GEDCKE, D. A., R. M. KEYSER, and T. R. TWOMEY, "A New Method for Counting Loss Correction with Uncertainty in Gamma Spectroscopy Applications," <http://www.ortec-online.com/download/Innovative-Method-Dead-Time-Correction-Nuclear-Spectroscopy%20.pdf>.

- [100] PRIESTLEY, E. and H. PHELAN (1971) “A stainless steel support grid for flow-proportional counter windows,” *Nuclear Instruments and Methods*, **96**(2), pp. 235 – 236.
URL <http://www.sciencedirect.com/science/article/pii/0029554X71903107>
- [101] McMASTER, W. H., N. K. DEL GRANDE, J. H. MALLETT, and J. H. HUBBELL (1969) “Compilation of X-ray cross sections,” *Lawrence Livermore National Laboratory Report*, **UCRL-50174**.
- [102] MARKWARDT, C. B. (2009) “Non-linear Least-squares Fitting in IDL with MPFIT,” in *Astronomical Data Analysis Software and Systems XVIII* (D. A. Bohlender, D. Durand, and P. Dowler, eds.), vol. 411 of *Astronomical Society of the Pacific Conference Series*, p. 251, 0902.2850.
- [103] BOGGS, S., J. BREGMAN, D. CARLSTROM, J. DAOU, M. DONAHUE, F. GIES, D. ANDLOCKMAN, D. MCCAMMON, J. PIPHER, D. POLLACCO, S. RIDGWAY, and R. STERN (2012) “2012 Senior Review of Operating Missions in the NASA Astrophysics Division,” *NASA*.
- [104] BONGIORNO, S. D., A. D. FALCONE, M. STROH, J. HOLDER, J. L. SKILTON, J. A. HINTON, N. GEHRELS, and J. GRUBE (2011) “A New TeV Binary: The Discovery of an Orbital Period in HESS J0632+057,” *ApJL*, **737**, L11, 1104.4519.
- [105] AHARONIAN, F., A. G. AKHPERJANIAN, K.-M. AYE, A. R. BAZERBACHI, M. BEILICKE, W. BENBOW, D. BERGE, P. BERGHAUS, K. BERNLÖHR, C. BOISSON, O. BOLZ, I. BRAUN, F. BREITLING, A. M. BROWN, J. BUSSONS GORDO, P. M. CHADWICK, L.-M. CHOUNET, R. CORNILS, L. COSTAMANTE, B. DEGRANGE, A. DJANNATI-ATAÏ, L. O’C. DRURY, G. DUBUS, D. EMMANOULOPOULOS, P. ESPIGAT, F. FEINSTEIN, P. FLEURY, G. FONTAINE, Y. FUCHS, S. FUNK, Y. A. GALLANT, B. GIEBELS, S. GILLESSEN, J. F. GLICENSTEIN, P. GORET, C. HADJICHRISTIDIS, M. HAUSER, G. HEINZELMANN, G. HENRI, G. HERMANN, J. A. HINTON, W. HOFMANN, M. HOLLERAN, D. HORNS, O. C. DE JAGER, S. JOHNSTON, B. KHÉLIFI, J. G. KIRK, N. KOMIN, A. KONOPELKO, I. J. LATHAM, R. LE GALLOU, A. LEMIÈRE, M. LEMOINE-GOUMARD, N. LEROY, O. MARTINEAU-HUYNH, T. LOHSE, A. MARCOWITH, C. MASTERSON, T. J. L. MCCOMB, M. DE NAUROIS, S. J. NOLAN, A. NOUTSOS, K. J. ORFORD, J. L. OSBORNE, M. OUCHRIF, M. PANTER, G. PELLETIER, S. PITA, G. PÜHLHOFER, M. PUNCH, B. C. RAUBENHEIMER, M. RAUE, J. RAUX, S. M. RAYNER, I. REDONDO, A. REIMER, O. REIMER, J. RIPKEN, L. ROB, L. ROLLAND, G. ROWELL, V. SAHAKIAN, L. SAUGÉ, S. SCHLENKER, R. SCHLICKEISER,

- C. SCHUSTER, U. SCHWANKE, M. SIEWERT, O. SKJÆRAASEN, H. SOL, R. STEENKAMP, C. STEGMANN, J.-P. TAVERNET, R. TERRIER, C. G. THÉORET, M. TLUCZYKONT, G. VASILEIADIS, C. VENTER, P. VINCENT, H. J. VÖLK, and S. J. WAGNER (2005) “Discovery of the binary pulsar PSR B1259-63 in very-high-energy gamma rays around periastron with HESS,” *Astronomy and Astrophysics*, **442**, pp. 1–10, arXiv:astro-ph/0506280.
- [106] AHARONIAN, F., A. G. AKHPERJANIAN, K.-M. AYE, A. R. BAZERBACHI, M. BEILICKE, W. BENBOW, D. BERGE, P. BERGHAUS, K. BERNLÖHR, C. BOISSON, O. BOLZ, V. BORREL, I. BRAUN, F. BREITLING, A. M. BROWN, J. B. GORDO, P. M. CHADWICK, L.-M. CHOUNET, R. CORNILS, L. COSTAMANTE, B. DEGRANGE, H. J. DICKINSON, A. DJANNATI-ATAÏ, L. O. DRURY, G. DUBUS, D. EMMANOULOPOULOS, P. ESPIGAT, F. FEINSTEIN, P. FLEURY, G. FONTAINE, Y. FUCHS, S. FUNK, Y. A. GALLANT, B. GIEBELS, S. GILLESSEN, J. F. GLICENSTEIN, P. GORET, C. HADJICHRISTIDIS, M. HAUSER, G. HEINZELMANN, G. HENRI, G. HERMANN, J. A. HINTON, W. HOFMANN, M. HOLLERAN, D. HORNS, A. JACHOLKOWSKA, O. C. DE JAGER, B. KHÉLIFI, N. KOMIN, A. KONOPELKO, I. J. LATHAM, R. LE GALLOU, A. LEMIÈRE, M. LEMOINE-GOUMARD, N. LEROY, T. LOHSE, A. MARCOWITH, J.-M. MARTIN, O. MARTINEAU-HUYNH, C. MASTERSON, T. J. L. MCCOMB, M. DE NAUROIS, S. J. NOLAN, A. NOUTSOS, K. J. ORFORD, J. L. OSBORNE, M. OUCHRIF, M. PANTER, G. PELLETIER, S. PITA, G. PÜHLHOFER, M. PUNCH, B. C. RAUBENHEIMER, M. RAUE, J. RAUX, S. M. RAYNER, A. REIMER, O. REIMER, J. RIPKEN, L. ROB, L. ROLLAND, G. ROWELL, V. SAHAKIAN, L. SAUGÉ, S. SCHLENKER, R. SCHLICKEISER, C. SCHUSTER, U. SCHWANKE, M. SIEWERT, H. SOL, D. SPANGLER, R. STEENKAMP, C. STEGMANN, J.-P. TAVERNET, R. TERRIER, C. G. THÉORET, M. TLUCZYKONT, G. VASILEIADIS, C. VENTER, P. VINCENT, H. J. VÖLK, and S. J. WAGNER (2005) “Discovery of Very High Energy Gamma Rays Associated with an X-ray Binary,” *Science*, **309**, pp. 746–749, arXiv:astro-ph/0508298.
- [107] ALBERT, J., E. ALIU, H. ANDERHUB, P. ANTORANZ, A. ARMADA, M. ASENSIO, C. BAIXERAS, J. A. BARRIO, M. BARTELT, H. BARTKO, D. BASTIERI, S. R. BAVIKADI, W. BEDNAREK, K. BERGER, C. BIGONGIARI, A. BILAND, E. BISESI, R. K. BOCK, P. BORDAS, V. BOSCH-RAMON, T. BRETZ, I. BRITVITCH, M. CAMARA, E. CARMONA, A. CHILINGARIAN, S. CIPRINI, J. A. COARASA, S. COMMICHAU, J. L. CONTRERAS, J. CORTINA, V. CURTEF, V. DANIELYAN, F. DAZZI, A. DE ANGELIS, R. DE LOS REYES, B. DE LOTTO, E. DOMINGO-SANTAMARÍA, D. DORNER, M. DORO, M. ERRANDO, M. FAGIOLINI, D. FERENC, E. FERNÁNDEZ, R. FIRPO, J. FLIX, M. V.

FONSECA, L. FONT, M. FUCHS, N. GALANTE, M. GARCZARCZYK, M. GAUG, M. GILLER, F. GOEBEL, D. HAKOBYAN, M. HAYASHIDA, T. HENGSTEBECK, D. HÖHNE, J. HOSE, C. C. HSU, P. G. ISAR, P. JACON, O. KALEKIN, R. KOSYRA, D. KRANICH, M. LAATIAOUI, A. LAILLE, T. LENISA, P. LIEBING, E. LINDFORS, S. LOMBARDI, F. LONGO, J. LÓPEZ, M. LÓPEZ, E. LORENZ, F. LUCARELLI, P. MAJUMDAR, G. MANEVA, K. MANNHEIM, O. MANSUTTI, M. MARIOTTI, M. MARTÍNEZ, K. MASE, D. MAZIN, C. MERCK, M. MEUCCI, M. MEYER, J. M. MIRANDA, R. MIRZOYAN, S. MIZOBUCHI, A. MORALEJO, K. NILSSON, E. OÑA-WILHELMI, R. ORDUÑA, N. OTTE, I. OYA, D. PANEQUE, R. PAOLETTI, J. M. PAREDES, M. PASANEN, D. PASCOLI, F. PAUSS, N. PAVEL, R. PEGNA, M. PERSIC, L. PERUZZO, A. PICCIOLI, M. POLLER, G. POOLEY, E. PRANDINI, A. RAYMERS, W. RHODE, M. RIBÓ, J. RICO, B. RIEGEL, M. RISSI, A. ROBERT, G. E. ROMERO, S. RÜGAMER, A. SAGGION, A. SÁNCHEZ, P. SARTORI, V. SCALZOTTO, V. SCAPIN, R. SCHMITT, T. SCHWEIZER, M. SHAYDUK, K. SHINOZAKI, S. N. SHORE, N. SIDRO, A. SILLANPÄÄ, D. SOB CZYNSKA, A. STAMERRA, L. S. STARK, L. TAKALO, P. TEMNIKOV, D. TESCARO, M. TESHIMA, N. TONELLO, A. TORRES, D. F. TORRES, N. TURINI, H. VANKOV, V. VITALE, R. M. WAGNER, T. WIBIG, W. WITTEK, R. ZANIN, and J. ZAPATERO (2006) “Variable Very-High-Energy Gamma-Ray Emission from the Microquasar LS I +61 303,” *Science*, **312**, pp. 1771–1773, arXiv:astro-ph/0605549.

- [108] ACCIARI, V. A., M. BEILICKE, G. BLAYLOCK, S. M. BRADBURY, J. H. BUCKLEY, V. BUGAEV, Y. BUTT, K. L. BYRUM, O. CELIK, A. CESARINI, L. CIUPIK, Y. C. K. CHOW, P. COGAN, P. COLIN, W. CUI, M. K. DANIEL, C. DUKE, T. ERGIN, A. D. FALCONE, S. J. FEGAN, J. P. FINLEY, P. FORTIN, L. F. FORTSON, D. GALL, K. GIBBS, G. H. GILLANDERS, J. GRUBE, R. GUENETTE, D. HANNA, E. HAYS, J. HOLDER, D. HORAN, S. B. HUGHES, C. M. HUI, T. B. HUMENSKY, P. KAARET, D. B. KIEDA, J. KILDEA, A. KONOPELKO, H. KRAWCZYNSKI, F. KRENNRICH, M. J. LANG, S. LEBOHEC, K. LEE, G. MAIER, A. MCCANN, M. MCCUTCHEON, J. MILLIS, P. MORIARTY, R. MUKHERJEE, T. NAGAI, R. A. ONG, D. PANDEL, J. S. PERKINS, F. PIZLO, M. POHL, J. QUINN, K. RAGAN, P. T. REYNOLDS, H. J. ROSE, M. SCHROEDTER, G. H. SEMBROSKI, A. W. SMITH, D. STEELE, S. P. SWORDY, J. A. TONER, L. VALCARCEL, V. V. VASSILIEV, R. WAGNER, S. P. WAKELY, J. E. WARD, T. C. WEEKES, A. WEINSTEIN, R. J. WHITE, D. A. WILLIAMS, S. A. WISSEL, M. WOOD, and B. ZITZER (2008) “VERITAS Observations of the γ -Ray Binary LS I +61 303,” *The Astrophysical Journal*, **679**, pp. 1427–1432, 0802.2363.

- [109] ACCIARI, V. A., E. ALIU, T. ARLEN, M. BAUTISTA, M. BEILICKE,

- W. BENBOW, M. BÖTTCHER, S. M. BRADBURY, V. BUGAEV, Y. BUTT, Y. BUTT, K. BYRUM, A. CANNON, A. CESARINI, Y. C. CHOW, L. CIUPIK, P. COGAN, P. COLIN, W. CUI, M. DANIEL, R. DICKHERBER, T. ERGIN, A. FALCONE, S. J. FEGAN, J. P. FINLEY, P. FORTIN, L. FORTSON, A. FURNISS, D. GALL, G. H. GILLANDERS, J. GRUBE, R. GUENETTE, G. GYUK, D. HANNA, E. HAYS, J. HOLDER, D. HORAN, C. M. HUI, T. B. HUMENSKY, P. KAARET, N. KARLSSON, D. KIEDA, J. KILDEA, A. KONOPELKO, H. KRAWCZYNSKI, F. KRENNRICH, M. J. LANG, S. LEBOHEC, G. MAIER, A. MCCANN, M. MCCUTCHEON, J. MILLIS, P. MORIARTY, R. MUKHERJEE, T. NAGAI, R. A. ONG, A. N. OTTE, D. PANDEL, J. S. PERKINS, J. S. PERKINS, M. POHL, J. QUINN, K. RAGAN, L. C. REYES, P. T. REYNOLDS, E. ROACHE, H. JOACHIM ROSE, M. SCHROEDTER, G. H. SEMBROSKI, A. W. SMITH, D. STEELE, M. STROH, S. SWORDY, M. THEILING, J. A. TONER, A. VARLOTTA, V. V. VASSILIEV, R. G. WAGNER, S. P. WAKELY, J. E. WARD, T. C. WEEKES, A. WEINSTEIN, R. J. WHITE, D. A. WILLIAMS, S. WISSEL, M. WOOD, and B. ZITZER (2009) “Multiwavelength Observations of LS I +61deg 303 with Veritas, Swift, and RXTE,” *The Astrophysical Journal*, **700**, pp. 1034–1041, 0904.4422.
- [110] CORBET, R. H. D., C. C. CHEUNG, M. KERR, R. DUBOIS, D. DONATO, G. A. CALIANDRO, M. J. COE, P. G. EDWARDS, M. D. FILIPOVIC, J. L. PAYNE, and J. STEVENS (2011) “1FGL J1018.6-5856: a New Gamma-ray Binary,” *The Astronomer’s Telegram*, **3221**, p. 1.
- [111] ALBERT, J., E. ALIU, H. ANDERHUB, P. ANTORANZ, A. ARMADA, C. BAIXERAS, J. A. BARRIO, H. BARTKO, D. BASTIERI, J. K. BECKER, W. BEDNAREK, K. BERGER, C. BIGONGIARI, A. BILAND, R. K. BOCK, P. BORDAS, V. BOSCH-RAMON, T. BRETZ, I. BRITVITCH, M. CAMARA, E. CARMONA, A. CHILINGARIAN, J. A. COARASA, S. COMMICHAU, J. L. CONTRERAS, J. CORTINA, M. T. COSTADO, V. CURTEF, V. DANIELYAN, F. DAZZI, A. DE ANGELIS, C. DELGADO, R. DE LOS REYES, B. DE LOTTO, E. DOMINGO-SANTAMARÍA, D. DORNER, M. DORO, M. ERRANDO, M. FAGIOLINI, D. FERENC, E. FERNÁNDEZ, R. FIRPO, J. FLIX, M. V. FONSECA, L. FONT, M. FUCHS, N. GALANTE, R. J. GARCÍA-LÓPEZ, M. GARCZARCZYK, M. GAUG, M. GILLER, F. GOEBEL, D. HAKOBYAN, M. HAYASHIDA, T. HENGSTEBECK, A. HERRERO, D. HÖHNE, J. HOSE, C. C. HSU, P. JACON, T. JOGLER, R. KOSYRA, D. KRANICH, R. KRITZER, A. LAILLE, E. LINDFORS, S. LOMBARDI, F. LONGO, J. LÓPEZ, M. LÓPEZ, E. LORENZ, P. MAJUMDAR, G. MANEVA, K. MANNHEIM, O. MANSUTTI, M. MARIOTTI, M. MARTÍNEZ, D. MAZIN, C. MERCK, M. MEUCCI, M. MEYER, J. M. MIRANDA, R. MIRZOYAN, S. MIZOBUCHI, A. MORALEJO,

D. NIETO, K. NILSSON, J. NINKOVIC, E. OÑA-WILHELMI, N. OTTE, I. OYA, M. PANNIELLO, R. PAOLETTI, J. M. PAREDES, M. PASANEN, D. PASCOLI, F. PAUSS, R. PEGNA, M. PERSIC, L. PERUZZO, A. PICCIOLI, E. PRANDINI, N. PUCHADES, A. RAYMERS, W. RHODE, M. RIBÓ, J. RICO, M. RISSI, A. ROBERT, S. RÜGAMER, A. SAGGION, T. SAITO, A. SÁNCHEZ, P. SARTORI, V. SCALZOTTO, V. SCAPIN, R. SCHMITT, T. SCHWEIZER, M. SHAYDUK, K. SHINOZAKI, S. N. SHORE, N. SIDRO, A. SILLANPÄÄ, D. SOBCHYZNSKA, A. STAMERRA, L. S. STARK, L. TAKALO, P. TEMNIKOV, D. TESCARO, M. TESHIMA, D. F. TORRES, N. TURINI, H. VANKOV, V. VITALE, R. M. WAGNER, T. WIBIG, W. WITTEK, F. ZANDANEL, R. ZANIN, and J. ZAPATERO (2007) “Very High Energy Gamma-Ray Radiation from the Stellar Mass Black Hole Binary Cygnus X-1,” *The Astrophysical Journal Letters*, **665**, pp. L51–L54, 0706.1505.

- [112] AHARONIAN, F. A., A. G. AKHPERJANIAN, A. R. BAZER-BACHI, B. BEHERA, M. BEILICKE, W. BENBOW, D. BERGE, K. BERNLÖHR, C. BOISSON, O. BOLZ, V. BORREL, I. BRAUN, E. BRION, A. M. BROWN, R. BÜHLER, I. BÜSCHING, T. BOUTELIER, S. CARRIGAN, P. M. CHADWICK, L.-M. CHOUNET, G. COIGNET, R. CORNILS, L. COSTAMANTE, B. DEGRANGE, H. J. DICKINSON, A. DJANNATI-ATAÏ, W. DOMAINKO, L. O’C. DRURY, G. DUBUS, K. EGBERTS, D. EMMANOULOPOULOS, P. ESPIGAT, C. FARNIER, F. FEINSTEIN, A. FIASSON, A. FÖRSTER, G. FONTAINE, S. FUNK, S. FUNK, M. FÜSSLING, Y. A. GALLANT, B. GIEBELS, J. F. GLICENSTEIN, B. GLÜCK, P. GORET, C. HADJICHRISTIDIS, D. HAUSER, M. HAUSER, G. HEINZELMANN, G. HENRI, G. HERMANN, J. A. HINTON, A. HOFFMANN, W. HOFMANN, M. HOLLERAN, S. HOPPE, D. HORNS, A. JACHOLKOWSKA, O. C. DE JAGER, E. KENDZIORRA, M. KERSCHHAGGL, B. KHÉLIFI, N. KOMIN, K. KOSACK, G. LAMANNA, I. J. LATHAM, R. LE GALLOU, A. LEMIÈRE, M. LEMOINE-GOUMARD, T. LOHSE, J. M. MARTIN, O. MARTINEAU-HUYNH, A. MARCOWITH, C. MASTERTSON, G. MAURIN, T. J. L. MCCOMB, E. MOULIN, M. DE NAUROIS, D. NEDBAL, S. J. NOLAN, A. NOUTSOS, J.-P. OLIVE, K. J. ORFORD, J. L. OSBORNE, M. PANTER, G. PEDALETTI, G. PELLETIER, P.-O. PETRUCCI, S. PITA, G. PÜHLHOFER, M. PUNCH, S. RANÇON, B. C. RAUBENHEIMER, M. RAUE, S. M. RAYNER, O. REIMER, J. RIPKEN, L. ROB, L. ROLLAND, S. ROSIER-LEES, G. ROWELL, J. RUPPEL, V. SAHAKIAN, A. SANTANGELO, L. SAUGÉ, S. SCHLENKER, R. SCHLICKEISER, R. SCHRÖDER, U. SCHWANKE, S. SCHWARZBURG, S. SCHWEMMER, A. SHALCHI, H. SOL, D. SPANGLER, R. STEENKAMP, C. STEGMANN, G. SUPERINA, P. H. TAM, J.-P. TAVERNET, R. TERRIER, M. TLUCZYKONT, C. VAN ELDIK,

- G. VASILEIADIS, C. VENTER, J. P. VIALLE, P. VINCENT, H. J. VÖLK, S. J. WAGNER, M. WARD, Y. MORIGUCHI, and Y. FUKUI (2007) “Discovery of a point-like very-high-energy γ -ray source in Monoceros,” *Astronomy and Astrophysics*, **469**, pp. L1–L4, 0704.0171.
- [113] HINTON, J. A., J. L. SKILTON, S. FUNK, J. BRUCKER, F. A. AHARONIAN, G. DUBUS, A. FIASSON, Y. GALLANT, W. HOFMANN, A. MARCOWITH, and O. REIMER (2009) “HESS J0632+057: A New Gamma-Ray Binary?” *The Astrophysical Journal Letters*, **690**, pp. L101–L104, 0809.0584.
- [114] FALCONE, A. D., J. GRUBE, J. HINTON, J. HOLDER, G. MAIER, R. MUKHERJEE, J. SKILTON, and M. STROH (2010) “Probing the Nature of the Unidentified TeV Gamma-Ray Source Hess J0632+057 with Swift,” *The Astrophysical Journal Letters*, **708**, pp. L52–L56, 0912.0941.
- [115] BURROWS, D. N., J. E. HILL, J. A. NOUSEK, J. A. KENNEA, A. WELLS, J. P. OSBORNE, A. F. ABBEY, A. BEARDMORE, K. MUKERJEE, A. D. T. SHORT, G. CHINCARINI, S. CAMPANA, O. CITTERIO, A. MORETTI, C. PAGANI, G. TAGLIAFERRI, P. GIOMMI, M. CAPALBI, F. TAMBURELLI, L. ANGELINI, G. CUSUMANO, H. W. BRÄUNINGER, W. BURKERT, and G. D. HARTNER (2005) “The Swift X-Ray Telescope,” *Space Science Reviews*, **120**, pp. 165–195, arXiv:astro-ph/0508071.
- [116] REA, N. and D. F. TORRES (2011) “The TeV Binary HESS J0632+057 in the Low and High X-Ray State,” *The Astrophysical Journal Letters*, **737**, L12, 1105.0601.
- [117] ACCIARI, V. A., E. ALIU, T. ARLEN, M. BEILICKE, W. BENBOW, D. BOLTUCH, S. M. BRADBURY, J. H. BUCKLEY, V. BUGAEV, K. BYRUM, A. CANNON, A. CESARINI, A. CESARINI, Y. C. CHOW, L. CIUPIK, P. COGAN, R. DICKHERBER, C. DUKE, T. ERGIN, A. FALCONE, S. J. FEGAN, J. P. FINLEY, G. FINNEGAN, P. FORTIN, L. FORTSON, A. FURNISS, K. GIBBS, G. H. GILLANDERS, J. GRUBE, R. GUENETTE, G. GYUK, D. HANNA, J. HOLDER, D. HORAN, C. M. HUI, T. B. HUMENSKY, A. IMRAN, P. KAARET, N. KARLSSON, M. KERTZMAN, D. KIEDA, J. KILDEA, A. KONOPELKO, H. KRAWCZYNSKI, F. KRENNRICH, M. J. LANG, S. LEBOHEC, S. LEBOHEC, G. MAIER, A. MCCANN, M. MCCUTCHEON, J. MILLIS, J. MILLIS, P. MORIARTY, R. MUKHERJEE, R. A. ONG, A. N. OTTE, D. PANDEL, J. S. PERKINS, D. PETRY, M. POHL, J. QUINN, K. RAGAN, L. C. REYES, P. T. REYNOLDS, H. J. ROSE, M. SCHROEDTER, G. H. SEMBROSKI, A. W. SMITH, D. STEELE, S. SWORDY, M. THEILING, J. A. TONER, A. VARLOTTA, V. V. VASSILIEV, S. VINCENT, R. G. WAGNER, S. P. WAKELY, J. E. WARD, T. C.

- WEEKES, A. WEINSTEIN, T. WEISGARBER, D. A. WILLIAMS, S. WISSEL, and M. WOOD (2009) “Evidence for Long-Term Gamma-Ray and X-Ray Variability from the Unidentified TeV Source HESS J0632+057,” *The Astrophysical Journal Letters*, **698**, pp. L94–L97, 0905.3139.
- [118] ONG, R. A. (2011) “VERITAS Reports Increased Activity of HESS J0632+057 in Very High Energy Gamma Rays,” *The Astronomer’s Telegram*, **3153**, p. 1.
- [119] MARIOTTI, M. (2011) “MAGIC confirms VHE gamma-ray emission from HESS J0632+057 between 7-9 Feb 2011,” *The Astronomer’s Telegram*, **3161**, p. 1.
- [120] FALCONE, A., S. BONGIORNO, M. STROH, and J. HOLDER (2011) “Increased X-ray activity and likely binary period of HESS J0632+057 Observed by Swift-XRT,” *The Astronomer’s Telegram*, **3152**, p. 1.
- [121] ARAGONA, C., M. V. MCSWAIN, and M. DE BECKER (2010) “HD 259440: The Proposed Optical Counterpart of the γ -ray Binary HESS J0632+057,” *The Astrophysical Journal*, **724**, pp. 306–312, 1009.2100.
- [122] SKILTON, J. L., M. PANDEY-POMMIER, J. A. HINTON, C. C. CHEUNG, F. A. AHARONIAN, J. BRUCKER, G. DUBUS, A. FIASSON, S. FUNK, Y. GALLANT, A. MARCOWITH, and O. REIMER (2009) “The radio counterpart of the likely TeV binary HESSJ0632+057,” *Monthly Notices of the Royal Astronomical Society*, **399**, pp. 317–322.
- [123] MOLDON, J., M. RIBO, and J. M. PAREDES (2011) “Detection of radio emission at mas scales from HESS J0632+057 with the e-EVN,” *The Astronomer’s Telegram*, **3180**, p. 1.
- [124] GEHRELS, N., G. CHINCARINI, P. GIOMMI, K. O. MASON, J. A. NOUSEK, A. A. WELLS, N. E. WHITE, S. D. BARTHELMY, D. N. BURROWS, L. R. COMINSKY, K. C. HURLEY, F. E. MARSHALL, P. MÉSZÁROS, P. W. A. ROMING, L. ANGELINI, L. M. BARBIER, T. BELLONI, S. CAMPANA, P. A. CARAVEO, M. M. CHESTER, O. CITTERIO, T. L. CLINE, M. S. CROPPER, J. R. CUMMINGS, A. J. DEAN, E. D. FEIGELSON, E. E. FENIMORE, D. A. FRAIL, A. S. FRUCHTER, G. P. GARMIRE, K. GENDREAU, G. GHISELLINI, J. GREINER, J. E. HILL, S. D. HUNSBERGER, H. A. KRIMM, S. R. KULKARNI, P. KUMAR, F. LEBRUN, N. M. LLOYD-RONNING, C. B. MARKWARDT, B. J. MATTSON, R. F. MUSHOTZKY, J. P. NORRIS, J. OSBORNE, B. PACZYNSKI, D. M. PALMER, H.-S. PARK, A. M. PARSONS, J. PAUL, M. J. REES, C. S. REYNOLDS, J. E. RHOADS, T. P. SASSEEN, B. E. SCHAEFER, A. T. SHORT, A. P. SMALE, I. A. SMITH, L. STELLA, G. TAGLIAFERRI, T. TAKAHASHI, M. TASHIRO, L. K.

- TOWNSLEY, J. TUELLER, M. J. L. TURNER, M. VIETRI, W. VOGES, M. J. WARD, R. WILLINGALE, F. M. ZERBI, and W. W. ZHANG (2004) “The Swift Gamma-Ray Burst Mission,” *The Astrophysical Journal*, **611**, pp. 1005–1020.
- [125] SMITH, A., P. KAARET, J. HOLDER, A. FALCONE, G. MAIER, D. PANDEL, and M. STROH (2009) “Long-Term X-Ray Monitoring of the TeV Binary LS I +61 303 With the Rossi X-Ray Timing Explorer,” *The Astrophysical Journal*, **693**, pp. 1621–1627.
- [126] PRESS, W. H., S. A. TEUKOLSKY, W. T. VETTERLING, and B. P. FLANERY (2007) *Numerical Recipes in C: The Art of Scientific Computing*, Cambridge University Press.
- [127] HORNE, J. H. and S. L. BALIUNAS (1986) “A prescription for period analysis of unevenly sampled time series,” *The Astrophysical Journal*, **302**, pp. 757–763.
- [128] CIPRINI, S., L. O. TAKALO, G. TOSTI, C. M. RAITERI, M. FIORUCCI, M. VILLATA, G. NUCCIARELLI, L. LANTERI, K. NILSSON, and J. A. ROS (2007) “Ten-year optical monitoring of PKS 0735+178: historical comparison, multiband behavior, and variability timescales,” *Astronomy and Astrophysics*, **467**, pp. 465–483, arXiv:astro-ph/0701420.
- [129] XIE, G., T. YI, H. LI, S. ZHOU, and L. CHEN (2008) “Periodicity Analysis of the Radio Curve of PKS 1510-089 and Implications for its Central Structure,” *The Astronomical Journal*, **135**, pp. 2212–2216.
- [130] EDELSON, R. A. and J. H. KROLIK (1988) “The discrete correlation function - A new method for analyzing unevenly sampled variability data,” *The Astrophysical Journal*, **333**, pp. 646–659.
- [131] ALEXANDER, T. (1997) “Is AGN Variability Correlated with Other AGN Properties? ZDCF Analysis of Small Samples of Sparse Light Curves,” in *Astronomical Time Series* (D. Maoz, A. Sternberg, and E. M. Leibowitz, eds.), vol. 218 of *Astrophysics and Space Science Library*, p. 163.
- [132] CASARES, J., M. RIBO, J. M. PAREDES, A. HERRERO, I. NEGUERUELA, and F. VILARDELL (2011) “Absence of radial velocity variations in MWC 148 during the recent activity of HESS J0632+057,” *The Astronomer’s Telegram*, **3209**, p. 1.
- [133] LI, J., D. F. TORRES, S. ZHANG, Y. CHEN, D. HADASCH, P. S. RAY, P. KRETSCHMAR, N. REA, and J. WANG (2011) “Long-term X-Ray Monitoring of LS I +61deg303: Analysis of Spectral Variability and Flares,” *The Astrophysical Journal*, **733**, 89, 1103.4205.

- [134] ZHAO, N., R. MALIK, and W. LIAO (2013), "Difference Amplifier Forms Heart of Precision Current Source," http://www.analog.com/library/analogDialogue/archives/43-09/current_source.html.

Vita

Stephen Bongiorno

Contact Information

Phone: (862) 207-1132

E-mail: stephen.bongiorno@gmail.com

Education and Work

- The Pennsylvania State University (2006 – 2013) Ph.D. Astronomy, August 2012. M.S. Astronomy, May 2008. Dissertation: *Characterization and Applications of Hybrid CMOS Detectors in X-ray Astronomy* Thesis Advisor: Dr. Abe Falcone.
- The Pennsylvania State University 2006 Research assistant working on the Precision Radial Velocity Spectrograph Pathfinder. Supervisor: Prof. Lawrence Ramsey
- The Pennsylvania State University (2001 – 2005) B.S. Physics B.S. Astronomy

Research Interests

1. The application of new physics, especially nano-fabrication techniques, to the design of next generation focal plane arrays.
2. The use of new and exotic materials to improve instrument performance.
3. The application of statistical techniques and novel algorithms to improve the performance of scientific data processing. I am also interested in the use of finite-element and opto-thermal-mechanical simulations to optimize instrument design.
4. The study of extreme astrophysical environments, such as black hole binaries, as a probe of new physics and particle acceleration mechanisms.